Volcanism as an Active Planetary Process on Venus

by

Martin Walter Airey

Thesis submitted to the University of Oxford
for the degree of Doctor of Philosophy
in
Earth Sciences

Department of Earth Sciences
and Wolfson College,
University of Oxford

Trinity, 2015

Supervised by
Prof. T. A. Mather and Prof. D. M. Pyle

Declaration

The contents of this thesis are all my own work, except where otherwise stated. The views and opinions expressed herein are mine and not necessarily those of any other person or body unless so attributed.

Citation: Martin Walter Airey (2015), Volcanism as an Active Planetary Process on Venus, D.Phil. Thesis, University of Oxford, Department of Earth Sciences, Oxford, UK.

Keywords: Venus, Modelling, Remote Sensing, Planetary Sciences, Volcanology

This thesis has been typeset using LaTeXand references were compiled using BibTeX.

Printed in the United Kingdom.

Abstract

Volcanism as an Active Planetary Process on Venus

Martin Walter Airey
Wolfson College, Oxford

Trinity, 2015

Volcanism has been a crucial planetary process in the evolution of Venus, shaping the surface and contributing to the formation of the atmosphere and clouds. Some of the key outstanding questions are whether or not volcanism is active today, and what range of volcanic styles have occurred in the past or may occur in the future. This project uses three methods of investigating these questions. Firstly, computer modelling is used to simulate volcanic processes under Venusian conditions using a steady-state, isothermal, homogeneous flow model. It was found that the addition of CO_2 to an H_2O-driven eruption reduces the H_2O requirement for explosive activity, and that eruptions possible on Venus may be detectable in Venus Express data. Next, radar datasets from both Venus and Earth were investigated with the aim of assessing relationships between differing volcanic deposits on Venus and their likely mode of formation, and using trends in the Earth radar data to inform us of what the Venus observations may be telling us. It was found that, in some cases, regional-scale radar observations may be useful in identifying deposit types, but the data used in the study were insufficient to define a globally applicable deposit identification scheme, pending further study. Finally, mapping and spatial analysis of volcanic features and rifts was performed to evaluate the nature of the interaction of volcanism within the global tectonic environment. Spatial relationships are consistent with aspects of the directional model of Venus' evolution, favouring a shift from globally dispersed, relatively small-scale, volcanism spread randomly across the planetary surface towards a gradually more rift-focused distribution indicative of a corresponding shift in global tectonic regime. These various strands are brought together here in order to contribute to our further understanding of volcanism as a fundamental Venusian planetary process.

Extended Abstract

Volcanism as an Active Planetary Process on Venus

Martin Walter Airey

Wolfson College, Oxford

Trinity, 2015

Volcanism has been a crucial planetary process in terms of the geological evolution of Venus' surface and atmosphere but one of the key outstanding questions is whether it is an ongoing planetary process today. The observations of long-term decline of atmospheric SO_2 punctuated by periodic rapid introductions of SO_2 detected at Venus' cloud tops have provided strong evidence for a volcanic input to the atmosphere, and when taken together with the high-resolution radar data recovered by the Magellan mission in the early 1990s provide compelling evidence for the past and current occurrence of volcanic processes on the surface of Venus. The Venus Express mission has provided additional evidence for volcanism in the form of thermal emissivity anomalies detected by the Visible and Infrared Thermal Imaging Spectrometer (VIRTIS), indicative of young relatively unweathered lava deposits, and infrared hot spot anomalies in the Venus Monitoring Camera (VMC) data found to intensify and subside between Venus Express observations suggesting current dynamic volcanic processes.

The objectives of this thesis were to assess the role of volcanism within the geological and atmospheric processes occurring on Venus, to explore whether or not

volcanism is currently active and what range of volcanic styles are observed, and to place Venusian volcanism into context with the global tectonic environment on Venus. These objectives were achieved firstly by using computer modelling of volcanic processes based on terrestrial modelling methods that are adapted to Venusian conditions. Next, radar datasets from both Venus and Earth were investigated with the aim of assessing relationships between differing volcanic deposits on Venus and their likely mode of formation, and using trends in the Earth radar data to inform us of what the Venus observations may be telling us. Finally, mapping and spatial analysis of volcanic features and rifts was performed to evaluate the nature of the interaction of volcanism within the global tectonic environment.

In the modelling section, the conditions that will promote explosive volcanic activity on Venus were investigated. Conduit processes were simulated using a steady-state, isothermal, homogeneous flow model in tandem with a degassing model. The response of exit pressure, exit velocity, and degree of volatile exsolution were explored over a range of volatile concentrations (H_2O and CO_2), magma temperatures, vent altitudes, and conduit geometries relevant to the Venusian environment. It was found that the addition of CO_2 to an H_2O-driven eruption increases the final pressure, velocity, and volume fraction gas. Increasing vent elevation leads to a greater degree of magma fragmentation, due to the decrease in the final pressure at the vent, resulting in a greater likelihood of explosive activity. Increasing the magmatic temperature generates higher final pressures, greater velocities, and lower final volume fraction gas values with a correspondingly lower chance of explosive volcanism. Cross-sectionally smaller, and/or deeper, conduits were more conducive to explosive activity.

Model runs show that for an explosive eruption to occur at Scathach Fluctus, a pyroclastic deposit at Venus' mean planetary radius (MPR), 4.5% H_2O or 3% H_2O with 3% CO_2 (from a 25 m radius conduit) would be required to initiate fragmentation; at Ma'at Mons ($\sim$9 km above MPR) only $\sim$2% H_2O is required. A buoyant plume

model was used to investigate plume behaviour. It was found that it was not possible to achieve a buoyant column from a 25 m radius conduit at Scathach Fluctus, but a buoyant column reaching up to ∼20 km above the vent could be generated at Ma'at Mons with an H_2O concentration of 4.7% (at 1300 K) or a mixed volatile concentration of 3% H_2O with 3% CO_2 (at 1200 K). The flux of volcanic gases to the lower atmosphere of Venus was also investigated, should explosive volcanism occur. Model results suggest explosive activity at Scathach Fluctus would result in an H_2O flux of $\sim 10^7$ kg s^{-1}. Were Scathach Fluctus emplaced in a single event, the model suggests that it may have been emplaced in a period of ∼15 days, supplying 1-2$\times 10^4$ Mt H_2O to the atmosphere locally. An eruption of this scale might increase local atmospheric H_2O abundance by several ppm over an area large enough to be detectable by near-infrared nightside sounding using the 1.18 μm spectral window such as that carried out by the Venus Express/VIRTIS spectrometer. Further interrogation of the VIRTIS dataset is recommended to search for ongoing volcanism on Venus.

In the radar analysis section, the measured and derived radar properties of volcanic and associated deposits on Venus were studied in order to characterise their physical and compositional properties, and their relationships to one another. The likely resulting geological materials and emplacement mechanisms were explored, allowing inferences into the eruptive style required to result in such conditions; specifically, whether or not explosive deposits could be identified. The identification of pyroclastic material has largely been qualitative historically, highlighting the requirement for a more quantitative approach to making potential deposit type identifications. By ground-truthing any differences in material radar properties with deposits of known origin on Earth, these alone could potentially be diagnostic of the mode of formation of volcanic deposits.

Synthetic aperture radar (SAR) and ancillary data sets (emissivity, reflectivity, altimetry, and RMS slope) from NASA's Magellan mission were collected for various

sites on Venus and compared with terrestrial deposits of known properties. The terrestrial data were collected from ESA's ASAR instrument on board the Envisat satellite, providing the most comparable SAR data possible, and NASA's MODIS instrument on board the Aqua satellite for the comparable reflectivity and emissivity data. In addition to the measured radar datasets and manual geomorphological measurements, numerous derived datasets were calculated from the Venus data, including the dielectric properties, density, and roughness (RMS height, correlation length, and a roughness proxy known as asperity for comparative purposes). A series of case studies was used to explore the information about the study areas available in the data acquired and the relationship between emissivity and rifts was explored to assess this as an indicator of recent activity.

The radar properties of the material from both planets were studied independently and plotted together (SAR backscatter, emissivity, and roughness) to look for whether or not trends in the terrestrial data were mirrored in the Venus data, aiding deposit identification. A potential radar-based indicator of deposit type was tentatively suggested (a relatively high or low emissivity preference dependent on deposit type) in the terrestrial data. The result of this analysis was that an accurate, globally applicable, method of deposit identification using purely radar data seems implausible based on this study, as the datasets were not sufficiently comparable due to the differing radar wavelengths. The trend in the terrestrial data that is observed through the ground-truthing was not apparent using the potential Venusian pyroclastic examples cited in this study. However, if taken on a region by region basis, there is often sufficient difference to form deposit type inferences locally. The potentially pyroclastic bright halos at Irnini and Anala Montes show slightly elevated emissivity relative to the flank material with which they coincide. This is in addition to the systematically and comparably elevated values of backscatter and all roughness properties between these two deposits. This is definitive evidence for a contrast in locally coincident material proper-

ties, and when taken in conjunction with the systematically lower densities of the halos, seems like compelling evidence for pyroclastic material. A global identification scheme is problematic, but smaller-scale regional studies can provide much more meaningful conclusions in comparative terms.

In the mapping and GIS section, new geospatial analysis was performed in ArcGIS, and the quantification of spatial relationships between volcanic features and rifts on Venus was achieved and applied to planetary evolutionary concepts. The rifts and volcanic features evident on Venus were mapped from existing databases; the maps were then combined and modified to form a new hybrid database for the most intensely rifted region on Venus (the Beta-Atla-Themis, BAT, region). Once the volcanic features were mapped, spatial analysis allowed the quantification of geospatial relationships to answer the following questions: 1) how do certain volcanic features occur relative to others of their own kind, 2) how do they occur relative to features of other kinds, and 3) how do they occur relative to rift axes? Firstly, the nearest neighbour index (NNI) was calculated for each type of volcanic feature. This quantity determines the ratio of the observed mean distance between points to the expected mean distance between points in a random distribution and gives an indication of clustering. The mean random NNI of corresponding sample sizes was calculated for comparison with the real populations. To determine the features' relationship with the rift axes, the distance of each feature point on the map from the nearest rift was measured in order to identify any preferred distance from, or affinity for occurring near, rifts. These distances were measured once more with only the distance to the young rifts considered. Population distribution histograms were produced for all these data as well as the corresponding results recorded using the previously selected random datasets for comparison. In order to display on the map where any clustering may be concentrated, feature kernel density maps were also produced.

The analyses of these data defined new evidence supporting aspects of the directional model of Venus' evolution. This shift from the globally dispersed, relatively small-scale, volcanism spread randomly across the planetary surface towards the gradually more rift-focused distribution is indicative of a corresponding shift in global tectonic regime. The model stages suggested here are that of a stagnant lid scenario, with widely dispersed, discrete zones of small plume-fed activity, followed by a transition via gradual conductive cooling to that of a subcrustal spreading regime whereby continued and ongoing volcanism may persist in tandem with the directional model background.

Through these various strands, this thesis contributes to furthering our understanding of volcanism as a fundamental planetary process in the Venus system. In the process, the combination of the observations from the synthesis of the different approaches converge to provide some key findings: volcanism on Venus is likely to be active today, explosive volcanism is potentially possible given certain model assumptions, and there may therefore be more volatiles in the mantle than previously thought.

Acknowledgements

My D.Phil studentship was generously funded by the Science and Technology Facilities Council, without which I could have not undertaken this project. Additional funds were received from the Volcanic and Magmatic Studies Group, the Geological Remote Sensing Group, the Universities Space Research Association, and the Earth Sciences Departmental Burdett-Coutts fund. The additional sources enabled me to attend numerous national and international conferences, building a strong and ongoing professional network.

It has been a pleasure and a privilege to have worked under the keen supervision of Tamsin Mather and David Pyle, whose encouragement and expertise have guided me through the process from concept to completion. I am a more thorough and confident researcher as a result of their mentoring and advice.

I am also very grateful to my collaborators on various projects. In particular, Colin Wilson for his endless enthusiasm and invaluable discussions, Richard Ghail for his guidance with radar interpretation and methods, Lori Glaze for her limitless encouragement and guidance, and Karen Aplin for many useful discussions. I appreciate the time of all of these people, who have been most forthcoming with their wealth of knowledge on Venus and planetary processes. Additional thanks also go to Lori Glaze for the use of her subaerial plume code, with which I could perform additional modelling analyses.

I would like to extend my gratitude also to the European Space Agency for ap-

proving my proposal for a data allowance, facilitating additional comparative radar work.

Further thanks go to the administrative, computing, and technical staff in the Department who have answered my many queries and ensured smooth progression from arriving in Oxford, traversing the milestones of D.Phil study, and putting together this work.

Finally, my family deserve a very heartfelt thank you for their undying love and support in so many ways. Without their patience and sacrifice, this would not have been possible and I owe them a huge debt of gratitude.

Contents

List of Figures

List of Tables

List of Acronyms

ALTA	Altimeter Horn Antenna
APVC	Altiplano-Puna Volcanic Complex
ASAR	Advanced Synthetic Aperture Radar
ASPERA	Analyzer of Space Plasmas and Energetic Atoms
AU	Astronomical Unit
BAT	Beta-Atla-Themis
CIPW	Cross, Iddings, Pirsson, and Washington
DN	Digital Number
EAR	East African Rift
EARS	East African Rift System
ESA	European Space Agency
GIS	Geographic Information System
GRS	Gamma Ray Spectral
GVP	Global Volcanism Program
HGA	High Gain Antenna
IR	Infrared
IS	Image Swath
JPL	Jet Propulsion Laboratory
LIL	Large Lithophile Elements

LIP	Large Igneous Province
MESSENGER	Mercury Surface, Space Environment, Geochemistry, and Ranging
MODIS	Moderate-Resolution Imaging Spectrometer
MORB	Mid-Ocean Ridge Basalt
MPR	Mean Planetary Radius
NASA	National Aeronautics and Space Administration
NEST	Next ESA SAR Toolbox
NMORB	Normal Mid-Ocean Ridge Basalt
NNI	Nearest Neighbour Index
NVR	Nabro Volcanic Range
OIB	Ocean Island Basalt
PFS	Planetary Fourier Spectrometer
PVO	Pioneer Venus Orbiter
RMS	Root Mean Square
SAR	Synthetic Aperture Radar
SOIR	Solar Occultation in the Infrared
SPA	Stationary Phase Approximation
SPICAV	Spectroscopy for Investigation of Characteristics of the Atmosphere of Venus
SPM	Small Perturbation Model
SRTM	Shuttle Radar Topography Mission
SSD	Steep-sided Dome
USGS	United States Geological Survey
UV	Ultraviolet
VeRa	Venus Radio Science Experiment
VIRA	Venus International Reference Atmosphere

VIRTIS	Visible and Infrared Thermal Imaging Spectrometer
VMC	Venus Monitoring Camera
VTTS	Valley of Ten Thousand Smokes
XRF	X-Ray Fluorescence

Chapter 1

Introduction

Volcanism has been an important process in terms of the evolution of Venus and may continue to be so today. The following introduction aims to put volcanism on Venus into context by giving a broad overview of our understanding of the planetary processes occurring on Venus. The interlinking geological, atmospheric, and exospheric processes will be addressed in turn following a brief overview and discussion of the history of the study of our closest neighbour. This chapter then concludes with a description of how this project aims to extend our previous knowledge of volcanism on Venus.

1.1 Background

1.1.1 Overview

Venus, the second terrestrial planet from our star at ∼0.7 AU, orbits the Sun between Mercury and Earth in the inner Solar system. It has long been considered a sister planet to our own due to the similarities in terms of its size and mass with a mean planetary radius of 6051.8 km and a mass of 4.87×10^{24} kg (0.950 and 0.816 times those of Earth, respectively) (*Williams*, 2013). This however, is where the similarity ends. Venus has an orbital period of ∼224 Earth days and a very slow retrograde rotation which completes one rotation about its axis every ∼243 Earth days. As a result of this, a day on Venus is longer than a year. The surface of Venus is characterised by extreme

conditions compared with Earth, with ∼9.2 MPa surface atmospheric pressure and a mean surface temperature of ∼730 K (*Taylor*, 2010). These conditions are primarily due to the dense CO_2-rich atmosphere.

Even with its closer proximity to the Sun, the surface of Venus actually receives less solar radiation than the Earth due to the highly reflective H_2SO_4 clouds with a very high Bond albedo of ∼0.9 (*Mallama et al.*, 2006; *Williams*, 2013). In spite of this, the intense greenhouse effect enables the high surface temperatures to be achieved. In contrast to Earth, Venus is a dry planet, with the complete absence of H_2O in its liquid state and only very little present in its gaseous form the atmosphere. The mantle is also thought to be depleted of water; this has important implications that will be discussed later (section 1.2.4).

The study of the planet Venus and the dynamic interactions between its geology, atmosphere, and climate provides us with a unique case study with which to explore the effects of climate warming and the evolution of extreme environments on a planetary scale (*Taylor and Grinspoon*, 2009; *Taylor*, 2011). By devising and refining Venus climate models (e.g. *Bullock and Grinspoon*, 1996), we can potentially use the results to improve Earth-based climate models with which to improve our forecasting ability and, as a result, make better informed decisions about the future of our own planet. In the wider context, a fuller understanding of the atmospheres of terrestrial planets can aid us in our search for exoplanets from gaining insights into how planetary systems evolve and how surface conditions respond to external stressors.

Another subject, that has captured much interest, is the possibility of the emergence of life on other planets – Venus included. Venus seems to harbour a harsh, hostile environment, not one conducive to developing life forms; however, the possibility remains. Indeed, isotopic evidence for a once much wetter (and also cooler due the H_2O driven removal of atmospheric CO_2 via chemical weathering processes) environment suggests that conditions may have been more favourable for life in the geological past (*Donahue et al.*, 1982; *Grinspoon*, 1993; *Donahue*, 1999; *Barabash et al.*, 2007a, also see section 1.2.4). Further study of our sister planet will eventually give us answers to

many questions over a broad range of topics and enrich our understanding of the Solar system and indeed the universe.

1.1.2 History of exploration - Venera to Magellan

Humankind has known of the existence of the planet Venus since our earliest ancestors gazed skyward; however, its true relationship with Earth was not initially appreciated. Some ancient civilisations initially named it as two separate entities, the Morning and Evening stars, also known as Phosphorous and Hesperus or Lucifer and Vesper to the Greeks and Romans, respectively. This illusion is due to the planet's inferior orbit to Earth and its illumination by the Sun at sunrise and sunset at different stages of its orbit. The Greeks, however, accepted the Babylonian's view that it was in fact one planet. The misconception held by some that it was two celestial bodies was later further re-evaluated through conceptual developments such as the Copernican heliocentric model of the Solar system (*Copernicus*, 1543).

In more recent times, with the birth of the technological age, a more direct approach to the study of Venus could be realised. Following a period of Earth-based radar observations in the late 1950s and early 1960s (*Richardson*, 1955, 1958; *Mayer et al.*, 1958; *Sagan*, 1960; *Barrett*, 1961; *Pettengill et al.*, 1962, and many others), the ongoing, albeit sporadic, study of Venus utilising spacecraft technology began in 1961 with the Venera 1 mission. Although contact was lost and this mission was unsuccessful, it signalled the beginning of an intense period of Venus spacecraft missions throughout the 1960s, '70s, and '80s, most notably the Russian Venera program and Vega missions and the USA's Mariner and Pioneer missions; see Table 1.1 for a summary of recent Venus exploration. This period began to bear fruit in 1962 with the successful flyby of Mariner 2, which gave us our first impression of the extreme surface temperature inferred from microwave measurements (*Barath et al.*, 1964; *Pollack and Sagan*, 1967). A string of failed missions followed until the coincident Venera 4/Mariner 5 successes of 1967. Venera 4 successfully entered the Venusian atmosphere in October 1967 from where the descent probe transmitted pressure, temperature, and compositional data

Table 1.1: Summary of spaceborne missions to Venus since 1961.

Mission	Country	Type	Success	Launch	Arrival	Notes
Sputnik 7	USSR	Flyby	No	Feb '61		
Venera 1	USSR	Flyby	No	Feb '61		
Mariner 1	USA	Flyby	No	Jul '62		
Sputnik 19	USSR	Lander	No	Aug '62		
Mariner 2	USA	Flyby	Yes	Aug '62	Dec '62	First successful mission
Sputnik 20	USSR	Flyby	No	Sep '62		
Sputnik 21	USSR	Flyby	No	Sep '62		
Kosmos 21	USSR	Flyby	No	Nov '64		
Venera 1964A	USSR	Flyby	No	Feb '64		
Venera 1964B	USSR	Flyby	No	Mar '64		
Kosmos 27	USSR	Flyby	No	Mar '64		
Zond 1	USSR	Flyby	No	Apr '64		
Venera 2	USSR	Flyby	No	Nov '65		
Kosmos 96	USSR	Flyby	No	Nov '65		
Venera 1965A	USSR	Flyby	No	Nov '65		
Venera 4	USSR	Probe	Yes	Jun '67	Oct '67	First in situ probe
Mariner 5	USA	Flyby	Yes	Jun '67	Oct '67	
Kosmos 167	USSR	Probe	No	Jul '67		
Venera 5	USSR	Probe	Yes	Jan '69	May '69	
Venera 6	USSR	Probe	Yes	Jan '69	May '69	
Venera 7	USSR	Lander	Yes	Aug '70	Dec '70	First landing
Kosmos 359	USSR	Lander	No	Aug '70		
Venera 8	USSR	Lander	Yes	Mar '72	Jul '72	
Kosmos 482	USSR	Lander	No	Mar '72		
Mariner 10	USA	Flyby	Yes	Nov '73	Feb '74	
Venera 9	USSR	Orbiter/Lander	Yes	Jun '75	Aug '75	First surface images
Venera 10	USSR	Orbiter/Lander	Yes	Jun '75	Aug '75	
Pioneer Venus 1	USA	Orbiter	Yes	May '78	Dec '78	First global map
Pioneer Venus 2	USA	Probe	Yes	Aug '78	Dec '78	
Venera 11	USSR	Orbiter/Lander	Yes	Sep '78	Dec '78	
Venera 12	USSR	Orbiter/Lander	Yes	Sep '78	Dec '78	
Venera 13	USSR	Orbiter/Lander	Yes	Oct '81	Mar '82	
Venera 14	USSR	Orbiter/Lander	Yes	Nov '81	Mar '82	
Venera 15	USSR	Orbiter	Yes	Jun '83	Oct '83	
Venera 16	USSR	Orbiter	Yes	Jun '83	Oct '83	
Vega 1	USSR	Lander/Balloon	Yes	Dec '84	Jun '85	
Vega 2	USSR	Orbiter/Lander	Yes	Dec '84	Jun '85	
Magellan	USA	Orbiter	Yes	May '89	Aug '90	SAR map - 98%
Galileo	USA	Flyby	Yes	Oct '89	Feb '90	
Cassini-Huygens	USA	Flyby	Yes	Oct '97	Apr '98 Jun '99	
MESSENGER	USA	Flyby	Yes	Aug '05	Oct '06 Jun '07	
Venus Express	Europe	Orbiter	Yes	Nov '05	Jun '06	
Akatsuki	Japan	Orbiter	No	May '10		Retry orbit 2015

back to Earth; these data confirmed the high temperature conditions, gave our first impression of the high atmospheric pressure (*Avduevsk et al.*, 1968), and provided the first in situ measurements of the atmospheric chemical composition of predominantly CO_2 with secondary N_2 (*Vinograd et al.*, 1968). The combined success of this mission with that of the Mariner 5 flyby gave us our first good overall knowledge of Venus' atmosphere and its planetary scale physical and chemical characteristics. Subsequent missions up to the mid-1980s followed with varying degrees of success, including the extended Venera programme (Veneras 5-16), Mariner 10, Pioneer Venus Orbiter (PVO),

and Vegas 1 & 2, providing a wealth of data on the planet's atmosphere, ionosphere, magnetic properties, and surface composition. This period saw the first successful landing on the planet's surface by Venera 7, the first images from the surface provided by Venera 9, the first evidence for lightning by Venera 11, the first X-ray fluorescence (XRF) bulk geochemical analysis of surface material by Venera 13, and the first global mapping exercise by PVO. In addition to mapping the vast majority of the planet at a resolution of ∼150 km, PVO carried an impressive payload of 17 instruments to monitor the atmosphere, clouds, and magnetic and gravitational properties of Venus as well as the solar wind and provided prodigious data.

The next two decades following this intense period of activity saw a hiatus in dedicated Venus exploration with the exception of the USA's Magellan mission (and the Galileo flyby en route to Jupiter in 1989). In August 1990, the Magellan spacecraft entered orbit around Venus. Over the duration of the mission, a synthetic aperture radar mapped 98% of the surface of Venus at a resolution resampled to 75 m/pixel from an original (variable with latitude) resolution of >100 m/pixel, allowing detailed observations of surface features. This remains the highest resolution mapping exercise of Venus to date. There followed four other flyby exercises associated with missions to other planets, Cassini-Huygens in 1998 and 1999 en route to Saturn, and MESSENGER in 2006 and 2007 en route to Mercury.

1.1.3 History of exploration - Venus Express

In the most recent phase of Venus-specific exploration, following on from the success of the Mars Express project, ESA developed the Venus Express spacecraft, which went into orbit around Venus in April 2006. The orbiter had a payload of seven instruments with which to investigate the Venus environment (See Figure 1.1), a summary of which follows (after *Svedhem et al.*, 2007a).

SPICAV/SOIR (SPectroscopy for Investigation of Characteristics of the Atmosphere of Venus/Solar Occultation in the InfraRed) was a suite of three spectrometers with which to investigate the atmosphere of Venus in solar and stellar occultation, limb,

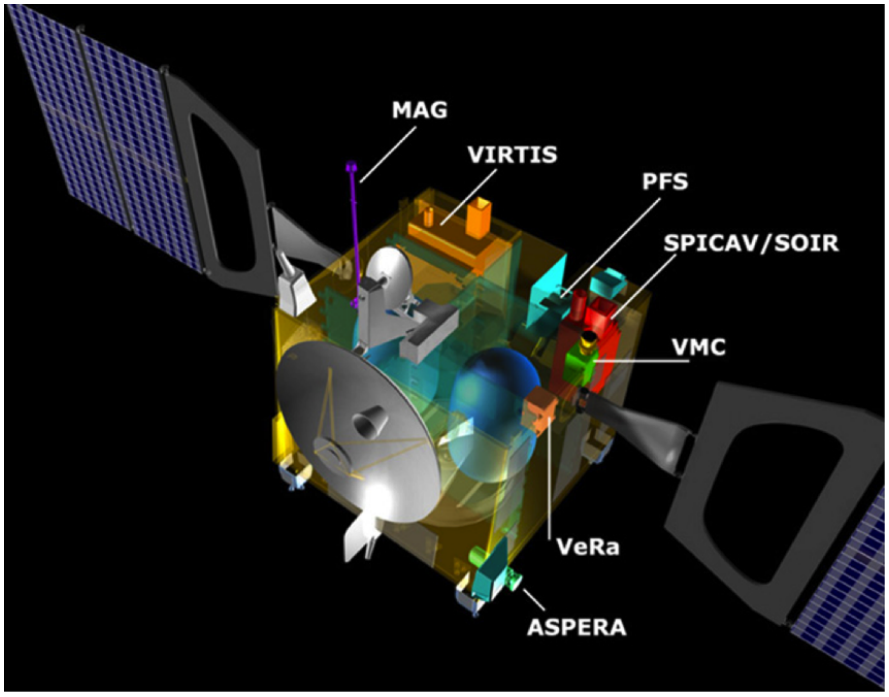

Figure 1.1: Computer simulated image of Venus Express showing the instrumentation layout. See text for description. Spacecraft is 1.7 × 1.7 × 1.5 m and the solar panel span is ∼6 m. From *Svedhem et al.* (2007a).

and nadir modes. SPICAV had UV and IR modes, whereas SOIR operated in the IR only. By exploiting various wavelengths, this range of spectrometers allowed the sensing of various chemical species including SO_2, SO, H_2O, HDO, COS, CO, HCl, and HF at a range of altitudes above the cloud tops using stellar and solar sources (*Bertaux et al.*, 2007). Venus Express had two other spectrometers on board; the ill-fated PFS (Planetary Fourier Spectrometer), a high-resolution IR spectrometer that malfunctioned and was stuck in its closed position, and VIRTIS (Visible and InfraRed Thermal Imaging Spectrometer). VIRTIS had multiple objectives: to measure trace gases in the lower atmosphere (by peering through spectral 'windows' in the dense cloud deck), surface thermal emissivity, gases and aerosols at the cloud tops, atmospheric dynamics, and the mesospheric temperature profile (*Baines et al.*, 2006; *Drossart et al.*, 2007).

VeRa (Venus Express Radio science experiment) was an instrument with multiple objectives (*Häusler et al.*, 2006). Primarily, VeRa mapped the vertical structure of Venus' atmosphere and ionosphere using radio signals. High-resolution sounding cap-

tured density and temperature profiles from below the cloud deck to an altitude of ∼100 km and H_2SO_4 concentration below the clouds by means of radio occultation. In addition, the ionospheric electron density could be measured up to the ionopause (∼600 km). VeRa also had surface goals including gravity measurements and targeted radar sounding objectives. Also studying ionospheric processes on Venus was ASPERA-4 (Analyzer of Space Plasma and EneRgetic Atoms), which was designed to characterise the effects of the solar wind on the atmosphere using various sensors: two neutral particle detectors, a neutral particle imager, an electron spectrometer, and an ion mass analyzer (*Barabash et al.*, 2007b).

Also aboard Venus Express were the Venus Monitoring Camera (VMC) and the magnetometer (MAG). VMC was a wide-angle camera with the primary objective of studying atmosphere and cloud dynamics by tracking cloud features and bright spots. In addition to nadir imaging, limb imaging was also possible in order to characterise haze distribution and the wind field within the atmosphere (*Markiewicz et al.*, 2007). MAG measured the magnetic properties of Venus (*Zhang et al.*, 2006), which are largely induced by solar wind-ionosphere processes, as Venus has no internally produced magnetic field. MAG was also designed to search for signals of lightning by measuring the electromagnetic waves associated with possible atmospheric electrical discharges (*Russell et al.*, 2006).

Approaching the end of the mission lifetime, an aerobraking campaign was undertaken in 2014 to test the procedure and make bonus in situ observations of the atmospheric density. MAG and ASPERA were also utilised in this campaign to make further in situ measurements. The spacecraft descended into Venus' atmosphere for the final time in December 2014, with contact finally being lost in January 2015.

1.2 Planetary Processes

1.2.1 Formation and evolution

The Solar system is thought to have formed by gravitational collapse of a cloud of interstellar dust and gas. This formed the Sun and a protoplanetary accretionary disc, from which all the planets formed over a few 10s of million years during the same planet-forming episode ∼4.6 Ga ago (*Woolfson*, 2000; *Bouvier and Wadhwa*, 2010). Earth, Venus, and Mars are, it follows, despite the very different conditions on their surfaces today (see Table 1.2), of roughly the same age and composition and so must have taken divergent evolutionary paths from similar original states to achieve their current states (*Taylor*, 2011).

Mars, being much smaller than both Earth and Venus, seems to have cooled sufficiently so that significant volcanism no longer occurs, with a best estimate of the geothermal surface heat flux being ∼15 mW m^{-2} (*Clifford et al.*, 2010) compared with 65-101 mW m^{-2} on Earth (*Pollack et al.*, 1993a). With no magnetic field to protect it, most of Mars' atmosphere was stripped away by the solar wind and collisional erosion leaving a cold tenuous atmosphere in its place (*Melosh and Vickery*, 1989; *Jakosky et al.*, 1994). Earth's atmosphere is thought to have once been much more CO_2-rich as vast carbonate reservoirs bear testament (*Kasting*, 1993). The presence of liquid water has allowed carbon sequestration on an enormous scale and the evolution of photosynthesising organisms which, amongst other factors, has left the planet with a very different atmosphere today (*Holland*, 2006).

Venus, however, has retained its primordial CO_2 atmosphere, despite its lack of an internal magnetic field. This is due to a strong gravitational pull on a denser atmosphere and Venus' induced magnetosphere, generated by the interaction between the charged particles of the solar wind and Venus' ionosphere (*Bertucci et al.*, 2011), having some shielding effect. Both these factors act to hold and maintain Venus' atmosphere. The dense CO_2 atmosphere now maintains an intense greenhouse effect, where the incoming solar radiation is trapped by this strong greenhouse gas, resulting in the high

Table 1.2: Current atmospheric data for Venus, Earth, and Mars. The atmospheric compositions are given in mole fractions with ∼0 meaning undetermined, but very small. From *Taylor* (2010).

	Venus	Earth	Mars
Atmosphere			
Molecular weight (g)	43.44	28.98 (dry)	43.49
Surface temperature (K)	730	288	220
Surface pressure (MPa)	9.2	0.1	0.0007
Mass (kg)	4.77×10^{20}	5.30×10^{18}	$\sim10^{16}$
Composition			
Carbon dioxide	0.96	0.0003	0.95
Nitrogen	0.035	0.770	0.027
Argon	0.00007	0.0093	0.016
Water vapour	∼0.0001	∼0.01	∼0.0003
Oxygen	∼0	0.21	0.0013
Sulphur dioxide	150 ppm	0.2 ppb	∼0
Carbon monoxide	40 ppm	0.12 ppm	700 ppm
Neon	5 ppm	18 ppm	2.5 ppm

surface temperature found on Venus. Strong evidence suggests ongoing volcanic activity (*Esposito*, 1985; *Smrekar et al.*, 2010; *Marcq et al.*, 2013; *Shalygin et al.*, 2015). If this is the case then CO_2 will be actively replenished in Venus' atmosphere, along with H_2O and SO_2, which undergo photochemical reactions to sustain the H_2SO_4 clouds (*Bullock and Grinspoon*, 2001).

1.2.2 Geology

Study of the radar images gathered during the Magellan mission suggests that the geology of Venus is dominated by igneous processes. In evidence are volcanic landforms ranging from clusters of small shield volcanoes as small as ∼1 km in diameter, to voluminous lava flows covering up to $\sim10^4$ km^2 (*Esposito et al.*, 2007), and extensional/compressional surface features that are considered to be due to subsurface processes associated with magmatic centres (*Crumpler and Aubele*, 2000) (see section 1.2.3). There has been no recorded evidence to suggest the occurrence of metamorphic rocks, which is not to suggest that examples may not occur locally, however the lack of substantial plate tectonic processes (see section 1.2.3) will obviously inhibit the trans-

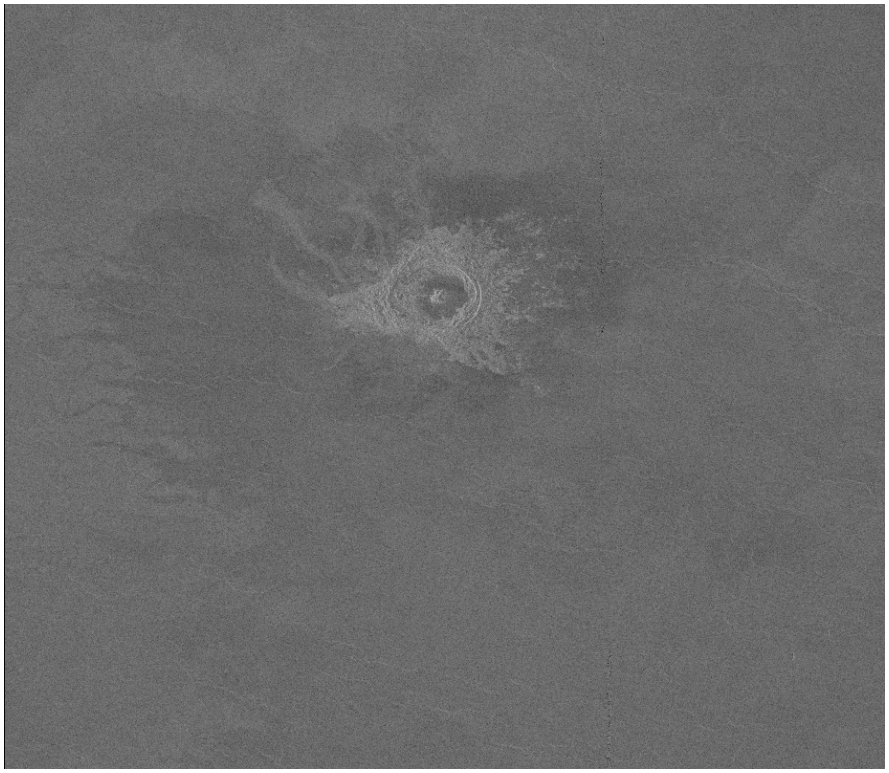

Figure 1.2: Impact crater 'Jeanne' situated in Sedna Planitia. Image centred at 39.9°N 331.6°E and illuminated from the left. The proximal radar-bright ejecta deposits and distal radar-dark fine deposits to the NE suggest an oblique impact from the SW. Note the central peak characteristic of craters between ∼16-40 km in diameter (*Schaber et al.*, 1992). The crater is ∼20 km in diameter. NASA/JPL.

port of metamorphosed material to the surface. The absence of any liquid water at Venus' surface and in its atmosphere restricts any sedimentary deposits to those that do not involve the physical and/or chemical interaction with H_2O. Certain regions of radar dark deposits associated with impact craters that may represent redistributed fines (*Campbell et al.*, 1992) (Figure 1.2), and structures formed by aeolian processes such as wind streaks (Figures 1.3 and 1.4), dunes (Figure 1.4), and yardangs (Figure 1.5) are also observed on Venus (*Greeley et al.*, 1992).

Seven of the Russian lander missions achieved successful landings on the plains of Venus and were able to carry out geochemical surveys and transmit the data before they were irreparably damaged by the hostile conditions at the surface. Figure 1.6 shows the landing sites and Table 1.3 provides a summary of conditions at these sites. Veneras 8, 9, 10, 13, & 14, and Vegas 1 & 2 performed X-ray fluorescence (XRF) analyses of

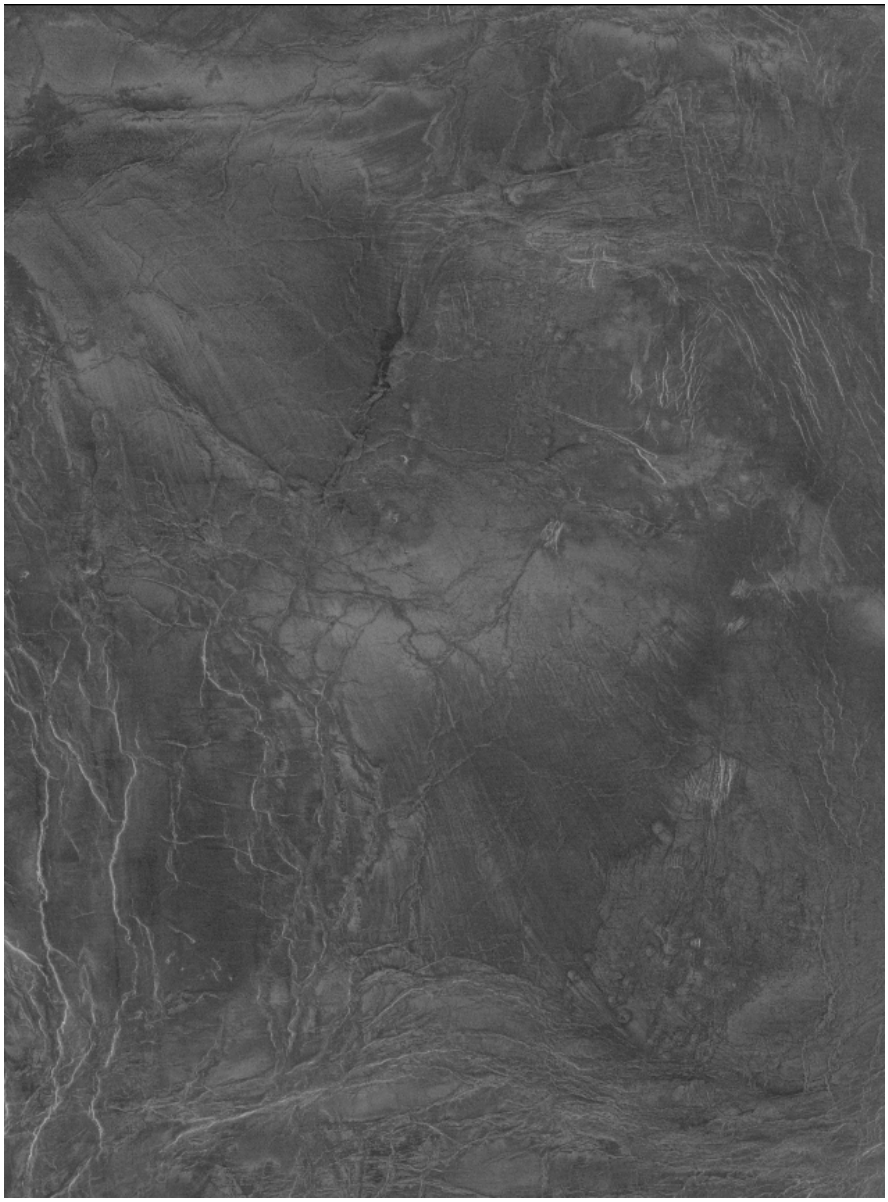

Figure 1.3: A clear example of wind streaks oriented NW-SE located on Akhtamar Planitia ∼100 km NE of Mead crater – the largest impact crater on Venus (*Ford et al.*, 1993). Image centred at 15.5°N 60.2°E and illuminated from the left. Fan streaks in the lower right of the image indicate a northwesterly wind direction. Image is ∼110 km across. NASA/JPL.

the soil samples and/or gamma-ray spectral (GRS) analyses of K, U, and Th. These data are summarised in Table 1.4 (Kargel, et al., 1993). These analyses show that the bulk geochemical properties suggest that the rock types at the Venera 14 and Vega 2 sites are tholeiitic basalts with silica contents of ∼50 wt% and K_2O + Na_2O of ∼2 wt%, similar in composition to Mid-ocean ridge basalts (MORBs) on Earth (*Engel and*

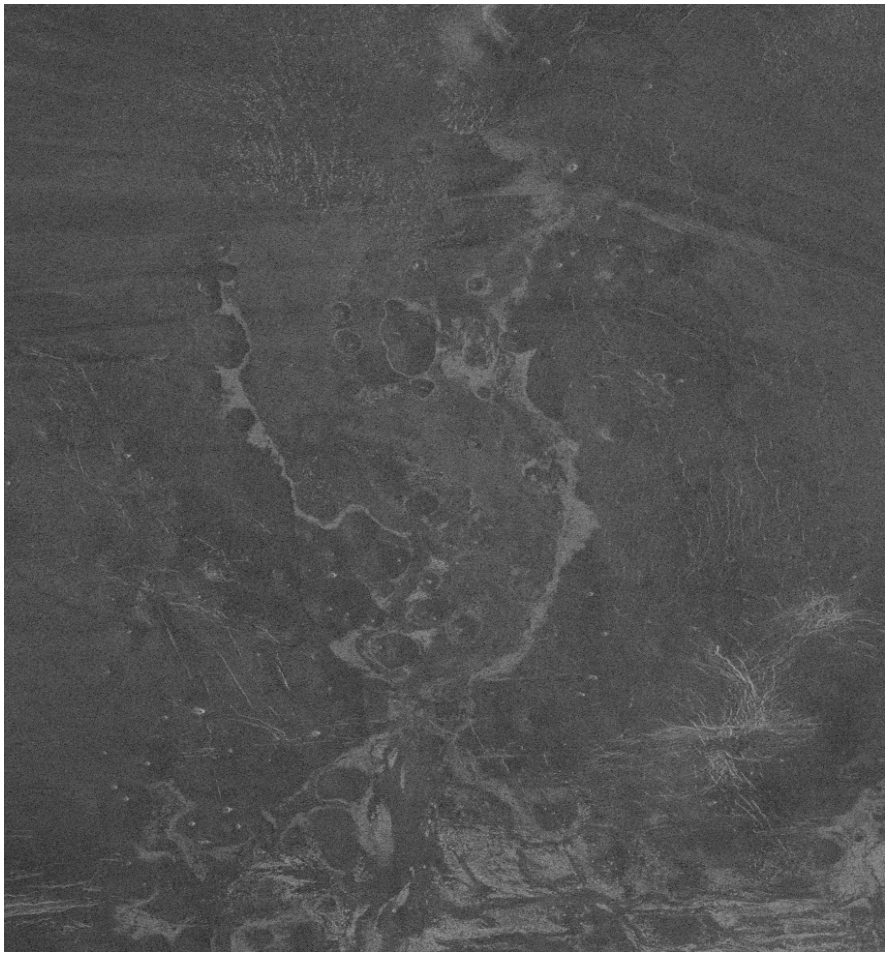

Figure 1.4: Dune field located in the north of Lavinia Planitia. Image centred at 25.2°S 339.7°E and illuminated from the left. Dune morphology indicative of a wind direction from the east. Note also another example of wind streaks at the top of the field of view. Image is ∼100 km across. NASA/JPL.

Engel, 1964). These rocks constitute primitive material derived from partial melting of a mantle source, probably as a result of a rifting/upwelling mechanism.

The material analysed at the Venera 13 site however, is somewhat different. It has much higher alkali content, most notably the potassium content, which is greater than twice the average potassium content of alkali basalts on Earth. The normalised mineralogical analysis states that orthoclase feldspar and rarer feldspathoidic minerals occur in preference to plagioclase in this sample. *Kargel et al.* (1993) classify this sample as a leucitite, a form of alkali-rich mafic rock containing the potassic aluminosilicate mineral leucite found scarcely on Earth. It has been proposed that likely mechanisms for

Figure 1.5: Yardangs located in the south of Akhtamar Planitia. Image centred at 8.84°N 60.0°E and illuminated from the left. It is difficult to discern whether the wind direction is SW-NE or NE-SW. Image is ∼60 km across. NASA/JPL.

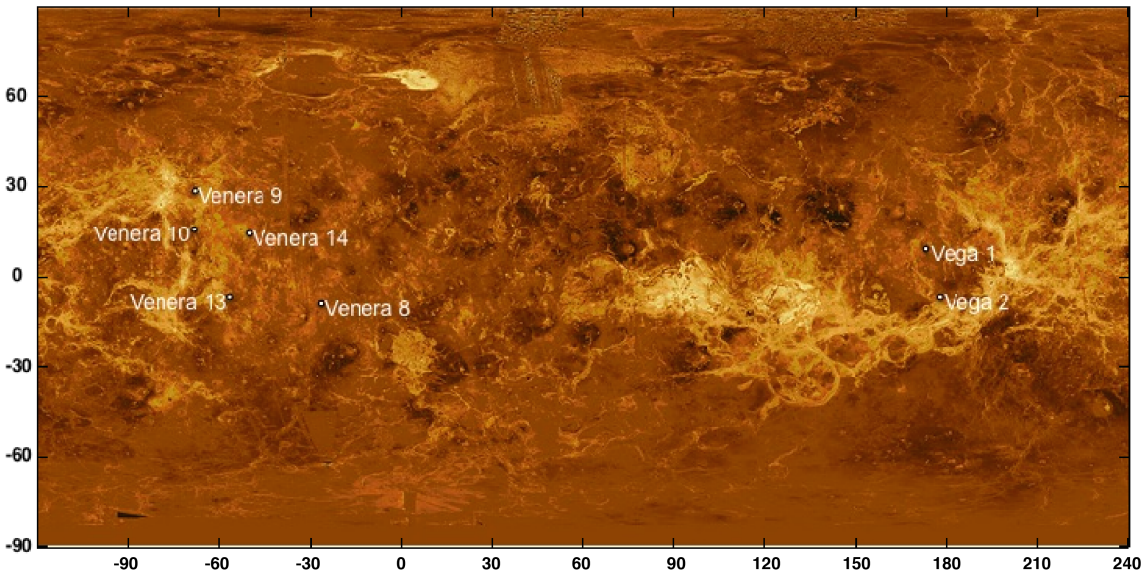

Figure 1.6: Global Magellan SAR mosaic with colour scale relating to radar backscatter intensity as described in chapter 3, labelled with the seven sites visited by the Russian landers (*Kargel et al.*, 1993). Background image, NASA/JPL.

Table 1.3: Coordinates and geological descriptions of Venus probe landing sites. From *Treiman* (2007) (After *Kargel et al.*, 1993; *Abdrakhimov and Basilevsky*, 2002; *Fegley*, 2004)

Lander	Lat (°)	Long (°)	Geography	Geology
Venera 8	-10.70	335.24	E Navka Planitia	Mottled plains with small cones and pancake domes in a possible corona.
Venera 9	31.01	291.64	NE slope Beta Regio	Aikhylu Chasma rift system in lava flows from Devana Chasma/Beta Regio.
Venera 10	15.42	291.51	SE margin Bets Regio	Probably from small shield volcano, Samodiva Mons, to S. Possibly older flows of nearby coronae.
Venera 13	-7.55	303.69	Navka Planitia, E of Phoebe Regio	Dark plains flows from rift system. Near domes and possible corona.
Venera 14	13.05	310.19	Navka Planitia, E of Phoebe Regio	Landing ellipse centred on caldera of small shield volcano (Panina Patera).
Vega 1	8.10	175.85	Rusalka Planitia, N of Aphrodite Terra	Dark, smooth, widely fractured lava plains.
Vega 2	-7.14	177.67	Rusalka Planitia, E of Aphrodite Terra	Dark, smooth, widely fractured lava plains. Between Eigin and Sith coronae.

Table 1.4: XRF and GRS analyses of the seven soil samples analysed by the Russian lander missions, all of which landed in regions composed of plains material. Oxides in wt% (XRF), elements in ppm (GRS), and mineralogy in CIPW normative wt%. (From *Kargel et al.*, 1993)

		Venera 8	Venera 9	Venera 10	Venera 13	Venera 14	Vega 1	Vega 2
SiO_2		-	-	-	45.8±3.0	50.0±3.6	-	50.8±3.2
MgO		-	-	-	11.6±6.2	8.3±3.3	-	12.8±3.7
FeO		-	-	-	9.4±2.2	9.0±1.8	-	7.7±1.1
CaO		-	-	-	7.2±1.0	10.6±1.2	-	8.3±0.7
Al_2O_3		-	-	-	16.0±3.0	18.4±2.6	-	17.8±1.8
TiO_2		-	-	-	1.6±0.5	1.28±0.4	-	0.22±0.1
MnO		-	-	-	0.20±0.10	0.16±0.08	-	0.16±0.12
K_2O		-	-	-	4.1±0.63	0.21±0.07	-	0.11±0.08
Na_2O		-	-	-	4.1±2.5	2.0±1.0	-	2.0±1.0
K		40000±12000	4700±800	3000±1600	-	-	4500±2200	4000±2000
U		2.2±0.7	0.60±0.16	0.46±0.26	-	-	0.64±0.47	0.68±0.38
Th		6.5±0.2	3.65±0.42	0.70±0.34	-	-	1.5±1.2	2.0±1.0
K-spar	or	-	-	-	10.2	1.2	-	0.7
Plag	ab	-	-	-	0.0	17.0	-	17.0
	an	-	-	-	13.1	40.6	-	39.3
Fld-oid	lc	-	-	-	11.2	0.0	-	0.0
	ne	-	-	-	18.8	0.0	-	0.0
Cpx	wo	-	-	-	9.4	5.0	-	0.8
	en	-	-	-	5.8	2.8	-	0.5
	fs	-	-	-	3.0	2.0	-	0.2
Opx	en	-	-	-	0.0	14.2	-	20.8
	fs	-	-	-	0.0	10.1	-	9.2
Olivine	fo	-	-	-	16.2	2.6	-	7.4
	fa	-	-	-	9.3	2.1	-	3.6
Oxide	il	-	-	-	3.0	2.4	-	0.4
Total		-	-	-	100.0	100.0	-	99.9

the formation of this rock type on Venus could be: (a) melting of peridotite which had previously undergone alkaline metasomatism at high pressure (7-10 GPa), or (b) melting of CO_2-saturated peridotite near 2 GPa (*Barsukov*, 1992). More recent analysis suggests that the alkali enrichment could be due to differentiation processes associated with the 'shield field' in which Venera 8 landed, as opposed to the flood basalts characteristic of the other landing sites (*Basilevsky*, 1997).

With a lack of any better data, the samples from the Veneras 9, 10, and Vega 1 sites are considered to be similar in composition to the MORB-like Venera 14 and Vega

2 samples, and the K-rich Venera 8 sample is considered to be similar in composition to the leucititic Venera 13 sample (*Kargel et al.*, 1993).

The GRS analyses of K, U, and Th have found all the Venera and Vega samples to be enriched with respect to NMORB (normal MORB) in these radioactive elements. Veneras 9 and 10, and Vegas 1 and 2 moderately so and Venera 8 greatly so; it is also assumed that they are similarly enriched in the other large-ion lithophile (LIL) elements (*Nikolaeva and Ariskin*, 1999). The reasons for this are not clear but possible scenarios could include a mantle source of less Earth-like composition, fractionation processes not yet considered (*Nikolaeva and Ariskin*, 1999), or indeed a smaller degree of partial melting.

Venus is characterised by a broadly unimodal topography with ∼80% of the planet's surface within ±1 km of the mean planetary radius (*Pettengill et al.*, 1980). On a global scale, the most obvious surface observation is the contrast between the planitiae (vast lowland regions) thought to be composed of basaltic material, and the tesserae (highly deformed highland regions) of uncertain composition. Low-emissivity anomalies found in the analysis of 1.01 μm infrared VMC data are, however, suggestive of a more felsic composition for these highland terrains (*Basilevsky et al.*, 2012). All the tesserae have been heavily tectonized and occur in stratigraphically older positions than the surrounding plains (*Ivanov and Head*, 2011). The planitiae, representing the majority of the planet's surface, ∼72% (*Ivanov and Head*, 2011), are mostly composed of lava flows, some on a scale comparative to Large Igneous Provinces (LIPs) on Earth (*Ernst and Desnoyers*, 2004), and buttress against the highland regions.

According to the cratering record, the crust appears to be quite young, with a mean age of 300-600 Ma (*Nimmo and McKenzie*, 1998). The fact that the vast majority of the planet's ∼103 craters appear to post-date the planitiae and that they are randomly distributed across the surface has been taken to suggest that the crust was recycled in a global overturning event, which resurfaced the whole planet in a single brief episode (lasting several 10s to a few 100s Ma) (*Phillips et al.*, 1992; *Schaber et al.*, 1992; *Strom et al.*, 1994). This global resurfacing model has found support during further study of

Venus, although it is not universally accepted and remains controversial. For example, more recent statistical work on cratering and resurfacing has modelled equilibrium resurfacing scenarios that can feasibly result in the current observed surface conditions (*Bjonnes et al.*, 2012).

1.2.3 Tectonics and volcanism

The upper mantle of Venus is probably relatively dry compared with that of Earth, as there seems to be no process evident by which previously outgassed water is returned to the mantle, such as the subduction of oceanic lithosphere on Earth (*Nimmo and McKenzie*, 1998). An anhydrous mantle would be more viscous than a hydrous one with a viscosity of $\sim 3 \times 10^{20}$ Pa s predicted by numerical modelling (*Nimmo and McKenzie*, 1996), an order of magnitude higher than that on Earth of $\sim 3 \times 10^{19}$ Pa s as estimated at Hawai'i by *Watson and McKenzie* (1991). The apparent complete absence of plate tectonic features on Venus could be largely due to this lack of water, as this would generate a high viscous drag on the base of the lithosphere and the (usually water-induced) formation of a low-velocity zone of partial melt would be inhibited, also hindering plate motion (*Nimmo and McKenzie*, 1998; *Richards et al.*, 2001). This effect would also be compounded by the fact that the surface temperature would reduce the density of the crust, also inhibiting subduction processes (*Anderson*, 1981), and by the increased crustal fault strength able to accommodate stresses eight times those on Earth, as modelled by *Foster and Nimmo* (1996).

As a result of these self-reinforcing processes, the lithosphere of Venus is probably characterised by a 'stagnant lid' scenario (*Turcotte*, 1993). This scenario has implications for Venus' heat flow; convective models have estimated that the surface heat flux of Venus is 8-25 mW m^{-2} (*Nimmo and McKenzie*, 1996; *Smrekar and Parmentier*, 1996; *Solomatov and Moresi*, 1996). If one assumes a similar annual internal radiogenic heat generation to Earth of 8.6×10^{20} J (*Clauser*, 2011) or equivalently 2.7×10^{13} W, (not unreasonable, given the GRS data in the previous section), then even at the upper estimate of 0.025 W m^{-2}, which gives planetary value of $4 \times \pi \times (6051 \times 10^3$

m)^2×2.5×10^{-2} W m^{-2} = 1.15×10^{13} W, there is clearly a large discrepancy between internal heat production and heat loss. This observation is suggestive of the global catastrophic resurfacing model due to the build up of internal heat leading to global episodes of volcanism.

Veneras 13 and 14 were also equipped with seismometers. Venera 13 did not detect anything but Venera 14 detected two distinct microseisms with amplitudes of < 1 μm. It was concluded that these could have originated from the potentially volcanic regions of Beta Regio or Theia Mons, from which the lander was within a reasonable distance to detect a signal of that amplitude (*Ksanfomaliti et al.*, 1982). The authors highlight the possibility of wind-blown pebbles affecting the seismometer but stress that any contamination by such means is unlikely. It is difficult to form any conclusions as to how seismically active Venus is overall due to the lack of geophysical data. It is likely, however, to have a tectonic component associated with regions of (potentially active) rifting such as Beta and Phoebe Regiones, and a volcanic component associated with the (also potentially active) widespread volcanism and related processes discussed later in this section. One would expect the very high surface temperature on Venus to inhibit brittle failure in the crust by increasing its ductility, however the potentially anhydrous nature of the crust would have the counter-effect in that a lower water content would act to decrease the ductility of the crustal material (*Shirley*, 1998). The net effect of this is unknown and, as a result of this, it is currently impossible to tell to what degree Venus could be currently seismically active. Future surface exploration with improved, more robust, instrumentation will hopefully address this issue.

Volcanism on Venus is almost certainly predominantly basaltic, given the available radar and geochemical data. It follows that these lavas were more than likely formed by partial melting of mantle peridotite with a similar composition to that on Earth. Volcanic surface features on Venus seem to be widely distributed across the planet, in contrast to Earth where these features tend to be more concentrated around plate margins (*Head et al.*, 1992). Nine topographic rises or 'hot spot' regions have been identified that are thought to be associated with regional mantle upwelling (*Stofan*

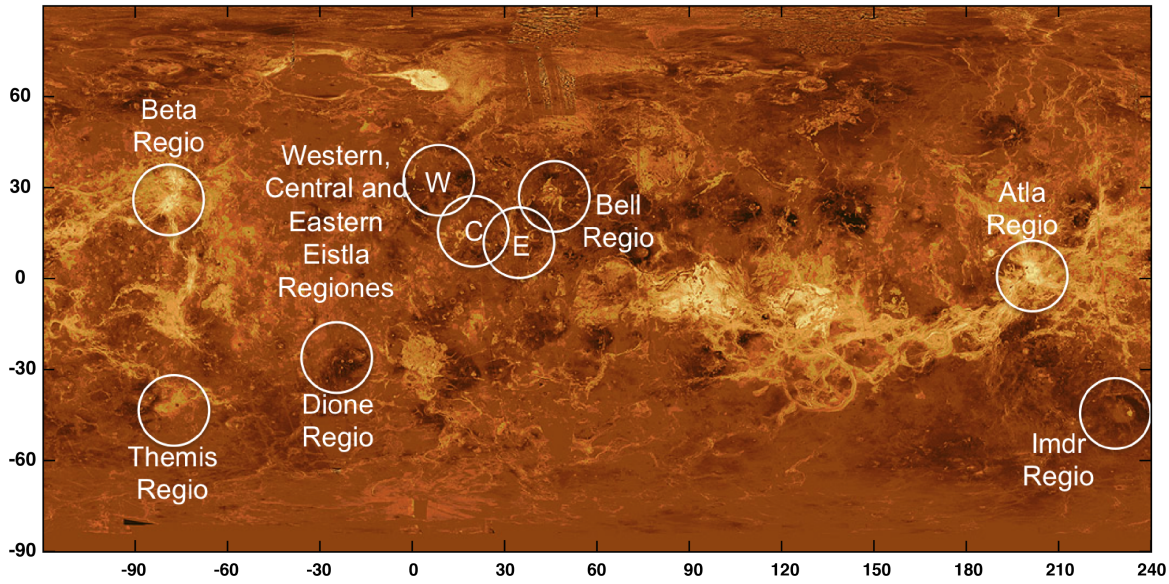

Figure 1.7: Global Magellan SAR mosaic with colour scale relating to radar backscatter intensity, labelled with the nine identified topographic rises thought to be associated with regional hot spot activity (from *Stofan et al.*, 1995). Background image, NASA/JPL.

et al., 1995). These nine regions are highlighted on the Magellan SAR F-map mosaic in Figure 1.7.

The ways in which Venusian volcanism manifests at the surface are in some ways similar to, and in some ways contrasting with, those on Earth. Edifices resembling Earth's shield volcanoes are numerous on Venus and are estimated to number in the region 10^5-10^6 (*Crumpler et al.*, 1997); they occur as individual volcanoes and in large volcanic fields. Volcanoes resembling the composite volcanoes of Earth are somewhat less numerous. As well as these, strange formations apparently unique to Venus in our Solar system also occur known as coronae, arachnoids, novae, steep-sided domes, and ticks. Many lava flows can also be seen in the form of canali, flow fields and voluminous outpourings known as festoons, of which only three are known (*Head et al.*, 1992). All the volcanic centres, magmatic centres, coronae and related features have been extensively classified and catalogued in *Head et al.* (1992) and *Crumpler and Aubele* (2000); the reader is directed there for a thorough compilation of all these structures. A brief summary of their key features is provided in Table 1.5. There follows a discussion of these types of volcanic formations based on these systems of classification with

Table 1.5: Size distribution of, and areas covered by, volcanological features on Venus from Magellan data.

Feature	Number mapped[1]	Approx. average diameter (km)[1]	Approx. average area (km^2)[1]	Notes
Shield fields	556	150	17,700	Clusters of small volcanoes.
Intermediate volcanoes	274	25	490	Shields, SSDs[3], ticks[3], and fluted domes[3]. Some assoc. with LVs. Some occur in small groups.
Large volcanoes	156	400	125,600	Isolated edifices.
Calderas	86	60	2,900	No associated edifice.
Coronae	176	250	49,000	Annular and radial fracturing.
Arachnoids	259	115	10,400	Like coronae; Spiders on web appearance.
Novae	50	190	28,300	A.K.A. radial fracture centres.
Lava floods	53	350[2]	128,200	
Lava channels	50	250[2]	?	A.K.A. canali.

morphological descriptions and proposed mechanisms of formation.

Large volcanoes, classed as volcanoes with a diameter ≥ 100 km, are overwhelmingly of the shield volcano variety, tending to be of relatively low relief, averaging only $\sim$1.5 km high (e.g. Sapas Mons, Figure 1.8). They are preferentially located at mid elevations with $\sim$94% of a sample of 123 large volcanoes analysed by *Keddie and Head* (1994) having bases occurring between -1 km and +1.5 km of the MPR. There is the notable exception of Colette Patera, which rises $\sim$900 m from its base at $\sim$3 km +MPR. Large volcanoes are characterised by radial lava flows of probably basaltic composition and are commonly associated with regional-scale volcanic features such as topographic rises possibly caused by hot spot activity and regions with some rifting characteristics. Some have central depressions that may be a result of the removal of dynamic support in the edifice (*Herrick et al.*, 2005). The apparent morphology, situation, and aspect ratio suggest primitive magma sources and effusive activity. *Crumpler and Aubele* (2000) identify 168 features in this classification.

Intermediately sized volcanoes are those that fall in the range $\geq$20 km and $<$100 km in diameter, *Crumpler and Aubele* (2000) identify 289 of these features. This class of volcano is much more morphologically diverse than the large volcanoes, comprising the shield type with radial lava flows and 'steep-sided' or 'pancake' domes. The standard

[1]Data from *Head et al.* (1992)

[2]Length

[3]Steep-sided domes, ticks, and fluted domes are wide, flat-topped volcanoes with varying degrees of mass-wasting affecting the flanks as described in the text.

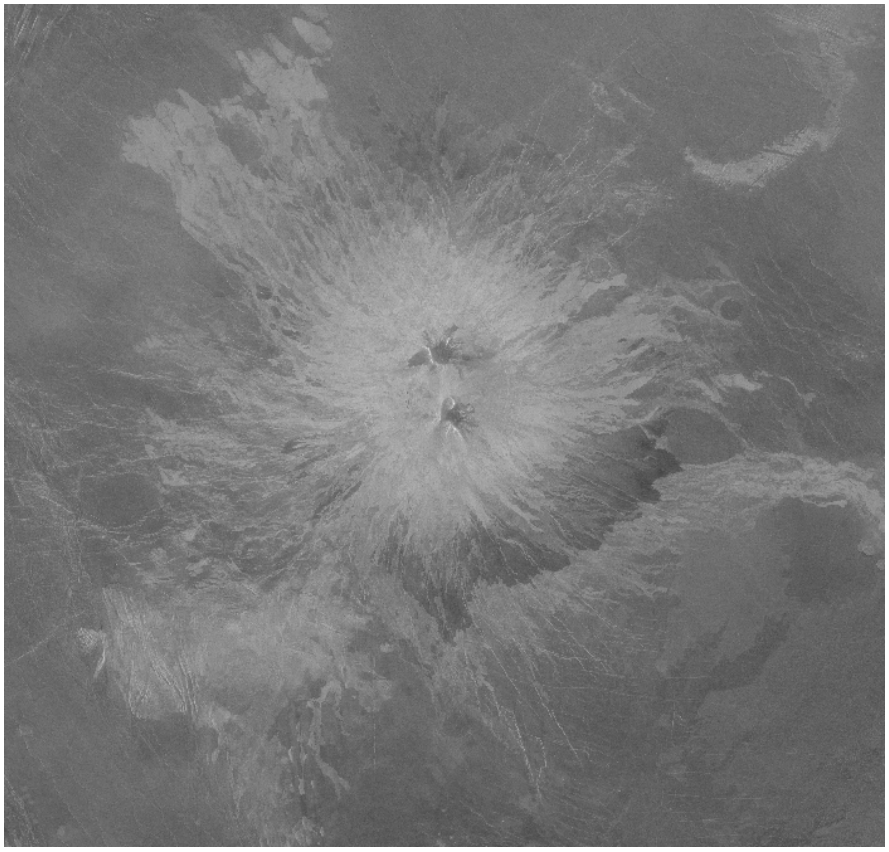

Figure 1.8: Sapas Mons, a large shield volcano, situated in Atla Regio rising ∼1.5 km above the local topography. Image is ∼1000 km across. Note the dual summit plateaux, numerous radar-bright lava flows, and the incidence of radar-dark flow material on the SE flank interpreted to have been formed of smoother material. Image centred at 12.3°N 8.3°E and illuminated from the left. NASA/JPL.

shield type intermediate volcanoes are of a similar origin to the large volcanoes. They are found in similar regions of large-scale volcanic influence and have a comparative morphological style suggesting similar sources. The curious steep-sided domes (Figure 1.9), representing more than half of this classification, have provoked much debate as to their formation. They mostly fall in the range 20-30 km diameter, but can occur up to 70 km in diameter (*Head et al.*, 1992). They are characterised by flat tops, steep sides and small summit depressions; they resemble the dacite domes one finds on Earth, suggesting a magma source of high viscosity, but having volumes orders of magnitude larger (*Pavri et al.*, 1992). Two potential modes of formation for these structures have classically been considered: magmatic evolution within the crust into more felsic compositions (*Pavri et al.*, 1992; *Fink et al.*, 1993; *Ivanov and Head*, 1999),

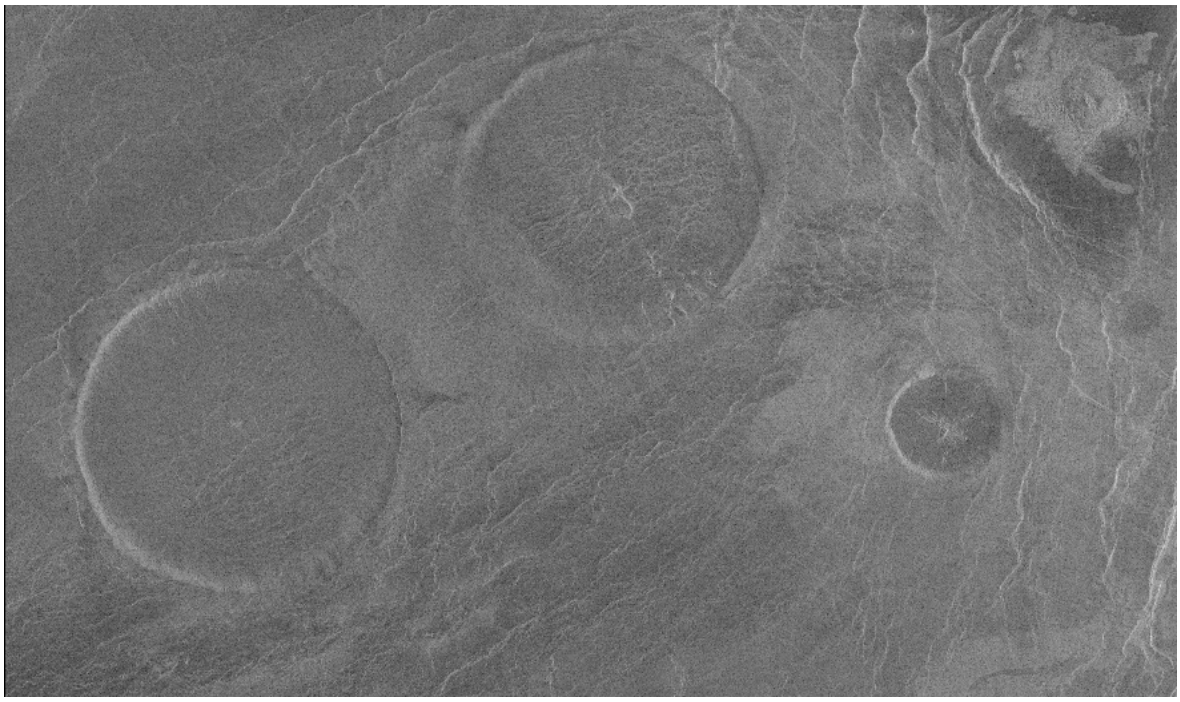

Figure 1.9: Steep-sided domes situated in Eistla Regio. Image centred at 12.3°N 8.3°E and illuminated from the left. The two larger domes are ∼65 km in diameter and <1 km in height. NASA/JPL.

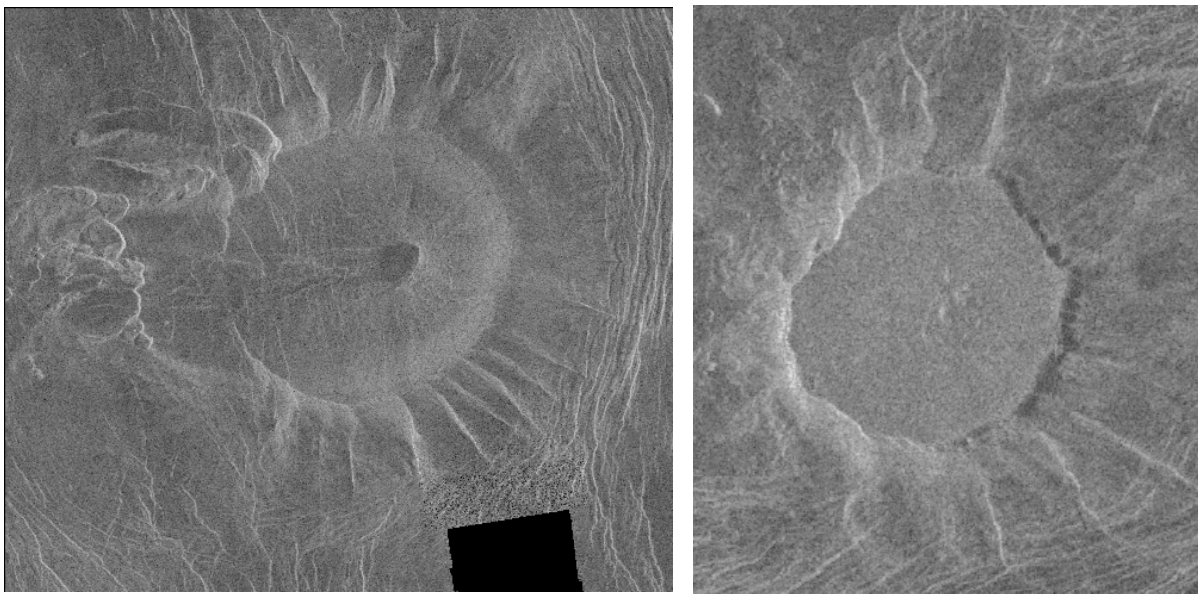

(a) (b)

Figure 1.10: (a) a 'tick', and (b) a fluted dome, both with many radial ridges resulting from mass wasting processes. Note the central vent in (a) and flat summits of both structures. Image in (a) centred at 18.5°S 5.6°E and illuminated from the left; image ∼70 km across. Image in (b) centred at 11.4°S 206.7°E and illuminated from the left; image ∼35 km across. NASA/JPL.

and the emplacement of basaltic material (*Pavri et al.*, 1992; *Stofan et al.*, 2000). The former suggestion requires build up of a steep sided edifice due to the high viscosity preventing extensive outward flow of lava. The latter seems more consistent with the smooth textured, flat-topped characteristics of the features as endogenous growth beneath a stable crust, which is continually fracturing and annealing during formation, is more likely to develop given a low viscosity lava (*Stofan et al.*, 2000). The classification of steep-sided domes also has diversity within it: 'ticks' (named so due to their appearance, Figure 1.10a) and fluted domes (Figure 1.10b) are a sub-classification of steep-sided domes with radial ridges possibly resulting from erosional/mass wasting processes.

Small volcanoes ($<$ 20 km in diameter) occur in vast numbers approaching 10^6, occurring associated with larger, regional volcanic structures and on plains too; they encompass all the aforementioned morphological types. Although they are individually too numerous to catalogue, 647 volcanic fields consisting of small volcanoes, known as 'shield fields' have been identified (*Crumpler and Aubele*, 2000), see Figure 1.11. It is clear from their tendency to cluster in these 'fields' that they occur over large subsurface magma sources or magma supply systems, presumed to feed the concentrated groups of volcanoes (*Head et al.*, 1991, 1992; *Head and Wilson*, 1992).

Isolated calderas occur widespread over the planet; 97 are identified by *Crumpler and Aubele* (2000) (e.g. Figure 1.12). Calderas are defined as topographically low depressions associated with collapse mechanisms operating in a volcanic centre. They occur commonly up to a diameter of $\sim$100 km but can achieve diameters up to $\sim$200 km. They lack any obvious association with a volcanic edifice, but may be a feature of a larger-scale topographic rise (*Head et al.*, 1992).

Figure 1.11: Shield field situated in Aibarchin Planitia. Image centred at 78.4°S 43.0°E and illuminated from the left. The image is 250 km across. NASA/JPL.

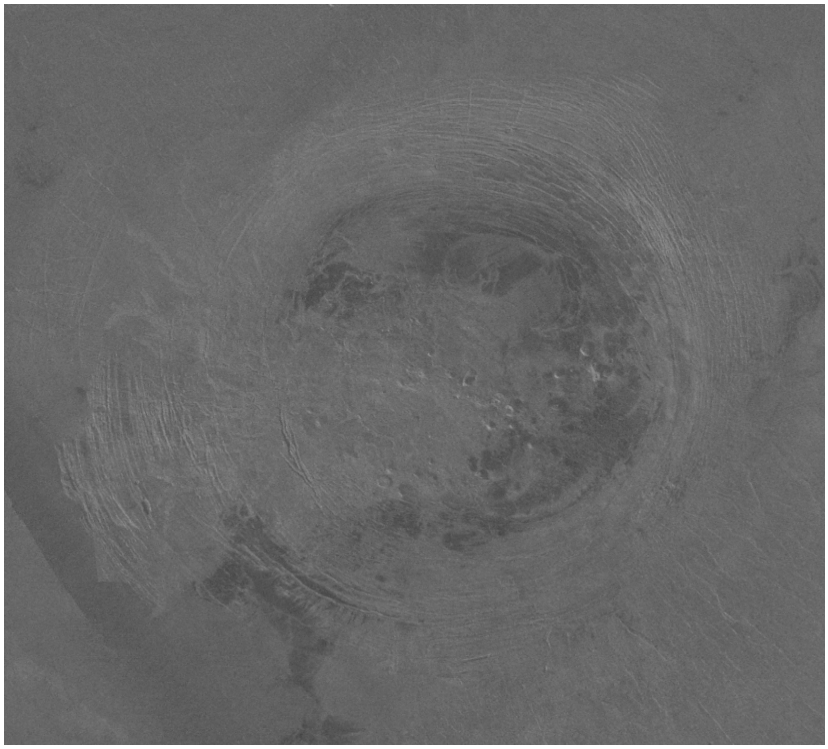

Figure 1.12: Isolated caldera structure situated in Laimdota Planitia. Image centred at 73°S 99°E and illuminated from the left. Numerous shield volcanoes and radar-bright flows occur within the depression. The base of the caldera depression is in fact ∼1 km lower than the surrounding terrain (*Crumpler and Aubele*, 2000). Image is ∼225 km across. NASA/JPL.

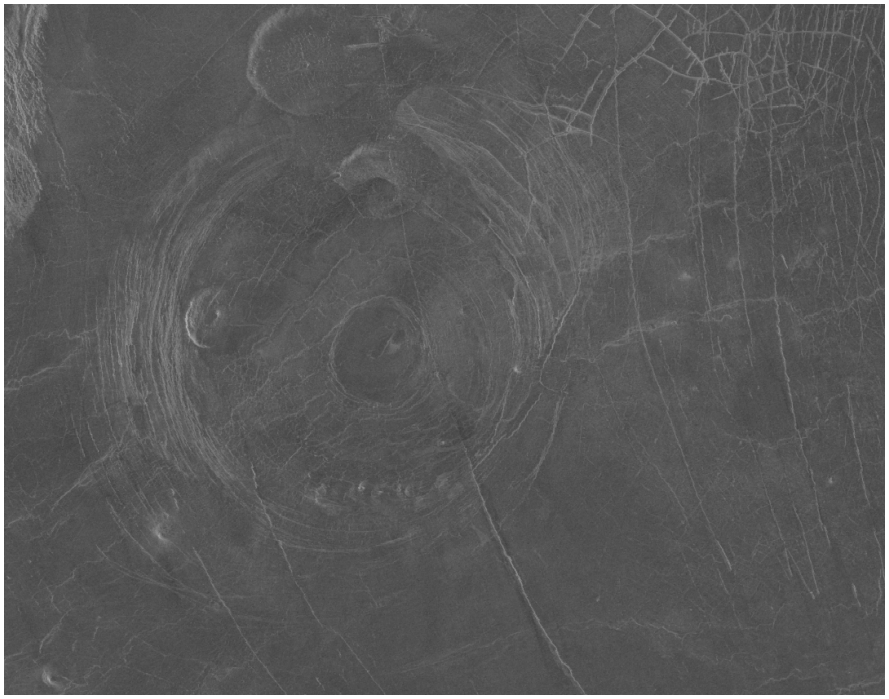

Figure 1.13: Aine corona, otherwise known as Fotla corona situated in Dsonkwa Regio. Image centred at 58.5°S 163.9°E and illuminated from the left. The corona itself is ∼200 km in diameter. Note the associated steep-sided domes and small volcanoes situated within and around the corona. NASA/JPL.

Coronae (e.g. Figure 1.13) are commonly ∼200 km diameter but can reach sizes of ∼1000 km; 208 such structures were identified by *Crumpler and Aubele* (2000). Originally thought to be impact craters based on ground-based observations, the return of the Venera 15 & 16 data allowed more detailed scrutiny of them and early study proposed their origin as that of reworked large impact basins (*Barsukov et al.*, 1986). The best current model for their formation involves the loading of a magmatic plume/chamber (*Smrekar and Stofan*, 1999) or region of partial melt associated with the top of an ascending magma body (*Dombard et al.*, 2007) at the base of the lithosphere, causing upward flexure and radial fracturing and graben formation from the magmatic centre. Subsequent gravitational relaxation and subsidence of the region then results in the distinctive annular fracturing. Coronae are often associated with localised volcanic activity of a great range of sizes, from shield fields of small volcanoes to the occurrence of large volcanoes within the corona region.

Similar to coronae, Venus has many features that can be considered as a sub-

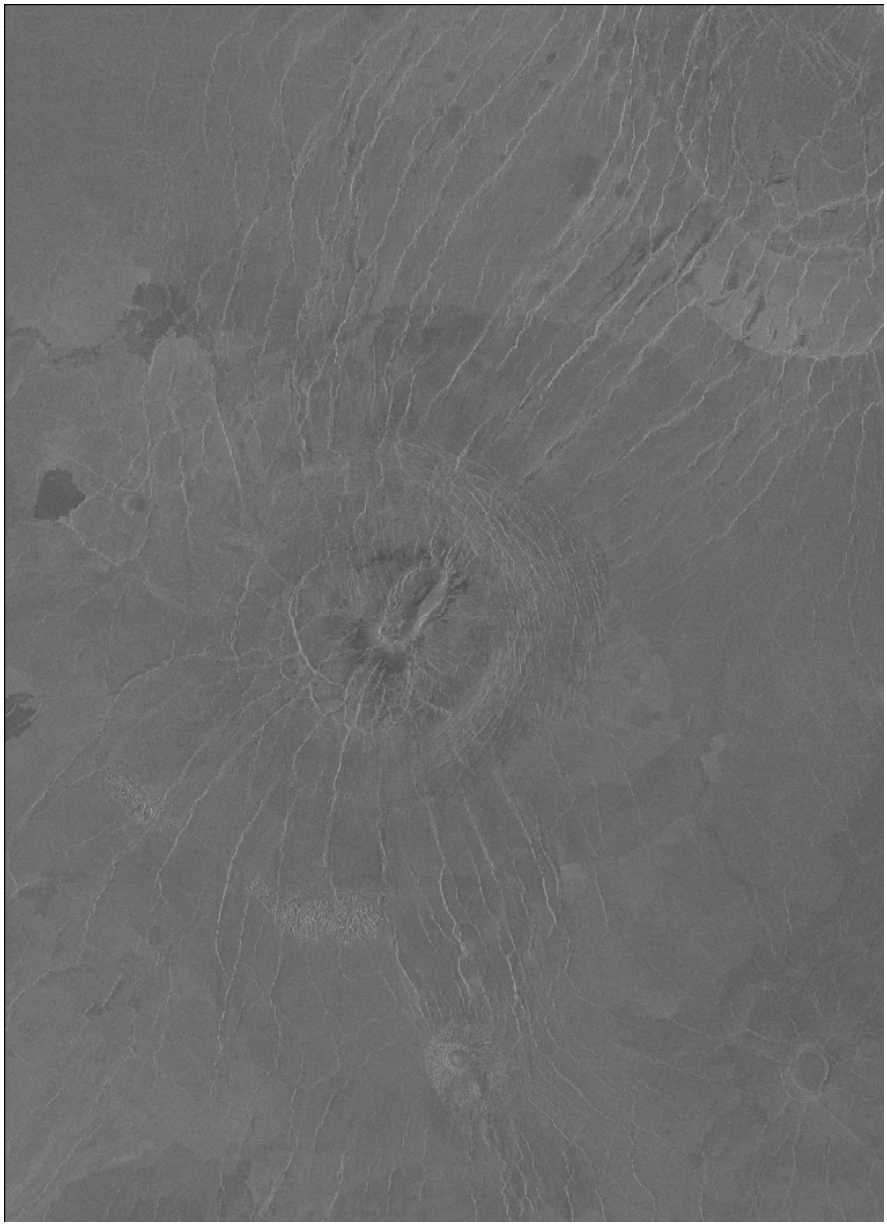

Figure 1.14: Arachnoid situated in Ganiki Planitia. Image centred at 40.5°N 214.3°E and illuminated form the left. Note the extensive radial fracturing giving the spider-like appearance. Image is ∼275 km across. NASA/JPL.

classification thereof, namely arachnoids (e.g. Figure 1.14) and novae (e.g. Figure 1.15) (265 and 64, respectively, identified by *Crumpler and Aubele* (2000)). Arachnoids seem simply to be a variation on the coronae in that their appearance is similar, except that they have a higher ratio of radial to annular fractures and that they tend to be smaller (<200 km). Arachnoids are commonly associated with ridge belts, possibly associated with regions of extension and rifting (*Head et al.*, 1992; *Krassilnikov*,

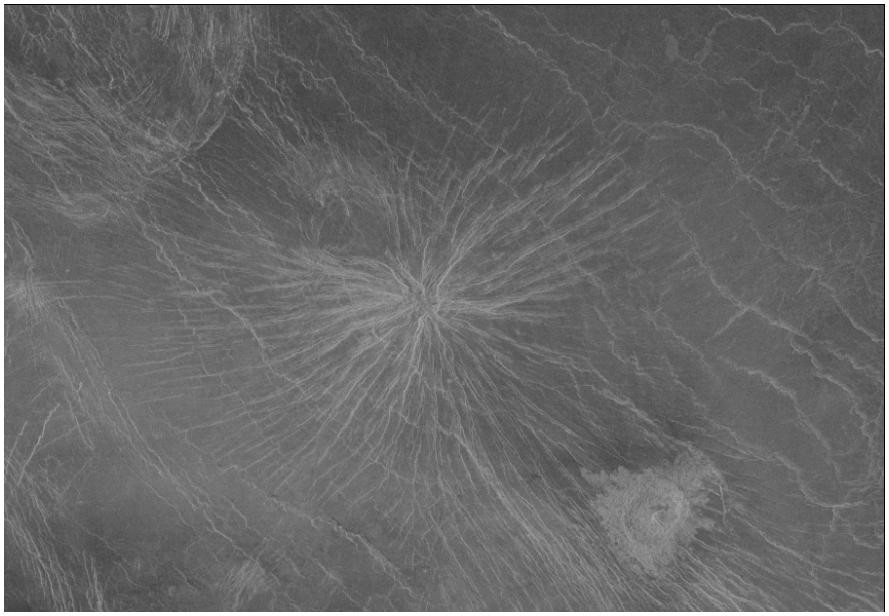

Figure 1.15: Nova, or radial fracture centre, situated at Bereghinya Planitia. Image centred at 34.2°N 22.0°E and illuminated from the left. These features are heavily dominated by the radial fracturing and lack the concentric features of coronae. Image is ∼300 km across. NASA/JPL.

2002). Novae, otherwise referred to as 'radial fracture centres', are characterised solely by radial fractures and graben radiating from a central point associated with tensile fracturing of the crust caused by an upwelling mantle body (*Krassilnikov and Head*, 2003). It has been proposed that novae are the precursory formation to coronae and arachnoids, before the radial/annular structure has had time to develop fully (*Aittola and Kostama*, 2002). If this is true, it may not always be the case, as not all coronae display radial fracturing, therefore the uplift and tensional fracturing is not a prerequisite of generation of the concentric surface expression of the relaxation phase characteristic of coronae (*Krassilnikov and Head*, 2003).

These volcanic/magmatic centres of activity are complemented by surface expressions of the products of volcanism. Expansive lava plains cover the vast majority of the planet's surface (*Ivanov and Head*, 2011), and have been interpreted as evidence for the global resurfacing model. Although most volcanoes on Venus seem to postdate the plains emplacement, some have been identified that are embayed by plains flows (*López*, 2011), suggestive of a more gradual, periodic resurfacing history. Rare

occurrences of high relief localised flows, with diameters ∼300 km known as festoons (e.g. Figure 1.16) appear to have a rheology similar to that of the material that forms the steep-sided domes, and may have a similar origin. Only three such flows are documented (*Head et al.*, 1992). Finally, channels incised by lava flows know as canali (e.g. Figure 1.17), some of which extend for thousands of km, are commonly observed on Venus. They attain widths of up to 10 km in places and can have simple or complex anastomosing/braided types (*Crumpler and Aubele*, 2000). Quite what carved these channels is unclear; a substance of very low viscosity would be required to remain molten and travel for these distances and generate this meander geometry (*Bray et al.*, 2007). Substances proposed that could have feasibly formed these canali include komatiitic or high Fe-Ti "lunar" type basalts (*Gregg and Greeley*, 1993), carbonatite lava flows with water like flow rheologies (*Kargel et al.*, 1994; *Williams-Jones et al.*, 1998) and even aqueous solutions created by release (possibly by volcanism) of hydrous minerals trapped in the crust (*Jones and Pickering*, 2003).

Volcanism has clearly been a crucial planetary process in terms of the geological evolution of Venus' surface but one of the key outstanding questions is whether it is an ongoing planetary process today. As described above, it is suggested that the cratering history prior to ∼600 Ma has been erased by crustal resurfacing and, of the impact craters that have occurred since, only very few are embayed by lava flows (*Phillips et al.*, 1992; *Schaber et al.*, 1992; *Herrick and Phillips*, 1994; *Strom et al.*, 1994; *Collins et al.*, 1999). This evidence is supportive of the periodic catastrophic resurfacing model followed by relative volcanic quiet; however, a recent study proposes evidence for a great deal more post-impact volcanic modification of craters than previously thought (*Herrick and Rumpf*, 2011). Indeed, some might argue that the global catastrophic resurfacing model, based purely on the cratering record, is becoming somewhat outdated in light of ongoing discoveries and the compilation of evidence in favour of ongoing volcanism such as the statistical work carried out by *Bjonnes et al.* (2012) mentioned previously. The observations of long-term decline of atmospheric SO_2 punctuated by periodic rapid introductions of SO_2 detected at Venus' cloud tops (e.g. *Esposito*, 1984,

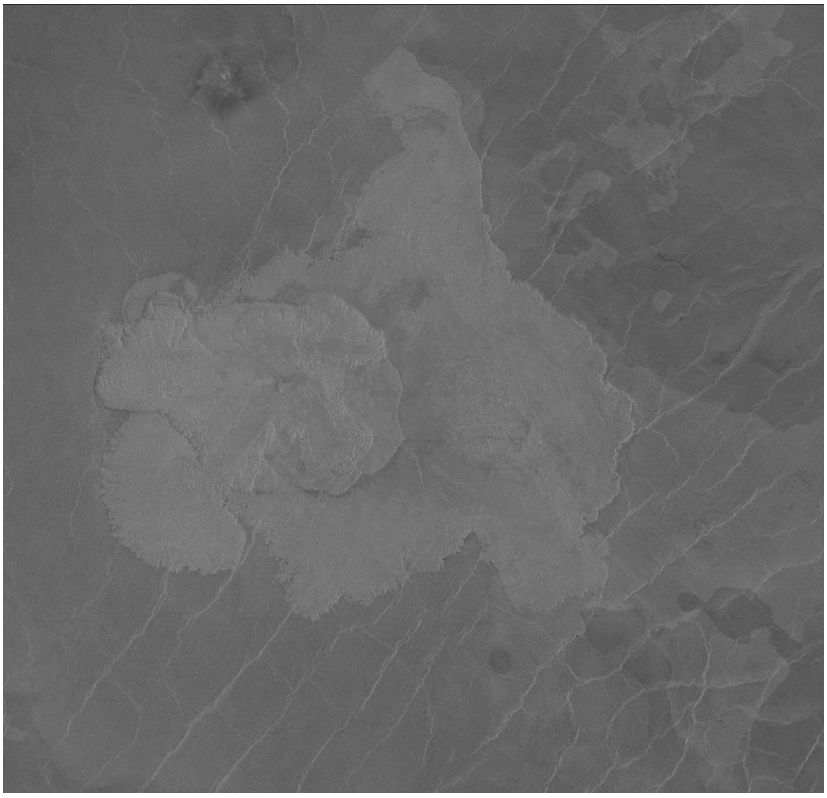

Figure 1.16: One of the few festoon flows observed on Venus at Zhibek Planitia. Image centred at 37.6°S 165.5°E and illuminated from the right. Note the apparent similarity with steep-sided domes in terms of flow rheology suggestive of very viscous material. Image is ∼300 km across. NASA/JPL.

1985; *Esposito et al.*, 1997; *Belyaev et al.*, 2008; *Marcq et al.*, 2013) classically provided strong evidence for a volcanic input to the atmosphere, and these observations have subsequently been reinforced with new measurements, see Figure 1.18 (*Marcq et al.*, 2013). This, together with the high-resolution radar data recovered by the Magellan mission in the early 1990s (*Head et al.*, 1991) provides compelling evidence for the past and current occurrence of volcanic processes on the surface of Venus. The Venus Express mission has provided additional evidence for volcanism in the form of thermal emissivity anomalies detected by the VIRTIS instrument, indicative of young, relatively unweathered lava deposits (*Smrekar et al.*, 2010) and infrared hot spot anomalies in the VMC data found to intensify and subside between Venus Express observations suggesting current dynamic volcanic processes (*Shalygin et al.*, 2015).

It is important to identify what part is played by volcanism in the highly complex

Figure 1.17: Canali situated in Lo Shen Valles, northern Tahmina Planitia, just south of Ovda Regio. Image centred at 12.8°S 89.2°E and illuminated from the left. Image is ∼600 km across. NASA/JPL.

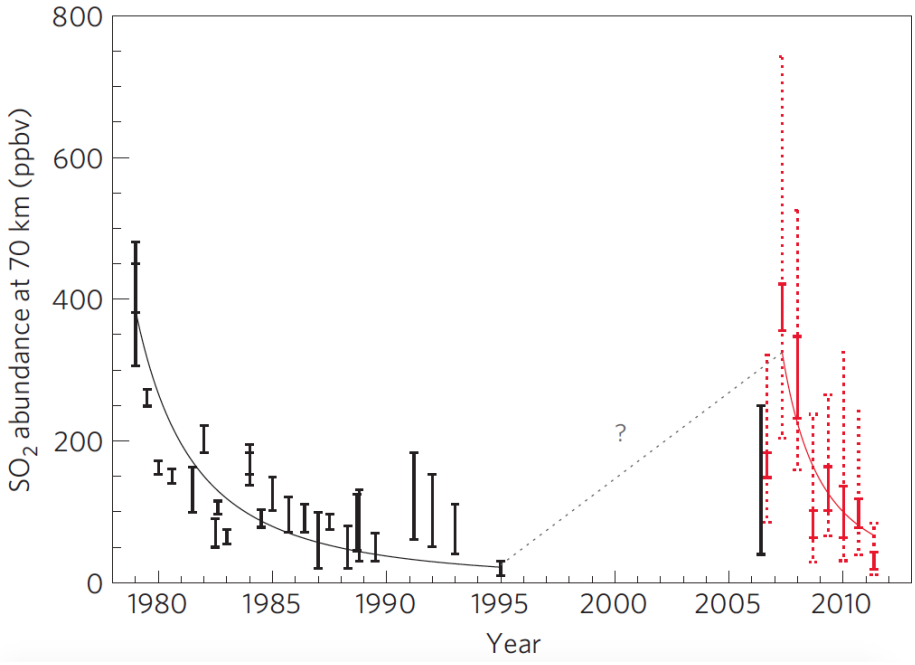

Figure 1.18: Atmospheric SO_2 above Venus' clouds since 1978. The SO_2 content in ppb volume is considered at the level of 40 mbar (∼69-70 km). Pre-1995 data derived from Pioneer Venus UV spectrometer, International Ultraviolet Explorer UV spectrometer, Venera 15 Fourier spectrometer, sounding rocket telescope observations, and Hubble Space Telescope observations; they are compiled in *Esposito et al.* (1997). More recent data published in *Belyaev et al.* (2008) and *Marcq et al.* (2013). Figure reproduced from *Marcq et al.* (2013).

global scale planetary interactions on Venus and, from this brief summary, it is clear that a lot is still unknown and hypotheses are continually being contested about the large-scale volcanological processes on Venus.

1.2.4 Atmosphere and clouds

Following the speculative nature of the earliest writings on the characteristics of Venus' atmosphere, initial observations based on ground-based microwave measurements in ∼3 and ∼9 cm wave bands made between 1956 and 1958 suggested surface temperatures of ∼500-600 K (*Mayer et al.*, 1958; *Barrett*, 1960) and ∼640-750 K (*Sagan*, 1962). Estimates of the composition varied, but early models, e.g. *Barrett* (1960), assumed that the atmosphere consisted of ∼75% CO_2, ∼22-25% N_2, and ∼0-3% H_2O. Since then, our knowledge has been improving with every spaceborne mission, from the first glimpse of surface conditions by Mariner 2's microwave radiometer measurements, to the multitude of results provided by Venus Express.

Venera 4 gave us the first in situ analysis of Venus' atmosphere interpreted as 90 ±10% CO_2, < 7% N_2, 0.4-1.6% O_2, and 1-8 ppm H_2O, and a surface temperature of ∼675 K (*Vinograd et al.*, 1968). We now know that the composition is more like 96% CO_2 with 3.5% N_2 and ∼0.5% trace species (see Table 1.2) and a surface temperature of ∼730 K (*Taylor*, 2010).

The temperature profile of Venus was derived from a combination of direct measurements made by the Venera and Vega entry probes and infrared remote sounding carried out by Pioneer Venus Orbiter from ∼100 km down to ∼30 km altitude (*Taylor et al.*, 1979a), later extrapolated to the known surface temperature based on the adiabatic temperature gradient to produce the profile shown in Figure 1.19; Earth's profile is given for comparison (*Taylor and Grinspoon*, 2009). It is clear that higher up in Venus' atmosphere, where the pressure regime is similar to that of Earth, the temperature regime is also very similar. Below this level on Venus, temperature increases adiabatically with pressure.

The atmosphere that we see on Venus today is the result of planetary outgassing

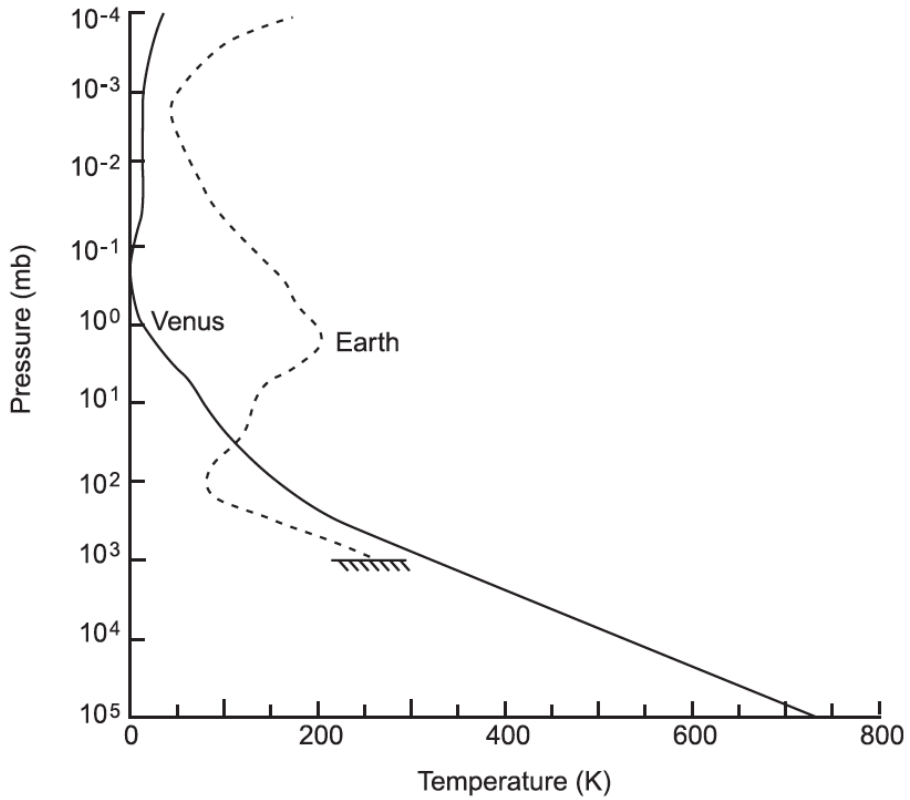

Figure 1.19: Comparison of Venus' and Earth's temperature profiles as a function of atmospheric pressure (from *Taylor and Grinspoon* (2009)).

and delivery by meteoroids, with the original primordial atmosphere having been lost or drastically altered in the early stages of solar system evolution (*Taylor and Grinspoon*, 2009). The overwhelming dominance of CO_2 in the atmosphere is due to the lack of any CO_2 sinks on the planet such as the dissolution of CO_2 in liquid water to form carbonic acid reacting with rock, and the absorption by photosynthesising organisms. There is, however, the proposed CO_2 source of volcanic emissions. This combination of factors results in the high build up of CO_2 in the atmosphere (*López et al.*, 1998). An unchecked increase in this gas results in an unrestrained temperature increase and what is known as a 'runaway greenhouse effect'. The temperature may be buffered at its current value by surface interactions between atmospheric CO_2 and surface materials according to the equilibrium reaction $CaCO_3 + SiO_2 \leftrightarrow CaSiO_3 + CO_2$ (*Urey*, 1952), although it has been noted that unknown processes are required to also be operating in order to achieve equilibrium (*Bullock and Grinspoon*, 1996).

It can be inferred that Venus' atmosphere was once much wetter than it is now from the following evidence. Water molecules in the upper atmosphere are dissociated by UV photolysis and the ions escape to space. As hydrogen and deuterium ions escape, the lighter hydrogen ions escape preferentially due to their lighter mass, resulting in an increase in the ratio of D/H (*Donahue et al.*, 1982). Observations from Pioneer Venus Orbiter gave a D/H ratio of more than one hundred times that on Earth (*Donahue et al.*, 1982; *De Bergh et al.*, 1991; *Grinspoon*, 1993; *Donahue*, 1999). From this deuterium enrichment, and the inference that most of the H_2O in Venus' crust and mantle has been outgassed without replenishment, it is clear that most of the global inventory of H_2O has been lost to space. Indeed, it has been noted (*Bullock and Grinspoon*, 2001) that this steady decline of H_2O over geologically moderately short time scales (100s Ma) implies that Venus had 100 times as much water vapour in its atmosphere 800 Ma ago than it does today.

The importance of SO_2 in Venus' atmosphere is widely recognised in terms of evidence for volcanism, contribution to greenhouse warming, and cloud formation. Even though it is one of the minor constituents of the atmosphere, there is ∼100,000 times as much SO_2 in Venus' atmosphere than in Earth's (*Taylor and Grinspoon*, 2009). As a result of this, it is a well-studied constituent of Venus' atmosphere. As noted above, *Esposito* (1985), and later *Marcq et al.* (2013), recognised the significance in the apparent long-term trends in SO_2 concentrations as evidence for episodic volcanism or some long-term cyclical trends in atmospheric circulatory behaviour, see Figure 1.18. Indeed, without some process introducing SO_2 into the atmosphere, it has been suggested using evidence from laboratory measurements that, in just 1.9 Ma, all the SO_2 in Venus' atmosphere could have been removed due to the reaction $SO_2 + CaCO_3 \leftrightarrow CaSO_4 + CO$ at the surface (*Fegley and Prinn*, 1989) if sufficient calcite is present, although *Bullock and Grinspoon* (2001) re-evaluate this with further modelling to >20 Ma. This continued presence and periodic reintroduction of SO_2 to the atmosphere is suggestive of an active source, such as a volcanic input.

Early study of the cloud structure and composition on Venus using data from PVO

and the Mariner and Venera probes provided evidence for an H_2SO_4-rich cloud deck at ∼45-70 km with thinner hazes above and below (*Young*, 1973; *Esposito et al.*, 1983). These clouds are highly reflective, with a Bond albedo of ∼0.9 (*Mallama et al.*, 2006), resulting in only a small proportion of solar radiation incident on the planet being absorbed by the atmosphere. The global-scale characteristics consist of a strongly convecting region between the equator and a latitude of ∼40°S, a more streaky region between ∼40-60°S dominated by more zonal flow, a cold polar collar at ∼60°S, and a dual polar vortex at the pole (*Titov et al.*, 2008); it has been shown that the northern hemisphere atmosphere has a similar structure (*Taylor et al.*, 1980; *Zasova et al.*, 2007). The study by *Titov et al.* (2008) combined the use of VMC and VIRTIS aboard Venus Express to produce a model of the thermal and morphological structure of the cloud top. The cloud-top altitude was found to drop from a very homogeneous altitude of ∼72 km between the equator and ∼50°S to a polar depression of ∼64 km. The use of VMC here exploited the waveband sensitive to detecting an unknown strongly UV-absorbing substance characteristic of the upper cloud layer (0.365 μm); the bright and dark contrasting markings could be concluded to mark compositional changes, not morphological, due to the homogeneity of the cloud-top altitude noted earlier (*Titov et al.*, 2008).

Recent analysis of SPICAV/SOIR data by *Belyaev et al.* (2008) led to the conclusion that SO_2 concentrations at the cloud top vary with latitude from ∼1 ppm for low latitudes (23-30°) to 0.1 ppm for high latitudes (69-88°). Further work with data gathered using SPICAV-IR operating in nadir configuration has provided evidence of a reasonably strong correlation between SO_2 concentration and cloud top altitude, where higher clouds have characteristically greater SO_2 concentrations, possibly due to some dynamic origin (*Marcq et al.*, 2011). The authors claim that this relationship is stronger than that with latitude described by *Belyaev et al.* (2008) even though the overall trend is common to both. This observation also seems to correlate in some dynamic way with cloud top H_2O concentrations, which vary in the reverse manner (*Cottini et al.*, 2012). Finally, by using SOIR in solar occultation for 65-80 km and SPICAV-UV in

stellar occultation for 85-105 km, *Belyaev et al.* (2012) were able to generate an almost continuous vertical profile above the clouds of SO and SO_2. They found that there are two distinct SO_2 layers in Venus' mesosphere, 0.02-0.2 ppm at 65-80 km and 0.05-2 ppm at 85-105 km, and also that the SO and SO_2 profiles from the upper mesosphere form an X-shape indicative of a strong photochemical dependence on one another. In addition to this, the study by *Belyaev et al.* (2012) also confirms the dependence of SO_2 concentration on latitude/cloud top altitude mentioned previously. These two distinct SO_2 bands above the clouds are a product of the sulphur chemistry occurring at these altitudes. The first attempt to model the mixing ratios of sulphur oxides using standard chemistry by *Yung and DeMore* (1982) failed to identify the upper layer of SO_2, and instead predicted a continual decline with altitude. Subsequent ground-based observations (*Sandor et al.*, 2010) and observations by Venus Express (*Belyaev et al.*, 2009) detected this increased SO_2 concentration band and forced a re-evaluation of sulphur chemistry in Venus' mesosphere. In response to this, *Zhang et al.* (2010) modelled the sulphur chemistry with the modification of an additional source of SO_2 at ∼100 km. In this work, it was postulated that this additional SO_2 is provided via the photolysis of H_2SO_4 vapour (previously evaporated from H_2SO_4 aerosols) into SO_3 followed by further photodissociation into SO_2. The SO_2 created in this way could then be supplied to this upper band from above, resulting in a model more consistent with the observed profile.

The occurrence of the clouds is due to photo-assisted reactions between SO_2 and O (itself derived from the photodissociation of CO_2 into CO and O) to create SO_3, and between SO_3 and H_2O to create H_2SO_4 aerosols at an altitude of ∼62-68 km, which persist down to the cloud base (∼48 km (*Pollack et al.*, 1993b)) where the temperature becomes too high and the aerosols thermally decompose (*Esposito et al.*, 1983; *Bullock and Grinspoon*, 2001). Within the cloud deck, H_2SO_4 and H_2O are thought to be in chemical equilibrium with a shift in dominance from a dry H_2O-poor upper layer grading into a moister H_2O-rich lower layer as a result of the strong temperature dependence of this equilibrium (*Bullock and Grinspoon*, 2001). The aerosol inventory

is supplemented by the condensation from the H_2SO_4 vapour reservoir below the cloud base (*Krasnopolsky and Pollack*, 1994; *James et al.*, 1997).

The cloud particle size spectrometer experiment aboard the Pioneer Venus probe measured a range of particle sizes (*Knollenberg and Hunten*, 1980); subsequent cloud modelling exercises have gone on to be refined and recognise four particle size categories and particle size distributions from size modes 1 (very small, 0.30 ± 0.44 μm), 2 (medium, 1.00 ± 0.25 μm), 2' (medium, 1.40 ± 0.21 μm), and 3 (large, 3.65 ± 0.25 μm) (*Crisp*, 1986; *Grinspoon et al.*, 1993; *Pollack et al.*, 1993b; *Krasnopolsky and Pollack*, 1994; *Barstow et al.*, 2012). The results of the *Crisp* (1986) study show a bimodal distribution in the upper clouds above ∼57 km (modes 1 and 2) and a trimodal size distribution in the lower/middle clouds below ∼57 km (modes 1, 2', and 3), the other models may vary slightly but are in general agreement. In addition to the altitudinal variation in particle size, there is also a general latitudinal variation where the average particle size is constant over most of the planet, but does tend to increase towards the poles (*Carlson et al.*, 1993; *Wilson et al.*, 2008) suggesting differences in cloud formation processes at high latitudes.

In terms of the global-scale circulatory dynamics of Venus, various three-dimensional GCMs have been developed. The overall large-scale processes on which these all agree are summarised here (*Yamamoto and Takahashi*, 2003; *Lee et al.*, 2005; *Lee*, 2006; *Lee et al.*, 2007; *Lebonnois et al.*, 2010; *Yamamoto*, 2011). There is a single Hadley cell in each hemisphere providing a slow meridional poleward flow at an altitude of ∼50 km from the equator to ∼60°N and S where it descends and flows equatorward. Within ∼60° of the equator, strong zonal jets develop as a result of their angular momentum in dominantly meridional flow, which create the characteristic streaky cloud appearance when imaged in UV (*Titov et al.*, 2012). This circulatory regime, with wind speeds up to and exceeding 100 m s^{-1} achieves what is known as 'superrotation' above ∼40 km, where the atmosphere travels faster round the planet than the planet itself rotates. Below 40 km, the wind speeds are much slower, being only 0-3 m s^{-1} at the surface. At ∼60-70°, the cold polar collar, a zonal jet that extends around the planet, develops

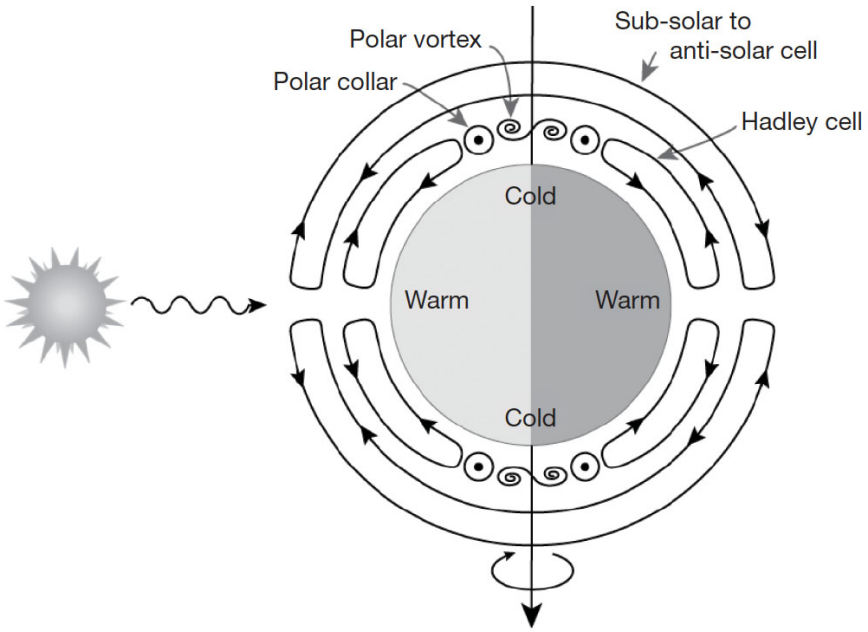

Figure 1.20: Summary schematic to show the planetary-scale circulatory behaviour of Venus' atmosphere as discussed in the text (from *Svedhem et al.*, 2007b)

between the Hadley cell and the polar twin vortices, which characterise the circulation at the poles. These vortices occur as cold, dense air is forced to descend rapidly at the poles into a strongly zonal angular momentum regime. At altitudes of >100-120 km, the circulatory regime in the thermosphere is somewhat different; here, a sub-solar to anti-solar planetary circulation regime has been interpreted from oxygen airglow measurements detected by Venus Express at the anti-solar point, furthest from the Sun on Venus' nightside (*Svedhem et al.*, 2007b). This airglow results from the recombination of oxygen atoms, previously dissociated from CO_2 on the dayside, into molecular oxygen as they flow toward the surface at the far edge of the cell at the anti-solar point. Figure 1.20 summarises the key features of Venus' atmospheric circulation.

1.2.5 Lightning

Lightning can be generated due to discharges of electromagnetic energy across electrostatic fields generated by the separation of charged particles within clouds (*Aplin*, 2006; *Harrison et al.*, 2008) and also volcanic plumes (*James et al.*, 2000; *Mather and*

Harrison, 2006; *James et al.*, 2008). On Venus, as the clouds are some ∼50 km above the planet's surface (in contrast to Earth, where clouds are generally only found in the range 1-10 km (*Russell et al.*, 2011)), if lightning occurs it is expected that it will be characterised by intra- and inter-cloud discharges as cloud-surface discharges are unlikely (*Russell et al.*, 2011). Proposed evidence for lightning on Venus came from: (i) the electromagnetic radiation measured by the Venera 11-14 landers (*Ksanfomaliti et al.*, 1983), (ii) electromagnetic radio wave pulses known as whistlers consistent with an atmospheric origin found during acquisition of data by Pioneer Venus as it passed through the upper atmosphere (*Taylor et al.*, 1979b; *Strangeway et al.*, 1993), (iii) radio waves interpreted to be generated by lightning by Galileo (*Gurnett et al.*, 1991), (iv) magnetic measurements by MAG aboard Venus Express (*Russell et al.*, 2007b, 2008), and (v) optical detections reported during limb observations by Venera 9 (*Krasnopolsky*, 1980) and from ground based telescope observations (*Hansell et al.*, 1995).

The occurrence of lightning on Venus is still controversial, however, as a theoretical study of the charge balance within Venus' clouds demonstrates (*Michael et al.*, 2009). This modelling study concluded that the density of charged particles created by interactions between the cosmic rays and neutral particles, along with the calculated high value of electrical conductivity, is insufficient to allow the generation of lightning strokes between 40-70 km, i.e. the cloud deck, due to any apparent degree of charge separation being short-circuited before an adequate electrostatic field can develop.

Atmospheric lightning on Venus could also be very important in terms of high-temperature chemistry such as nitrogen fixing reactions (*Krasnopolsky*, 1983, 2006). *Krasnopolsky* (2006) cites lightning as the source of NO absorption bands detected in the absorption spectrum of the lower atmosphere of Venus (below 60 km) by ground based spectral observations using NASA's infrared telescope facility on Mauna Kea, Hawai'i. This conclusion was formed due to the fact that lightning is the only potential source of this particular chemical species in Venus' lower atmosphere. Other potentially important high P/T reactions that could occur in lightning in Venus' at-

mosphere include the breakdown of the ubiquitous CO_2 into CO and O as reproduced experimentally by *Robledo-Martinez et al.* (2011) at temperatures up to 2.9×10^4 K under a pressure of 2 atm ($\sim$45 km altitude on Venus). These processes have wider implications for the minor constituent cycles in Venus' atmosphere.

The occurrence of conditions that may allow lightning generation within volcanically generated subaerial plumes of ash, aerosols, and gas are widely documented on Earth (*Gilbert et al.*, 1991; *James et al.*, 2000; *Miura et al.*, 2002; *Mather and Harrison*, 2006; *James et al.*, 2008). On Venus, explosive plume-forming eruptions may only occur where magma fragments within the conduit, as the absence of any liquid water on Venus means that phreatomagmatic processes will not occur. Charging of particles via fractoemission and tribocharging during eruptions is followed by preferential settling out and within-plume dynamics, which separates the charge and ultimately generates an electric field. The process of charge separation is largely driven by particle size variation where polarity varies as a function of particle size and as the larger particles settle faster, charge separation occurs. The gas and aerosol phases of the plume may also accommodate a different charge from the ash phases and be similarly separated by plume dynamics (*Gilbert et al.*, 1991; *James et al.*, 2000; *Miura et al.*, 2002; *Mather and Harrison*, 2006; *James et al.*, 2008). Although it is unclear why charge polarity should vary as a function of particle size, it has been suggested that some post-particle-generation process such as ion scavenging could potentially affect particle size as a function of polarity as a dynamic process during settling (*James et al.*, 2000). The direct consequence of these processes is the discharge of energy across the potential gradient in a manner similar to that occurring in the clouds. If it indeed exists, plume related lightning on Venus is occurring at significantly higher pressures than its counterpart within the cloud layer.

It is hoped that future missions to Venus will elucidate the conflicting evidence on this matter. Venus Express data, the return of Akatsuki (Venus Climate Orbiter) to Venus in late 2015 and possible future descent probe/balloon missions may provide further evidence for or against the occurrence of lightning on Venus.

1.2.6 Exosphere

Venus lacks an intrinsic magnetic field generated by a liquid outer core; Earth's magnetic field deflects the solar wind. As a consequence of this, the interaction between the solar wind and the upper atmosphere is very different on Venus, see Figure 1.21 (*Russell et al.*, 2007a). The charged particles in the solar wind interacting with the charged particles of Venus' ionosphere generate currents, which form a magnetic field draped around the planet. This boundary deflects the solar wind around the planet in a 'magnetosheath' preceded by a 'bow shock' where the plasma stream slows on its approach to the induced magnetosphere (*Bertucci et al.*, 2011).

Pioneer Venus Orbiter collected spectral data from Venus' ionosphere over its 14 year mission with a plasma analyser and ion-neutral mass spectrometer, encompassing an entire solar cycle, including two solar maxima occurring in 1979 and 1988 (*Brace and Kliore*, 1991). Initial observations were compared with dayside model ion concentrations by *Nagy et al.* (1980); the results were in good general agreement for most ionic species produced in Venus' upper atmosphere and characterised the resulting plasma environment as being dominated by CO_2^+ and O_2^+ up to ∼200 km. These species then decline with altitude as O^+, C^+, and N^+ become more dominant following further photoionization. The liberated electron concentrations have more recently been measured by the ASPERA instrument on Venus Express (*Coates et al.*, 2008). At the altitude where the magnetic pressure equals the thermal plasma pressure, a steep gradient in ion density occurs known as the ionopause, the location of which is strongly dependent on the incident solar wind pressure (*Russell et al.*, 2007a) and therefore varies with latitude, averaging ∼350-900 km at solar zenith angles of 0-90°, respectively (*Brace and Kliore*, 1991), as well as with the solar maxima-minima cycles. These processes result in a dynamic exosphere with the steady loss of ions produced by photoionization to space over time.

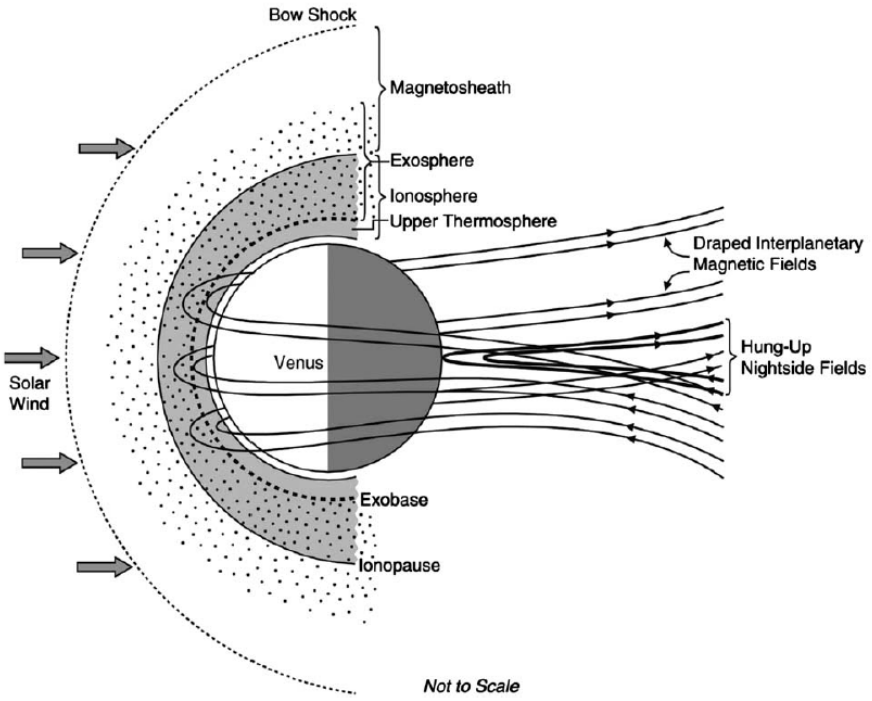

Figure 1.21: Schematic diagram of the solar wind interaction with Venus' upper atmosphere and the resulting induced magnetosphere (from *Russell et al.*, 2007a)

1.3 Objectives

The objectives of this thesis are as follows:

- to assess the role of volcanism within the various planetary processes described in section 1.2
- to explore whether or not volcanism is currently active
- to investigate the range of styles of volcanism that may occur on Venus
- to place Venusian volcanism into context with the global tectonic environment

These objectives will be achieved firstly by using computer modelling of volcanic processes based on models developed for terrestrial volcanism, adapted to Venusian conditions. Using this approach, the environmental requirements for various types of volcanic styles to occur may be evaluated to provide more detailed insight into these processes under Venusian conditions. Radar datasets from both Venus and Earth are

investigated with the aim of assessing relationships between differing volcanic deposits on Venus and their likely mode of formation, and using trends in the Earth radar data to inform us of what the Venus observations may be telling us. Finally, the mapping of volcanic features and rifts, and subsequent spatial analysis, enables the nature of the interaction of volcanism within the global tectonic environment to be evaluated. Through these related strands, the aim is to provide a coherent investigation that improves our understanding of volcanism as a fundamental planetary process in the Venus system.

Chapter 2

Computer modelling of volcanic eruption processes on Venus

This chapter is based upon the following published work: Airey, M. W., T. A. Mather, D. M. Pyle, L. S. Glaze, R. C. Ghail, and C. F. Wilson (2015), Explosive volcanic activity on Venus: The roles of volatile contribution, degassing, and external environment, *Planetary and Space Science, 113-114, 33-48*, doi:10.1016/j.pss.2015.01.009

2.1 Introduction

Volcanoes and their deposits are some of the most widespread and recognisable geological features in Venus' surface record (*Head et al.*, 1992; *Ford et al.*, 1993; *Crumpler and Aubele*, 2000; *Ivanov and Head*, 2011). Volcanic landforms include clusters of small shield volcanoes ranging from <1 km to 10s km in diameter ('shield fields'), large volcanoes up to ∼1000 km in diameter, steep-sided domes, isolated calderas not associated with an obvious edifice, and stress-induced surface deformation features known as coronae and novae (*Head et al.*, 1992) thought to be associated with shallow magma bodies (*McGovern and Solomon*, 1998). The broad variety of volcanic features on Venus suggests a corresponding variety of processes responsible for their formation.

Whether or not explosive eruptions occur on Venus has been the subject of debate

(e.g. *Thornhill*, 1993; *Fagents and Wilson*, 1995; *Glaze et al.*, 2011), as the conditions affecting the physical processes of eruption on Venus are very different from those on Earth. Lava flows have been recognised globally, while pyroclastic density currents and fallout deposits are apparently rare or absent. It has proved difficult to determine the nature of these less common volcanic deposits seen in the radar imagery of Venus and confirmation of an explosive origin has so far mostly proved to be controversial (*Campbell and Rogers*, 1994; *Keddie and Head*, 1995; *McGill*, 2000; *Grosfils et al.*, 2011). One recent exception is a proposed pyroclastic deposit known as Scathach Fluctus, identified by *Ghail and Wilson* (2013). This pyroclastic interpretation was arrived at via a combination of radar characteristics, flow morphology, and flow interaction with other geomorphological features.

Establishing whether explosive volcanism occurs on Venus might yield further clues concerning subsurface conditions on Venus and would better inform our understanding of atmospheric processes such as the apparent SO_2 variations detected by Pioneer Venus (*Esposito*, 1985), and later Venus Express (*Marcq et al.*, 2013). In terms of atmospheric interactions, understanding the heights that explosive plumes might achieve is also key. This study aims to better understand the eruptive behaviour of volcanoes on Venus through consideration of the factors affecting these processes.

2.1.1 Explosive volcanism

The processes resulting in terrestrial explosive volcanism have been widely documented in numerous articles on magma ascent dynamics (e.g. *Wilson et al.*, 1980; *Woods*, 1995; *Papale et al.*, 1998; *Papale and Polacci*, 1999) and the magma degassing behaviour that leads to it has been extensively modelled (*Newman and Lowenstern*, 2002; *Lesne et al.*, 2011; *Witham et al.*, 2012). Whether or not explosive volcanism results in a buoyant plume has also been extensively described in previous work on eruption column physics (*Wilson et al.*, 1978; *Sparks*, 1986; *Woods*, 1988; *Valentine and Wohletz*, 1989; *Woods*, 1995, and others). A parcel of magma that decompresses sufficiently and exsolves enough of the volatile gas phase to initiate fragmentation within the conduit, either

when the gas volume fraction in the mixture exceeds a critical value (*Sparks*, 1978), or the magma suffers brittle failure and fragments (*Gonnermann and Manga*, 2003; *Tuffen and Dingwell*, 2005), is then emitted from the vent into the overlying atmosphere as a volcanic plume, initially in a momentum-driven 'gas thrust' regime. The column will collapse into a fountain unless enough atmospheric gas can be entrained, heated by the clasts within the plume, expand, and become buoyant. The column is then considered to be in a buoyancy-driven 'convective' regime, and will continue to rise and expand until it reaches the level of neutral buoyancy. At this level, the column spreads laterally in an 'umbrella' region (*Sparks*, 1986).

The first application of subaerial plume modelling under Venus conditions was carried out by *Thornhill* (1993); the minimum initial parameter values required for explosive activity were identified by applying the model of *Woods* (1988) to Venusian environmental conditions. A case study by *Robinson et al.* (1995) applied the same model to Ma'at Mons and suggested that explosive volcanism could have been responsible for the elevated atmospheric SO_2 concentrations detected by Pioneer Venus (*Esposito*, 1985). A further suite of studies estimated the overall plume height attainable by explosive volcanic eruption columns over a range of boundary conditions similar to those chosen for this study (*Glaze*, 1999), and with circular vs. linear vent geometries (*Glaze et al.*, 2011). In this study, a conduit flow dynamics model, not previously applied to Venusian conditions is linked via a jet decompression model with an established plume dynamics model, which has previously been applied to Venus (*Glaze et al.*, 1997). In addition to this, the model includes CO_2 as an accessory volatile species to H_2O. Previous models only included H_2O but on Venus CO_2 may be of comparatively greater significance in terms of plume dynamics than on Earth when considering the potentially smaller concentration of magmatic H_2O (see section 2.1.3) making its inclusion an important innovation.

When conducting an investigation into what may characterise the eruptive style of volcanoes, a broad array of environmental, chemical, and physical factors must be considered. The physical and chemical properties of the atmosphere into which erupted

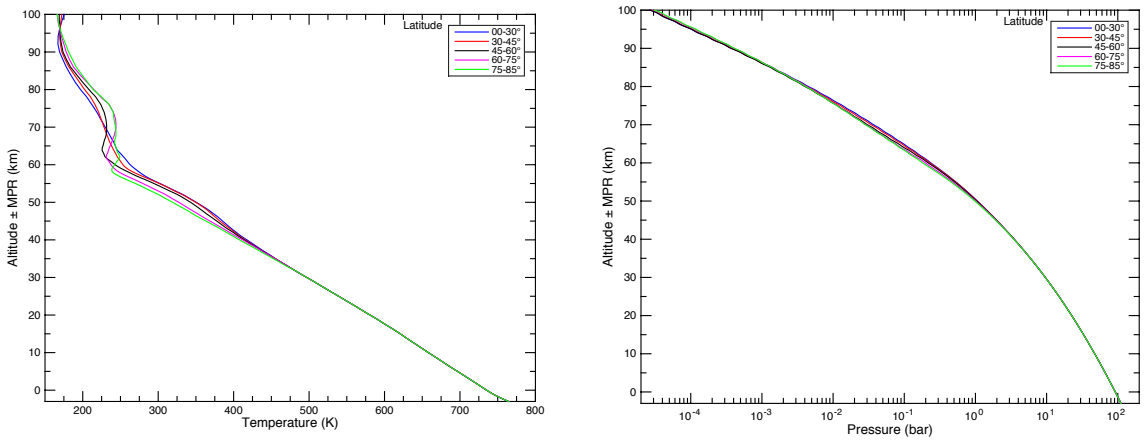

(a) (b)

Figure 2.1: Profiles through the Venus atmosphere from -3 km to 100 km relative to MPR of (a) temperature, and (b) pressure. Line colours correspond to profiles representative of latitudinal ranges as given in the key. Data from 100 to 0 km from *Seiff et al.* (1985) and extrapolated to -3 km.

material is injected have a strong control on plume behaviour and cause the process of plume generation to differ between Venus and Earth as do the material properties and the volatile load of the magma.

2.1.2 Environmental conditions on Venus

Venus has a dense CO_2-dominated atmosphere enshrouded in thick sulphuric acid clouds. The atmospheric composition of Venus is provided in Table 1.2 alongside those of Earth and Mars for comparison. At the mean planetary radius (MPR, ∼6051.8 km) the atmospheric pressure is ∼9.2 MPa and its temperature is ∼730 K due to the high atmospheric density and intense greenhouse effect (*Seiff et al.*, 1985). These factors inhibit explosivity by inhibiting magma fragmentation due to vesiculation, and reducing the plume-atmosphere boundary temperature contrast, respectively. Both the pressure and temperature are strongly altitude dependent, however, and diminish rapidly with altitude into conditions more conducive to the occurrence of explosive volcanism (see Figure 2.1). The altitude of the surface of Venus ranges between ∼-2 and ∼+9 km of the MPR.

The chemical composition of the atmosphere is an important factor since the pres-

ence of atmospheric water vapour can influence column dynamics by releasing latent heat and therefore enhancing buoyancy (*Glaze et al.*, 1997) above the altitude at which it condenses within the plume. This effect, however, is not significant in volcanic plumes on Venus because the atmosphere contains negligible water vapour (see Table 1.2). The value of the constant g (acceleration due to gravity) is slightly smaller on Venus, 8.41 m s^{-2} as opposed to 9.81 m s^{-2} on Earth, resulting in a smaller effect on magma pressure change during ascent (as later described in equation 2.1) and therefore column momentum flux on Venus than on Earth.

2.1.3 The characteristics of Venus magmas

The chemical composition of magma is important when modelling conduit processes because it affects the viscosity and fluid dynamic response of the decompressing magma flow (*Sparks*, 1978). With the exception of one anomalous site (Venera 13, which detected alkalic rocks), the bulk geochemical analyses carried out by the Russian Venera and Vega landers (Table 1.4), at sites located on lava plains and flows characteristic of most (>70%, *Ivanov and Head* (2011)) of the planetary surface, are consistent with a weathered basaltic surface composition (*Treiman*, 2007). Indeed, the numerous shield volcanoes evident on Venus appear analogous to basaltic shield volcanoes and seamounts on Earth. Steep-sided domes have been cited as evidence for a more felsic composition (*Pavri et al.*, 1992) but this is controversial and an evolved basaltic source has been proposed instead (*Stofan et al.*, 2000).

The concentration of the main volatile phases within the ascending magma are also very important when simulating eruptions since it has a very strong control on magma explosivity and the resulting exit velocity at the vent (*Wilson et al.*, 1980). In contrast to terrestrial studies, in which the magmatic volatiles are known to be predominantly H_2O, Venus is thought to have a drier mantle (*Nimmo and McKenzie*, 1998) in which the planetary inventory of H_2O was outgassed and incorporated into the thick clouds or broken down by UV photodissociation and lost to space from the upper atmosphere (*Donahue et al.*, 1982; *De Bergh et al.*, 1991; *Grinspoon*, 1993; *Donahue*,

1999). Therefore, the more prominent role of magmatic CO_2 is explored here, in addition to H_2O. H_2O, however is the chief volatile modelled here, not least because it is a readily observable component (by Venus Express) in the lowest scale heights (up to ∼25 km) on Venus (*Bézard et al.*, 2009, 2011), and therefore a ideal target in the search for volcanic emissions at the surface.

2.2 Methods

2.2.1 Initial conditions

This study models a simulated crustal host rock and magma source of a composition similar to that at the Venera 14 site (Table 1.4) and comparable to terrestrial tholeiitic basalt. This appears to be the least-weathered and best analogue for typical Venusian crust and magmas. The volatile phase of the magma is modelled to contain varying contributions of H_2O and CO_2 to simulate different likely volatile scenarios, as the true contributions are unknown. To more accurately quantify conduit/plume behaviour, future work should also include SO_2 explicitly in models.

In terms of physical conditions that affect column dynamics, key parameters to consider include the density of crustal material, which determines the lithostatic pressure at depth in the crust, and the conduit geometry, which affects the pressure gradient along the depth of the conduit modelled (*Wilson et al.*, 1980). In this study, basalt of density 2800 kg m^{-3} encloses a cylindrical conduit of a 25 m radius, constant along its length, with the exception of the results discussed in section 2.3.5, which explores the effects of other conduit radii. The key property of the magma controlling explosivity is its viscosity, which is a function of composition, volume of exsolved gas, and temperature, and is simulated over the range 1200-1700 K (encompassing the range representative of typical terrestrial basaltic magmas). Crystallisation in the magma is not simulated here to simplify the model and 0% solids is used in all model runs. The depth of the magma chamber influences the degree of volatile saturation at the base of the conduit, which can affect conduit processes; this study uses a conduit length of

5 km, with the exception of the results discussed in section 2.3.6, which explores the effects of other conduit lengths.

2.2.2 Model setup

In order to simulate the processes occurring within the ascending magma, a simple conduit flow code (section 2.2.3) was combined with outputs from a model for the solubility of C,O,H,S,Cl species in basaltic magmas, SolEx (*Witham et al.*, 2012). In the original work of *Witham et al.* (2012), the SolEx model, based on the original code of *Dixon* (1997), was compared with the experimental work of *Lesne et al.* (2011) and was found to match experimental data reasonably well. Also in that study, the model was compared with the models of *Newman and Lowenstern* (2002) and *Papale et al.* (2006); it was found to match the former well for mid-ocean ridge basalt melts (MORB) and the latter for ocean island basalt melts (OIB). As a result, I suggest that SolEx represented a model that could effectively simulate a wide range of basaltic compositions.

SolEx can be parameterised to run for all the initial conditions considered here and produces output covering the full range of pressures required. Therefore, using SolEx provides a thorough treatment of the degassing regimes without the need to incorporate this aspect into the conduit model. SolEx output was generated for closed-system degassing in several volatile scenarios, incorporating various contributions from H_2O and CO_2 and over a range of pressures from 0.5-400 MPa. These include the full range of pressures to be explored in the modelling exercise, bracketed by the lowest pressure of 4.74 MPa (atmospheric pressure at a vent 10 km above the MPR), and a pressure of $\sim$228 MPa, being the pressure at the base of a 10 km deep conduit (the deepest simulated conduit base, section 2.3.6) beneath a vent at MPR. The SolEx output variables, as a function of pressure, used in this study include the fraction of each volatile species dissolved in the magma, the total volume fraction of gas present as bubbles in the magma, and the relative contributions of each volatile species to that volume fraction.

Table 2.1: Conduit base pressures used in the model simulations for vent elevations up to 10 km on Earth and Venus. Values based on a magma density 2600 kg m^{-3}, g of 9.81 m s^{-2} (Earth) and 8.41 m s^{-2} (Venus), conduit length of 5 km, and atmospheric surface pressures as in Figure 2.1b.

	Vent elevation (km)										
	0	1	2	3	4	5	6	7	8	9	10
Base P (MPa)											
Earth	127.630	127.620	127.610	127.600	127.592	127.584	127.578	127.571	127.566	127.560	127.557
Venus	118.540	117.975	117.439	116.931	116.450	115.995	115.565	115.158	114.774	114.411	114.069

The conduit code (section 2.2.3) first of all reads in the SolEx data and interpolates all the variables to a 1 MPa resolution for use in the subsequent calculations. To specify the pressure regimes under investigation, atmospheric pressure data from the Venus International Reference Atmosphere (VIRA) (*Seiff et al.*, 1985) dataset were used for the 0-10 km range of vent altitudes, along with Earth pressures for comparison. Pressure at depth from all these starting positions is then calculated for both Venus and Earth, assuming basaltic crust, with magma of density 2600 kg m^{-3} and corresponding values of g being 8.41 m s^{-2} for Venus and 9.81 m s^{-2} for Earth. This produces a pressure profile unique to each vent altitude. Conduit base pressures at all elevations used in the model runs are specified in Table 2.1. These values are higher for Earth due to the higher value of g; they are more variable on Venus however, because the more variable atmospheric component represents a more significant fraction of the total pressure at a given depth.

After defining values for the fixed model variables (Table 2.2), the variables unique to the scenario are specified: the elevation, the initial wt% of each volatile in the magma and the magma temperature (ranges shown in Table 2.2). The ranges of these inputs are simply intended to cover a representative range of scenarios. The conduit geometry is assumed circular and kept at a constant radius of 25 m and length of 5 km for the initial model runs. A constant radius of 25 m is chosen for the main study to represent a modest conduit for comparative purposes, and to reduce the necessity for an unwieldy amount of data. Although this conduit size is fairly small compared to other modelling studies that use fixed conduit radii (e.g. 40-63 m in *Papale et al.* (1998), 50 m in *Papale and Polacci* (1999)), it was chosen to be near the middle of the

Table 2.2: Fixed values and variable ranges used in the model runs. Fixed values represent favoured values for the main study; entries in italics represent ranges explored for individual investigations in sections 2.3.3-2.3.6.

	Fixed value	Min value	Max value
Conduit length	5 km	*4 km*	*10 km*
Conduit radius	25 m	*10 m*	*100 m*
Initial magma density	2600 kg m^{-3}		
Crustal density	2800 kg m^{-3}		
Acceleration due to gravity	8.41 m s^{-2}		
Elevation ± MPR	0 km	*0 km*	*10 km*
H_2O wt%		1%	5%
CO_2 wt%		0%	3%
Magma temperature	1200 K	*1200 K*	*1700 K*

typical range observed for conduits on Earth (e.g. *Scandone and Malone*, 1985; *Papale and Dobran*, 1994; *Diez*, 2006). The magnitude of the effect of varying this property is explored in section 2.3.5. Vents of this radius, or indeed the larger radii used by *Papale et al.* (1998), would not be visible at the Magellan radar resolution, which is sampled to 75 m pixels from an original (variable with latitude) resolution of >100 m (*Ford et al.*, 1993). The 5 km depth to chamber is chosen to represent a standard base condition for the models and is kept constant in order to reduce the overall number of variables. This approach is similar to that of *Papale et al.* (1998) and *Papale and Polacci* (1999), where a conduit length of 7 km is used; the effect of conduit length is explored in section 2.3.6. Volatile-saturated magma viscosity is calculated using the method of *Giordano et al.* (2008) with the Venera 14 composition and stored in a matrix from which values can be retrieved corresponding to the temperature of the magma in that run.

2.2.3 Model details

The core of the model is the steady-state, homogeneous flow conduit code, adapted from the previous models of *Mastin and Ghiorso* (2000) and *Diez* (2006), which were themselves based on the work of *Woods* (1995). In contrast to previous models that use the Runge-Kutta 4^{th} order iterative method to solve the differential equations, this uses

an iterative loop, which manually calculates (or retrieves) values for twelve properties at regular intervals from the base of the conduit to the vent and inserts them into a results matrix. The step size is set small enough (1 m) so that the solution will be equivalent to what it would have been had the Runge-Kutta method been employed. This slightly different approach enables data not generated within the code, such as the SolEx data, to be easily retrieved via a look-up table within the iterations. The MATLAB code is available in Appendix A.

First of all the depth is recorded, followed by the pressure in the mixture at that depth. This starts with the initial value for the maximum depth calculated previously (section 2.2.2) along with an incremental change according to equation 2.1,

$$\frac{dp_c}{dz_c}\left(1-\frac{u_c^2}{u_s^2}\right) = -\rho_c g - \frac{\rho_c u_c^2 f}{r_c} \tag{2.1}$$

where dp_c is the change in pressure in the conduit, z_c is the vertical increment (1 m), u_c is the magma velocity, u_s is the acoustic velocity in the mixture, ρ_c is the density of the mixture, g is the acceleration due to gravity, r_c is the conduit radius, and f is a friction term. The friction term is calculated using equation 2.2. The first term represents the frictional component due to the viscosity of the magma and the second, f_0, is a constant that represents the effect of friction imposed by the roughness of the conduit walls. This constant is taken to be 0.0025, a value generally used to represent a rough walled eruptive conduit (e.g. *Wilson et al.*, 1980),

$$f = \frac{16\eta}{\rho_c u_c D} + f_0 \tag{2.2}$$

where D is the conduit diameter and η is the viscosity of the gas-liquid mixture and is calculated using equation 2.3a below the fragmentation depth (volume fraction gas $\leq$0.75) or 2.3b above (volume fraction gas >0.75),

$$\eta = \frac{\eta_m}{1-\phi} \tag{2.3a}$$

$$\eta = \eta_g \left(1 - \left(\frac{1-\phi}{0.62}\right)\right)^{-1.56} \tag{2.3b}$$

where η_m is the volatile-saturated isothermal magma viscosity corresponding to the fixed model magma temperature, η_g is the gas viscosity (taken to be $5.3 \times 10^{-5} Pa\ s$), and ϕ is the volume fraction gas corresponding to the local pressure taken from SolEx.

The values of H_2O and CO_2 wt% dissolved in the magma are recorded individually and summed, and the total volume fraction of gas is recorded. From these, the mass fraction of the gas exsolved from the magma (equation 2.4), and the mixed gas constant resulting from the various volatile components (equation 2.5) are calculated,

$$n_c = \frac{n_{c0} - n_m}{1 - n_m} \tag{2.4}$$

$$R_{mixed} = (n_{H_2O} \times R_{H_2O}) + (n_{CO_2} \times R_{CO_2}) \tag{2.5}$$

where n_c is the mass fraction of exsolved gas, n_{c0} is the original volatile content, n_m is the pressure-dependent volatile mass fraction in the magma (from SolEx), R is the gas constant for the corresponding subscript, and n_{H_2O} & n_{CO_2} are the relative contributions of the corresponding volatiles (from SolEx). Next, the mixture density and ascent velocity are calculated using equations 2.6 and 2.7,

$$\frac{1}{\rho_c} = \frac{n_c R_{mixed} T_m}{p_c} + \frac{1 - n_c}{\rho_m} \tag{2.6}$$

$$u_c = \frac{Q}{\rho_c A} \tag{2.7}$$

where T_m is the magma temperature, Q is the mass flux, and A is the cross-sectional

area of the conduit. Q is calculated using equation 2.8,

$$Q = \rho_{c0} u_{c0} A \tag{2.8}$$

where ρ_{c0} is the initial magma density and u_{c0} is the starting magma velocity, being initially 1 m s^{-1}, but subsequently modified as described later. The acoustic velocity of the mixture and Mach number of the ascending magma are then calculated using equations 2.9 (using the method of *Wilson et al.* (1980)) and 2.10,

$$u_s = \sqrt{\left(\frac{R_{mixed} T_m}{n_c}\right)} \left(n_c + (1 - n_c) \frac{p_c}{\rho_m R_{mixed} T_m}\right) \tag{2.9}$$

$$M = \frac{u_c}{u_s} \tag{2.10}$$

where M is the Mach number. These calculations are performed for each entry in the results matrix and the conditions at the vent are then assessed. If the pressure at the vent is equal to the atmospheric pressure, the eruption occurs at its subsonic velocity. If however sonic conditions are achieved at some point in the conduit of constant radius, meaning the flow is choked, the mixture can no longer decompress and therefore can no longer accelerate. The mixture must therefore erupt at $M = 1$. If none of these conditions are met, a shooting solution method is employed, where the initial velocity is increased in diminishing increments (increasing Q) until either atmospheric pressure (subsonic eruption) or $M = 1$ (choked flow) is attained. The final values are then stored in a new matrix corresponding to unique conditions of volatile regime, elevation, and magma temperature.

For the purposes of this study, scenarios that exceeded a volume fraction of 0.75 at the vent are assumed to erupt explosively as this is where the bubbly liquid regime transitions to the gas with suspended liquid droplets regime (*Sparks*, 1978). Caution must be exercised in applying this criterion because the fragmentation process is more complex and occurs at a range of values between 0.7-0.8 volume fraction gas. Factors thought to define the point of fragmentation include the point at which the gas over-

pressure exceeds the tensile strength of the magma, causing bubble disruption (*Zhang*, 1999), or when the rapid decompression causes rapid bubble growth such that the deformation rate exceeds that of the structural relaxation rate of the magma (*Papale*, 1999). Future modelling work to capture these relatively poorly constrained processes is to be encouraged but is beyond the scope of this study.

A subsequent test is carried out to ascertain whether or not the resulting plume achieves buoyancy. In order to do this the results of the conduit flow model are used as input to a subaerial plume dynamics model (*Glaze et al.*, 1997), based on the work of *Woods* (1988) and *Morton et al.* (1956). This code generates values for the plume height and the neutral buoyancy height (if buoyant). When linking these models, the jet decompression to atmospheric pressure upon eruption is accounted for using a linking code (MATLAB code available in Appendix B) based on the method of *Woods and Bower* (1995) as follows.

The conditions above the vent, where the pressure of the jet has decompressed sufficiently to be in equilibrium with atmospheric pressure, can be evaluated first of all by using the approximation for the jet density described in equation 2.11,

$$\rho_d \sim \frac{p_{atm}}{n_{c0} R_{mixed} T_m} \tag{2.11}$$

where ρ_d is the density of the decompressed jet and p_{atm} is the atmospheric pressure. The velocity resulting from jet decompression is calculated using equation 2.12,

$$u_d = \left(n_{c0} R_{mixed} T_m\right)^{0.5} \alpha\beta \left(1 + \frac{n_c}{n_{c0}\alpha\beta^2}\left(1 - \frac{p_{atm}}{p_c}\right)\right) \tag{2.12}$$

where u_d is the velocity of the decompressed jet and

$$\alpha = 1 + \frac{(1 - n_c)\, p_c}{n_c R_{mixed} T_m \rho_m} \tag{2.13}$$

$$\beta = \frac{n_{c0} - n_m}{n_{c0}^{0.5}\left(n_{c0} - \frac{n_m}{2}\left(1 + \frac{p_c}{R_{mixed} T_m \rho_m}\right)\right)^{0.5}} \tag{2.14}$$

Using these newly calculated variables, the physical dimensions of the jet can then be calculated using equations 2.15 and 2.16,

$$A_d = \frac{Q}{u_d \rho_d} \tag{2.15}$$

$$r_d = \left(\frac{A_d}{\pi} \right)^{0.5} \tag{2.16}$$

where A_d and r_d are the new values for the cross-sectional area and radius of the decompressed jet.

The output from this intermediate model, where all parameters correspond to the fully decompressed jet, is then used with the original subaerial plume model of *Glaze et al.* (1997). The plume model details are not reproduced here for clarity, but are described exhaustively in the cited article. Parameter regions where buoyant plumes occur, and the volume fraction gas values, are mapped onto the conduit exit velocity datasets to identify up to three distinct regions of volcanic styles: effusive, explosive collapsing, and explosive buoyant.

2.3 Results

2.3.1 Model testing and validation

In order to validate the conduit flow code, a series of comparison runs were performed with the existing conduit flow code of *Mastin and Ghiorso* (2000), Conflow version 1.0.5. Although these codes under comparison were based fundamentally on the same constitutive relationships and governing equations, the effects of the differing approach taken with the degassing calculations (i.e. SolEx vs. that hard-coded into the Mastin model) are explored in this comparative analysis. Pure H_2O was modelled as the volatile phase (Conflow is not capable of simulating CO_2) from a 5 km deep, 25 m radius conduit/vent under Venusian surface conditions at MPR with magma of 1200 K temperature and a base pressure of 118.54 MPa. Figure 2.2 shows the profiles for

pressure, volume fraction gas, Mach number, and velocity from each of the two models for H_2O concentrations of 1, 2, 3, 4, and 5% respectively. The plots also show the final value of each property, describing conditions simulated at the vent.

The two models show a good overall match. This is true in particular in terms of pressure, the prediction of which is the primary aim of the conduit model. The disparity between the two sets of results in the case of the volume fraction gas, and the resultant velocity, is due largely to differences between SolEx and the degassing calculations employed in Conflow. In contrast to SolEx, which uses the calculations of *Dixon* (1997) to quantify the melt/vapour partitioning of volatiles, Conflow uses the MELTS method of *Ghiorso and Sack* (1995) to calculate the chemical potential of water in the melt and the method of *Haar et al.* (1984) to calculate the chemical potential of water in the vapour phase. The mass fraction of water in the melt is then adjusted until the chemical potential is the same as that of the H_2O vapour.

In order to also include CO_2, an H_2O/CO_2 volatile mix was modelled in SolEx, and adapted the gas constants as appropriate in the calculations. To explore the effect of this mixed volatile phase, the degassing of basalt was modelled at a temperature of 1200 K with varying volatile inventories in SolEx. Figure 2.3 shows the results when keeping the H_2O content fixed (3%) and calculating the effect of increasing the CO_2 composition from 0-3%. As expected, the increase in CO_2 (along with the increase in total volatile content) results in deeper onset of degassing, due to the much lower solubility of CO_2, and a higher total volume fraction at all pressures until 0 MPa. When the substitution of H_2O with CO_2 is considered (Figure 2.4), the trend at high pressures shows an increase in the volume fraction gas with increasing CO_2 contribution as expected. However, at lower pressures the curves intersect resulting in an inversion in the trend of the degree of exsolution i.e. at a given pressure, say 25 MPa, an increase in the contribution from CO_2 results in a decrease in the volume fraction of gas. This could partly be due to the use of the model beyond its calibrated range for CO_2, as only examples of <1 wt% CO_2 are explored/compared with experimental data in the original work of *Witham et al.* (2012) and therefore results for high-CO_2 runs are

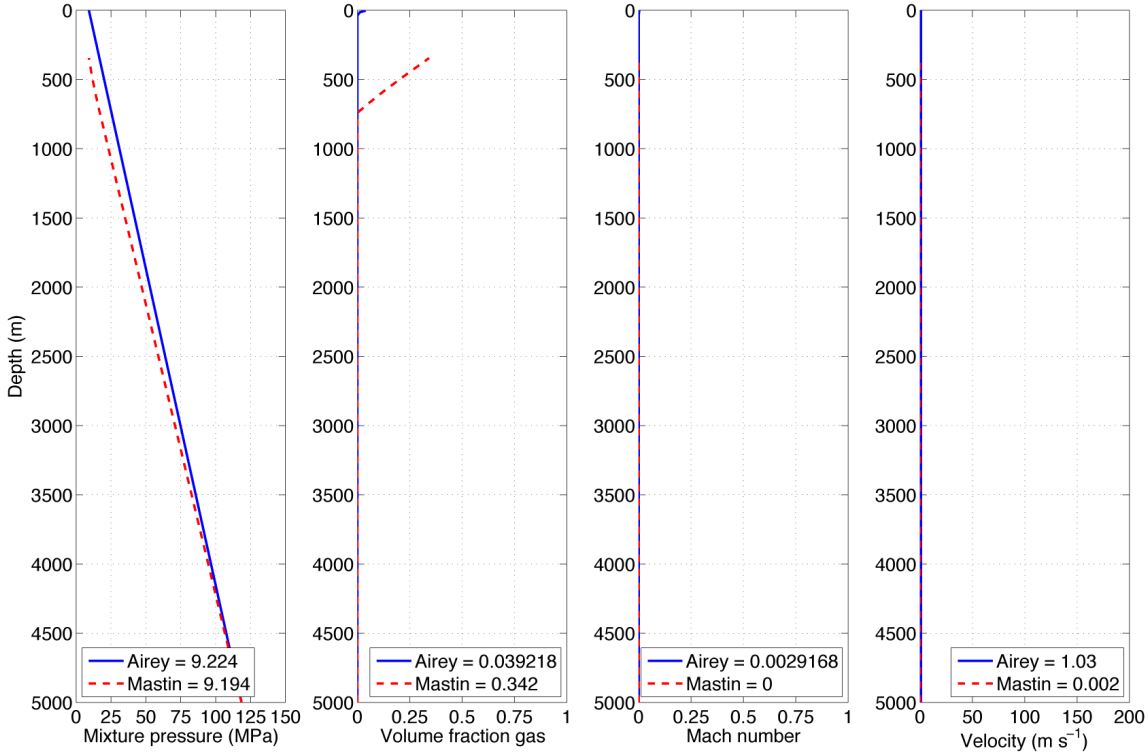
Depth (m)
Mixture pressure (MPa)
Airey = 9.224
Mastin = 9.194
Volume fraction gas
Airey = 0.039218
Mastin = 0.342
Mach number
Airey = 0.0029168
Mastin = 0
Velocity (m s^{-1})
Airey = 1.03
Mastin = 0.002

(a)

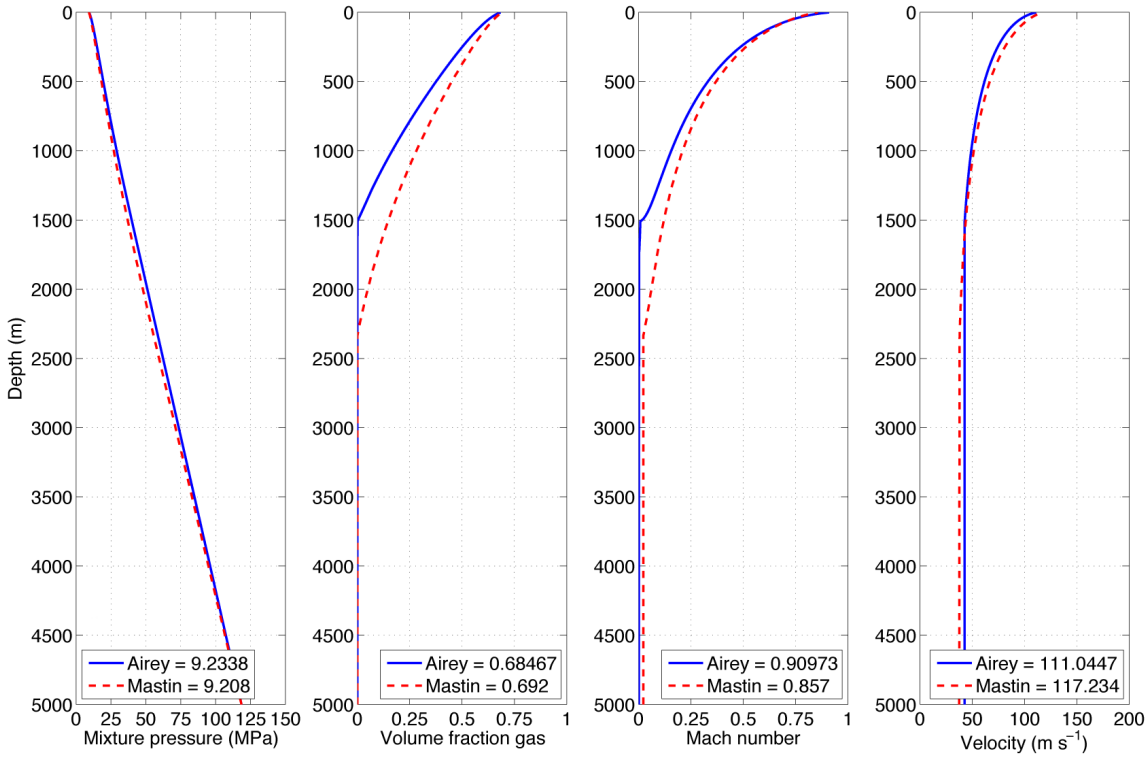
Depth (m)
Mixture pressure (MPa)
Airey = 9.2338
Mastin = 9.208
Volume fraction gas
Airey = 0.68467
Mastin = 0.692
Mach number
Airey = 0.90973
Mastin = 0.857
Velocity (m s^{-1})
Airey = 111.0447
Mastin = 117.234

(b)

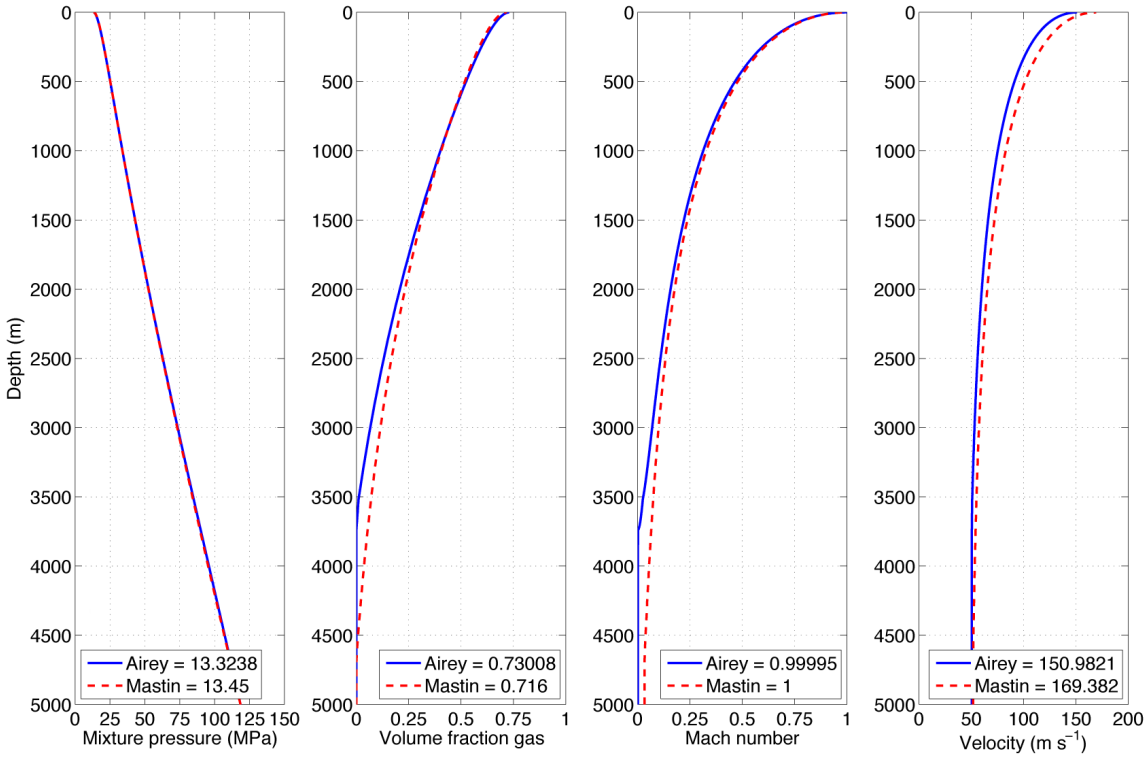
Depth (m)
Airey = 13.3238
Mastin = 13.45
Mixture pressure (MPa)
Airey = 0.73008
Mastin = 0.716
Volume fraction gas
Airey = 0.99995
Mastin = 1
Mach number
Airey = 150.9821
Mastin = 169.382
Velocity (m s^{-1})

(c)

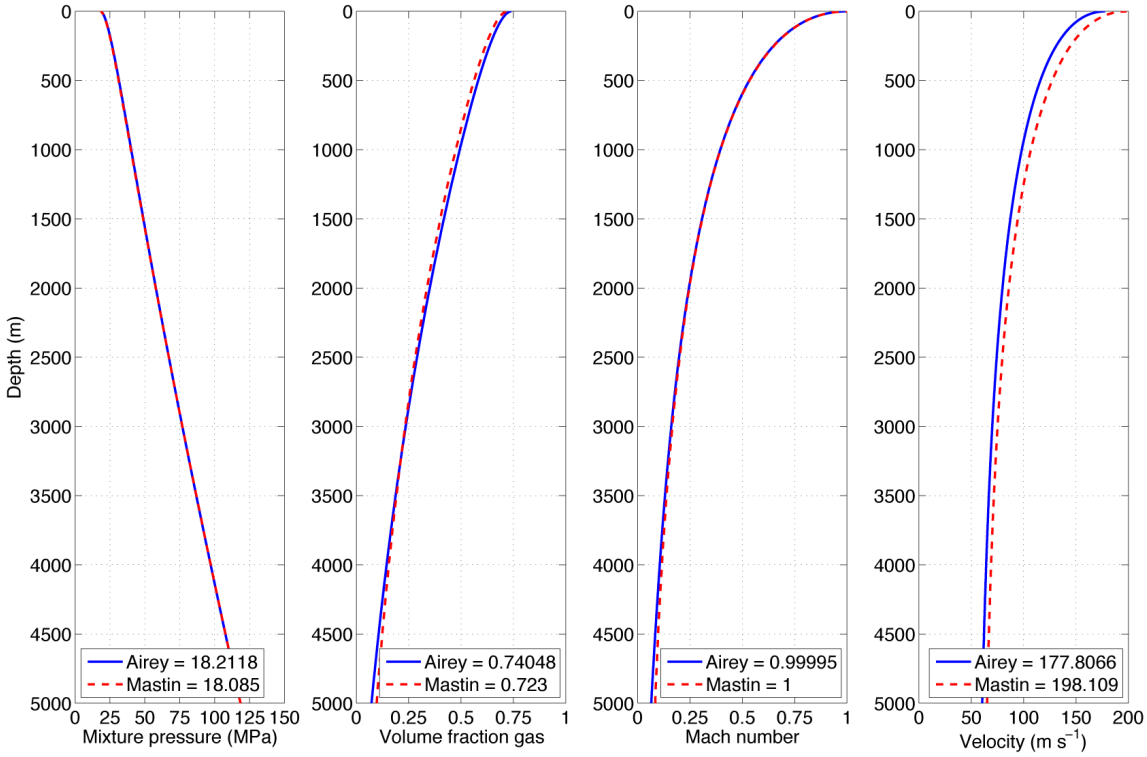
Depth (m)
Airey = 18.2118
Mastin = 18.085
Mixture pressure (MPa)
Airey = 0.74048
Mastin = 0.723
Volume fraction gas
Airey = 0.99995
Mastin = 1
Mach number
Airey = 177.8066
Mastin = 198.109
Velocity (m s^{-1})

(d)

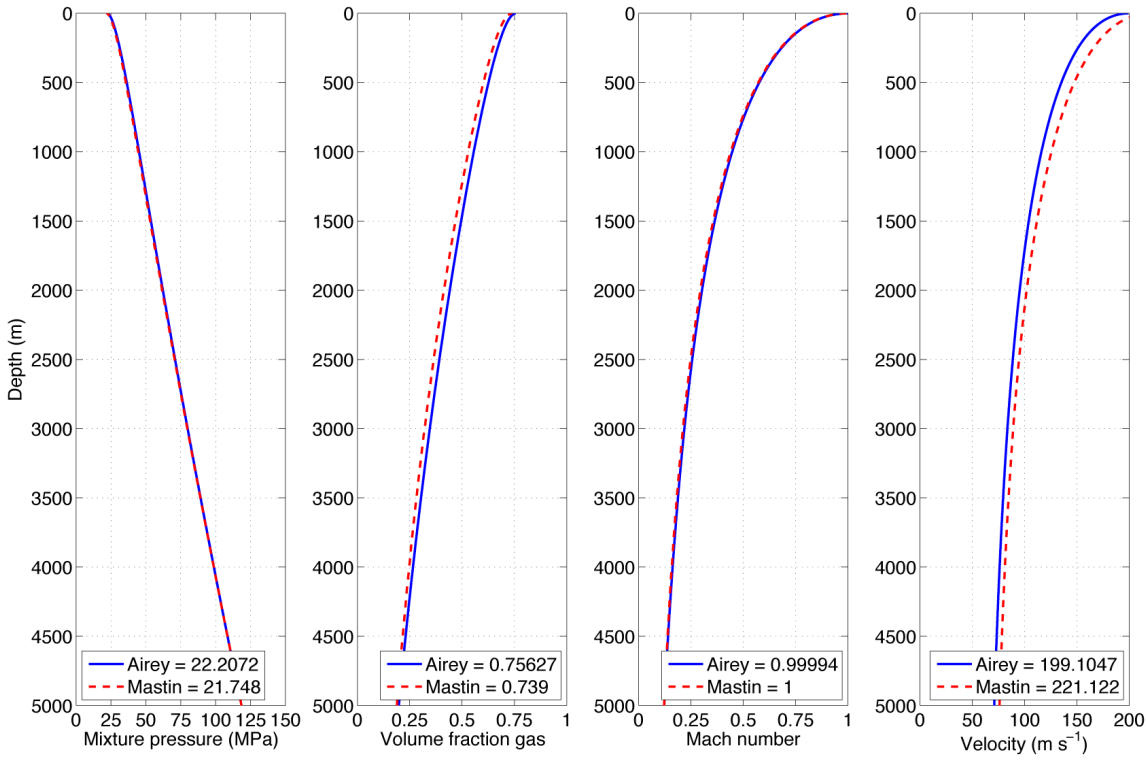

(e)

Figure 2.2: Conduit flow model comparisons between the existing model of *Mastin and Ghiorso* (2000) (red, dashed curves) and the model developed in the current study (blue, solid curves) for a) 1% H_2O, b) 2% H_2O, c) 3% H_2O, d) 4% H_2O and e) 5% H_2O. The values of pressure, volume fraction gas, Mach number, and velocity stated in the key represent the final value recorded at the vent (i.e. depth = 0 m)

considered with caution.

2.3.2 Effect of CO_2 addition on volatile exsolution and velocity

Figures 2.5a and 2.5b show the modelled conditions at the vent on both Earth and Venus when the H_2O concentration of a magma is kept constant (3%), but the CO_2 concentration is varied. The models were run for a 5 km long, 25 m radius conduit with magma temperature 1200 K and base pressures of 127.63 MPa (Earth) or 118.54 MPa (Venus). As the final pressure at the vent increases with the initial additional CO_2, so does the exit velocity. Where CO_2 concentration is >1% on Earth and >0.5% on Venus the volume fraction of exsolved gas also increases with addition of CO_2. Below these thresholds however, there is an initial drop in volume fraction of exsolved gas with

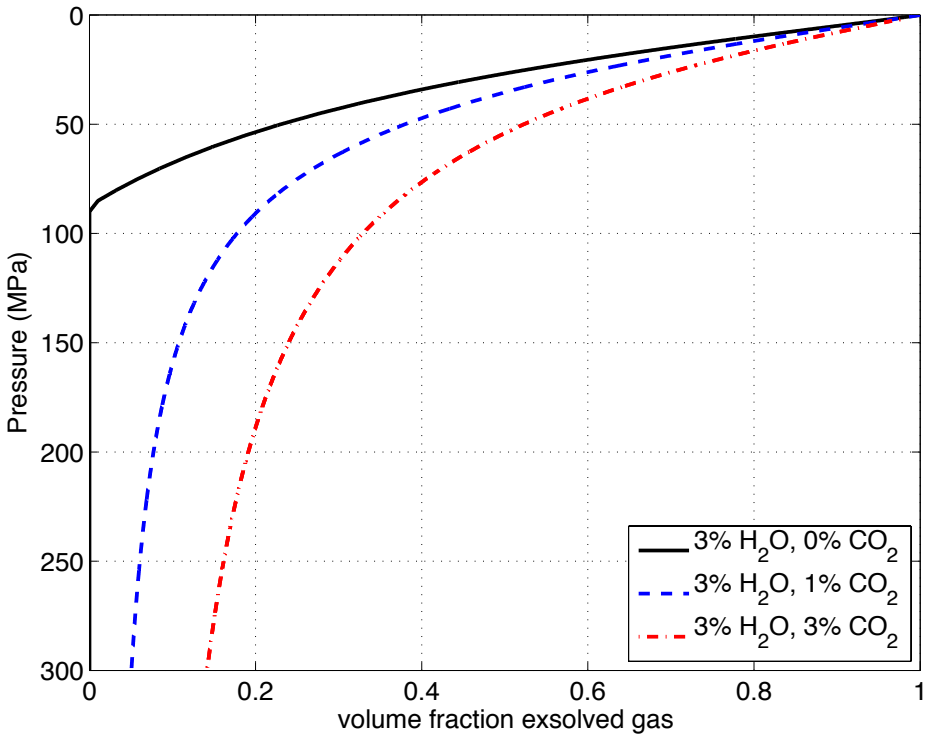

Figure 2.3: Volume fraction exsolved gas in a basaltic magma as a function of confining pressure for various initial volatile concentrations, from 3 wt% H_2O to 3 wt% H_2O + 3 wt% CO_2.

the introduction of CO_2 to the magma. The increase in initial magmatic CO_2 content alters the pressure gradient within the conduit resulting in a higher magmatic pressure at any given point in the conduit (shown in Figure 2.5 for the surface). The result of this is a greater proportion of the gas phase being stable dissolved in the magma up to a point (1% on Earth, 0.5% on Venus in this example), after which further addition increases the degree of total gas exsolution. This change occurs as a greater volume of total volatile is present and the effect of increased gas volume outweighs that of the increased pressure. On Earth, the effect on volatile exsolution of adding CO_2 does not return the volume fraction gas to values greater than the original, pre-CO_2 value when modelled up to an additional 3%. On Venus however, once $\gtrsim$2% additional CO_2 has been added, the volume of exsolved gas exceeds the original pre-CO_2 value.

To illustrate other initial H_2O scenarios on Venus, Figure 2.6 shows the same data as displayed in Figure 2.5b for 3% initial H_2O (corresponding to the orange lines on

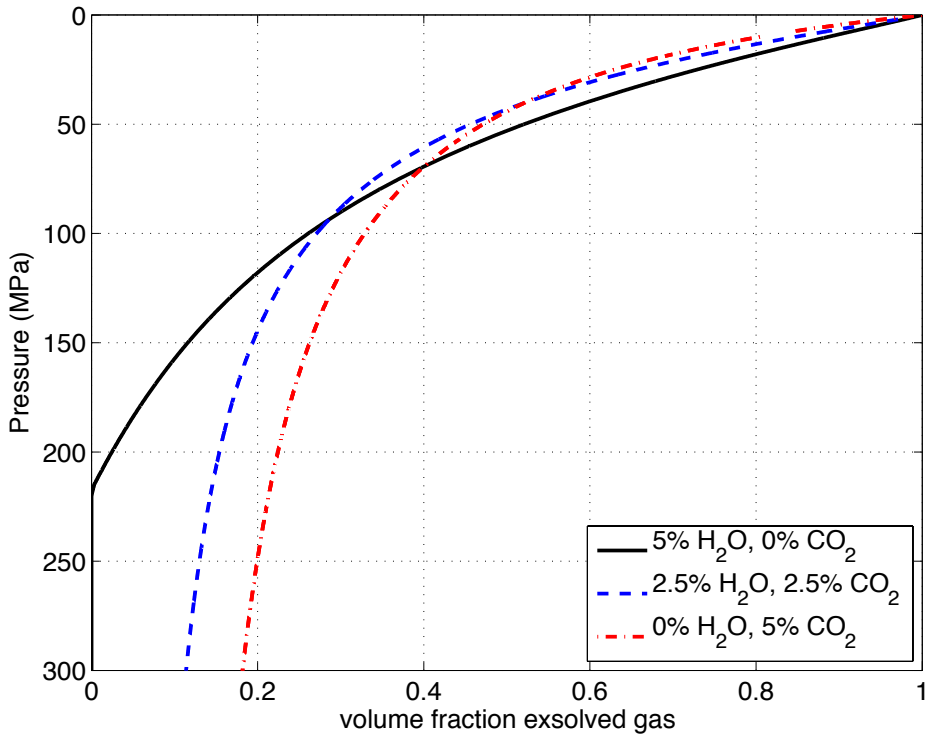

Figure 2.4: Volume fraction exsolved gas in a basaltic magma as a function of confining pressure for a constant initial volatile content of 5% with varying contributions from H_2O and CO_2 as shown in the key.

Figure 2.6), along with those for 1, 2, 4, and 5%. The inital drop in volume fraction gas with the introduction of CO_2 is not seen in magmas with >4% initial H_2O, as the higher relative proportion of H_2O dominates the gas phase. The addition of CO_2 required for magma fragmentation to occur (crossing the dotted line) can be seen to decrease with increasing base H_2O, e.g. 3% H_2O + 3% CO_2, 4% H_2O + 1.3% CO_2, and >4.5% H_2O + 0% CO_2. All magmas are choked in the conduit, with the exception of all 1% H_2O runs and 2% H_2O + $\lesssim$0.1% CO_2 (up to ~0.05 $CO_2/(H_2O + CO_2)$ on Figure 2.6b), which erupt subsonically.

2.3.3 Effect of variations in elevation

The decrease in atmospheric pressure with elevation on Venus can be seen in Figure 2.1b. This has an effect on conduit processes, as the confining environment is less extreme and therefore the total pressure at the base of the conduit is lower for higher

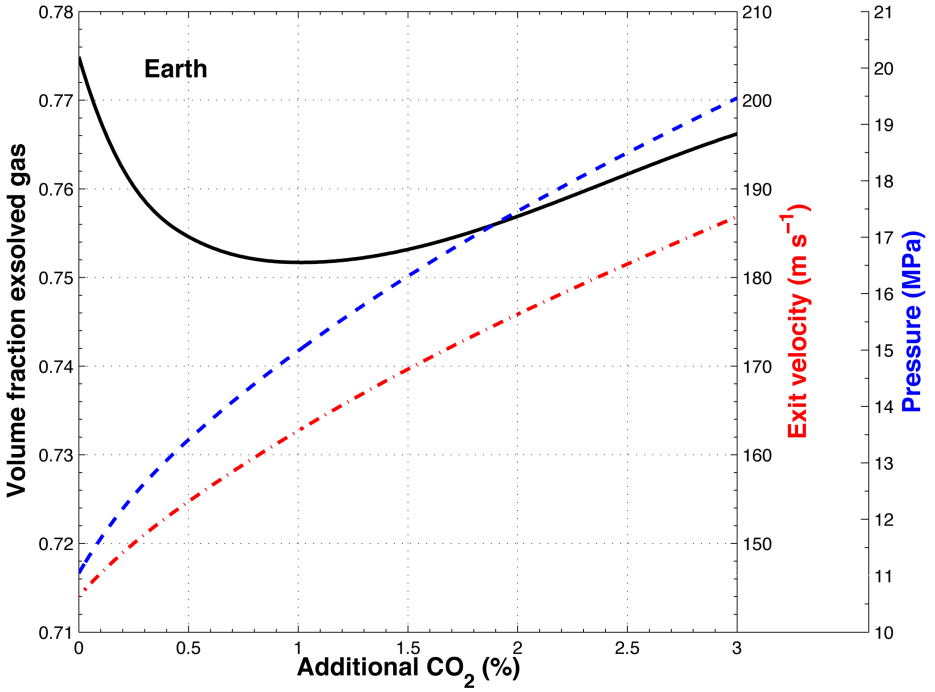

(a)

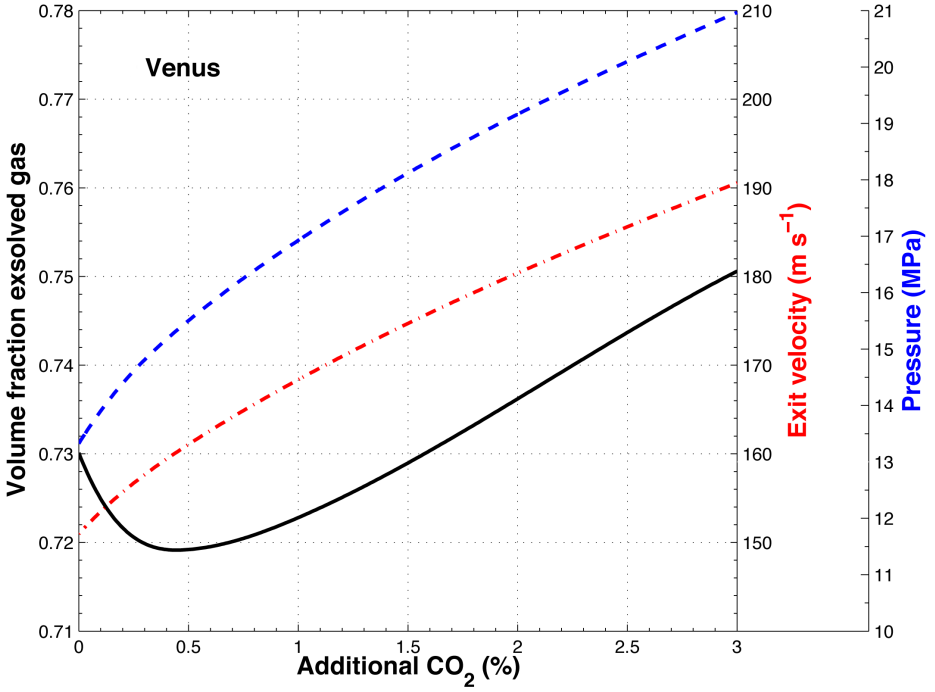

(b)

Figure 2.5: The response of volume fraction gas (black, solid curves), exit velocity (red, dot-dash curves), and pressure (blue, dashed curves) to an increasing concentration of CO_2 (0-3%) added to magma of constant H_2O concentration (3%). Values correspond to conditions at the volcanic vent of radius 25 m above a conduit of 5 km length, and a magmatic temperature of 1200 K at a) Earth's surface and b) Venus' MPR. Base pressures are 127.63 MPa (Earth) or 118.54 MPa (Venus).

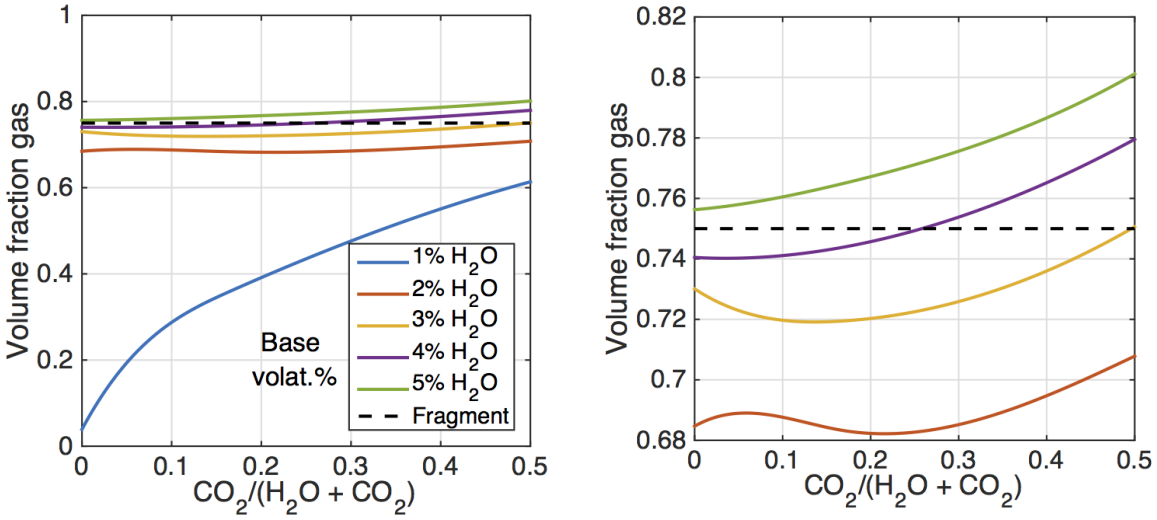

Figure 2.6: The response of volume fraction gas to an increasing proportion on CO_2 in magmas on Venus as in Figure 2.5b, but with initial H_2O concentrations varying from a) 1 to 5%, and b) detail of 2 to 5%. Initial conditions as in Figure 2.5b

elevation vents. Model runs were simulated for elevations up to 10 km above MPR to recreate the range of volcanic vent incidences observed on Venus. These were again run with a conduit of 5 km length and 25 m radius, a magma temperature of 1200 K, and base pressures as in Table 2.1. The same scenarios used in Figure 2.5 were used to explore the effects of elevation on vent pressure, velocity, and volatile exsolution. Results of three examples of volatile combinations (3% H_2O with 0%, 1%, and 3% additional CO_2) are shown in Figure 2.7. An increase in vent pressure and exit velocity with CO_2 addition is observed, as is the drop/rise in volume fraction gas seen in the previous section. The effect of increasing altitude is to decrease the vent pressure and increase the volume fraction of gas in the magma. This is due to the decrease in lithostatic pressure at any given depth in the conduit, allowing more of the volatile phase to be stable as gas bubbles in the magma. The actual fall in vent pressure with altitude is less than the fall in surface atmospheric pressure with vent altitude, $\sim 1.2 \times 10^5$ Pa km^{-1} in contrast to $\sim 4.5 \times 10^5$ Pa km^{-1}, an effect of the flows being choked and therefore unable to fully decompress. The effect on velocity of increasing altitude is almost negligible. This is because, as the eruptions are all choked in these examples,

they erupt at their sonic velocity. The sonic velocity decreases only very slightly with decreasing pressure, and therefore increasing altitude, by $\sim$0.3 m s^{-1} km^{-1}. As these model runs were all simulated at an isothermal 1200 K, the dependency of sonic velocity on temperature is not represented in these results.

2.3.4 Effect of variations in magma temperature

So far all model runs have been conducted at the conservative temperature, in terms of typical terrestrial basaltic eruptions, of 1200 K in order to compare the effects of other variables. If however, the effect of hotter magmas within a reasonable range based on terrestrial temperatures is considered, further effects on magma properties at the vent become apparent. Figure 2.8 introduces this new variable into the existing model examples, being representative of magmas containing 3% H_2O with 0%, 1%, and 3% CO_2, respectively. These simulations were again run with conduits of 5 km length and 25 m radius, and base pressures as in Table 3. It is apparent that, at any given altitude, an increase in magma temperature results in an increase in exit velocity and a decrease in volume fraction gas. The increased temperature reduces the viscosity of the magma allowing higher velocities to be attained due to reduced friction with the conduit walls. The effect of this, however, is to reduce the magnitude of the drop in pressure with ascent resulting in a higher pressure at the vent and a correspondingly lower degree of volatile exsolution.

2.3.5 Effect of variations in conduit radius

The geometry of the conduit through which the ascending magma propagates is another important factor to consider. Thus far, the conduit geometry used in all model runs has been a perfect cylindrical tube of a constant 25 m radius. In reality a great range of sizes can occur. Although linear geometries are not considered here, the effects of varying the size of a cylindrical conduit are explored in Figure 2.9. When maintaining constant magma temperature, elevation, and volatile composition/concentration (1200 K, MPR, 118.54 MPa base pressure, 3% H_2O, 0% CO_2), it is clear that circular conduits

of a larger cross sectional area favour higher velocities (as increasing D reduces the friction term in equation 2.2), and less volatile exsolution due to the higher conduit pressure. Up to ∼50 m radius, even small variations in conduit size can be seen to have

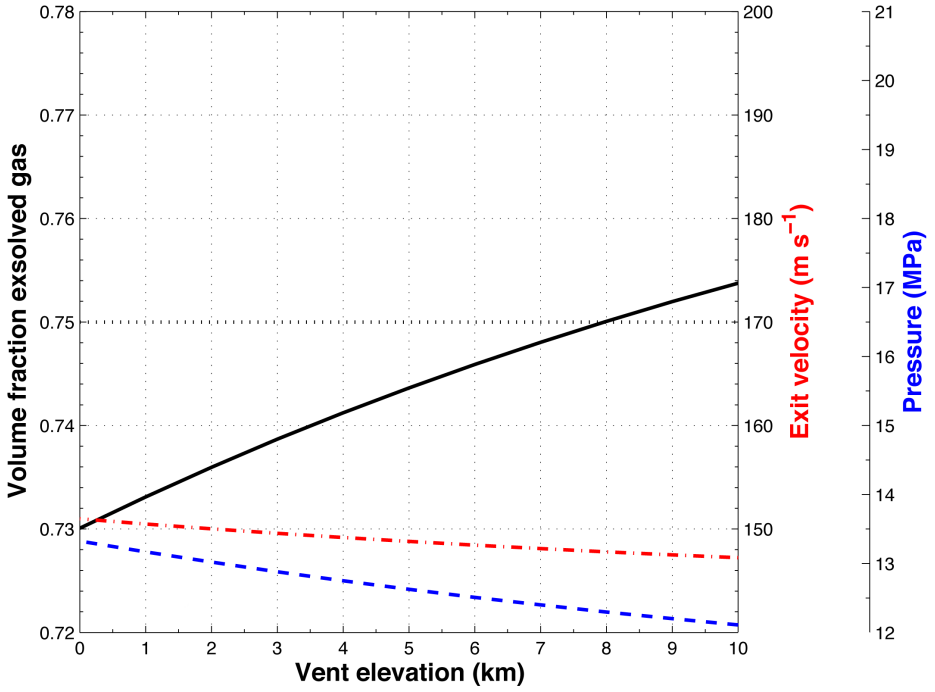

(a)

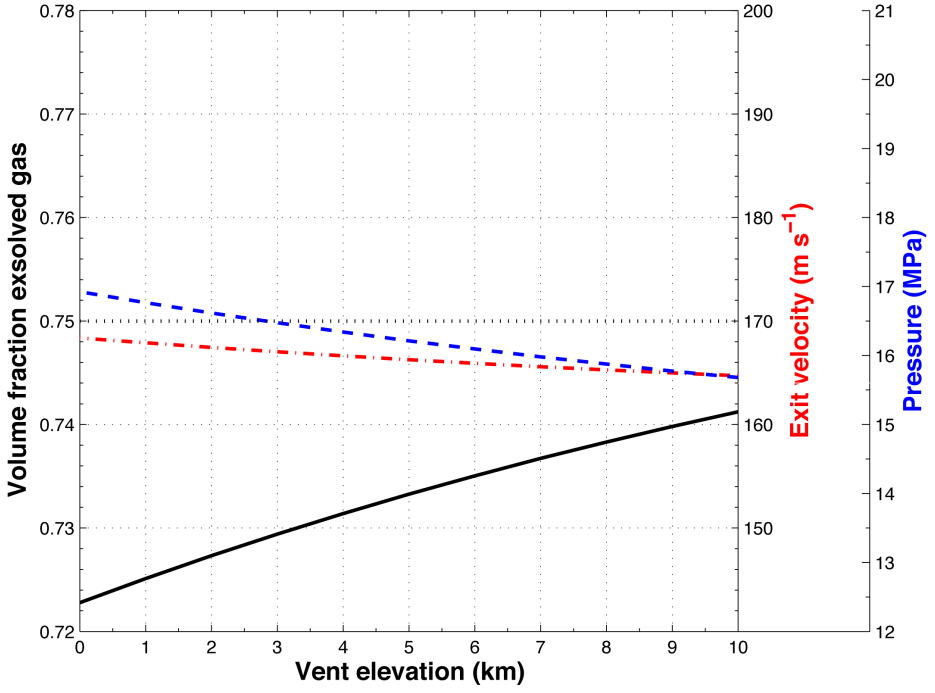

(b)

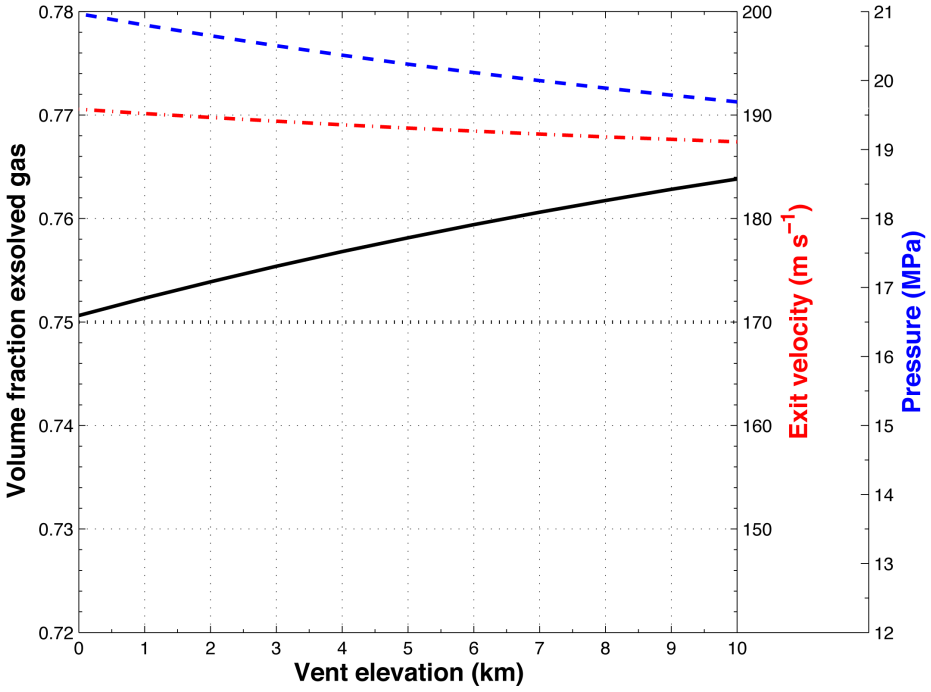

(c)

Figure 2.7: Effects of elevation on volume fraction gas (black, solid curves), exit velocity (red, dot-dash curves), and vent pressure (blue, dashed curves) at a 25 m radius volcanic conduit on Venus with a basaltic magma of 1200 K, 3% H_2O, and an additional a) 0%, b) 1%, and c) 3% CO_2. The horizontal dotted line corresponds to the estimated fragmentation criterion. Base pressures as in Table 2.1.

pronounced effects on these properties. At radii over 50-100 m, the magnitude of the effect of increasing the conduit size decreases, eventually approaching an asymptotic value corresponding to the individual scenario conditions.

2.3.6 Effect of variations in conduit length

The bulk of this study considers a constant conduit length of 5 km, however varying the conduit length in these simulations affects the results as described in Figure 2.10. Base pressures range from ∼97 MPa at 4 km long conduits to ∼229 MPa for 10 km long conduits. Simulations are run at 3% H_2O, 25 m conduit radius and 1200 K magma temperature. Longer conduits result in lower velocities but have only a very minor effect, <4 m s^{-1} with an increase in depth of 6 km. The effect on volatile exsolution, however, is more prominent. Increasing the conduit length alters the pressure gradient

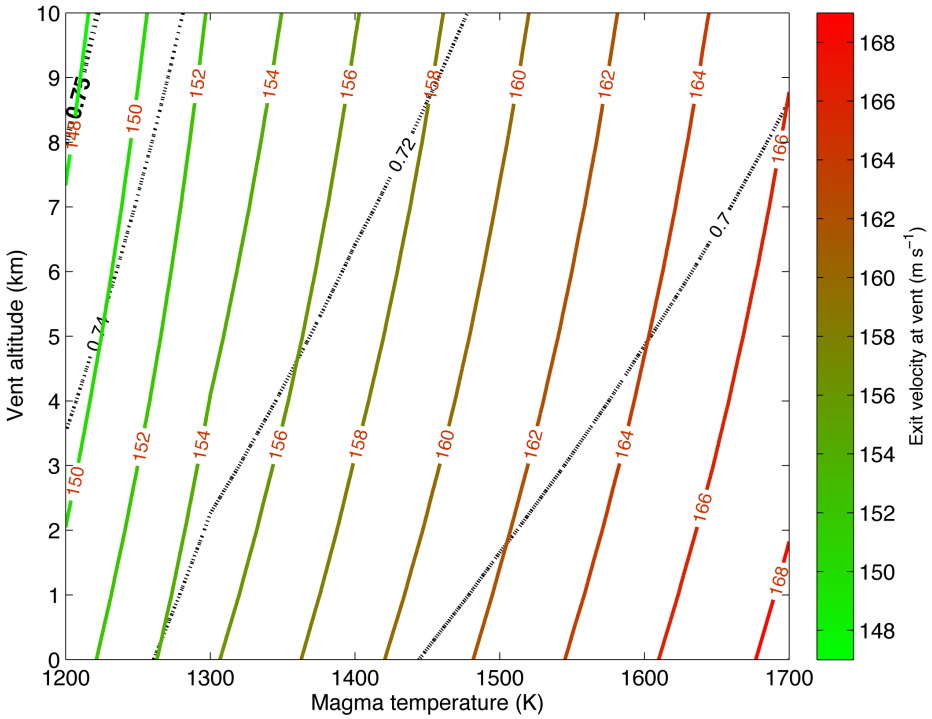
Vent altitude (km)
Magma temperature (K)
Exit velocity at vent (m s^{-1})
0.74
0.72
0.7

(a)

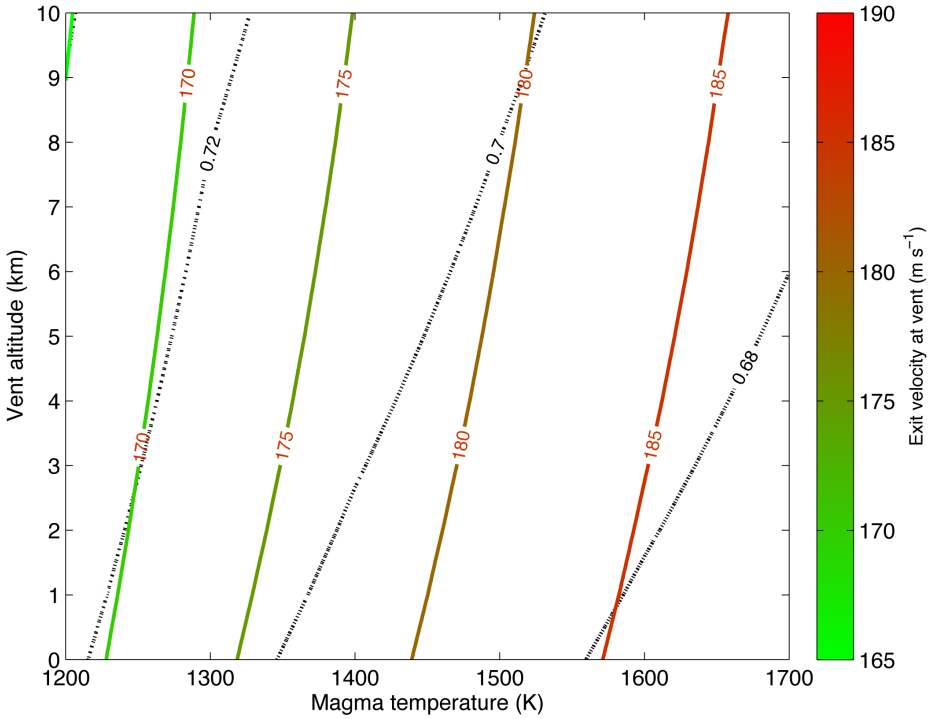
Vent altitude (km)
Magma temperature (K)
Exit velocity at vent (m s^{-1})
0.72
0.7
0.68

(b)

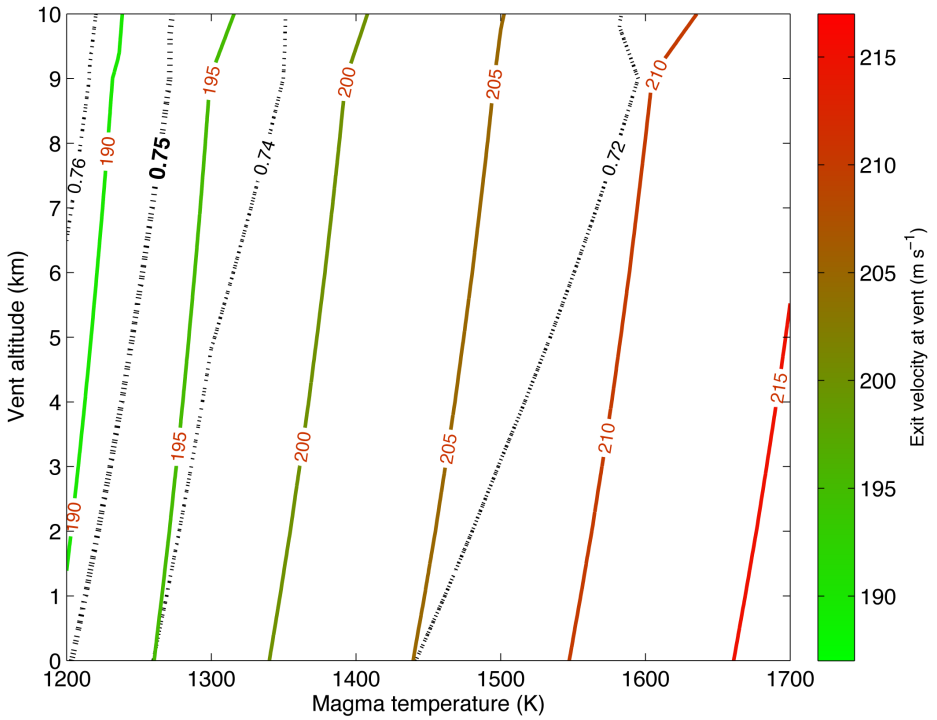

(c)

Figure 2.8: Volume fraction gas (black, dashed contours) and exit velocity (coloured, solid contours) as a function of vent altitude and magma temperature. The fragmentation threshold, volume fraction gas = 0.75, is highlighted in bold. Models run for a basaltic magma emerging from a 5 km deep, 25 m radius conduit with 3% H_2O and an additional a) 0%, b) 1%, and c) 3% CO_2. Base pressures as in Table 2.1.

such that deeper chambers result in a lower conduit pressure immediately prior to eruption, increasing the degree of exsolution and the likelihood of fragmentation within the conduit.

2.3.7 Jet decompression of choked flows at the vent

Upon eruption at the surface, an overpressured choked flow will rapidly decompress to atmospheric pressure resulting in an increase in the eruption column velocity and radius. Figures 2.11 and 2.12 show the effect of jet decompression on velocity and column radius respectively, as a function of volatile content, above the vent. The contrast between a given conduit pressure and atmospheric pressure is much more pronounced on Earth than it is on Venus as a result of the much higher atmospheric

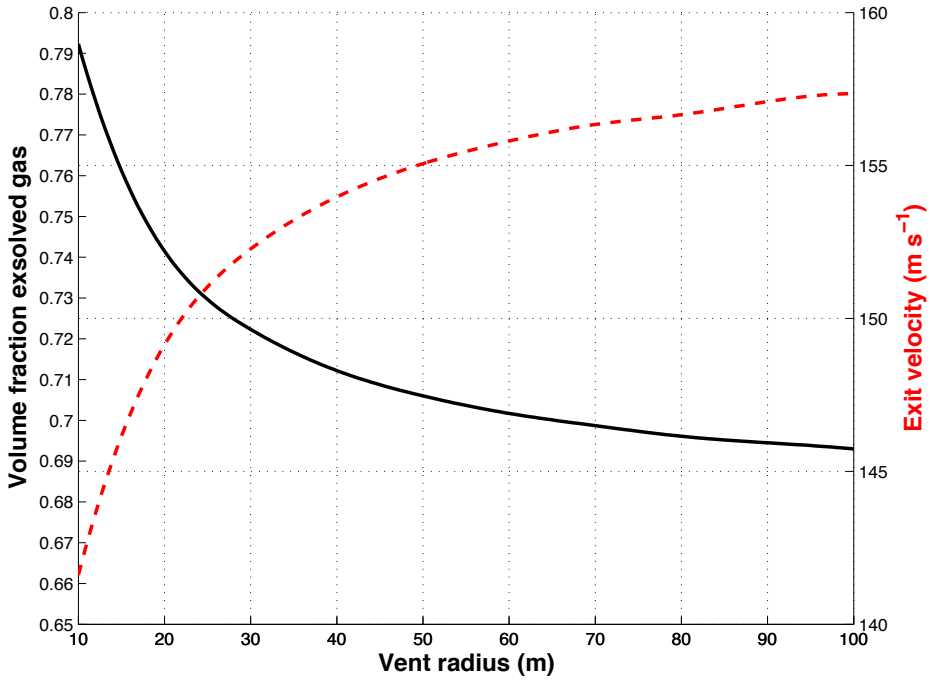

Figure 2.9: Volume fraction exsolved gas (black, solid curve) and exit velocity (red, dashed curve) as a function of conduit radius for a basaltic magma erupting at Venus' MPR with a 5 km long conduit, 3% H_2O, a magma temperature of 1200 K, and a base pressure of 118.54 MPa.

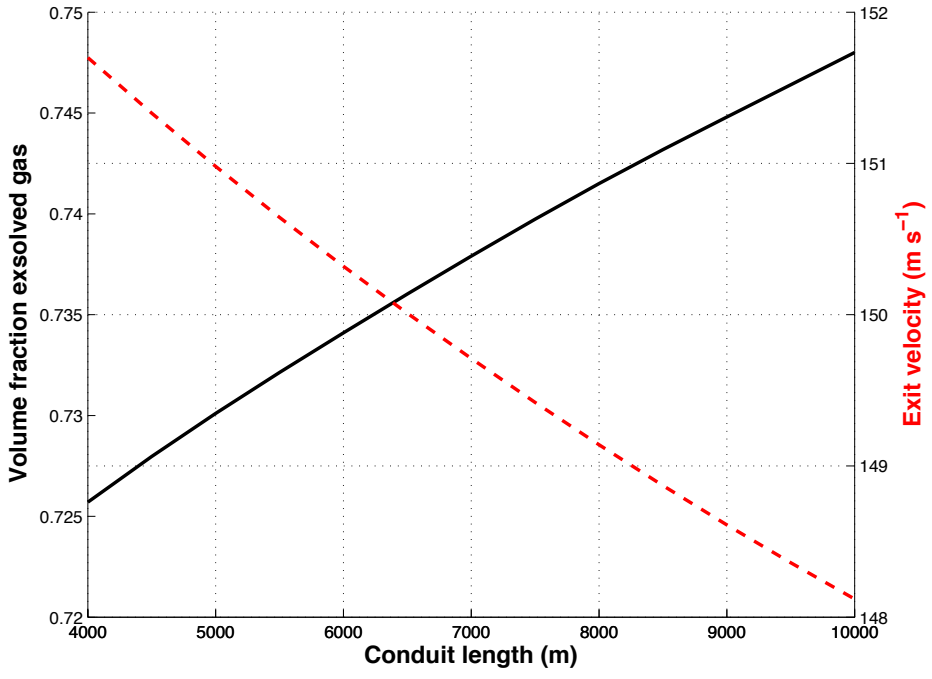

Figure 2.10: Volume fraction exsolved gas (black, solid curve) and exit velocity (red, dashed curve) as a function of conduit length for a basaltic magma erupting at Venus' MPR with a conduit of radius 25 m, 3% H_2O, and a magma temperature of 1200 K.

pressure on Venus. The examples shown in Figures 2.11 and 2.12 are for jets emerging at the MPR from a 5 km long conduit of 25 m radius with magma of Venera 14 composition (Table 1.4), a temperature of 1200 K, and base pressures of 127.63 MPa (Earth) or 118.54 MPa (Venus).

The changes to jet variables caused by decompression on Earth can clearly have an important influence on plume behaviour. Considering a magmatic H_2O range of 1-5% (Figures 2.11a and 2.12a) and the initial conditions specified above, an increase in velocity of ∼70% and an increase in column radius to ∼4-10 times the initial value can occur. When using these results in column buoyancy modelling, jet decompression is therefore an important process to consider. When adding CO_2 to a scenario with a constant magmatic H_2O concentration of 3% (Figures 2.11b and 2.12b), the effect is similar, but rather less pronounced.

When the above conditions are applied to Venus it is found that the effects are subtler, with a velocity increase of up to ∼35% between 2-5% H_2O (eruptions with <2% H_2O erupting subsonically), and a column radius increasing by only a few metres (Figures 2.11a and 2.12a). As with the terrestrial example, adding CO_2 to a base value of 3% H_2O has a small but significant effect on these column properties (Figures 2.11b and 2.12b); the velocity with an increase of up to ∼35% when given a large additional input of CO_2, and the radius increase being negligible. These results for Venus are only applicable as input to the plume buoyancy model, under these base conditions, to H_2O concentrations >4.5% (Figures 2.11a and 2.12a) and H_2O = 3% with >3% additional CO_2 (Figures 2.11b and 2.12b) i.e. where the volume fraction gas exceeds 0.75. Below these thresholds, the jets would collapse following decompression regardless, as the unfragmented material cannot undergo the column buoyancy processes involving atmospheric entrainment described in section 2.1.1 (unless sufficient further fragmentation occurs upon jet decompression).

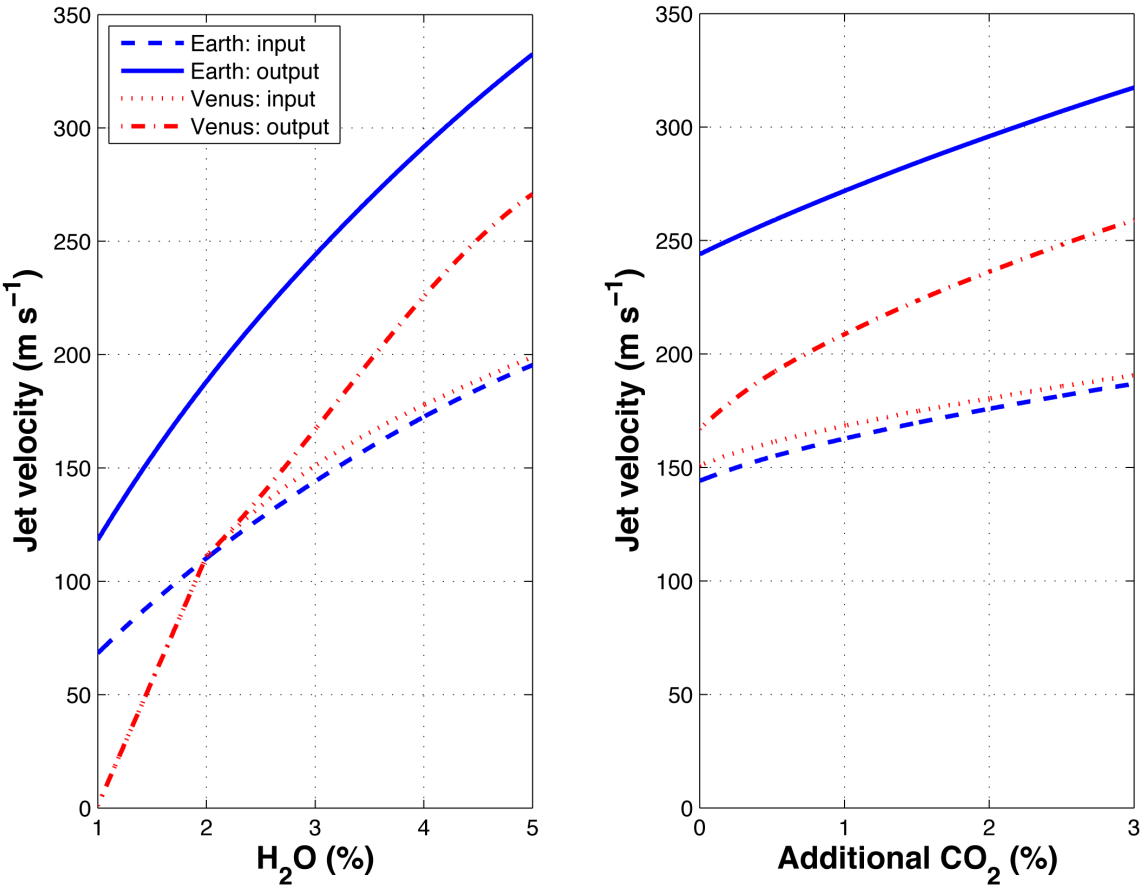

(a) (b)

Figure 2.11: The effect of jet decompression on jet velocity from a 5 km long conduit of radius 25 m with magma of Venera 14 composition, magma temperature of 1200 K, base pressures of 127.63 MPa (Earth) or 118.54 MPa (Venus), and (a) H_2O concentrations from 1-5%, or (b) CO_2 concentrations up to 3% added to a constant H_2O concentration of 3%. Results are compared for Earth and Venus as described in the key; 'input' data correspond to the initial velocity at the vent immediately upon eruption and 'output' data correspond to the final velocity when the jet has decompressed to local atmospheric pressure.

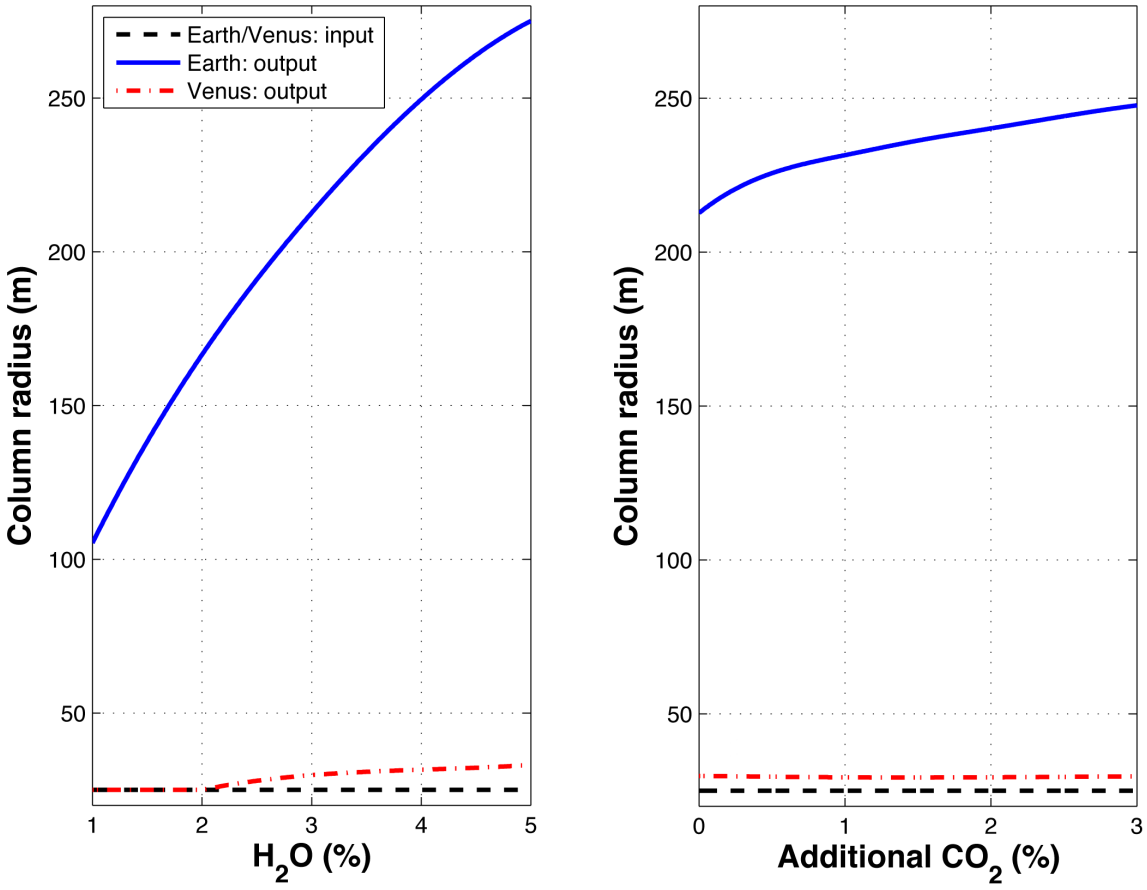

(a) (b)

Figure 2.12: The effect of jet decompression on eruption column radius from a 5 km long conduit of radius 25 m with magma of Venera 14 composition, magma temperature of 1200 K, base pressures of 127.63 MPa (Earth) or 118.54 MPa (Venus), and (a) H_2O concentrations from 1-5%, or (b) CO_2 concentrations up to 3% added to a constant H_2O concentration of 3%. Results are compared for Earth and Venus as described in the key; 'input' data correspond to the initial column radius immediately upon eruption, i.e. the vent radius of 25 m in all cases on both Earth and Venus, and 'output' data correspond to the final column radius when the jet has decompressed to local atmospheric pressure.

2.4 Discussion

2.4.1 Explosivity of eruptions

A great many factors influence the behaviour of volcanic events. As discussed above, the potential for explosive volcanic activity on Venus is often discounted because of the high atmospheric pressure compared with Earth. Adopting the method of a critical threshold for magmatic fragmentation, here assumed to be a volume fraction of 0.75 gas in the magmatic mixture (*Sparks*, 1978), the modelling suggests that there are certain scenarios in which explosive volcanism is feasible on Venus. As discussed above, fragmentation processes are more complex and occur at a range of values between 0.7-0.8 volume fraction gas and are also influenced by other factors such as the tensile strength of the magma and the structural relaxation rate of the magma (*Papale*, 1999; *Zhang*, 1999).

One of the major considerations when investigating whether or not explosive volcanism may occur is the requirement in terms of the initial concentration of volatiles in the magma. As discussed above, the interior of Venus may well be considerably drier than Earth's and so it is worth considering the effect of lower H_2O concentrations and the role of CO_2. On its own, CO_2 as the primary volatile phase cannot be responsible for explosive volcanism. Model runs with pure CO_2 have demonstrated that a magma of 1200 K emerging from a 25 m radius conduit would require a CO_2 concentration in excess of $\sim$6.5% at an altitude of 10 km above MPR, or $\sim$7.5% at the MPR in order to achieve the fragmentation. However, it is probable that minor volatile phases such as CO_2 contribute to the volatile inventory, thereby reducing the total H_2O requirement for explosive volcanism to occur. If this is the case, accessory volatiles are likely to be required in much higher concentrations, i.e. $>$1%, than are commonly found on Earth. Although plate tectonics is apparently absent on Venus, it is likely that a wide variety of melt source regions occur on Venus through other tectonic and fractionation processes, and that these may concentrate volatile rich material.

Although this might suggest that sufficient CO_2 as a primary volatile is unlikely,

other mechanisms could result in this volatile causing explosive behaviour. For example, as the atmosphere of Venus is a supercritical fluid, it could potentially circulate through the upper crust and gather in fluid-rich pockets that could violently mix with ascending magma resulting in an explosive response. Alternatively, degassing of a stalled magma body may cause the build up of pressure and transient vulcanian activity (*Fagents and Wilson*, 1995).

This modelling exercise shows that if explosive volcanism does occur, H_2O is very likely required in magmatic systems. Evidence in support of excess H_2O in the mantle includes the possibility of re-fertilisation of the mantle with volatiles due to gravitational instabilities at the base of the lithosphere (*Elkins-Tanton et al.*, 2007) and in contrast to the D/H ratio, atmospheric Ar measurements indicate that as little as 25% of the planetary inventory of H_2O might have been outgassed from the interior (*Kaula*, 1999).

The Venus models presented here are based entirely on the most representative geochemical analysis available, the Venera 14 lander, which appears to have detected a tholeiitic-type basalt. No felsic material has so far been directly measured and using alternative lander data would only vary the model results a little. It is widely assumed that the vast majority of volcanic rocks on Venus are basaltic based on this, and on radar observations of lava flow morphology. This may indeed be the case but regions with a more felsic composition are certainly plausible and are inherently more likely to produce explosive behaviour because of their higher silica content and viscosity, although this is not directly modelled here. The 1 μm emissivity data retrieved by VIRTIS (Visible and Infrared Thermal Imaging Spectrometer on Venus Express) and processed by *Mueller et al.* (2008) show consistently low emissivity returns from tessera regions (deformed highland terrains) and are interpreted as more felsic material due to the lower emissivity of felsic minerals (e.g. quartz, feldspars) at this wavelength. *Pavri et al.* (1992) suggest that the steep-sided-domes seen on Venus could be the result of more felsic eruptions based on their inferred flow rheology. Geochemical modelling shows that more felsic source regions could be created as a result of fractional

crystallisation of rocks of Venera compositions (*Shellnutt*, 2013) in the presence of H_2O.

When modelling the effect of composition on magmatic processes, the effect of crystallisation should also be considered. In this work, a constant 0% solids is assumed. If, however, crystallisation did occur during magma ascent, the composition would vary as a function of melt fraction and volatiles would preferentially partition into the melt, thereby promoting bubble growth such that the volume fraction of gas in the conduit, and the viscosity, would increase (*Gonnermann and Manga*, 2012). Both of these processes increase the potential explosivity of the magma and, as a result, the values of requirements for fragmentation represent upper estimates.

Temperature also has an effect on viscosity. Figure 2.8 shows that by increasing the temperature, and therefore reducing the viscosity, the volume of exsolved gas attainable in the mixture is reduced. Cooler, more gas-rich, magmas therefore favour explosivity. In the absence of any data to the contrary, it is assumed that magmas on Venus erupt at similar temperatures to their terrestrial counterparts i.e. bracketed by the range of temperatures modelled in Figure 2.8 for basaltic eruptions.

It is likely that a wide variety of conduit geometries will occur on Venus. The Magellan radar data are not of sufficient resolution to show volcanic vents in detail, but the evidence for shield volcanoes of a vast range of sizes and large areas of rifting indicate a corresponding array of potential conduit geometries. All else being equal, these model results show that smaller vents, overlying smaller radius conduits, perhaps occurring as individual volcanoes in larger shield fields or in larger volcanic complexes, could theoretically produce localised explosive activity whereas larger examples would not.

The natural variation in conduit geometry is further complicated in that the perfect cylinder used in this study, although convenient for comparative purposes, is very unlikely to occur in nature. The conduit itself must transition from the geometries of magma source reservoir to dike to quasi-circular cross-sectional conduit. The complexities of modelling this are beyond the scope of this study, but represent an interesting challenge for future work. Transitional geometry such as this notwithstanding, the

work presented here provides a first-order suite of results based on these simplified assumptions.

Another complication with regards to the conduit geometry is that this study uses a steady-state approach with no treatment of an evolving conduit structure, i.e. a flaring of the conduit from parallel-sided to cone-shaped near the surface with time, due to abrasion and conduit wall collapse. The current work is most representative of the early stages of an eruption prior to the onset of this type of temporal conduit evolution. Over time, if conduit flaring occurs, the choking depth could migrate down the conduit, creating a solution more like that of a lithostatically pressure-balanced system, potentially resulting in the onset of supersonic flow below the surface (*Mitchell*, 2005b). Therefore, this work inherits a somewhat restricted range of possible exit velocities (either subsonic or choked). As a consequence, ongoing and long-term processes interpreted from this model should be considered with some degree of caution.

The effect of increasing altitude and the corresponding decrease of pressure in the conduit has a significant effect on generating conditions suitable for explosive volcanism. It is clear that the tops of Venus' highest peaks could host explosive vents at volatile concentrations considerably lower than those at the MPR. Volcanic peaks reaching up to ∼9 km occur on Venus and Figure 2.7 shows that, with the same volatile composition, volume fractions of gas could be ∼2% higher (Figure 2.7a) at that altitude (∼0.751) than at the MPR (∼0.73). This effect is greater on H_2O than CO_2 as apparent from the shallowing gradient of the volume fraction gas curves as CO_2 is increased from Figure 2.7a through to Figure 2.7c.

From the preceding discussion, it can be concluded that, under the right conditions, certain regions of Venus could generate explosive volcanic activity. For example a small conduit, say 30 m in diameter, with a relatively cool magma of ∼1200 K and 3% H_2O could achieve conditions comfortably within those favouring explosive activity, even at the MPR (Figure 2.9). It is clear that very high volatile contents are not necessarily required and explosive behaviour may be more widespread than initially thought.

2.4.2 Column buoyancy

Following discussion of whether explosive activity is possible, how these volcanic products would behave upon eruption was next explored. Using the output from the conduit and jet decompression models described here, subaerial behaviour in some example scenarios was simulated using a previously developed plume rise model (*Glaze et al.*, 1997; *Glaze*, 1999; *Glaze et al.*, 2011). These example results are explored and described using the following case studies in sections 2.4.3 and 2.4.4. It is known from previous work (*Wilson et al.*, 1978; *Sparks*, 1986; *Woods*, 1988; *Valentine and Wohletz*, 1989; *Woods*, 1995, and others), and confirmed in these model runs, that faster, hotter eruptions are more likely to achieve buoyancy by providing greater momentum and heating of entrained air with corresponding reduction in density. In addition to this, upon eruption of a choked flow, the emitted material rapidly decompresses to atmospheric conditions, resulting in an increased velocity and radius. This decompression process is less pronounced on Venus than it is on Earth for a given exit pressure (Figures 2.11 and 2.12) as the atmospheric pressure on Venus is almost two orders of magnitude higher. Nonetheless, this component of the eruption process may have an effect on whether or not a buoyant regime is attained and so is duly considered.

2.4.3 Scathach Fluctus

If, for illustrative purposes, Scathach Fluctus is used as a potential example of a site of explosive volcanism occurring at Venus' MPR, it allows us to explore initial constraints on eruptive conditions, should an event of this nature this occur. A full description of the deposit is provided in *Ghail and Wilson* (2013). Assuming this eruption occurred at 1200 K, from a vent at a similar elevation to the deposit itself and of radius 25 m, in order for it to behave explosively, the model shows there must have been an H_2O content of over 4.5% (which erupts at a volume fraction of 0.749, between Figures 2.2d and 2.2e). This volatile composition is not implausible based on H_2O concentrations of terrestrial magmas, although more characteristic of subduction zone settings (*Wallace*,

2005), and it is necessarily based on numerous assumptions. If, for example, the conduit was smaller, the vent was higher, or indeed both, the volatile requirement would be reduced accordingly (e.g. moving to the right in Figure 2.7a or to the left in Figure 2.9 increases the volume of exsolved gas). In addition to this, the result is based on the assumption that the composition of the magma responsible for the formation of Scathach Fluctus is the same as that at the Venera 14 site, although it remains possible that it was a more felsic source. With a lower initial H_2O concentration, explosive activity could potentially occur here given a sufficient concentration of an accessory volatile. When modelled with only 3% H_2O, it is found that close to an additional 3% of CO_2 would be required to initiate magma fragmentation, a total volatile content approaching 6% (Figure 2.5, where the volume fraction exsolved gas exceeds 0.75 with 3% H_2O and an additional 3% CO_2). Again, if this was the case, it seems likely that the eruption occurred through one or more smaller conduits, perhaps as part of a fissure system, as smaller conduits have lower volatile requirements in order to generate explosive eruptions (Figure 2.9).

Here it has been assumed that, as the deposit at Scathach Fluctus is interpreted as a gravity-driven flow, the style of eruption was that of a collapsing column, i.e. explosive at the vent but not sufficiently buoyant to achieve plume rise. Indeed, within the limits of the model, it was not possible to achieve a buoyant column from a 25 m radius conduit, even with H_2O modelled up to 10%. This is also partly because increasing the modelled magma temperature to promote buoyancy also reduces the volume fraction gas achievable at a given elevation. When increasing temperature, a regime is rapidly approached where column buoyancy is simply not possible (Figure 2.8).

2.4.4 Ma'at Mons

The next case study represents the extreme of elevation. Ma'at Mons is located at 0.5°N, 194.5°E and is the highest volcanic peak on Venus at ∼9 km above MPR. No explosive deposits have been identified based on radar data, however if pressure, and

by inference altitude, is thought to be the dominant property preventing explosivity it is instructive to explore how this environment contrasts with localities close to MPR such as Scathach Fluctus. Given the same parameters imposed in the previous case study (1200 K, 25 m radius), the H_2O concentration required is only ∼2% (erupting with a volume fraction of 0.749, Figure 2.13), less than half that required only 9 km lower. It is therefore highly probable that explosive activity can occur at higher elevations on Venus, especially so if the conduits are longer (Figure 2.10). A temperature of 1200 K was only capable of producing buoyant column rise with an H_2O concentration of >6.8% (reaching ∼18 km above the vent) or a mixed volatile concentration of 3% H_2O with 3% CO_2 (reaching ∼20 km above the vent). However with a temperature of 1300 K, a buoyant volcanic column reaching ∼20 km above the vent could be generated with a much more attainable H_2O concentration of >4.7%. Although higher temperatures favour buoyancy in an explosive eruption column, they also reduce the likelihood of fragmentation in the conduit. This results in a very narrow range of temperatures allowing buoyant columns to form with relatively low volatile contents, as is evident in these model findings. However, varying conduit geometry towards narrower conduits may reduce the volatile requirement for explosive behaviour and therefore column formation at the vent.

2.4.5 Effects on climate

The implications of this study are that effusive lava flow eruptions constitute the dominant eruptive mechanism on Venus, especially at low elevations, but that explosive pyroclastic eruptions such as the type that may have formed Scathach Fluctus could be more common than previously assumed. Even though the generation of buoyant volcanic plumes seems plausible from high elevation vents, such as the ∼28 km above MPR plume described as possible from Ma'at Mons in the previous section, it would appear that plumes reaching the cloud base (∼48 km above MPR) require very tightly constrained combinations of conditions, a finding which has also been noted in previous work (e.g. *Thornhill*, 1993; *Glaze*, 1999; *Glaze et al.*, 2011). These types of events are

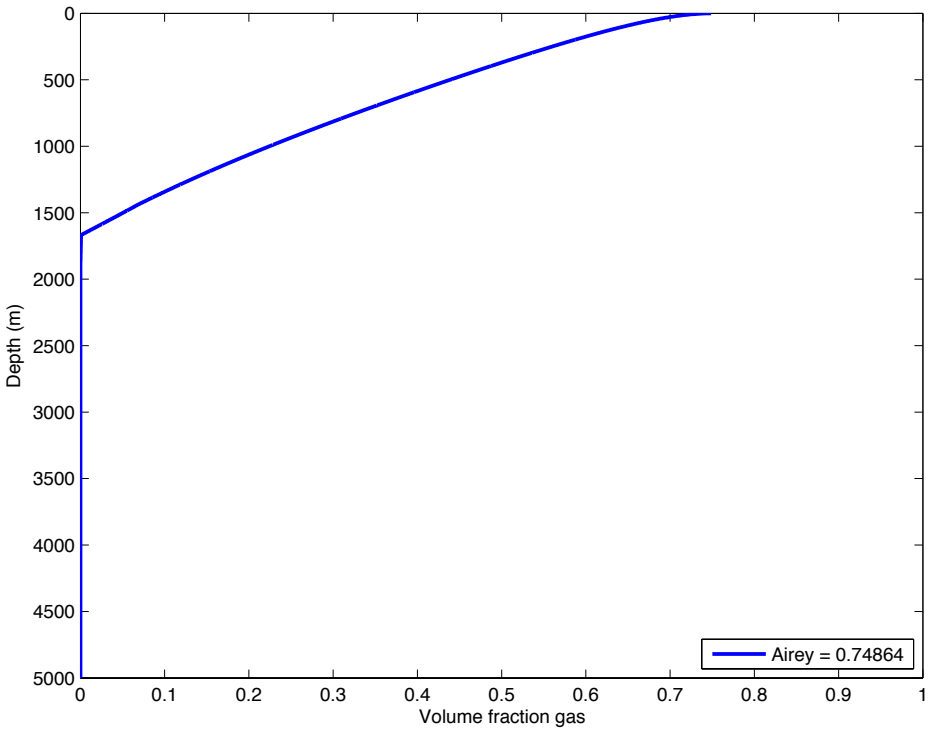

Figure 2.13: Model results of the response in terms of volume fraction of gas of the exsolution of volatiles in a basaltic magma of temperature 1200 K with 2% H_2O rising through a 5 km long, 25 m radius conduit to a vent of altitude 9 km. The value in the key is the final volume fraction H_2O of the mixture at the vent. Pressure at the conduit base is 114.41 MPa (Table 2.1).

unlikely but conceivable and would require a combination of conditions including high altitude, high volatile content, longer conduit, and/or small conduit radius. Therefore, even if they occur they are rare, and longer-term atmospheric circulation processes must be responsible for the regular introduction of volcanic gases to the upper troposphere, the cloud layers, and above the clouds.

However, should these buoyant plume forming volcanic events occur, rare or otherwise, they could have a profound impact on Venusian climate. Gases such as H_2O, CO_2 and SO_2 play a vital role in cloud chemistry, which strongly influences the radiation budget and planetary albedo. The addition of ash particles could be important in acting as cloud droplet nuclei. A volcanic input of gases cannot therefore be ruled out as the cause of the decadal SO_2 fluctuations seen in the Pioneer Venus Orbiter (*Esposito*, 1985) and Venus Express (*Marcq et al.*, 2013) observations, although other

plausible explanations such as atmospheric circulatory phenomena also exist.

2.4.6 Mass and H_2O fluxes to the atmosphere

The model results outlined in this work allow us to make some preliminary estimates of the flux of volcanic gases to Venus' lower atmosphere. If Scathach Fluctus was produced by an explosive volcanic event from a conduit of 25 m radius, requiring 4.5% H_2O as in the preceding case study (section 2.4.3), the corresponding mean magma mass flux predicted by the model is $\sim 3 \times 10^8$ kg s^{-1}. Therefore the estimated flux of H_2O to the atmosphere would be $\sim 14 \times 10^6$ kg s^{-1}. If the initial H_2O concentration is lower and compensated for with additional CO_2 (e.g. a 3% H_2O with 3% CO_2 mix), the corresponding mean magma mass and H_2O fluxes would be $\sim 3 \times 10^8$ kg s^{-1} and $\sim 9 \times 10^6$ kg s^{-1} respectively. The estimated flux of H_2O from this, and other, explosive events at around MPR is therefore estimated to be of the order $\sim 10^7$ kg s^{-1}. This figure of course assumes a small conduit radius; larger conduits would produce correspondingly higher fluxes. Since eruptions of this style will have a high volatile output, one consequence of volcanic activity would be transient lateral variations of H_2O in Venus' near-surface atmosphere. Water vapour near the surface (at ~5-25 km altitude) can be measured from orbit, by analysing 1.18 μm thermal emission on the nightside of Venus. Such observations were carried out by the VIRTIS spectrometer on Venus Express, but analyses to date have not yet detected any spatial variability (*Bézard et al.*, 2009), with a consistent H_2O concentration of 30 [-5 +10] ppm in Venus' altitude range 5-25 km above MPR (*Bézard et al.*, 2011). This highlights the importance of the ongoing search for evidence of volcanic processes on Venus through remote sensing of atmospheric and surface properties.

2.4.7 Deposit emplacement, emissions, and limits of detectability

The mass flux estimates in section 2.4.6, allow estimation of the duration of the emplacement of an explosive deposit of dimensions similar to Scathach Fluctus and the volcanic gas (H_2O) emission resulting from eruption. The model shows that a mass flux of $\gtrsim 3\times10^8$ kg s^{-1} is required to sustain an explosive volcanic event at the altitude of Scathach Fluctus. *Ghail and Wilson* (2013) estimate the volume of Scathach Fluctus to be 225-875 km^3, and the density to be close to 2000 kg m^{-3}, consistent with a welded ignimbrite (*Lepetit et al.*, 2009). Assuming a dense rock equivalent density of 2800 kg m^{-3}, this implies ∼30% void space. Therefore, to generate a volume of pyroclastic ejecta equivalent to the lower end of this estimate, a minimum of ∼150 km^3 or ∼4×10^5 Mt of magma must have been erupted. At a mass flux of ∼3×10^8 kg s^{-1}, the time to form Scathach Fluctus would be ∼15 days. Given the inferred H_2O concentrations of 3-4.5%, ∼4×10^5 Mt of magma would release ∼1-2$\times10^4$ Mt of H_2O over the duration of the eruption. The upper volume estimate however, implies an eruption sustained over a longer period of time in order to generate the additional material and/or a higher mass flux, generating more material per unit time. It is worth restating here the limitations of the steady-state, constant radius, nature of the model and the consequences on the applicability of the model to long-term processes mentioned in section 2.4.1. It is also worth noting that the deposit may have been emplaced by more than one event. However, this first-order analysis remains informative.

These findings coupled with the H_2O measurements described by *Bézard et al.* (2009) and *Bézard et al.* (2011), offers an opportunity for detecting volcanic signatures. Any perturbations to the consistent and low background concentration would be suggestive of an H_2O source to Venus' atmosphere. Spatial resolution of near-infrared nightside sounding of the surface is limited to ∼90-100 km, due to multiple scattering in the cloud deck (*Hashimoto and Imamura*, 2001); for water vapour mapping at altitudes of 10-20 km, the spatial resolution might therefore be expected to

be of order 60-70 km due to the closer proximity to the main cloud deck at 50 km altitude. The flux of H_2O will be dissipated by ambient winds, but the mean wind speed in the 0-20 km altitude range is only $\sim$10 m s^{-1} (*Kerzhanovich and Limaye*, 1985), so the mean residence time of air in this reference volume of 70 km diameter (to approximate the spatial footprint of near-IR water vapour sounding) would be about 2 hours. The pattern and rate of dissipation of the plume will depend on local atmospheric conditions, but if it is assumed that the emitted water vapour becomes well mixed over the lowest 20 km of the atmosphere and over a circular footprint of 70 km diameter, enough water vapour is emitted in 2 hours to double the amount of water vapour found in this volume, from an initial assumed concentration of 30 ppm to 60 ppm. This suggests that local concentrations of 60 ppm could be sustained for as long as the eruption continues, even when averaged over the spatial blurring distance of the near-IR sounding footprint. A further inference that can be made from this finding is that, if a detection of this magnitude is made, the volatile concentrations required to cause this anomaly are more likely to have resulted in a buoyant column at very high elevations or a collapsing column at low elevations. Therefore clues to the style of the eruption can be gathered from the elevation of the region above which the detection was made. While a thorough assessment of the detectability of such a plume would require more detailed consideration of plume dissipation mechanisms and rates, this first-order estimate of detectability suggests a renewed focus on analysis of the VIRTIS-M-IR dataset to search for near-surface water vapour variations.

2.5 Conclusions

By integrating the degassing model SolEx, geochemical lander data, measured atmospheric temperature and pressure profiles, and incorporating CO_2 as an accessory volatile to H_2O, a broad range of Venusian volcanic eruption scenarios were simulated. It was found found that the addition of CO_2 to an H_2O-driven eruption increases the final pressure, velocity, and volume fraction gas, the latter with an initial drop at a

small initial addition of the accessory volatile. Increasing elevation is conducive to a greater degree of magma fragmentation, due to the decrease in final pressure at the vent, resulting in a greater likelihood of explosive activity. The effect of increasing the magmatic temperature is to generate higher final pressures, greater velocities, and lower final volume fraction gas values with a correspondingly lower chance of explosive volcanism. Conduit geometry was found to be important, with cross-sectionally smaller and/or deeper conduits more conducive to explosive activity.

Two case studies highlight the strong influence of elevation on the likelihood of explosive activity. If explosive in nature, Scathach Fluctus at Venus' MPR requires 4.5% H_2O (from a 25 m radius conduit) in order to initiate magmatic fragmentation, whereas the highest peak, Ma'at Mons, requires less than half that concentration (i.e., 2% H_2O). It is also found that conditions that barely generate explosive behaviour at the MPR (4.5% H_2O or 3% each of H_2O and CO_2) are very close to those capable of generating not only explosive behaviour, but a buoyant volcanic column (4.7% H_2O or 3% H_2O with 3% CO_2) reaching up to ∼20 km at the summit of Ma'at Mons.

Volcanic input to Venus' atmosphere is considered a potentially important contributor to climatic processes on Venus. A relatively large global input to the lower atmosphere via small effusive eruptions, passive degassing, and pyroclastic events is likely to be the dominant volcano-atmosphere input. This modelling shows however, that the injection of volcanic material to higher atmospheric layers is feasible, if likely infrequent, and could play important roles in cloud chemistry and longer-term climate trends such as the measured decadal SO_2 fluctuations.

The inferred mass fluxes and H_2O concentrations suggested by these models provide some preliminary numerical estimates of the introduction of volcanic gases to the lower atmosphere of Venus. If it is accepted that Scathach Fluctus was produced by an explosive volcanic event from a conduit of 25 m radius, requiring 4.5% H_2O the estimated flux of H_2O to the atmosphere would be $\sim 14 \times 10^6$ kg s^{-1}. If the initial H_2O concentration is lower, and compensated for with additional CO_2 (e.g. 3% H_2O with 3% CO_2), the H_2O flux would be $\sim 9 \times 10^6$ kg s^{-1}. Larger conduits and volcanic complexes would

produce correspondingly higher fluxes. A sustained eruption of the scale of Scathach Fluctus could supply considerable quantities of H_2O to the atmosphere locally, over the course of the eruption. Despite the spatial blurring of the near-IR mapping of water vapour in the lower atmosphere, and the dissipation of emissions via wind, it is concluded that a sustained eruption with a flux of $\sim 10^7$ kg s^{-1} of magma could double the mean H_2O abundance even over the $\sim$70 km spatial resolution of near-IR mapping of water vapour in the deep atmosphere, which is a large enough signal to be detectable. Continued search for spatial and temporal variations in H_2O in the Venus Express/VIRTIS dataset is therefore recommended, as the ability for measurements to detect volcanic signatures is supported by these model conclusions.

Chapter 3

Radar analysis of volcanic features on Venus and comparisons with Earth

3.1 Introduction

The style of volcanism on Venus has long been considered to be dominantly effusive (e.g. *Garvin et al.*, 1982), and the question of whether or not volcanoes can behave explosively has been contentious since volcanoes were first identified on Venus (*Head and Wilson*, 1986; *Glaze*, 1999). Chapter 2 and *Airey et al.* (2015) describe how the conditions on Venus may suppress explosive behaviour due to the high atmospheric pressure and potentially H_2O-depleted mantle. Whether or not explosive activity is possible is not yet definitively resolved, and addressing this debate forms the primary motivation for this study. Compelling evidence for lava flows is abundant in the SAR data retrieved by Magellan, suggesting widespread effusive volcanism (*Head et al.*, 1992). However, evidence for explosive volcanism is not as widespread due to the difficulties in identifying deposits of this type in the SAR data and current lack of a technique with which to use radar signatures to make identifications. Regardless of their rarity, deposits that appear suggestive of a pyroclastic origin are observed and

have been suggested in other work (*Campbell and Rogers*, 1994; *McGill*, 2000; *Ghail and Wilson*, 2013). With *Ghail and Wilson* (2013) being a notable exception, identification of pyroclastic material has largely been qualitative, highlighting the requirement for a more quantitative approach to making potential deposit type identifications. By ground-truthing any differences in material radar properties with deposits of known origin on Earth, these alone could potentially be diagnostic of the mode of formation of volcanic deposits and could provide a powerful tool in the interpretation of planetary surfaces.

In this chapter, synthetic aperture radar (SAR) and ancillary data sets (emissivity, reflectivity, altimetry, and RMS slope described in 3.2.1) from NASA's Magellan mission are collected for various sites on Venus and compared with terrestrial deposits of known properties. The terrestrial data are collected from ESA's ASAR instrument on board the Envisat satellite, providing the comparable SAR data, and NASA's MODIS instrument on board the Aqua satellite for the comparable reflectivity and emissivity data. The use of Magellan's radar data has previously provided a wealth of information about Venus' surface such as the physical texture of the material from its scattering behaviour and derived roughness properties (*Tyler et al.*, 1992), and compositional and density information from the emissivity as described in section 3.2.2. For example, a distinct transition in emissivity is observed above an altitude of ∼2.5-5 km, probably due to a different dominant mineral phase stable at these P-T conditions (e.g. *Klose et al.*, 1992), as well as potentially recent volcanic deposits being suggested based on high emissivity anomalies that have not yet equilibrated with the local conditions (e.g. *Smrekar et al.*, 2010). In addition to studying the radar data from some specific Venus case studies, the following study explores whether or not further information can be gathered from these data when compared with terrestrial examples.

3.2 Methods

3.2.1 Data types

The SAR backscatter coefficient (σ_0) of a geological deposit is a quantification of the intensity of the radio wave returned to the emitting antenna after reflection from a planetary surface (*Ford et al.*, 1993; *Campbell*, 1995). This property varies as a function of the radar wavelength, the incidence angle, the roughness, and the dielectric constant of the material. This quantity is therefore a source of considerable physical and compositional information about the materials when considered alone or in conjunction with other properties (*Campbell and Campbell*, 1992; *Campbell*, 1994; *Campbell et al.*, 1999). In order to derive the most accurate information when comparing two or more values, the wavelength and incidence angle should ideally be the same. When comparing deposits on different planets, from instruments operating at different wavelengths, and at different viewing geometries (often resulting in incidence angles varying as a function of latitude), these dependencies must therefore be duly considered. Active microwave backscatter was collected at S-band by Magellan (12.6 cm) and at C-band by Envisat (5.6 cm).

The incidence angles of the SAR acquisitions cover a broadly similar range (∼15-46°), but for different reasons. Magellan's sensor is connected to its high gain antenna (HGA) in SAR mode, which is fixed at 25° off nadir. Spatial coverage requirements resulting from Magellan's elliptical orbit meant that attitude adjustments were required resulting in this range (Figure 3.1). Envisat's range of incidence angles was achieved by switching between seven image swath modes, each of which had its own sub-range of look angles (Figure 3.2).

The property of surface emissivity is a value between 0 and 1 stating how efficiently the material emits (and therefore absorbs) radiation relative to that of a black body (*Ford et al.*, 1993; *Campbell*, 1995), with 0 being a perfect reflector and 1 being a perfect emitter. It is an electrical property related to the dielectric constant of the material measured and can be indicative of composition, density, and state of weath-

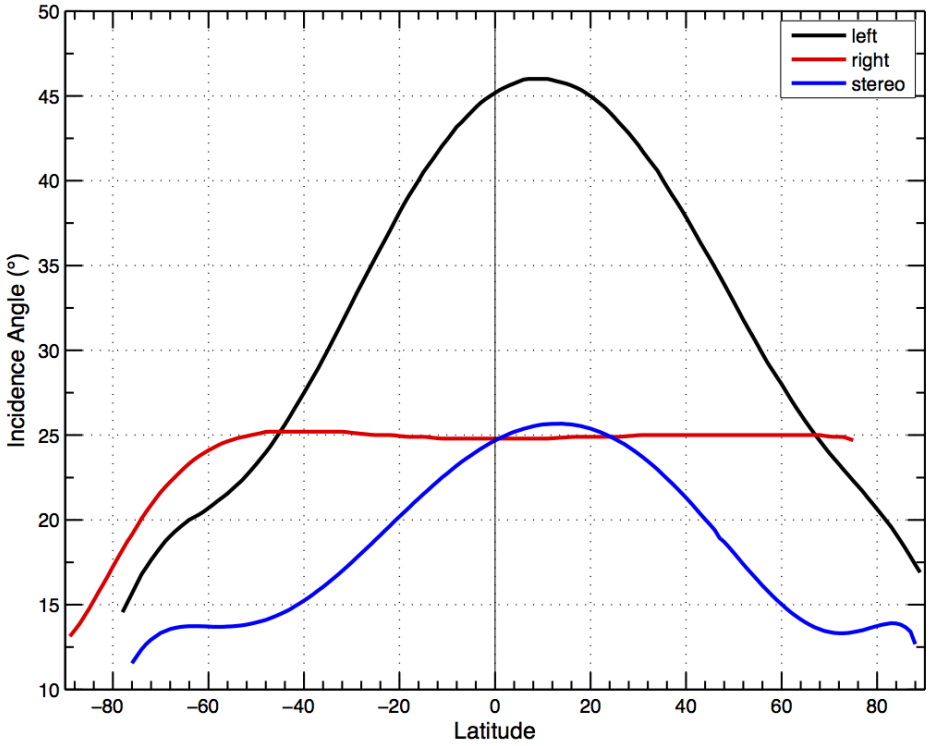

Figure 3.1: Incidence angle of Magellan antenna as a function of latitude; this study uses primarily left-looking data (black curve).

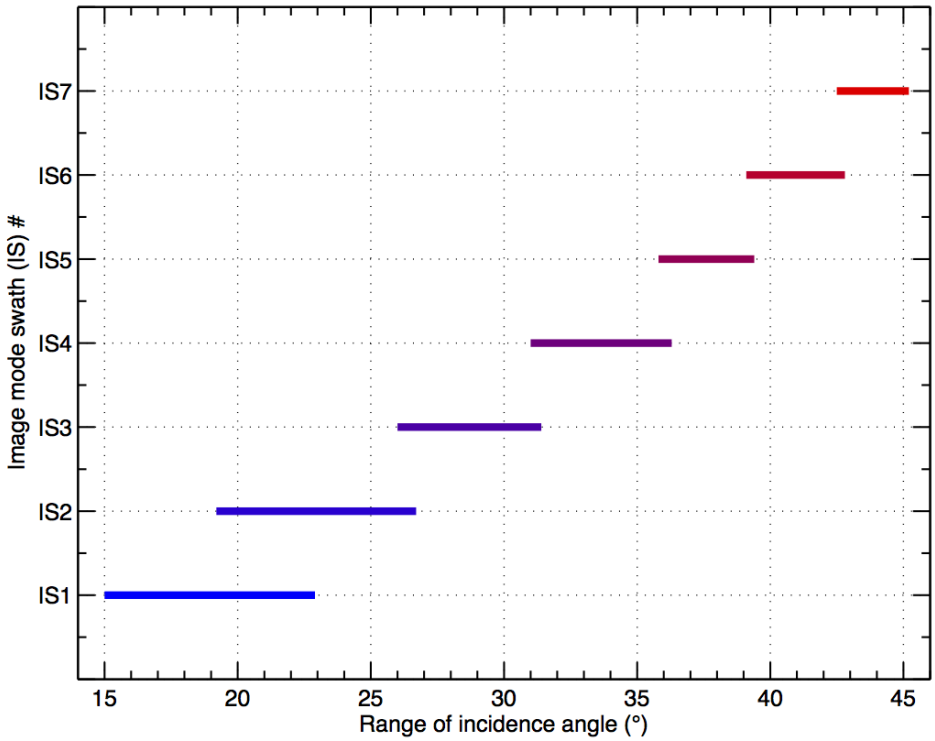

Figure 3.2: Ranges of incidence angles resulting from Envisat's various image swath modes (IS1 - IS7).

ering (*Campbell*, 1994). Magellan's HGA collected passive emissivity measurements at the same time as the SAR acquisition and at a corresponding wavelength, 12.6 cm. The MODIS terrestrial emissivity was retrieved in nadir mode, split into 36 bands, of which band 5 (1.24 μm) is retrieved here as no microwave data are available for Earth. Although all MODIS emissivity bands are at much shorter wavelengths than those from Magellan (even the longest available at ∼14 μm is far short of the Magellan microwave-scale emissivity), this exact band was selected so as to be as comparable as possible with future studies that may use the Venus Express VIRTIS data, which was collected at 1.01 μm.

Table 3.1: Summary of instruments used to retrieve radar datasets used in this study and their retrieval methods

	Venus		*Earth*	
Property	Instrument	Retrieval method	Instrument	Retrieval method
Backscatter coef.	HGA-SAR	Active SAR retrieval	ASAR	Active SAR retrieval
Reflectivity	ALTA	Active radar pulse retrieval	MODIS	Multispectral passive radiometry
Emissivity	HGA-Radiometer	Passive radiometry	MODIS	Multispectral passive radiometry
RMS slope	ALTA	Active radar pulse retrieval	N/A	N/A
Altimetry	ALTA	Active radar pulse retrieval	N/A	N/A

Table 3.2: Summary of viewing geometries and wavelengths of instruments used to detect the data described in sections 3.2.1 to 3.2.3

	Magellan			*Envisat*	*Aqua*
	HGA-SAR	HGA-Radiometer	ALTA	ASAR	MODIS
Incidence angle	Fixed 25° Attitude var. 15-46°	Fixed 25° Attitude var. 15-46°	Nadir	IS modes 1-7 15-46°	Nadir
Wavelength	12.6 cm	12.6 cm	12.6 cm	5.6 cm	1.24 μm

Roughness is quantified in terms of its RMS (root mean square) slope, RMS height, and correlation length, being the average slope (°), vertical surface variation (height, cm), and lateral surface variation (distance between peaks, cm) respectively. An estimate of the RMS slope is derived, along with estimates of altimetry and reflectivity, from Magellan's sensor operating through the lower-gain altimeter horn antenna

(ALTA). Based on the assumption that roughness is the same regardless of viewing angle, roughness parameters can be gathered by performing iterative calculations. These are based on the observations of two different backscatter values taken at different incidence angles using two scattering models until both values match. The parameters that can be obtained using this method are the RMS height and the correlation length which, when taken together, define the roughness properties of the deposit. Tables 3.1 and 3.2 summarise the retrieval methods and technical specifications for the data types collected in this chapter.

3.2.2 Data collection - Venus

All the Venus data used in this study were downloaded from `http://www.mapaplanet.org`. Each region studied was defined in terms of ranges in latitude and longitude, with corresponding data from each of the SAR, altimeter, emissivity, reflectivity, and RMS slope datasets collected. All these datasets were retrieved by the single sensor on Magellan operating in three modes: SAR (actively collecting the SAR radar data via the HGA), radiometry (passively collecting the emissivity data via the HGA), and altimeter (actively collecting altimetry, reflectivity, and RMS slope via the ALTA) (*Ford et al.*, 1993). The three properties collected in the altimeter mode were estimated based on their echo profiles when compared with the expected responses from pre-defined templates as described in *Ford and Pettengill* (1992).

Geographical (altitude, latitude, and longitude) and geomorphological (diameter, height, and flank slope) data were collected from a sample of ∼80 volcanoes from the catalogue of *Crumpler and Aubele* (2000), ranging from 20 to 1000 km in diameter. The diameter was measured using the ImageJ software package (available at `http://imagej.nih.gov/`), with the measuring tool scaled to the pixel resolution. The edifice height was collected using both direct measurements of base and summit altitudes from the Magellan altimeter, and calculated using the principle of parallax facilitated by the observation angle and assuming radial symmetry. The relationship used in deriving the latter is described by equation 3.1 (*Ford et al.*, 1993),

$$h = \left(\frac{r_e - r_f}{2}\right) \tan\theta \tag{3.1}$$

where h is the edifice height, r_e is the elongated (radar proximal) radius, r_f is the foreshortened (radar distal) radius, and θ is the incidence angle of the radar. The slope angle of the flank (ω) can be derived using similar principles in the relationship described in equation 3.2 (*Ford et al.*, 1993).

$$\omega = \arctan\left(\frac{1 - (r_f/r_e)}{1 + (r_f/r_e)} \tan\theta\right) \tag{3.2}$$

The radar backscatter coefficient for each volcano was collected for the flank and surrounding regional material, as well as any notable flows, diffuse deposits, or anomalous features. The method of measuring this property in each instance was to take three spot samples of 7×7 pixel means, from which overall mean values were calculated. This method was employed to get a more representative value for each feature and reduce the likelihood of erroneous values due to speckling. The value obtained is a pixel DN (digital number), which must subsequently be converted into the true σ_0 using equation 3.3 (*Campbell*, 1995).

$$\sigma_{0SAR} = 10^{0.02(DN_{SAR}-101)} \frac{0.0118\cos(\theta + 0.5)}{\left(\sin(\theta + 0.5) + 0.111\cos(\theta + 0.5)\right)^3} \tag{3.3}$$

In some cases, in order to better illustrate the dynamic range of values, the backscatter coefficient is displayed in its logarithmic form rather than the aforementioned "linear" form using equation 3.4.

$$\sigma_{0SAR}(dB) = 10\log_{10}\sigma_{0SAR}(linear) \tag{3.4}$$

The DN values for emissivity and reflectivity simply require scaling to the appropriate values (emissivity, e, and reflectivity, ρ) using equations 3.5 and 3.6 respectively (*Ford*, 1991).

$$e = 10^{-4}\left(DN_{em} - 1\right) \tag{3.5}$$

$$\rho_{re} = \frac{10^{-2}\left(DN_{re} - 1\right)}{2} \tag{3.6}$$

The dielectric constant, ε, was estimated using values for both the emissivity as described in equation 3.7 (*Le Gall et al.*, 2011) and for the reflectivity as derived from the relationship in equation 3.8 (*Ford et al.*, 1993) via a lookup table.

$$\varepsilon_{em} = \left(\frac{e - 2 - 2\sqrt{1-e}}{e}\right)^2 \tag{3.7}$$

$$\rho_{re} = \left|\frac{1 - \sqrt{\varepsilon_{re}}}{1 + \sqrt{\varepsilon_{re}}}\right|^2 \tag{3.8}$$

Using the value calculated in equation 3.7, the value of reflectivity could then also be derived from the emissivity using equation 3.9, which provides an identical value to the much simpler equation 3.10 (*Ford et al.*, 1993).

$$\rho_{em} = \left|\frac{1 - \sqrt{\varepsilon_{em}}}{1 + \sqrt{\varepsilon_{em}}}\right|^2 \tag{3.9}$$

$$\rho_{em} = 1 - e \tag{3.10}$$

The values of ε calculated using equations 3.7 and 3.8 were then also used to make further estimates of the material densities, r, using the relationships defined by *Ulaby et al.* (1990) in equation 3.11, and by *Krotikov* (1962) in equation 3.12. Figure 3.3 shows how these models vary as a function of ε. Both models provide similar solutions up to a dielectric constant of $\sim$7, from which point they diverge significantly at higher values of ε. Therefore density estimates of the few deposits with very high-ε in the following study are somewhat less reliable; however, the majority of deposits cited in the discussion have $\varepsilon \lesssim 7$.

$$r_{ul} = \frac{\ln\varepsilon}{\ln 1.96} 10^3 \tag{3.11}$$

$$r_{kr} = \frac{\sqrt{\varepsilon} - 1}{0.5} 10^3 \tag{3.12}$$

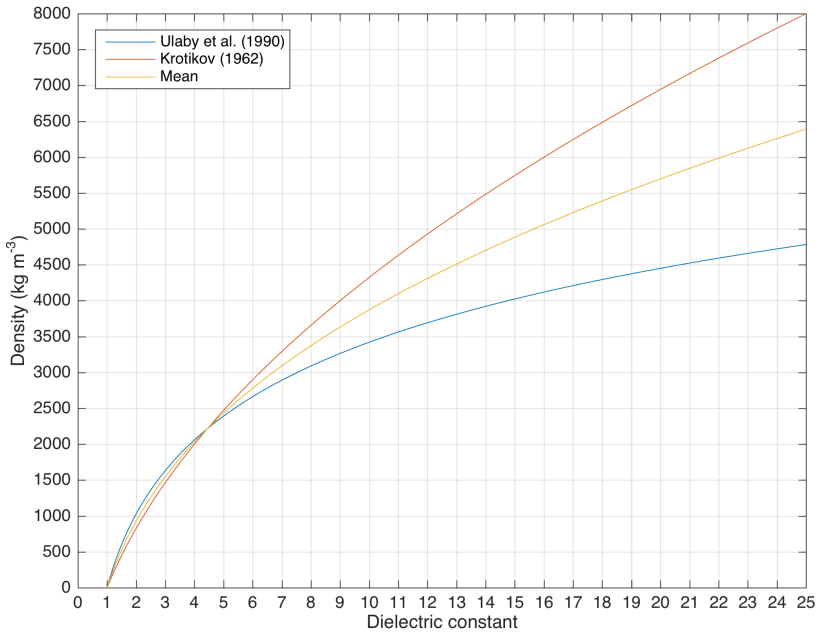

Figure 3.3: Density as a function of dielectric constant, ε, as determined using the empirical relationships of *Ulaby et al.* (1990) and *Krotikov* (1962). The mean between the two models is also shown.

The DN values from the RMS slope dataset derived from the altimeter bursts is converted into the true value of slope, ϕ (°), using equation 3.13 (*Ford*, 1991).

$$\phi = \frac{DN_{slope} - 1}{10} \tag{3.13}$$

Deriving the values of the other roughness parameters, RMS height (h) and correlation length (l), is non-trivial as there is no direct method of calculating these properties from the other datasets available as one must be known in order to solve for the other. However there are relationships between these values and other data collected in the

study inherent in the Stationary-Phase Approximation (SPA, equation 3.14) (e.g. *Kim et al.*, 1992; *Rodríguez et al.*, 1992), the Small Perturbation Model (SPM, equations 3.15 to 3.17) (*Fung and Chen*, 2010), and Hagfors (equations 3.18 and 3.19) (e.g. *Tyler et al.*, 1992) scattering models, and a technique was devised as part of his study with which to estimate both these properties. The concept behind this method assumes that the roughness is the same regardless of viewing geometry and that these scattering models converge on similar values for materials of the same roughness. The roughness was then calculated by applying the SPA and Hagfors models to the altimeter mode properties and the SPM to the SAR mode properties.

$$\sigma_{0alt} = \frac{\rho_{alt}^2 l^2 e^{-(l\tan\theta/2h)^2}}{4h^2\cos^4\theta} \tag{3.14}$$

$$\sigma_{0SAR} = 8k^4h^2\cos^4\theta\,|\alpha|^2\,W\,(2k\sin\theta) \tag{3.15}$$

where $k = \lambda/2\pi$, $\lambda = 12.6$ cm,

$$\alpha = \frac{\varepsilon_{SAR} - 1}{\left(\cos\theta + \sqrt{\varepsilon_{SAR} - \sin^2\theta}\right)^2} \tag{3.16}$$

and W is the power spectrum:

$$W\,(2k\sin\theta) = (l^2/2)\,e^{-(kl\sin\theta)} \tag{3.17}$$

$$\sigma_{0alt} = \frac{C\rho}{2}\left(\cos^4\theta + C\sin^2\theta\right)^{-3/2} \tag{3.18}$$

where

$$C^{-1/2} = \phi(radians) \tag{3.19}$$

The first step towards formulating a method of calculating h for both the altimeter-derived and SAR-derived properties is to use relationships and inputs derived purely

from the corresponding instrument mode. For the altimeter-derived calculations $\theta = 0$, as the altimeter operates in nadir geometry, allowing the equations to be greatly simplified. When simplified and rearranged to find h, the SPA takes the form of equation 3.20.

$$h_{alt} = \sqrt{\frac{\rho_{re}^2 l^2}{4\sigma_{0alt}}} \tag{3.20}$$

This equation can be solved by using the value for ρ_{re} calculated in equation 3.6, estimating l, and deriving a value for σ_{0alt} via the simplified Hagfors model described in equation 3.21 using the altimeter-derived variables ρ_{re} and ϕ.

$$\sigma_{0alt} = \frac{\rho_{re}}{\phi^2/2} \tag{3.21}$$

For the SAR-derived calculations, equations 3.15 to 3.17 must be used in their full form using variables collected purely in SAR geometry. When rearranged to find h, the SPM takes the form of equation 3.22.

$$h_{SAR} = \sqrt{\frac{\sigma_{0SAR}}{8k\cos^4\theta \left|\alpha\right|^2 W\left(2k\sin\theta\right)}} \tag{3.22}$$

This equation can be solved by using the known values of θ and λ (the radar wavelength, 12.6 cm), the SAR-derived values for σ_{0SAR} calculated in equation 3.3 and ε_{em} calculated in equation 3.7, and again by estimating l.

Now, the only unknown quantity in either calculation to find h is l, which had to be estimated in both cases. Returning to the assumption that roughness properties are the same for a given geological material regardless of viewing geometry, it is possible to iterate both calculations with increasing values for l until both values of h coincide. This was the method by which the roughness properties were defined in this study and the MATLAB code is available in Appendix C. In addition to these "true" roughness values, roughness proxies known as asperity were calculated with l set to the wavelength of the Magellan radar and ASAR for comparative purposes as described in section 3.4.

3.2.3 Data collection - Earth

For this aspect of the study, Envisat ASAR data were requested from ESA. The terrestrial sites for comparison with Venus were carefully selected based on certain criteria. A cross section of deposit types (comprising both effusive and explosive of a range of compositions) was required in order to look for trends between them. Another consideration was to look for well exposed sites with little vegetation, so as to get a true indication of the properties of the rock types themselves. The sites selected were as shown in Table 3.3.

Table 3.3: Terrestrial sites selected for comparison with Venus and their key deposits

Name	Location	Pyroclastic deposit	Basalt (non-explosive)	Rhyolite (non-explosive)	Trachyite (non-explosive)	Reference
Cordillera Occidental	Colombia	•				*Marsh et al.* (1995)
Cerro Galán	Argentina	•				*Folkes et al.* (2011)
Mt. Etna	Sicily		•			*Branca et al.* (2011)
Dabbahu	Ethiopia	•	•	•		*Field et al.* (2012)
Nabro Volcanic Range	Eritrea	•	•	•	•	*Wiart and Oppenheimer* (2005)
Ma'alalta	Ethiopia	•	•	•		*Wiart and Oppenheimer* (2005)
Altiplano-Puna Volcanic Complex	Bolivia	•				*Salisbury et al.* (2011)
Krafla	Iceland		•			*Rossi* (1997)
Soufrière Hills, Montserrat	W. Indies	•				*Cole et al.* (1998)
Katmai, Valley of 10,000 Smokes	AK, USA	•				*Fierstein and Wilson* (2005)
Kasatochi, Aleutian Islands	AK, USA	•				*Waythomas et al.* (2010)
Sarychev Peak, Kuril Islands	Russia	•				*Rybin et al.* (2011)

Following the selection procedure, ESA's Eoli-sa version 9.4.7 software was used to download data from the selected regions. The database was searched for the scenes with the least cloud cover. For each site, both local summer and winter scenes (in the same year wherever possible) were downloaded in order to explore the effects of seasonal differences on radar properties.

The MODIS (Aqua) data were all ordered using the USGS's Earth Explorer website (`http://earthexplorer.usgs.gov`) and downloaded with the Bulk Download Assis-

tant package. The data corresponding to the cloud-free footprints closest to the ASAR retrieval date for both Land Surface Temperature and Emissivity (Bands 31 and 32, ∼10.8-12.3 μm) and Land Surface Reflectance (Bands 1-7, ∼0.6-2.2 μm) were selected.

Once acquired, all these datasets were processed using ESA's NEST (Next ESA SAR Toolbox) version 4 software. The ASAR data DN values must first be converted into the backscatter coefficient σ_{0Earth} using equation 3.23 (*Rosich and Meadows*, 2004),

$$\sigma_{0Earth} = \frac{DN_{ASAR}}{K}\sin\theta \tag{3.23}$$

where K is the calibration factor provided with the ASAR metadata. The MODIS products could be loaded into NEST as their true values using the built-in product reader. In order to collect the values of σ_{0Earth}, ρ_{Earth}, and e_{Earth} for the flows and deposits in question, a polygon mask was created for each in NEST using the ASAR images in conjunction with the deposit locations described in the cited works in Table 3.3. As the polygons are fully georeferenced with respect to the data, it is then possible to transpose the polygon exactly onto the other datasets in the identical spatial dimensions. Average pixel values for these areas were then calculated and stored for later analysis. It was subsequently decided to derive emissivity from the reflectivity band ($e = 1 - \rho$) in the interest of future compatibility with the VIRTIS emissivity wavelength data rather than use bands 31 and 32. The reflectivity is the complement of emissivity, being a value between 0 and 1 describing the efficiency at which a particular wavelength is reflected from the surface of a material. Using these measured values, it was then possible to calculate an estimate of the dielectric constant using equation 3.7, and proxies for roughness, asperity (h), using the wavelengths of ASAR and Magellan for l with equation 3.22 to explore data comparisons with Venus.

3.3 Venus data analysis

3.3.1 Previous work and case study selection

In terms of identifying pyroclastic deposits on Venus, very little previous work has been undertaken. This is primarily due to the assumption that the high atmospheric surface pressure suppresses magma vesiculation, making explosive activity unlikely and highly localised (*Garvin et al.*, 1982; *Head and Wilson*, 1986; *Airey et al.*, 2015). In order to find valid targets for this study, the results from previous studies (*Barsukov et al.*, 1986; *Campbell and Rogers*, 1994; *Campbell et al.*, 1998; *McGill*, 2000; *Campbell and Campbell*, 2002; *Grosfils et al.*, 2011; *Ghail and Wilson*, 2013) were used as the basis for the case study selection.

Mapping of the Sappho Patera quadrangle by *McGill* (2000) included the region surrounding Irnini and Anala Montes (Figure 3.4). As part of the interpretation of deposits in this area, *McGill* (2000) identified halos occurring near the summits of these two features as coarse pyroclastic deposits. This was a qualitative observation based on their proximity to the summits, their diffuse margins and bright radar backscatter returns. The potentially pyroclastic deposits associated with Irnini Mons were also the subject of some unpublished preliminary quantitative analyses by *Campbell et al.* (1998). In that study, backscatter, emissivity, and dielectric properties were measured for the bright deposits identified by *McGill* (2000) and suggested to be potentially consistent with pyroclastic deposits having a rough texture. As a result of these observations, the current study focuses on both these edifices. The aim is to extend the quantitative survey to both sites (Irnini and Anala Montes), collect further direct measurements (e.g. SAR, emissivity) with which to derive new datasets (e.g. roughness, density) for analysis, and prepare these data for later comparison with Earth data to search for common trends (section 3.4).

Using early radar data retrieved by Veneras 15 and 16, *Barsukov et al.* (1986) speculate that a radar-bright area extending west from the summit of Tepev Mons, Bell Regio (Figure 3.11) could be a "pyroclastic train". Citing this observation as part

of a later study using Magellan data, *Campbell and Rogers* (1994) state that this is more likely to occur due to a high-dielectric mineral phase. However, they do further suggest that a radar-dark deposit with high emissivity to the south of Tepev Mons could be caused by windblown redistribution of pyroclastic or ejecta material, although state that explosive volcanic activity is unlikely. The mapping of this region in the Bell Regio quadrangle (*Campbell and Campbell*, 2002) classifies both these deposits as lobate lava flows, from Tepev Mons in the case of the summit material and from neighbouring Nyx Mons in the case of the radar-dark material. These contrasting observations led to the selection of this region for further analysis in the present work (section 3.3.3).

The identification of Scathach Fluctus as a pyroclastic deposit by *Ghail and Wilson* (2013) led to the selection of this feature for the comparison with Earth in section 3.4. Further detailed analysis is not included here due to the existing and recent detailed study (*Ghail and Wilson*, 2013). They concluded that this deposit was of pyroclastic origin based on several factors. These included the interaction of the flow with grabens and a small volcano during emplacement, and the nature of the flow margins appearing to be momentum-limited (characteristic of pyroclastic density currents) rather than cooling limited (characteristic of lava emplacement). Measurement of the pyroclastic deposit's radar characteristics led the authors to conclude that pyroclastic deposits may indeed be more common than previously thought, as the radar signature of Scathach Fluctus is not dissimilar to that of the majority of Venus' surface.

Ma'at Mons (section 3.3.4) was not selected for any potential examples of pyroclastic deposits, but rather for its unique value in being the volcano with the highest altitude summit on Venus. The range of lava flow types evident in the Magellan SAR images and the elevation range made this volcano an ideal site for further investigation. It is included as the fourth case study. The fact that both Ma'at Mons and Scathach Fluctus were also used as examples in chapter 2 makes their inclusion here of additional interest in the broader context. In addition to the above examples, a further deposit at Nijole Mons that is stated to possibly have an explosive origin (*Grosfils et al.*, 2011) is also included in section 3.4, although they state that it may also be a lava flow.

3.3.2 Case Studies 1 & 2 - Irnini and Anala Montes, Central Eistla Regio

Figure 3.4 is part of the full resolution (resampled to 75 m/pixel) SAR map generated from data collected by NASA's Magellan spacecraft. It shows the region known as Central Eistla Regio and contains two volcanic edifices, Irnini Mons at the top middle of the image and Anala Mons at the lower left centre of the image. Regional scale rift features can be seen trending NW-SE and SW-NE. Multiple lava flows extend radially from Anala Mons, and both Irnini and Anala Montes display diffuse, radar-bright 'halos' identified by *McGill* (2000) as deposits suggestive of coarse pyroclastic material deposited on their flanks, and shown in more detail in Figures 3.5 and 3.6 respectively.

Also of interest in this region is a patch of radar-bright material west of Irnini Mons (Figure 3.7) and an anomalous radar-dark, high-emissivity deposit on the south flank of Anala Mons (Figure 3.8). Table 3.4 contains the data collected from the Magellan datasets for this region. The regional properties are compared with those of the two volcanic features, themselves broken down into their flanks, their radar-bright halos, Irnini Mons' bright patch, and Anala Mons' digitate flows and anomalous feature.

The regional material, the edifice flank material of both volcanoes, and the digitate flows extending from Anala Mons seem to display very little variation from one another in any of the properties given in Table 3.4. This suggests that the whole region is built up of volcanic (probably basaltic) lava flows, and that the material making up the flanks of the volcanoes and flows surrounding them is broadly similar to that which constitutes the majority of the regional material. This particularly highlights the other features evident in the datasets.

The radar-bright halos on the flanks of the volcanoes both have very high radar backscatter returns (Table 3.4), indicative of rough, diffuse-scattering terrain. This is supported by the calculated roughness parameters, especially so with the RMS height, which has values of around 12-13 cm indicative of highly variable vertical surface height variation. These values are on a scale normally associated with the characteristically

rough tessera (the stratigraphically oldest unit on Venus consisting of mountainous, heavily-deformed regions (*Head et al.*, 1992)). Despite this, the diffuse nature and the way they seem to grade away from the edifice centre in terms of coverage implies the deposition of pyroclastic surge material. Inspection of the values derived for density implies that these diffuse deposits are considerably less dense than the surrounding flank and regional material. These observations, and the deposits' proximity to the likely locations of volcanic vents, suggest that they may be representative of pyroclastic material and therefore volcanism displaying some degree of explosive behaviour could feasibly have occurred. The slightly elevated values for emissivity and reduced values for dielectric constant of the deposits (Table 3.4) when compared with the flank material they mantle implies that they may have been emplaced somewhat more recently and therefore may not have undergone as extensive surface weathering with atmospheric oxides, which results in lower emissivity mineral phases (*Smrekar et al.*, 2010). A shaded topographic plot of the region is provided in Figure 3.9.

Table 3.4: Radar properties of features described in the text and illustrated in Figures 3.4 to 3.8. All values derived from the Magellan datasets, either directly measured from, or calculated from, the pixel values. Two values are provided for each of the dielectric constant (ε), reflectivity (ρ), and density (r) as they can be calculated from data collected from both the SAR antenna and altimeter using different methods, therefore providing reasonable upper and lower limits for their true values. The values for density are calculated as the mean between two previously devised empirical relationships (*Krotikov*, 1962; *Ulaby et al.*, 1990).

	Irnini Mons			*Anala Mons*				
	Flank	Halo	Bright patch	Flank	Halo	Anomalous feature	Flows	Regional
Backscatter (dB)	-18.54	-11.43	-10.76	-18.70	-12.22	-24.56	-18.70	-18.70
RMS slope (°)	3.2	4.1	1.5	3.1	4.1	4.3	3.4	2.7
RMS height (m)	0.0789	0.1335	0.0821	0.0736	0.1230	0.0820	0.0861	0.0753
Corr. Length (m)	5.745	8.143	11.533	5.601	7.197	5.394	5.715	6.605
Emissivity	0.813	0.848	0.809	0.800	0.830	0.912	0.830	0.830
Dielectric - SAR	6.36	5.18	6.52	6.87	5.79	3.39	5.79	5.77
Dielectric - Alt.	4.27	3.84	5.06	4.17	4.07	3.24	4.50	4.14
Reflectivity - SAR	0.187	0.152	0.191	0.200	0.171	0.088	0.171	0.170
Reflectivity - Alt.	0.121	0.105	0.148	0.118	0.114	0.082	0.129	0.117
Density - SAR	2896	2499	2947	3053	2712	1750	2712	2703
Density - Alt.	2145	1959	2454	2103	2061	1674	2239	2090

The isolated radar-bright patch to the west of Irnini Mons (Figure 3.7) requires further explanation. Although it appears, in terms of radar backscatter, that this deposit may have a common provenance with the halos associated with the volcanic

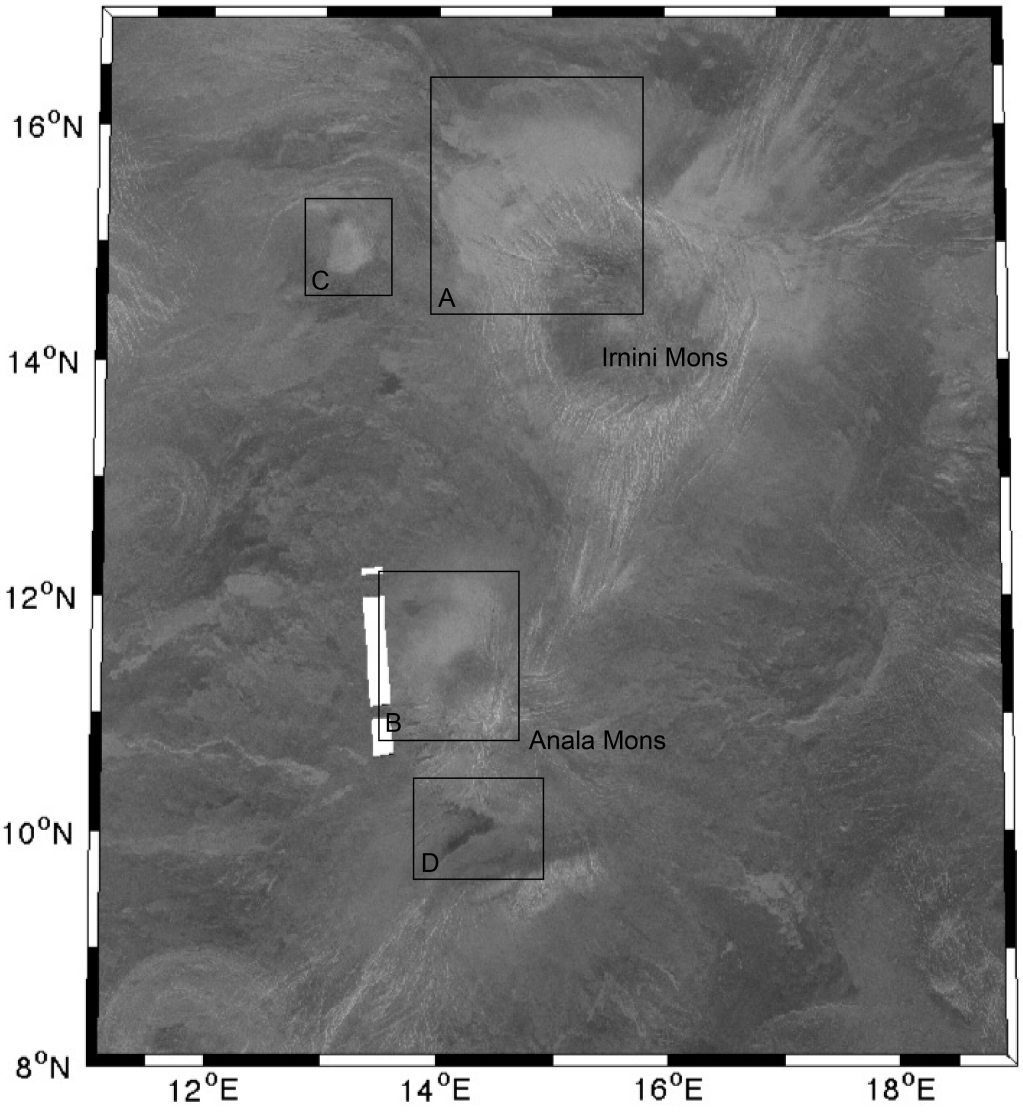

Figure 3.4: Magellan SAR image of Central Eistla Regio. Main features discussed in text. Areas A-D are expanded in Figures 3.5 to 3.8. White areas are data gaps.

centres, this may not be the case. The RMS height, although still moderately high, is not comparable to that of the halo deposits (Table 3.4). The correlation length, however, is very high compared with the other bright deposits suggesting a greater degree of long-wavelength surface variation. This deposit also does not display the elevated emissivity (Table 3.4); this suggests it could be a remnant of a past episode of similar volcanic activity, and is therefore not as fresh and relatively unweathered as the halos. The higher density and reduced small-scale roughness could of course be a

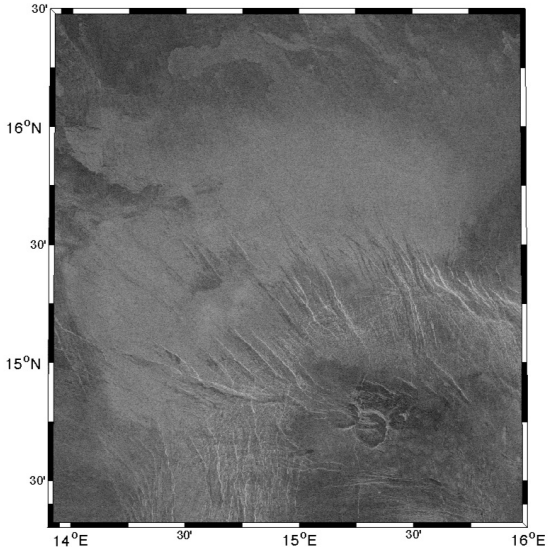

Figure 3.5: Detail of north-western flank of Irnini Mons showing diffuse deposit. Area A in Figure 3.4

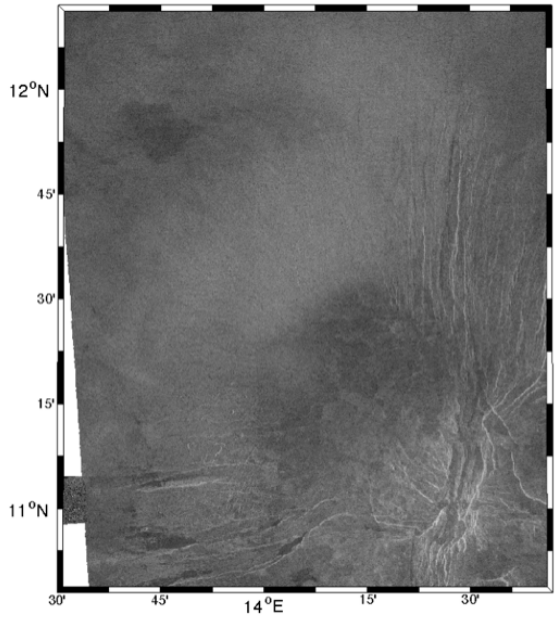

Figure 3.6: Detail of north-western flank of Anala Mons showing diffuse deposit. Area B in Figure 3.4

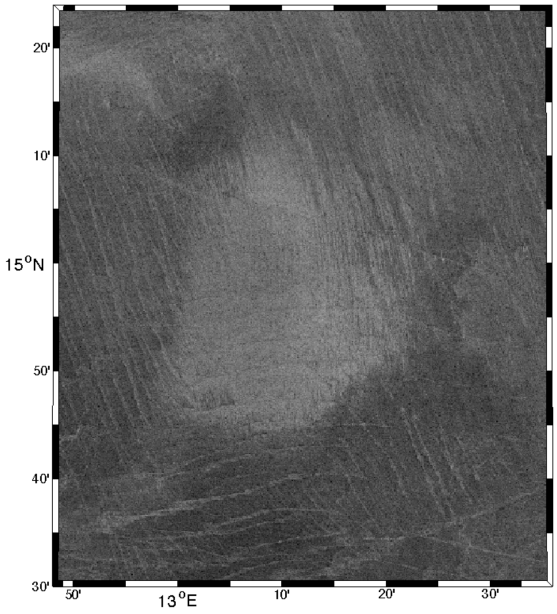

Figure 3.7: Isolated radar-bright patch to west of Irnini Mons. Area C in Figure 3.4

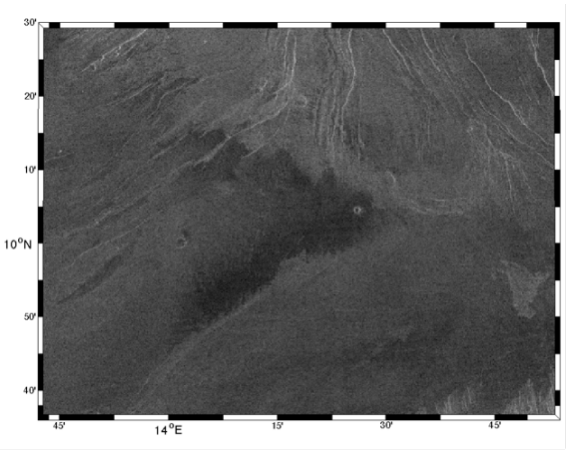

Figure 3.8: Anomalous, high-e, radar-dark feature on south flank of Anala Mons. Area D in Figure 3.4

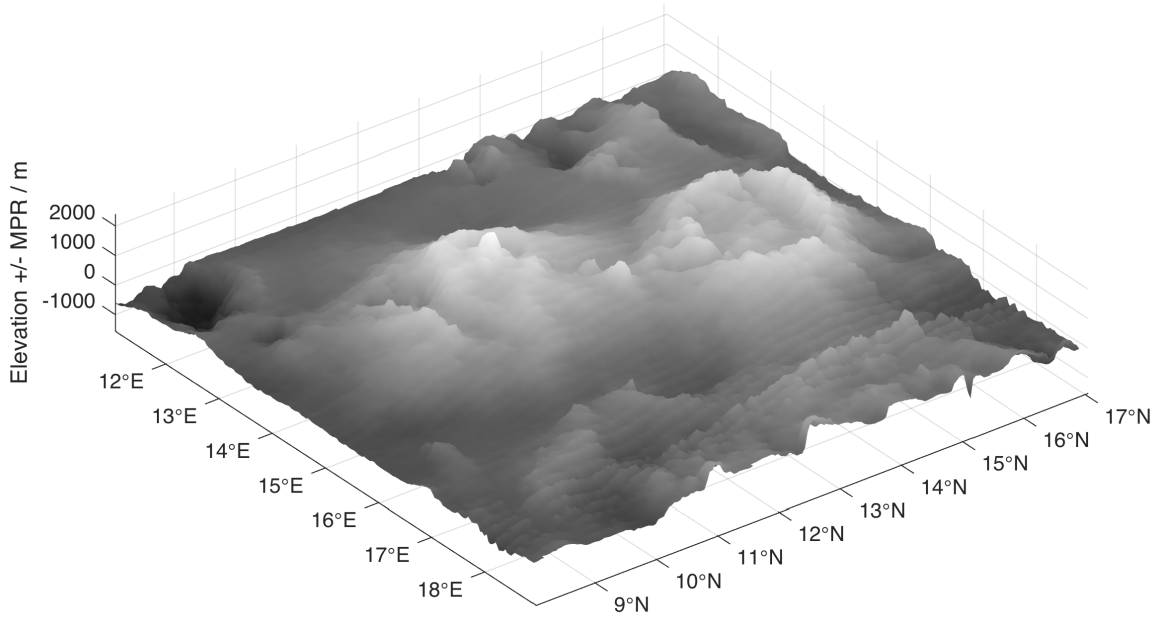

Figure 3.9: Topographic surface plot of region shown in Figure 3.4 with 50× vertical exaggeration showing the two prominent topographic rises. Greyscale varies with altitude.

product of a greater degree of physical surface weathering, acting to smooth the rough surface morphology of this type of flow and expose more densely compacted parts of the deposit. It is feasible that this represents an older episode of pyroclastic deposition.

The radar-dark, high-e, low-ε anomaly on the south flank of Anala Mons (Table 3.4, column 7) could potentially represent a pyroclastic deposit or lava flow (*McGill*, 2000). In contrast to the radar-bright halos discussed, the very low return from these deposits suggests a very smooth surface and, if pyroclastic in origin, suggests a more concentrated, fine-grained deposit following the local terrain (within a 'valley' between the central volcanic edifice and an E-W trending ridge feature, see Figures 3.9 and 3.10) resulting in a smoother surface as the underlying surface variation is masked. The high emissivity of this feature ($e = 0.912$, white patch in Figure 3.10) is indicative of geologically young material and therefore relatively recent volcanic activity.

Assuming that the preceding analyses of the available radar datasets imply the occurrence of eruptions forming pyroclastic deposits in the vicinity of the case study region, this assumption can be used, in conjunction with the model results in chapter 2, to attempt to impose some physical constraints on Venusian volcanism.

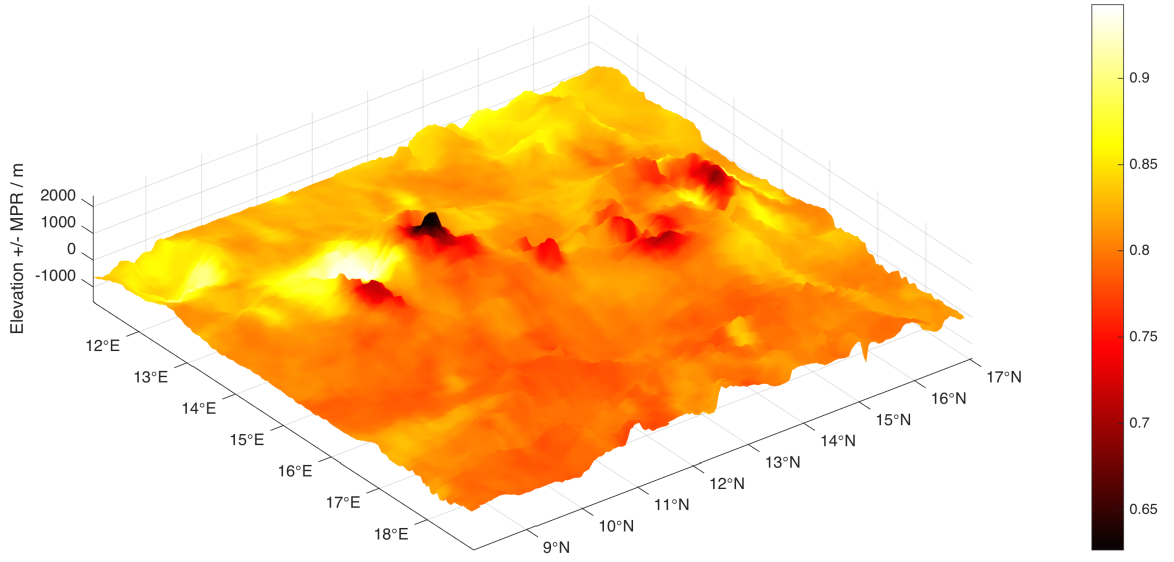

Figure 3.10: Topographic surface plot, as in Figure 3.9, of region shown in Figure 3.4 with 50× vertical exaggeration. Values for emissivity are overlain as indicated by the colour bar.

If, as the Magellan data suggest, pyroclastic deposits were emplaced here, explosive, collapsing plume-forming or ash fall volcanism must have been initiated in some form. Other mechanisms that could result in this kind of deposit cannot be ruled out. Discrete episodes of explosive volcanism (vulcanian-style eruptions) could result in similar deposits as described in *Fagents and Wilson* (1995). This mechanism would allow explosive activity to occur at lower volatile contents and temperatures, where degassed magmatic gases could potentially build up in cracks and fissures or be stored in shallow capped reservoirs. This would result in transient, episodic activity in contrast to the sustained collapsing fountain resulting from the conditions mentioned previously, but could potentially result in the deposits observed. At this location at least, some combination of conditions, such as elevated volatile concentrations or narrower conduit(s) (*Airey et al.*, 2015), may have produced explosive activity on a scale that could produce pyroclastic deposits capable of covering large areas ($\sim 1.8 \times 10^7$ km^2 in the case of the deposit depicted in Figure 3.5). It appears that these processes may have been occurring intermittently, as the (possibly) older isolated deposit seems to suggest.

3.3.3 Case Study 3 - Tepev Mons, Bell Regio

Figure 3.11 shows the Magellan SAR map of Tepev Mons, a ∼5 km above MPR volcanic edifice located in Bell Regio. The summit has two distinct calderas centred at 29.65°N, 44.85°E (hereafter referred to as the western caldera) and 29.55°N, 45.6°E (hereafter referred to as the eastern caldera). Inter-fingering bright and dark lava flows extend radially from the summit. The entire edifice is ∼350 km in diameter. The radar bright flows encircling the edifice originate from a pair of volcanic edifices known as Otafuku Tholi occurring at 28.9°N, 46.1°E and 28.7°N, 46.4°E (the easternmost of which is obscured by the data gap in the Magellan dataset) (*Campbell and Campbell*, 2002). In contrast to the previous case study, there are no obvious regional scale rifting structures associated with Tepev Mons or the surrounding area, so the style of volcanism here would be expected to be the product of an 'intraplate' style of volcanism (see chapter 4). Volcanic deposits occurring in the immediate vicinity of the western and eastern calderas appear somewhat different, those on the western caldera suggesting, again,

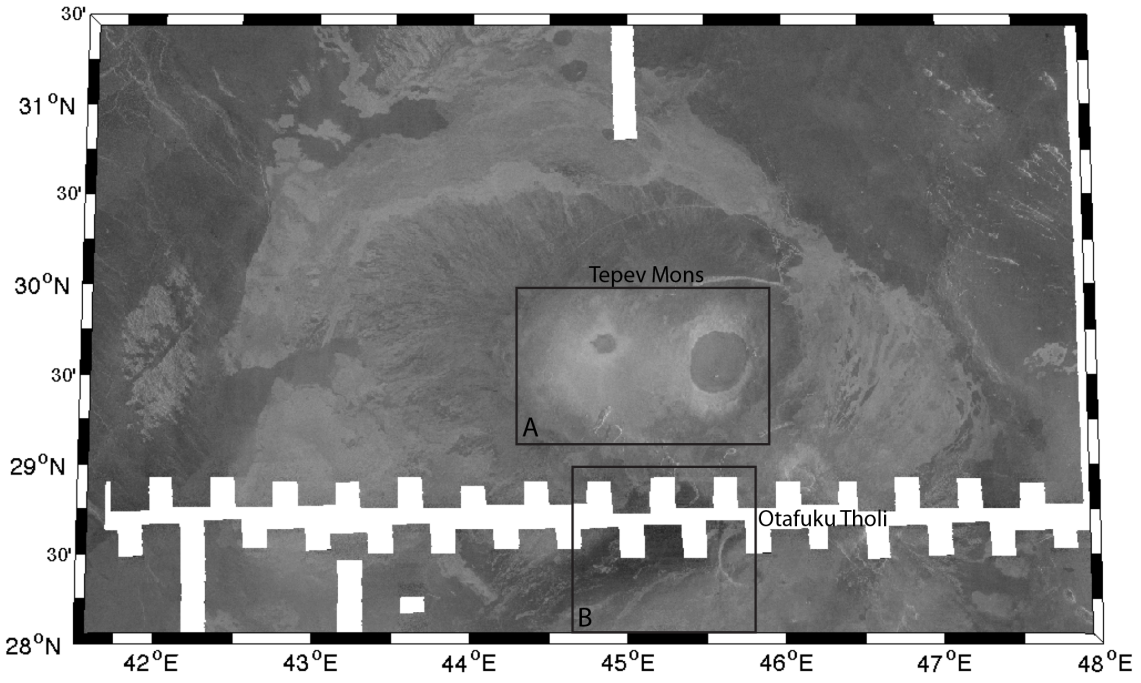

Figure 3.11: Magellan SAR image of Tepev Mons. Areas A and B are expanded in Figures 3.12 and 3.13. White areas are data gaps.

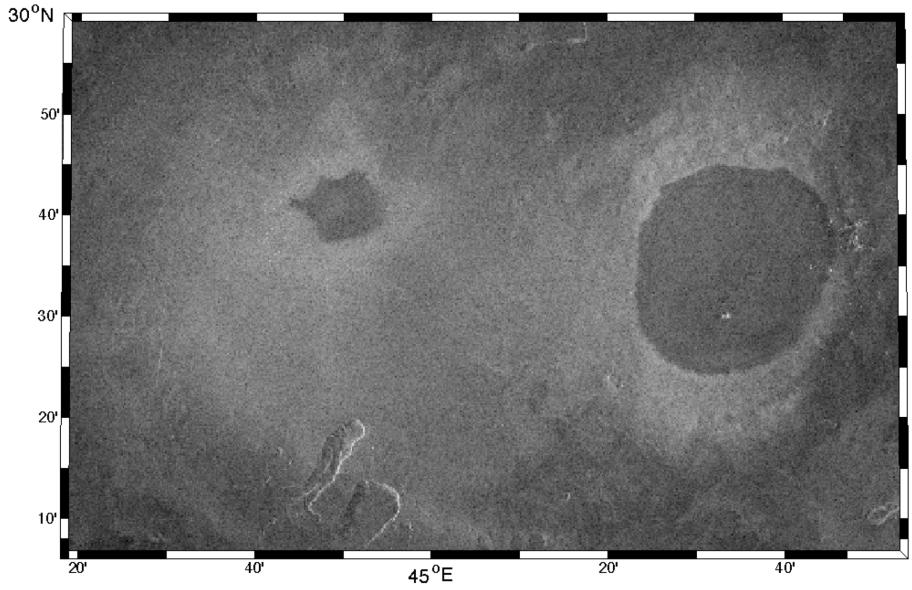

Figure 3.12: Detail of Tepev Mons' summit region. Area A in Figure 3.11

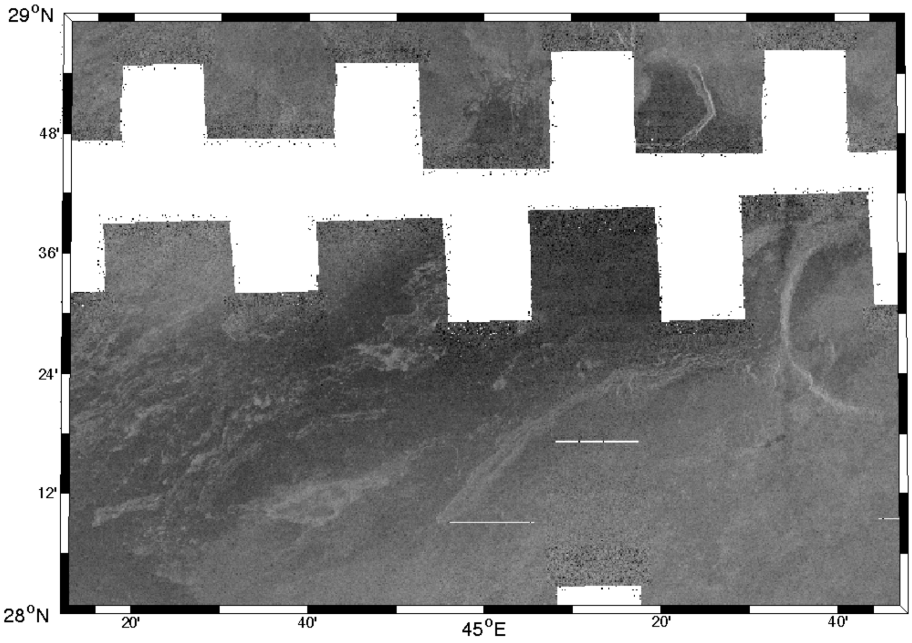

Figure 3.13: Detail of radar dark anomaly to the south of Tepev Mons. Area B in Figure 3.11. White areas are data gaps.

Table 3.5: Radar properties of features described in the text and illustrated in Figures 3.11 to 3.15. Data derivation described in caption to Table 3.4.

	Tepev Mons				*Otafuku Tholi*	
	Flank	Western caldera	Eastern caldera	Anomalous feature	Flows	Regional
Backscatter (dB)	-18.45	-6.90	-10.79	-23.57	-14.12	-21.67
RMS slope (°)	4.0	3.5	5.0	2.2	4.2	1.3
RMS height (m)	0.0875	0.0836	0.1010	0.0528	0.1184	0.0422
Corr. Length (m)	5.098	3.71	4.829	10.114	7.374	7.57
Emissivity	0.831	0.558	0.688	0.933	0.856	0.835
Dielectric - SAR	5.74	24.63	12.47	2.89	4.93	5.62
Dielectric - Alt.	4.27	10.11	4.09	2.18	3.59	4.27
Reflectivity - SAR	0.169	0.442	0.312	0.067	0.144	0.165
Reflectivity - Alt.	0.121	0.272	0.115	0.037	0.096	0.121
Density - SAR	2696	6344	4405	1490	2406	2518
Density - Alt.	2145	3899	2069	1056	1844	2145

a coarse mantling deposit; this region is detailed in Figure 3.12. Another radar-dark anomaly, similar to that on the south flank of Anala Mons, is also in evidence and shown in detail in Figure 3.13. The radar properties of these features are broken down in Table 3.5. A shaded topographic plot and topography with emissivity overlain are provided in Figures 3.14 and 3.15.

In this example, the edifice flanks and regional material are again very similar, indeed the compositional characteristics are virtually identical suggesting that they formed from the same local source of volcanic material and are of a similar age to have fully equilibrated in terms of surface-atmospheric chemistry. The difference in backscatter and related roughness is a reflection of the more variable surface topography of the lava flows in comparison with the smooth plains. The properties of the overlying lava flows from Otafuku Tholi are suggestive of deposits from the same magmatic source also, albeit somewhat younger (slightly higher-e and lower-ε), as the stratigraphic relationships also suggest. They display more variable vertical surface texture (RMS height and slope), a consequence of a lesser degree of weathering, again reflecting the relative youth of these deposits.

Tepev Mons is a higher altitude, steeper edifice than either of the examples in the previous case studies. It displays clear evidence of effusive activity as previously noted, however the surface deposits in the immediate vicinity of the two calderas require closer scrutiny. The western caldera seems to be covered by a diffuse mantling deposit, which could be potentially pyroclastic in origin, confined to a roughly circular region of ∼90

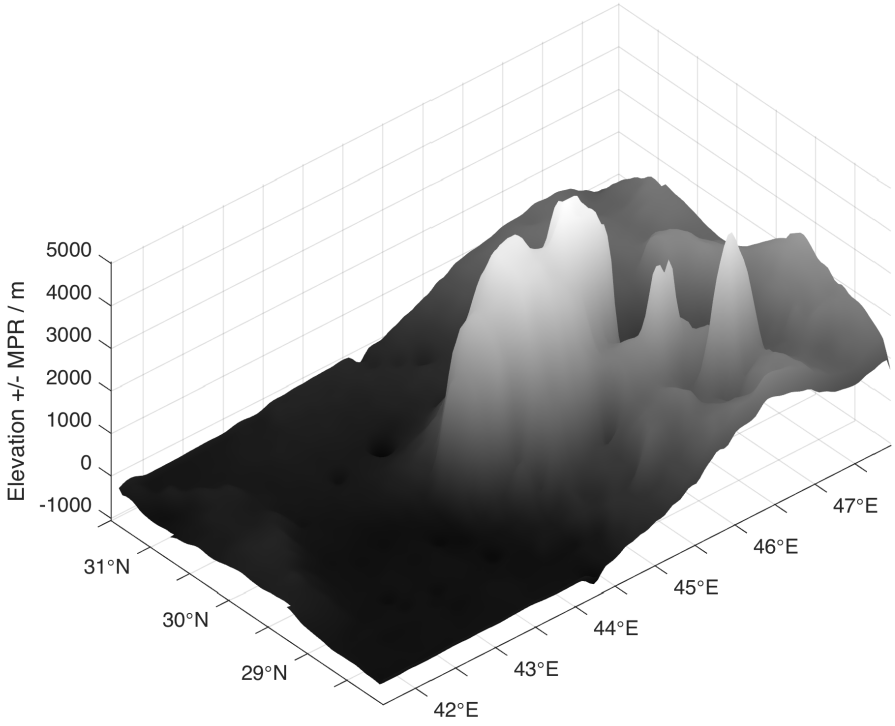

Figure 3.14: Topographic surface plot of region shown in Figure 3.11 with 50× vertical exaggeration showing the double summit peak of the main edifice (centre) and the two smaller peaks of Otafuku Tholi (right). Greyscale varies with altitude.

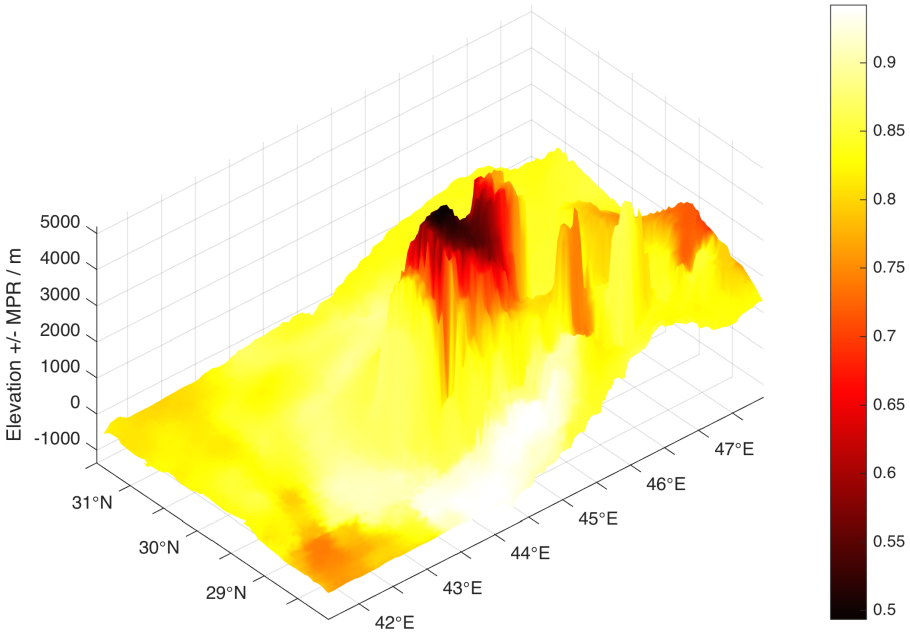

Figure 3.15: Topographic surface plot, as in Figure 3.14, of region shown in Figure 3.11 with 50× vertical exaggeration. Values for emissivity are overlain as indicated by the colour bar.

km in diameter centred on the caldera itself. The walls of the eastern caldera do not seem to be mantled by any such deposit, but are partially covered by the overlying deposit from the western caldera, which suggests differing styles of activity from the two volcanic centres. Figure 3.15 shows that the western caldera has the very low emissivity (0.558, Table 3.5) characteristic of high altitude stable mineral assemblages (*Klose et al.*, 1992), and has therefore equilibrated with the chemistry of the atmosphere under local conditions. This observation, along with the neighbouring (higher in altitude by some 400 m) eastern caldera displaying notably higher values of emissivity within the caldera walls and down the eastern flank (mean of 0.688, Table 3.5, but as high as 0.830 on eastern margin of summit) suggests that the eastern caldera represents a more recent, as yet unequilibrated, emplacement of volcanic material within the caldera. These observations are potentially indicative of a transition from explosive activity centred on the western caldera to less explosive activity centred on the eastern caldera over time.

The radar-dark flow detailed in Figure 3.13 is somewhat similar to the feature on the south flank of Anala Mons, and could well have a similar origin. It appears to be a later stage of material emplacement from the vicinity of Otafuku Tholi directed to the south-west and encircling the main edifice in a clockwise manner. It has been suggested that this could be a flow of a pyroclastic origin (*Campbell and Rogers*, 1994). This can clearly be seen on Figure 3.15 as the white, high-e region emanating from the locality of the westernmost Otafuku Tholus.

In summary, although inconclusive, the study of the radar data provides some evidence that the eruptive history of Tepev Mons potentially included phases of effusive and explosive activity. If the diffuse deposit surrounding the western caldera and the dark deposit from Otafuku Tholi do indeed represent the emplacement of pyroclastic material, two possibilities could potentially explain the alternating effusive-explosive sequence: (1) the alternating migration of more than one source of magma with different volatile contents to the surface, resulting in alternating high volatile explosive activity and low volatile effusive activity, and (2) the subsurface degassing and build

up of gas in cracks and fissures resulting in localised transient explosive activity upon failure as described in *Fagents and Wilson* (1995).

The summits of Tepev Mons are at 4.6-5.1 km above MPR. If scenario (1) is the case and a magmatic source for sustained explosive activity is required from a shallow magma chamber, material with a high volatile content would be required to generate explosive eruptions (*Airey et al.*, 2015). However, high volatile contents are unlikely and any type of explosive activity at low volatile concentrations could only be generated from small vents and, given this, for the resulting material to collapse locally, the magma temperature must be low enough to inhibit plume rise and more widespread dispersal. By contrast, a deep chamber could only feed sustained collapsing explosive activity from small vents and at low temperatures (*Airey et al.*, 2015). The narrow range of conditions that would feasibly result in explosive activity suggest that shallower ponded reservoirs of partially degassed magma could be intermittently released, or that scenario (2) is the preferred option for the origin of pyroclastic activity at this locality. Alternatively, a combination of both scenarios could potentially give the same result.

3.3.4 Case Study 4 - Ma'at Mons, Atla Regio

Ma'at Mons is Venus' highest volcanic peak at ∼9 km above MPR. It is a very large shield volcano with a diameter of ∼500 km located near the equator in the mountainous, rift-dominated Atla Regio. Figure 3.16 shows the Magellan SAR image of the case study region. Figures 3.17 and 3.18 are topographic surface plots of the study region shaded for elevation and emissivity, respectively; Figure 3.19 is a plan view of the surface emissivity for easy comparison with Figure 3.16. The flanks of Ma'at Mons are constituted entirely of lava flows with varying radar backscatter properties, most being radar-bright but with some radar-dark examples reflecting variability in surface roughness properties, and therefore flow type, of the deposits. It can be inferred from the rift setting for Ma'at Mons and its situation on a broad topographic rise that the region is fed by a mantle plume (*Stofan et al.*, 1995), and the rifting structures

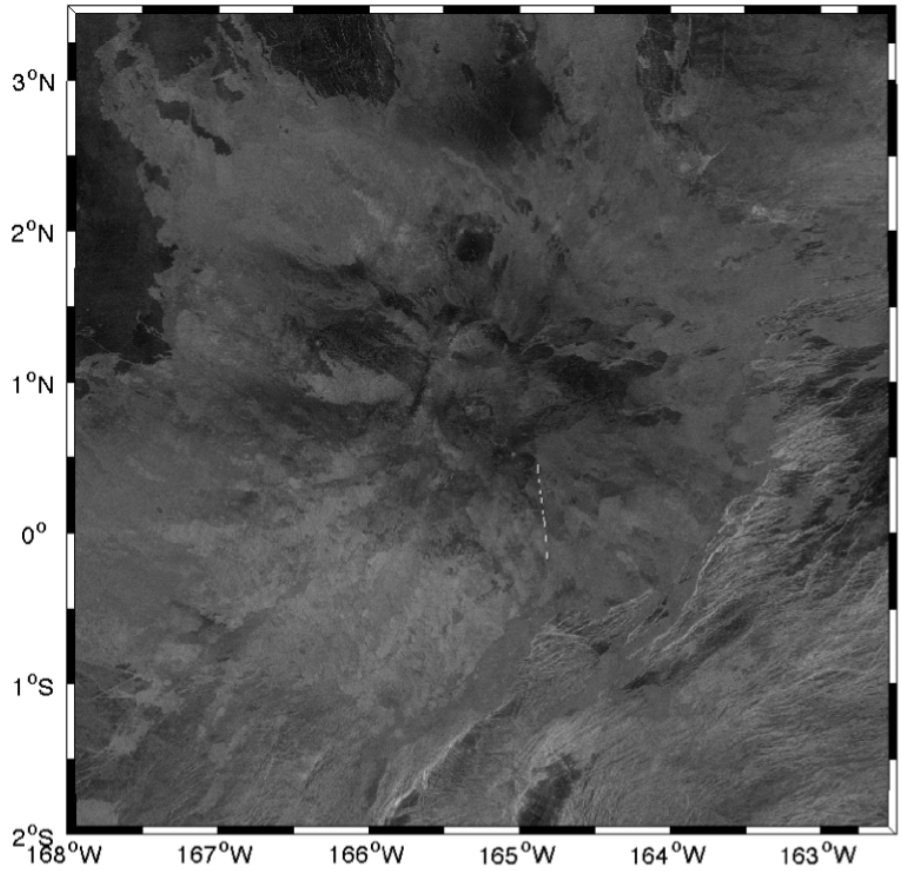

Figure 3.16: Magellan SAR image of Ma'at Mons. White dotted line in lower right centre is an artefact of radar processing.

indicate extensional processes oriented along linear rift systems, some of which have corona-chains suggestive of near-surface magma bodies along the rifts (*Senske et al.*, 1992).

Inspection of Figures 3.16 and 3.19 shows three broad classifications of lava flow type: (1) the very radar-bright, very low-e flow on the south-west flank centred at 1°S, 166°W, (2) the radar-dark, high-e flows close to the central caldera to the east, north and west, and (3) the intermediately-bright flows that constitute the rest of the edifice flanks. Table 3.6 provides an analysis of the radar properties of these flows. All flank material in this instance is distinct from the regional plains, meaning that the edifice itself, as evident in the radar imagery, has been built up on an existing substrate arising from a distinct episode of volcanism prior to the formation of the

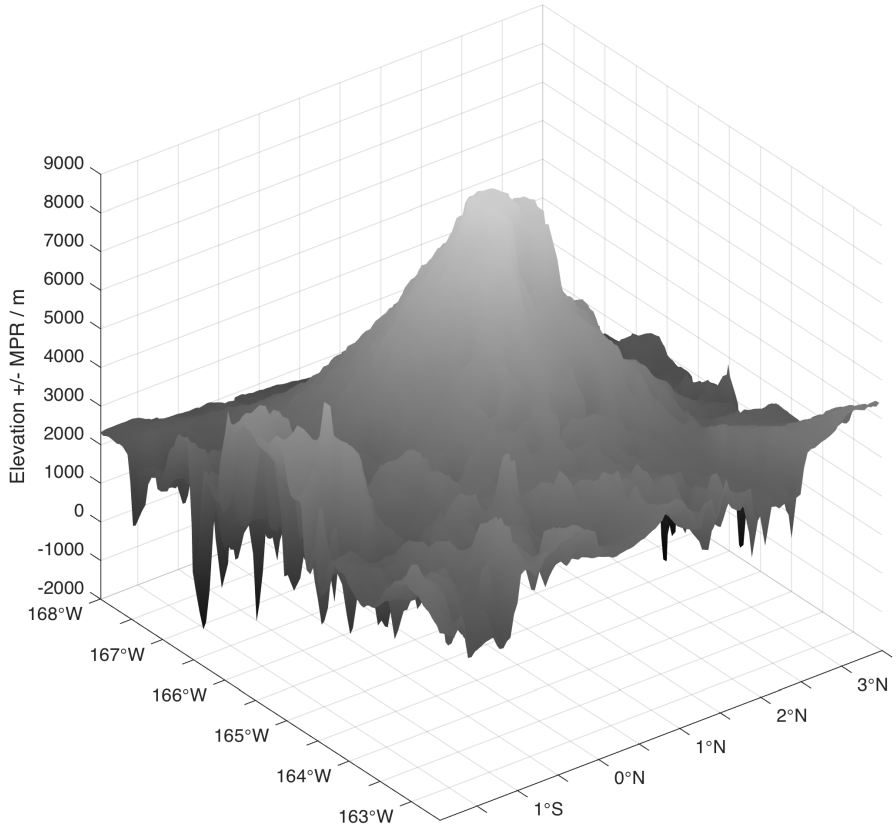

Figure 3.17: Topographic surface plot of region shown in Figure 3.16 with 50× vertical exaggeration. Greyscale varies with altitude.

present material making up the surface of Ma'at Mons. The variability in flow type on the flanks probably results from variability in magma composition.

Table 3.6: Radar properties of features described in the text and illustrated in Figures 3.16 to 3.19. Data derivation described in caption to Table 3.4.

	Ma'at Mons			
	Bright	Dark	Intermediate	
	Flow type 1	Flow type 2	Flow type 3	Regional
Backscatter (dB)	-7.92	-18.93	-11.59	-19.47
RMS slope (°)	5.5	6.2	5.6	2.0
RMS height (m)	0.1352	0.1483	0.1722	0.0711
Corr. Length (m)	3.945	6.813	7.133	9.44
Emissivity	0.623	0.934	0.848	0.890
Dielectric - SAR	17.48	2.85	5.20	3.97
Dielectric - Alt.	9.23	3.22	4.28	3.52
Reflectivity - SAR	0.377	0.066	0.153	0.110
Reflectivity - Alt.	0.255	0.081	0.122	0.093
Density - SAR	5308	1467	2507	2018
Density - Alt.	3690	1664	2150	1811

Flow type (1), a very rough, blocky lava field, has a very low emissivity as would be expected for high altitude material of sufficient age to be in chemical equilibrium

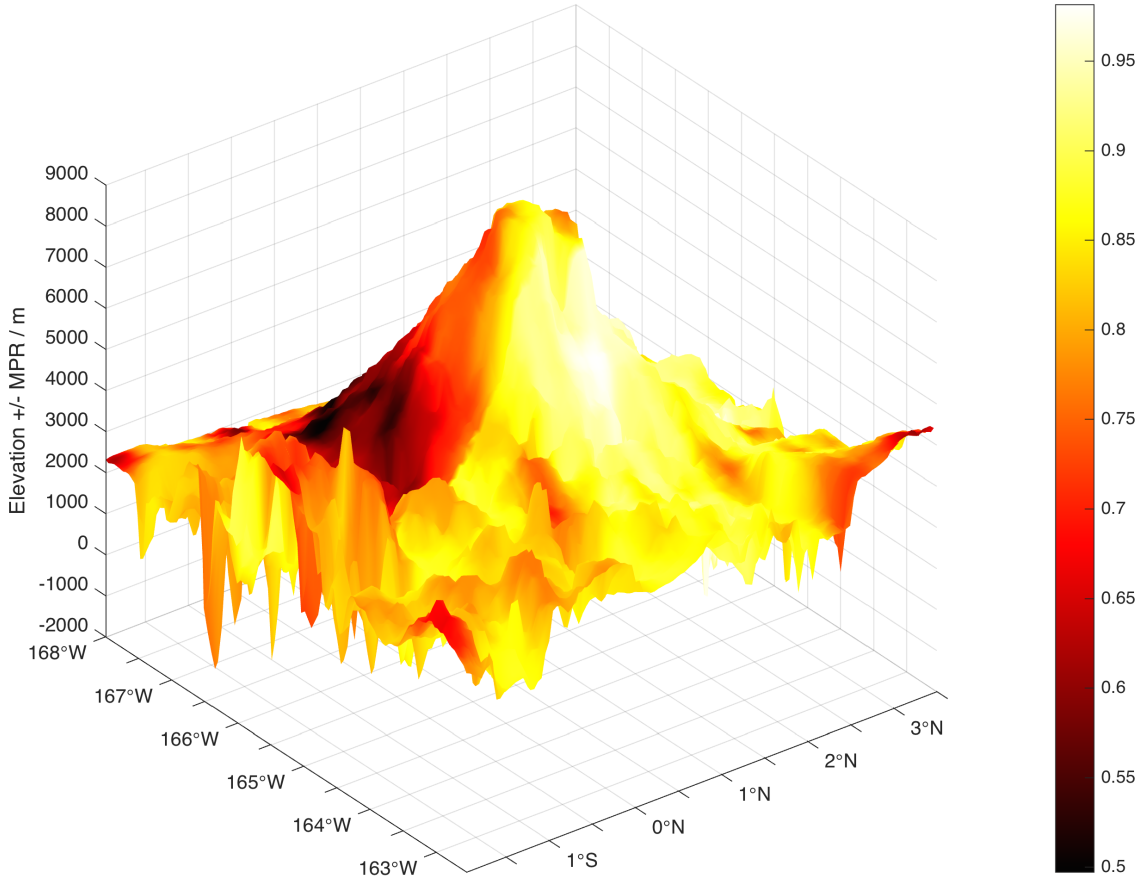

Figure 3.18: Topographic surface plot, as in Figure 3.17, of region shown in Figure 3.16 with 50× vertical exaggeration. Values for emissivity are overlain as indicated by the colour bar.

with Venus' atmosphere as discussed previously. However, in this example the deposit continues downslope to altitudes lower than that expected for volcanic deposits to meet this equilibrium condition. As noted by *Klose et al.* (1992), the critical elevation at which the transition from high to low emissivity generally occurs varies by height of peak and by location to be between ∼2.5-5 km above MPR. Figure 3.20a shows a scatter diagram of points corresponding to individual radar footprints from the Magellan emissivity data set. It shows a clear peak at just over 3 km altitude, which seems to correspond to this critical altitude, but a secondary anomalous peak occurs at ∼2 km caused by the low altitude component of low-e flow (flow type (1)) and suggests material that is out of equilibrium at lower altitudes. These features are more easily distinguished when the plot is compared with an example of the expected

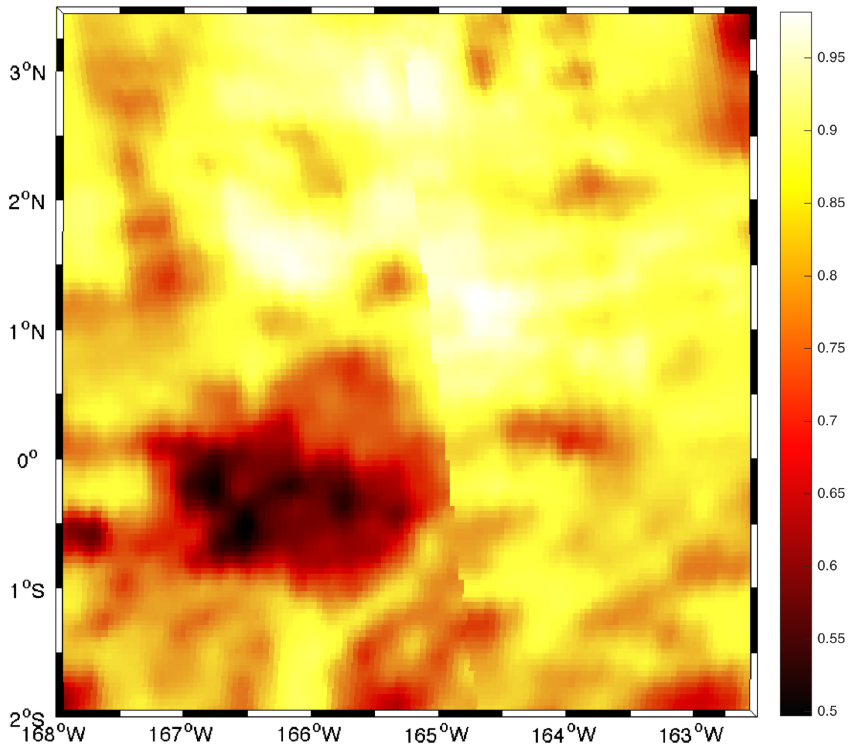

Figure 3.19: Plan view of emissivity values for region shown in Figure 3.16. Bright flows correspond to low-e anomalies and dark flows correspond with high-e anomalies.

altitude-dependent emissivity behaviour as shown in Figure 3.20b, taken from *Klose et al.* (1992), showing data from Ovda Regio (see Figure 3.21 for location). This could be due to a temperature anomaly, as the altitude-dependent relationship is itself affected by the temperature profile (*Klose et al.*, 1992), or it could even potentially be due to a local chemical anomaly in the composition of the atmosphere due to localised volcanic outgassing as suggested by *Robinson and Wood* (1993). In any case, this flow field appears to be older than the north flank based on this relationship of emissivity.

Flow type (2), with its very high (up to ∼1) values of emissivity, represents very young deposits still rich in low-ε minerals. These appear to be the youngest flows on Ma'at Mons and have a smooth, low-backscatter appearance characteristic of a fine-grained deposit mantling the rocky substrate. The RMS height for this dark deposit quoted in Table 3.6 would suggest a rougher surface, however this value is probably elevated by the much coarser slope data overlapping the small areas of deposition. It

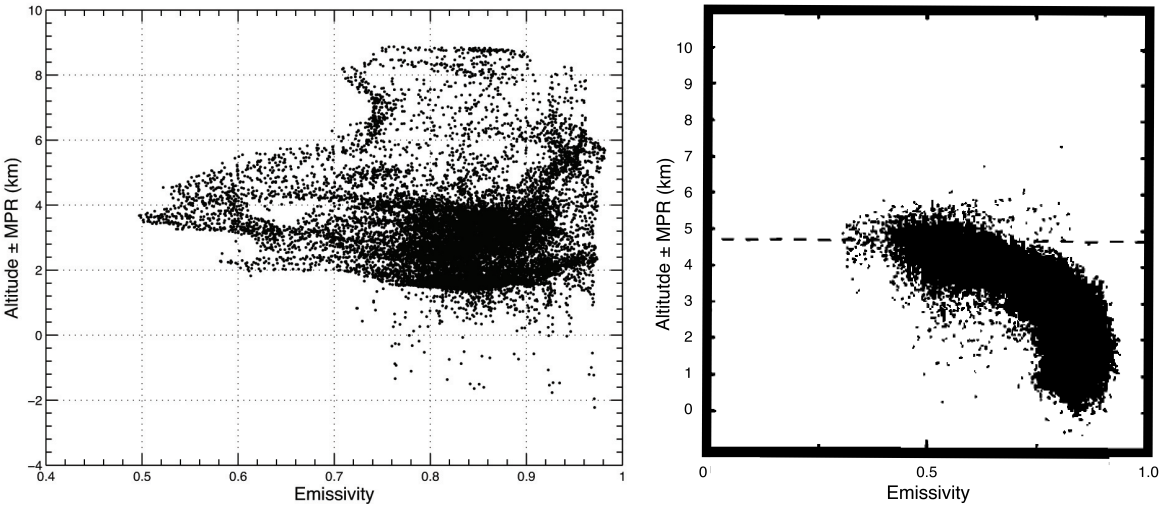

(a) (b)

Figure 3.20: Scatter plots of emissivity covering a) the total area in Figure 3.19, and b) an example from Ovda Regio taken from *Klose et al.* (1992) for comparison. Each point corresponds to a radar footprint (i.e. pixel) from the Magellan emissivity data set.

could potentially represent pyroclastic deposition (*Campbell*, 1995), although this is contentious and not clear from the available data. This deposit is discernable in Figure 3.20, where the cluster of points with very high emissivity (and very low dielectric constant) at ∼6 km represents this feature.

Considering the widespread occurrence of flow type (3), the presence of such a large volume of high altitude rock, which is not yet of sufficient age to have reached chemical equilibrium, indicates recent, large-volume, effusive volcanic activity focussed on the west, north, and east flanks. Effusive flow-forming volcanism is clearly the dominant depositional process in this locality.

The tectonic setting of this volcano could result in the occurrence of deep and/or shallow source regions; this could explain the variability in the properties of the deposits. The implications of this for interpreting the style of activity in this region are somewhat problematic. If, as has been previously proposed (*Robinson et al.*, 1995; *Glaze*, 1999), explosive volcanism of some type has occurred from Ma'at Mons, the radar-dark flows on the north flank could feasibly be evidence of pyroclastic deposits, supporting the occurrence of explosive volcanism. This evidence is inconclusive however.

3.3.5 Emissivity at rifts

In order to investigate emissivity as an indicator of recent volcanic activity, profiles were mapped across a selection of major regions of rifting (labelled I-IV on Figure 3.21) as identified in previous work (e.g. *Head et al.*, 1992; *Ivanov and Head*, 2011), on the surface of Venus. Figures 3.22 to 3.25 illustrate these profiles.

Figure 3.22 shows two roughly parallel chasmata (Diana and Dali) trending WSW-ENE. Profile A shows the rift cross section at around 60-110 km, with a central peak standing proud of the surrounding terrain. The emissivity displays mainly the planetary average and it is hard to attribute any particular features to the rift structure itself. However, north of the rift there is a low-emissivity region of diffuse, moderately radar-bright (compared with the surrounding plains), deposits. This is crosscut by a darker feature, which corresponds to the dip in emissivity at ∼35 km into the profile. At this low altitude, a low-e deposit such as this implies the presence of a high-ε mineral phase in order to depress the emissivity below expected values for basalt. Profiles B and C, across the central part of the rift complex, show broad sites of ridged terrain with broad signals of roughly anti-correlation. This could suggest young material at the topographic lows indicating the recent emplacement of volcanic material within the main rift depression. The easternmost profile, D, shows the ridge axis at ∼150 - 200 km with no significant emissivity response.

Figure 3.23 shows three profiles across Devana Chasma, which links Beta Regio in the north with Phoebe Regio in the south. Profile E crosses a broad topographic rise extending 3-4 km above the surrounding topography. This strongly correlates with an emissivity low reaching a minimum of 0.6 at the peak of the ridge. This is due to the high-elevation, low-e anomaly described in section 3.1. The most interesting aspect of this profile is where the rift axis shows a topographic trough at ∼220 km, the eastern side of which coincides with a higher-emissivity peak in the low-emissivity region. This strongly indicates young material that is out of equilibrium with its surroundings. Profiles F and G do not show this kind of response; there are smaller scale variations in the topography and emissivity within the confines of the rift axis but nothing to

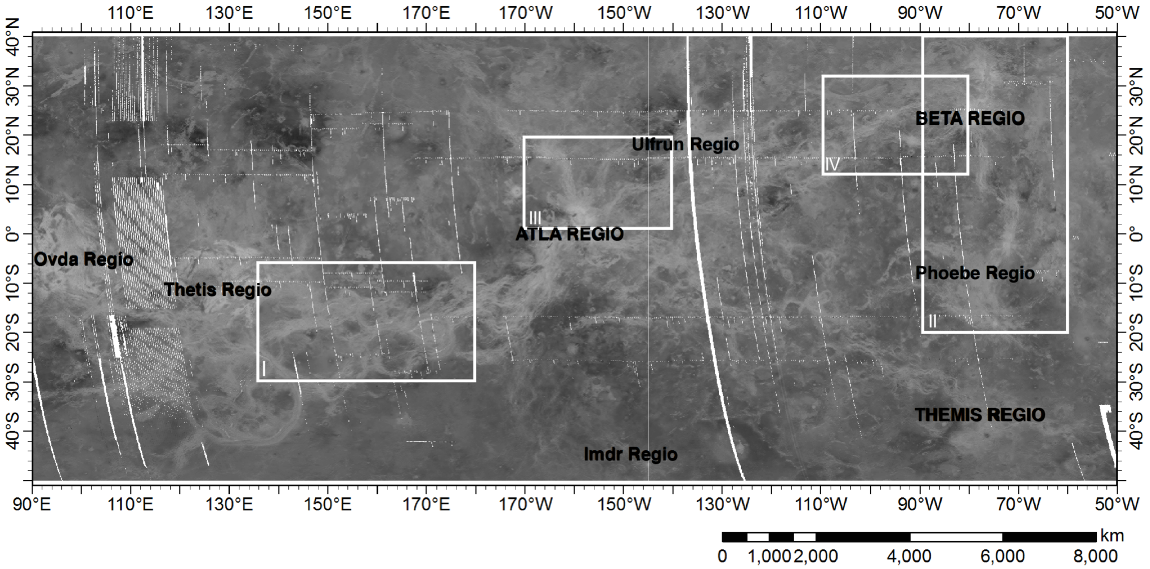

Figure 3.21: SAR map of the equatorial region of Venus. Labels I-IV correspond to the subregions in Figures 3.22 to 3.25.

strongly suggest anything on the scale of profile E. There is however a region of elevated emissivity in profile G centered at ∼350 km along the profile, which coincides with a region of tessera unrelated to rift processes.

Figure 3.24 shows part of northern Atla Regio that features three crosscutting rift features. Profiles H and I show the emissivity variation across Ganis Chasma. These both show central rift features with central peaks. In both cases certain topographic low features are incident with emissivity highs, for example at 90 km and 70 km in profiles H and I respectively. Again this could be evidence for young material and in the case of profile H, the emissivity high coincides with the recently reported active volcanism at Ganis Chasma (*Shalygin et al.*, 2015), further supporting this finding. The features in profiles J, K, and L are not as pronounced across Tkashi-Mapa and Zewana Chasmata, however their central rift topographic lows are possibly central to a low-frequency central peak. Although this is tentative at best in J and K, it is slightly more pronounced in profile L.

Figure 3.25 is a rift complex between Asteria and Beta Regiones. Profile M across Hecate Chasma shows relatively high emissivity compared with the planetary average and has a distinct anti-correlation with the topography, which could signify some dif-

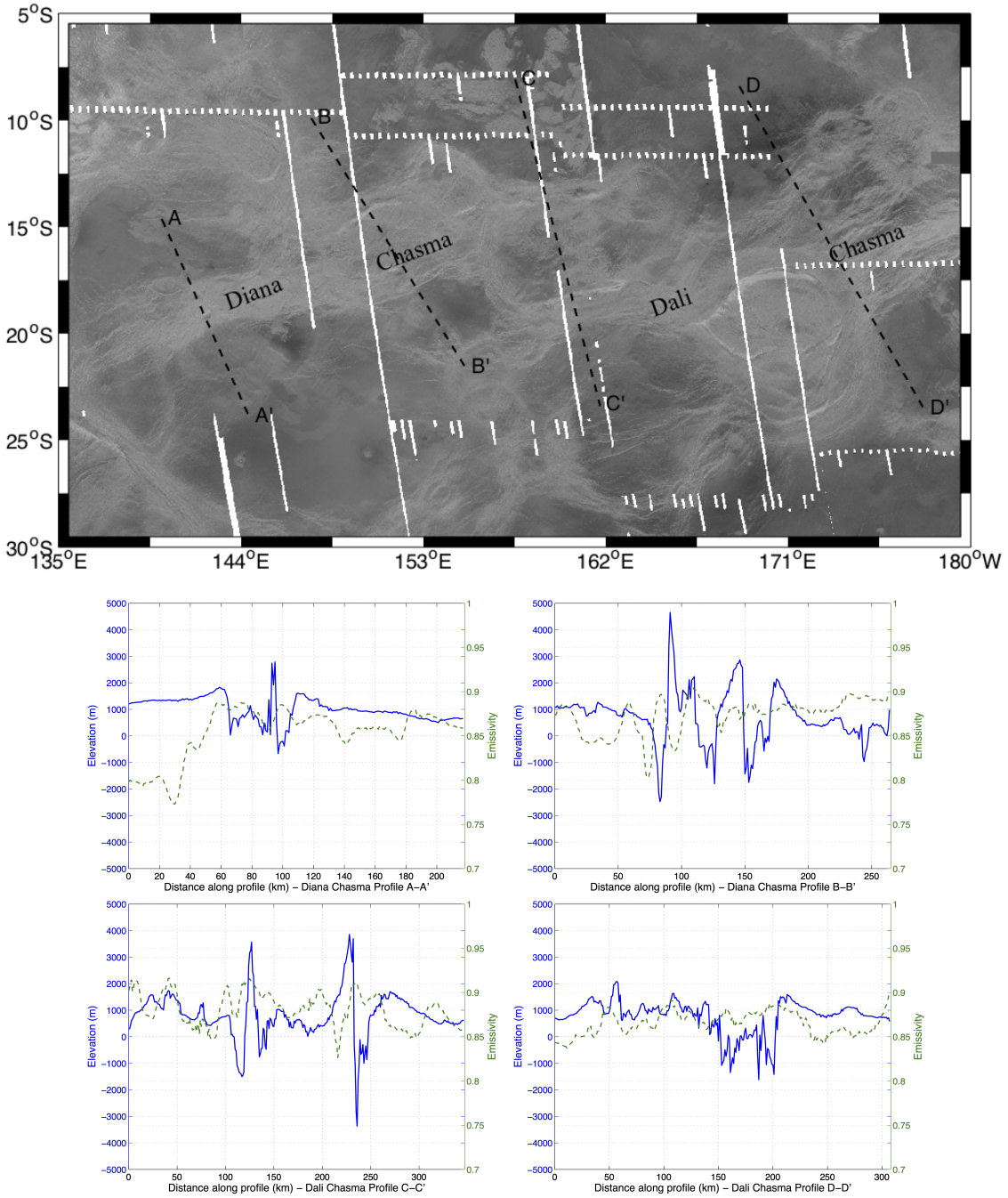

Figure 3.22: Elevation and emissivity profiles across Dali and Diana Chasmata. Area identified as I in Figure 3.21. Profile locations A, B, C, and D indicated on the map correspond to the letters in the profile x-axis labels.

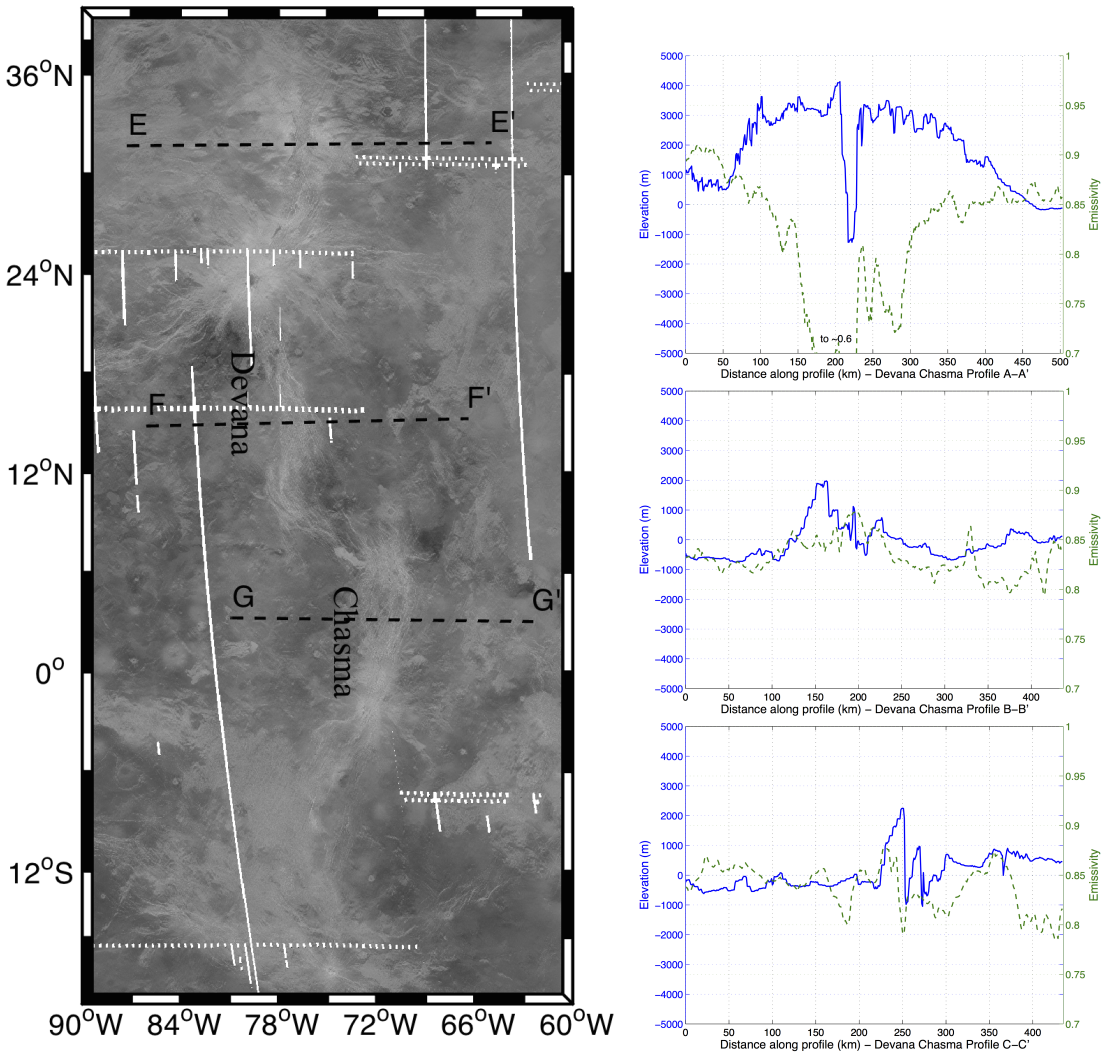

Figure 3.23: Elevation and emissivity profiles across Devana Chasma. Area identified as II in Figure 3.21. Profile locations E, F, and G indicated on the map correspond to the letters in the profile x-axis labels.

fuse volcanic activity across the region. Latona Chasma (profile N) also displays an emissivity peak co-incident with the rift low at 90 km suggesting that the WSW-ENE feature could be active along its length. Zverine Chasma (profile O), in contrast, shows rather stable conditions across the rift axis, indicative of less, or less recent, activity on this segment of the rift.

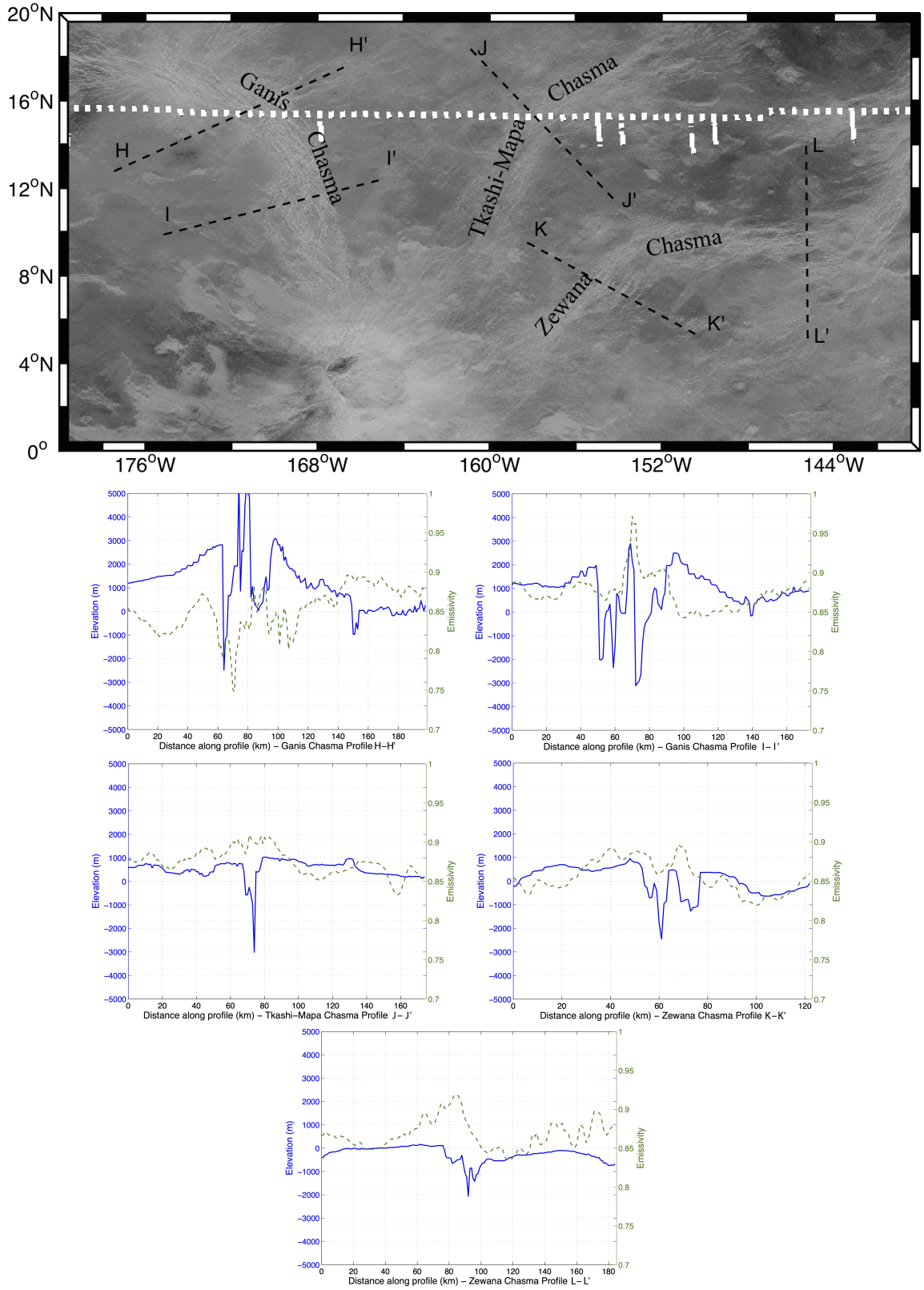

Figure 3.24: Elevation and emissivity profiles across Ganis, Tkashi-Mapa, and Zewana Chasmata. Area identified as III in Figure 3.21. Profile locations H, I, J, K, and L indicated on the map correspond to the letters in the profile x-axis labels.

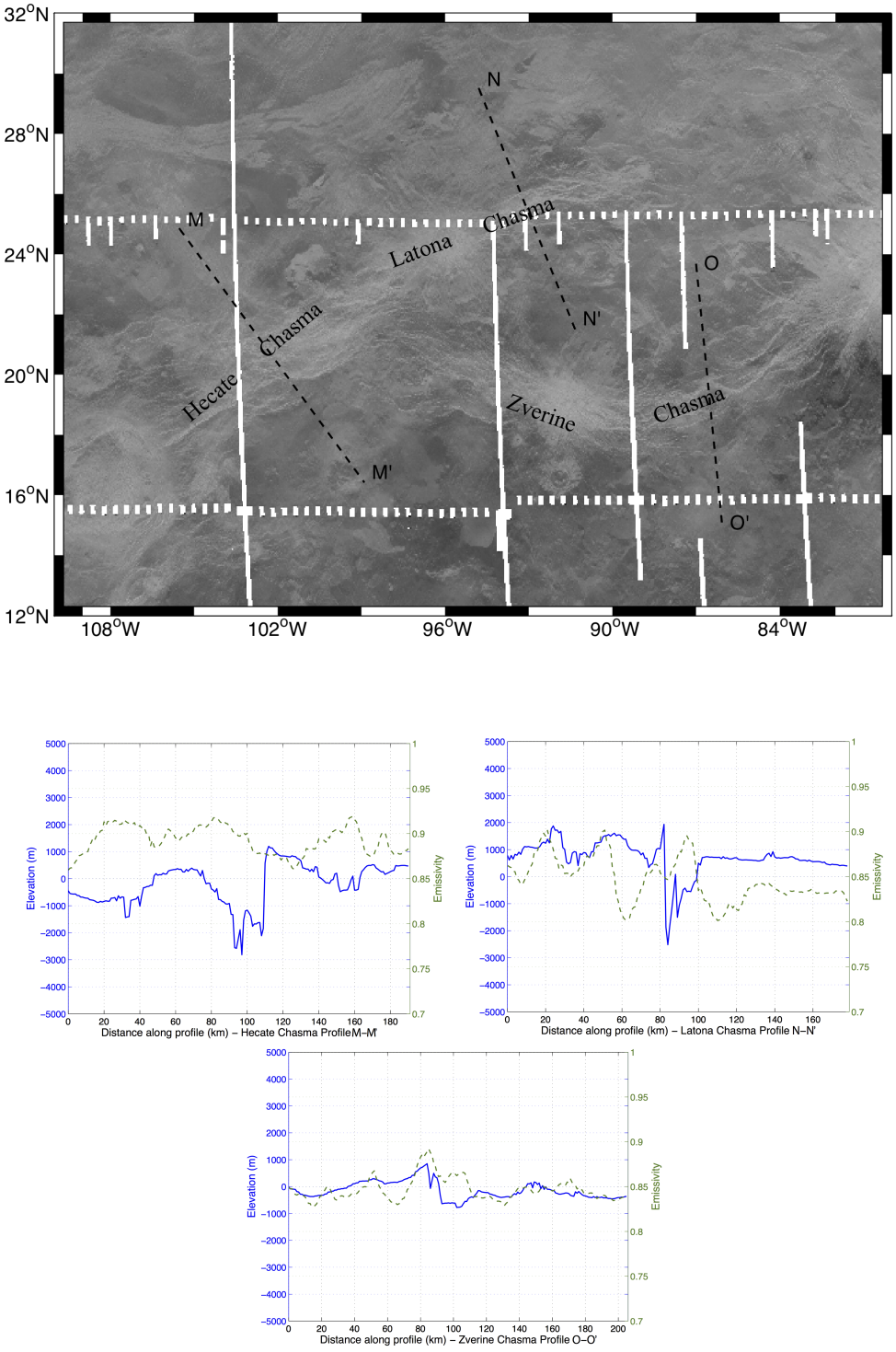

Figure 3.25: Elevation and emissivity profiles across Hecate, Latona, and Zverine Chasmata. Area identified as IV in Figure 3.21. Profile locations M, N, and O indicated on the map correspond to the letters in the profile x-axis labels.

3.4 Venus - Earth Comparison

3.4.1 Radar backscatter

The two SAR datasets used in this study offer the most directly comparable SAR data available, although the radar sensors operate at somewhat different wavelengths. Magellan's sensor operates at 12.6 cm (S-band), whereas the ASAR instrument operates at 5.6 cm (C-band), this will affect the comparability of the two. However, previous work (*Campbell and Campbell*, 1992) has facilitated some quantification of this comparability by simulating synthetic S-band data for Hawai'i using interpolation of measured C-band and L-band backscatter values. The degree to which there is a disparity between the original C-band and simulated S-band seems to depend on the roughness scale of the deposits. Where S-band data were simulated for 'a'a deposits there was very little difference between the two; the mean difference was a value ∼7% lower than the C-band backscatter value. For smoother deposits however (pahoehoe flows), there was again a tendency towards lower values in the simulated data, but with a much larger mean difference of ∼28%. It is evident from these data that one can be much more confident in the comparable nature of these two wavelengths for rougher surfaces. This is due to the radar backscatter being much more sensitive to roughness variations on the scale of the wavelength, irrespective of incidence angle.

Figure 3.26 shows the backscatter values of various terrestrial lava flows (this study (red data) and *Campbell and Campbell* (1992) (black data)), terrestrial pyroclastic deposits (this study (blue data)), Venusian volcanic flank, flow, and potentially pyroclastic deposits (all this study (gold data)). The terrestrial data are in their original C-band form (ASAR IS2, 4, and 6 for blue and red data (see Figure 3.2) and AirSAR for black data) and the Venusian data are in their original S-band form. The Venusian possible pyroclastics cited in this section are summarised in Table 3.7 and their radar characteristics are summarised in Table 3.8.

Table 3.7: Summary of examples used as possible pyroclastics in this study, with case study sections where relevant and key references in which deposits are first suggested as possibly pyroclastic in origin

Name	Case Study	Section	Reference
Irnini Mons halo	1	3.3.2	*McGill* (2000)
Irnini Mons isolated deposit	1	3.3.2	*McGill* (2000)
Anala Mons halo	2	3.3.2	*McGill* (2000)
Tepev Mons summit	3	3.3.3	*Campbell and Rogers* (1994)
Nijole Mons	N/A	N/A	*Grosfils et al.* (2011)
Scathach Fluctus	N/A	N/A	*Ghail and Wilson* (2013)

Table 3.8: Radar properties of examples used as possible pyroclastics in this study.

Name	σ_0 (dB)	Emissivity	Inc. angle (°)	Asperity (56 mm)	Asperity (126 mm)
Irnini Mons halo	-11.43	0.848	45.8	10.35	16.07
Irnini Mons isolated deposit	-10.76	0.809	45.8	10.30	16.00
Anala Mons halo	-12.22	0.830	46.0	9.15	14.27
Tepev Mons summit	-6.90	0.558	42.5	10.29	14.86
Nijole Mons	-14.44	0.856	35.9	5.15	6.37
Scathach Fluctus	-14.20	0.837	40.0	8.47	11.57

The general trend in these data is decreasing backscatter intensity with increasing incidence angle for a particular flow type. This is to be expected from general radar scattering behaviour and the overall data range corresponds to the roughness curve characteristic of a material with a 'moderately rough' to 'rough' character at Magellan wavelength (Figure 3.26 and original data in 3.27). These classifications are quantified as the magnitude of the surface height variations relative to the radar wavelength; the terrestrial data appear to be consistently rougher relative to these curves due to an artefact of the shorter wavelength.

At smaller incidence angles there appears to be a tendency for the pyroclastic deposits (blue symbols) to follow the 'moderately rough' trend from Figure 3.27. However, the same deposits when measured at larger incidence angle appear to plot closer

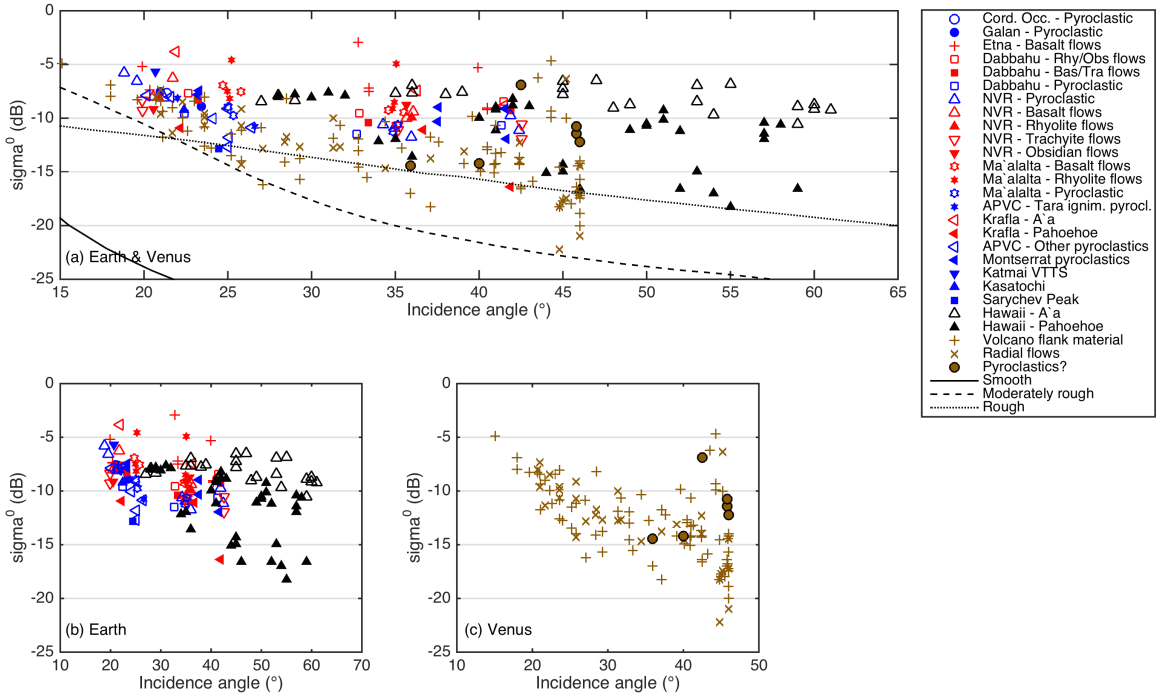

Figure 3.26: Radar backscatter as a function of incidence angle for various volcanic deposits on (a) Earth and Venus, (b) Earth, and (c) Venus. Blue data are Earth explosive, red data are Earth lavas, black data points from hawai'i lava flows in *Campbell and Campbell* (1992), and gold data are from Venusian deposits as stated in the key.

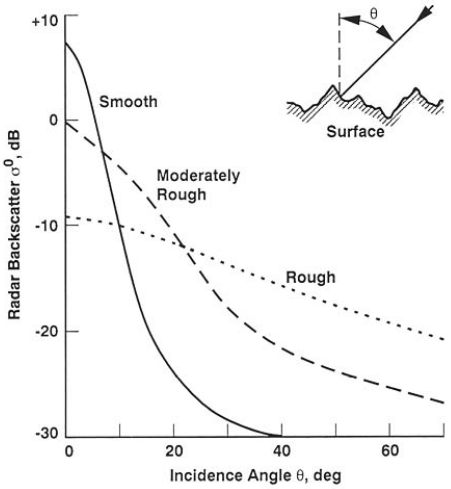

Figure 3.27: Radar backscatter as a function of incidence angle for representative surfaces (From *Ford et al.*, 1993)

to the 'rough' curve. There is much more spread in the lava flow data, although this can largely be accounted for by the variety of flow types. Take for example the two flow types at Krafla measured at all three image modes; the 'a'a flow value is consistently higher than the pahoehoe flow at all incidence angles. This of course arises from the rougher textures characteristic of blocky 'a'a flows. This association is also clearly evident in the Hawai'i data. Although the fact that the pyroclastic data follow a trend quite closely is reassuring, its similarity to the other deposits does not facilitate any form of deposit identification from backscatter alone; other data sets are therefore required.

3.4.2 Emissivity

Emissivity data are plotted as the diamonds, circles, and stars in Figure 3.28 c-e as a function of backscatter for all the Venus deposits previously shown in Figure 3.26.

The markers are colour-coded by incidence angle, as backscatter values are dependent on this as seen earlier. Most Venusian deposits show a rather narrow range of emissivity values, averaging at ∼0.85. The low emissivity (∼0.6) deposits in figures 3.28d and 3.28e are above the critical low-e altitude on Ma'at Mons and Tepev Mons respectively. The possible pyroclastics in figure 3.28e are, again, indistinguishable from the flank and flow deposits. Although the Venusian volcano flank deposits are clustered together tightly, the flows show a greater variety of properties. The extension of the flow data into the lower part of Figure 3.28d may be the result of younger flows having smoother, less weathered surfaces. There is even one data point with an emissivity higher than 0.9, this corresponds to the dark flows on the northern flank of Ma'at Mons described in section 3.3.4 indicative of young, smooth flows whose mineral assemblage has not yet equilibrated with the atmospheric thermodynamic and chemical conditions.

Superimposed on these data in Figure 3.28f, and shown separately in Figures 3.28a and 3.28b, are the Earth derived emissivity values, again for the same deposits stated in Table 3.3. These data are not strictly comparable as they are derived from a much shorter wavelength instrument (1.24 μm). No Earth emissivity data anywhere near

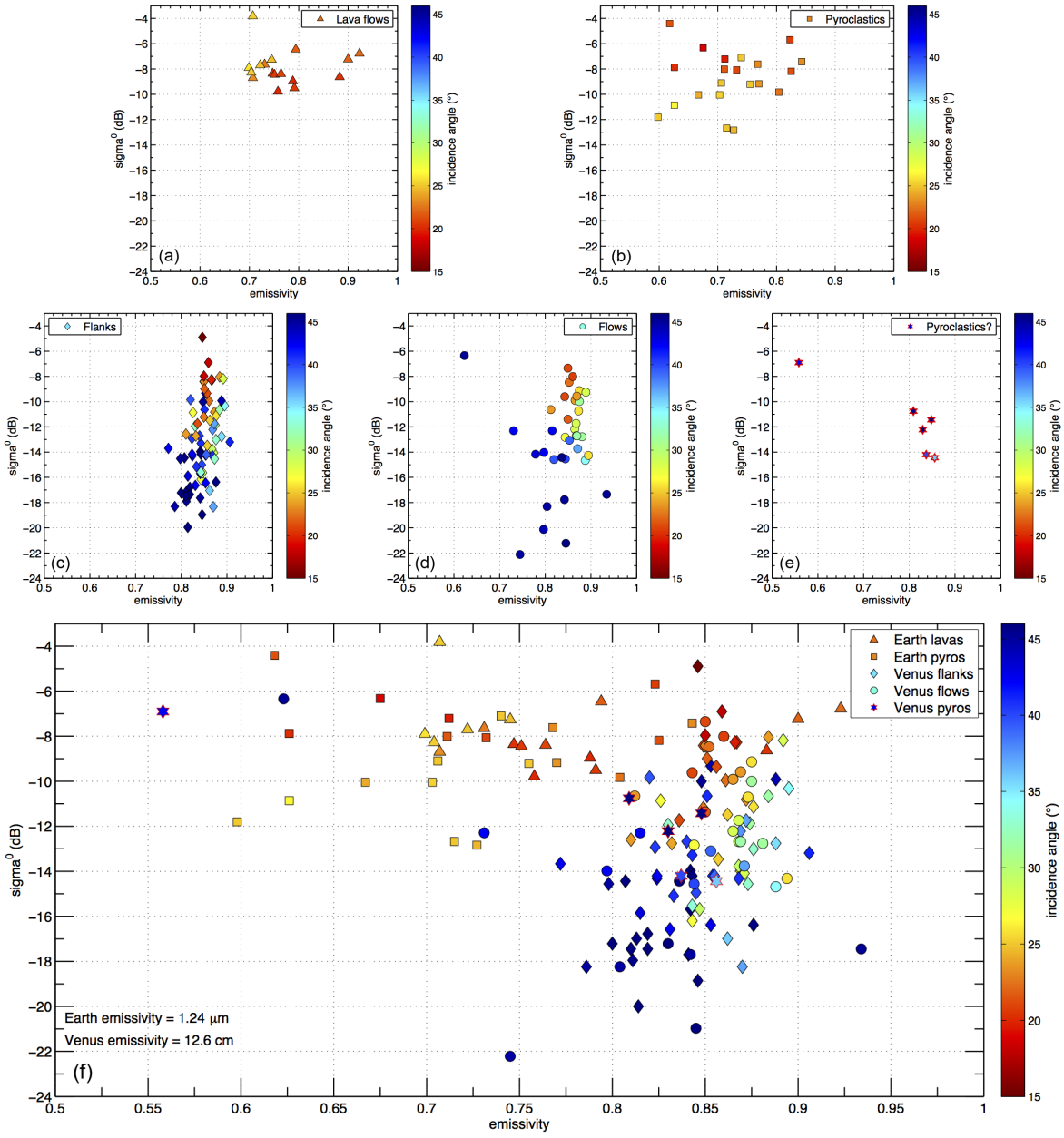

Figure 3.28: Emissivity of various geological deposits as a function of radar backscatter for (a) terrestrial lavas, (b) terrestrial pyroclastic deposits, (c) Venusian volcano flank material, (d) Venusian lava flows, (e) potentially pyroclastic deposits on Venus, and (f) all the above plotted together. Venus emissivity at 12.6 cm and Earth emissivity at 1.24 μm

the Magellan wavelength is currently available, so the 1.24 μm data were gathered due to their similarity in wavelength to another Venus emissivity data set (Venus Express VIRTIS at 1.01 μm) that may be used in future for comparison. Nonetheless, these data show some interesting trends and future work should investigate whether these are

mirrored in the VIRTIS data. Figures 3.28a and 3.28b show Earth emissivity data for lava flows and pyroclastic deposits respectively. Both data sets concentrate in the 0.7 to 0.8 region for emissivity, but differ in the detail. The lava flow data include a branch into the higher-emissivity region whereas the pyroclastics have a tendency towards lower emissivity values; this could turn out to be an important factor in identifying deposit types based on their radar properties.

3.4.3 Roughness

The roughness properties calculated in sections 3.2.2 and 3.2.3 are less straightforward to compare using their true values. Therefore, for comparative purposes, focussing on trends rather than absolute values, the derived property of asperity is used in this section. Figure 3.29 shows how the calculated values for asperity vary with backscatter and incidence angle. This demonstrates the dependency of asperity on radar backscatter, increasing in a quasi linear fashion. The gradient of this linear relationship is itself a function of the incidence angle. The terrestrial data, although initially appearing distinct from the Venus data, show similar values for asperity collected at similar incidence angles. When considered in this context, the actual pyroclastic deposits on Earth and the proposed pyroclastic deposits on Venus both plot on the expected gradient for the incidence angles at which they are measured. This makes differentiation of deposit types problematic as there appears to be no clear distinction between the two.

Figure 3.30 shows how the measured deposits' values of asperity relate to their emissivity. Asperity was calculated and compared for both Earth and Venus at each instrument's wavelength, 126 mm and 56 mm (Figures 3.30a and 3.30b respectively) in order to compare like with like. There do appear to be distinct regions of point clusters. The Venus flanks and flows occupy relatively broad ranges of both asperity and emissivity, although the vast majority occur within a somewhat narrower range focussed at $\sim$6 mm asperity and an emissivity of $\sim$0.85. Some of the outliers show more extreme deviations from this although these can largely be accounted for by the low-e, high elevation anomaly (i.e. the flow and possible pyroclastic deposit in the top left

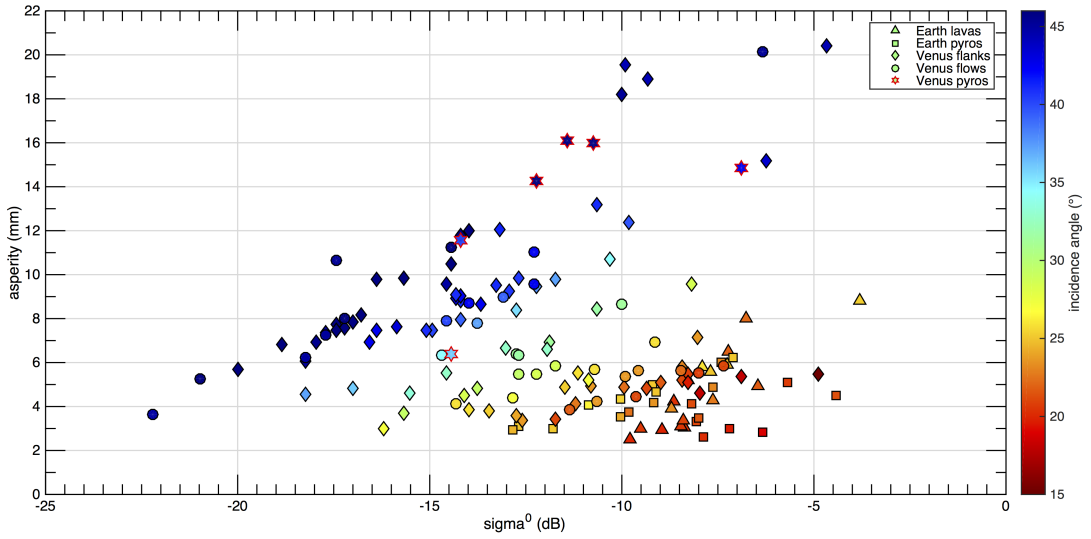

Figure 3.29: Asperity (at 126 mm wavelength) as a function of radar backscatter and incidence angle for deposits on Earth and Venus.

of the plot), and the heavier influence of incidence angle on elevated asperities (Figure 3.29). It is interesting to note however, that five out of the six possible pyroclastic deposits fall within either an emissivity range of 0.81-0.86 or an asperity range of 8.5-10.5 mm, with four out of the six occurring in both. Although the sample size is very small, and these are not all definite identifications, this does provide the first tenuous evidence for a diagnostic radar signature for pyroclastic deposits. Of course, this could be due entirely to the fact that they are observed at similar incidence angles and that global emissivity is largely within this range in any case, but it indicates how best to approach future studies of this kind.

In terms of the Earth data, again the tendency is for pyroclastic deposits to favour low emissivity and lava flows to favour high emissivity. The range in which the two coincide, in what appears to be a terrestrial average of ∼0.70-0.75, is ∼0.10 lower than the Venus average. This could again be due to the difference in wavelength so is not diagnostic of a systematic difference, indeed, the unused band 31 and 32 terrestrial emissivity data averaged higher than for Venus at >0.90.

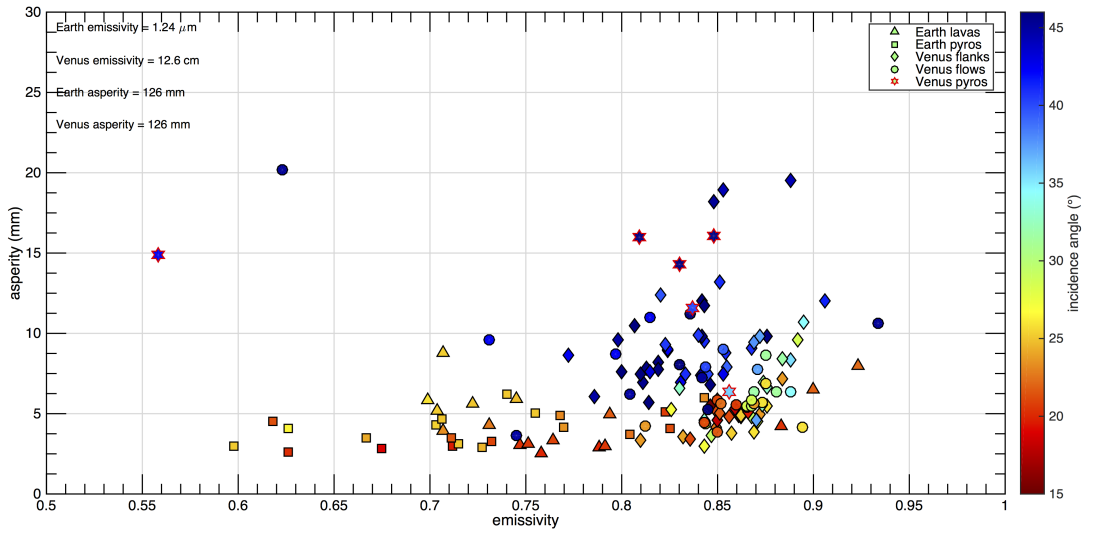

(a)

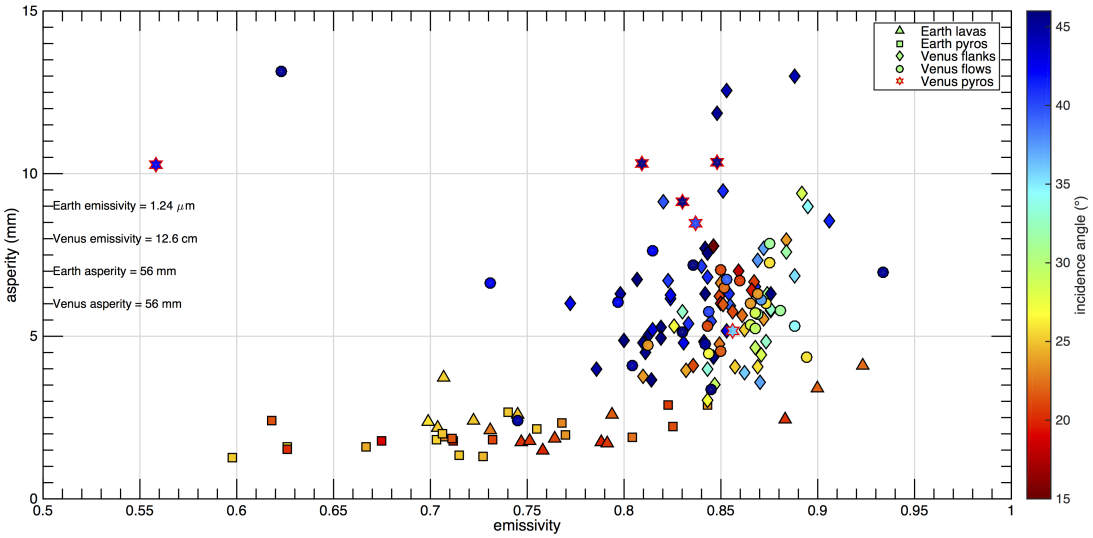

(b)

Figure 3.30: Scatter plots of asperity as a function of emissivity at (a) 126 mm wavelength, and (b) 56 mm wavelength.

3.5 Deposit identification

Given the analyses in sections 3.3 and 3.4, an accurate, globally applicable, method of deposit identification using purely radar data seems implausible. The trend in the terrestrial data that is indicative of a relatively high or low emissivity preference dependent on deposit type observed through the ground-truthing is not apparent here using the potential Venusian examples cited in this study. However, if taken on a region by region basis, there is often sufficient difference to form deposit type inferences locally. For example, the potentially pyroclastic bright halos at Irnini and Anala Montes (Figures 3.4 to 3.6) show slightly elevated e relative to the flank material with which they coincide. This is in addition to the systematically and comparably elevated values of backscatter and all roughness properties (Table 3.4) between these two deposits. This is definitive evidence for a contrast in locally coincident material properties, and when taken in conjunction with the systematically lower densities of the halos, seems like compelling evidence for pyroclastic material.

Using the radar datasets acquired for this study, it is apparent that these observations may not be translatable to other regions e.g. the radar properties of the bright deposits on Tepev Mons' summit do not bear any resemblance to the seemingly visually similar (in the SAR images) deposits at Irnini and Anala Montes. Scathach Fluctus, on the other hand, has properties very similar to those of the halos, with an emissivity of 0.837, σ_0 of 0.038 ($\sim$-14.2 dB), and asperity (at 126 mm) of 11.6 mm (Table 3.8). However, the identification of Scathach Fluctus was aided by its contrast with the anomalously low-e plains upon which it was deposited. The much higher backscatter and lower emissivity displayed at Tepev Mons makes it much less comparable to either Scathach Fluctus or the Irnini and Anala Montes halos, although the roughness appears similar. Even though the backscatter is much higher here, the low emissivity is indicative of a high dielectric mineral phase, resulting in the asperity (roughness) of the deposit appearing very similar as the dielectric constant is important in the scattering behaviour. This could be evidence to suggest that it is pyroclastic in origin, as the

material is texturally similar, and the higher backscatter is simply due to the differing mineralogy at that altitude. This, however, remains somewhat speculative without further evidence. The deposits at Nijole Mons appear to be much smoother than the other possible pyroclastics consistent with the lower backscatter, unlike Scathach Fluctus, which has a similar backscatter to Nijole Mons but appears rougher in terms of asperity. The radar signature at Nijole Mons is therefore inconsistent with the other possible pyroclastics, suggesting an alternative origin such as lava flows.

The range of properties that may possibly be indicative of pyroclastic material according to the examples cited in this study actually differs very little from the vast majority of Venusian surface material, including plains and lava flows (*Ghail and Wilson*, 2013). Therefore, a global identification scheme is problematic, but smaller-scale regional studies can provide much more meaningful conclusions in comparative terms.

3.6 Conclusions

Collecting radar properties of geological surfaces is of immense scientific value in planetary science. The methods and case studies in this chapter have allowed the study of specific regions on Venus, and likely deposit types and relationships to be explored. On Earth, there is the benefit of already knowing the deposit characteristics via ground-truthing and therefore attributing the radar responses to particular deposit types. It was found possible to determine geological relationships on Venus on a case by case basis, where the unique properties of different geological surfaces allowed the styles of volcanic behaviour to be inferred and geological histories to be hypothesised. Evidence has been found to potentially support explosive activity (possible pyroclastic deposits at Irnini, Anala, and Tepev Montes) and recent volcanic activity in the form of young lava flows (dark, high-e flows on Ma'at Mons' northern flank and elevated emissivity coincident with IR anomalies detected by Venus Express at Ganis Chasma). These techniques can be applied to many more regions on Venus to gain further insight into styles and timing of volcanic events on Venus.

The comparative aspect of the chapter, attempting to identify the style of emplacement of volcanic deposits on Venus, is severely hampered by the differing data types. It was found that it is not possible to find definitive comparable trends between the datasets for the two planets due to the effects on the data resulting from the differing instrument wavelengths. It remains unclear whether or not more comparable data will be able to positively identify any trends in the data, however some positive indicators from this work, such as a potentially narrow range of radar properties indicative of Venusian pyroclastic deposits, and the possible high-e lava, low-e pyroclastic trend evident in the Earth data that may be reflected in the Venusian data given better data types such as the more comparable VIRTIS 1.01 μm IR data.

Chapter 4

The distribution of volcanic centres on Venus and Earth

4.1 Introduction

On Earth, the lithosphere, comprising discrete plates of the crust and upper mantle, is being continuously recycled via the process of plate tectonics. Material is added to lithospheric plates at mid-ocean ridges, which are then transported over the weaker asthenosphere to subduction zones where they are destroyed and recycled. Continental crust is less dense than oceanic crust, so continental materials commonly escape subduction. On Venus however, it is proposed that a single global plate constitutes the lithosphere in what is known as a stagnant lid regime (summarised and compared with plate tectonics on Earth in Figure 4.1. In this regime, it is assumed that there is no low-viscosity asthenosphere, but instead elastic, 'rigid' mantle lithosphere passes with increasing depth to high-viscosity convecting mantle material, transitioning when a rheological boundary is crossed (*Solomatov and Moresi*, 1996). This regime inhibits plate motion and requires conduction to be the dominant heat loss mechanism, supplemented by periodic global volcanic resurfacing events (*Turcotte*, 1993). The crust of Venus is hot and buoyant, due to the high surface temperature of ∼730 K (*Taylor*, 2010), and this buoyancy is proposed to prevent it from being subducted (*Anderson*,

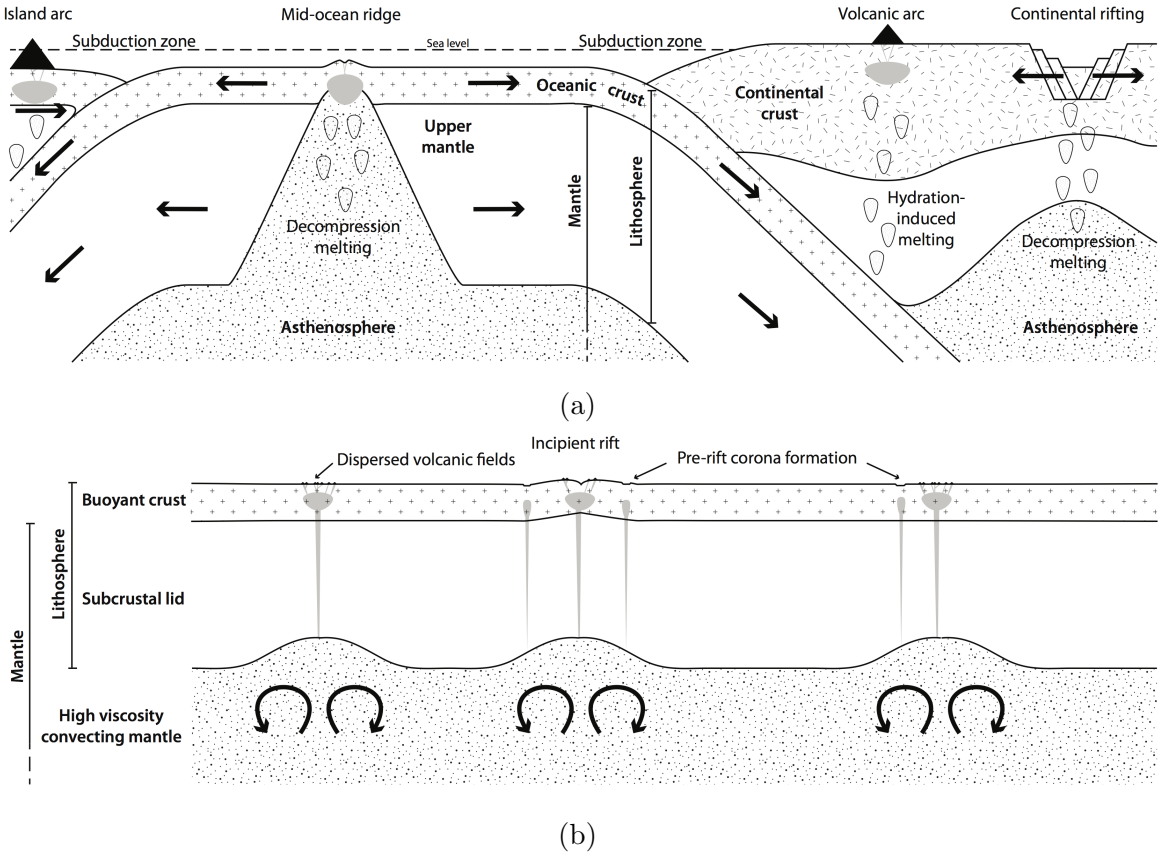

Figure 4.1: Idealised sketch summaries of (a) terrestrial plate tectonics, and (b) a stagnant lid regime on Venus (e.g. *Solomatov and Moresi*, 1996) as discussed in the text. Not to scale.

1981; *Nimmo and McKenzie*, 1998). There is however abundant evidence for tectonic processes in the form of extensional (rifts/faults), and compressional (mountain formation/wrinkle ridges) features (*Ivanov and Head*, 2011, 2015). On Earth, spreading at rifts facilitates decompression melting and migration of magma to shallow crustal depths resulting in volcanic activity at the surface coincident with, or very close to, the rift axis (e.g. *McKenzie and Bickle*, 1988; *Langmuir et al.*, 1992; *Perfit and Davidson*, 2000). However, under a stagnant lid scenario one would not necessarily expect an Earth-like distribution of rift related volcanic features. The currently poorly understood tectonic environment of Venus requires further study in order to fully understand any potential interactions between the underlying Venusian tectonics and volcanism at the surface.

In order to understand the link between surface rifting and volcanism on Venus, the

nature of volcanism must first be characterised. Following the SAR (synthetic aperture radar) data returned from Venus by the NASA Magellan mission in the 1990s, numerous descriptive articles heralded the beginning of our detailed understanding of volcanic features on Venus (e.g. *Guest et al.*, 1992; *Head et al.*, 1992; *McKenzie et al.*, 1992; *Pavri et al.*, 1992; *Stofan et al.*, 1992; *Gregg and Greeley*, 1993, and others). These observations built on the legacy of Earth-based observations as well as the Venera and Pioneer programs. Most notable among these Magellan-based studies in terms of characterising the classification and global cataloguing of features was *Head et al.* (1992). This work classified volcanic edifices ranging from a few km in diameter, commonly occurring in clusters known as shield fields, to immense volcanoes hundreds of km in diameter.

Many of the intermediately-sized volcanoes show a characteristic wide, flat-topped morphology and were classified as steep-sided domes. Some of these display mass-wasting features on their flanks leading to their subclassification as fluted domes. Isolated calderas not associated with an obvious volcanic edifice were also identified and catalogued, as well as another subclassification of intermediately-sized volcanoes known as anemones, which derive their name from the radiating "petal-like" radar-bright lava flows. In addition to volcanoes, *Head et al.* (1992) also catalogue a family of volcano-tectonic features, first described by *Barsukov et al.* (1984), known as coronae, novae, and arachnoids displaying, to a greater or lesser extent, concentric fractures (coronae), radial fractures (novae), or a combination of the two (arachnoids); these features are collectively termed 'coronoids' henceforth in this study.

The wide array of shield and cone volcanoes on Venus occurs in a variety of environments, providing clues as to their method of formation. The largest volcanoes may achieve their large size by virtue of the apparent lack of plate motion concentrating plume activity beneath a particular region of the crust for an extended period of time (*Stofan et al.*, 2001a). They frequently coincide with regional topographic rises and rift junctions (*Stofan et al.*, 1995). The large range of volcanic edifice sizes suggests a correspondingly large range of magnitude of mantle features impinging on the

lithosphere, with the broad geographic distribution interpreted as evidence for mantle plumes more numerous than on Earth (*Stofan and Smrekar*, 2005). The nature of the smallest volcanoes, and their tendency to occur in discrete fields, implies that they may be formed by distinct individual small-scale eruptions occurring over a magma source (*Ivanov and Head*, 2004). They tend to be relatively old features according to the geological history model of *Basilevsky and Head* (1998), predominantly pre-dating the regional plains stratigraphic marker described in *Ivanov and Head* (2004).

Formation mechanisms for the steep-sided and fluted domes are still uncertain, although several theories have been proposed. *Pavri et al.* (1992) proposed two processes of formation, extrusion of an evolved, high viscosity magma, or of a volatile-enhanced basaltic foam. Later work developed a model describing a basaltic lava, with a cooling crust that is continually fracturing and annealing whilst spreading laterally into the distinctive pancake shape (*Stofan et al.*, 2000). It has been previously noted qualitatively that these features commonly occur in clusters (*Pavri et al.*, 1992; *Ivanov and Head*, 1999).

Venus also hosts an apparently unique family of volcano-tectonic features called coronae, novae, and arachnoids. These have attracted a wealth of research into their formation mechanisms and distribution. It has long been suggested that these features occur due to the upwelling of magma diapirs or plumes (*Janes et al.*, 1992; *Squyres et al.*, 1992; *Stofan et al.*, 1992; *Smrekar and Stofan*, 1997). It has been proposed that these may form a genetic continuum; that is, the three distinct forms may be generated by different stages of the same fundamental process, with radial fracturing characteristic of novae associated with mantle upwellings and fracture annuli characteristic of coronae associated with subsequent subsidence (*Stofan et al.*, 1992).

Stofan et al. (2001b) break down the corona population into two subdivisions: type 1 coronae with >50% fracture annuli and the much more poorly defined type 2 coronae with <50% fracture annuli, the former occurring predominantly on rifts and fracture belts and the latter occurring predominantly on the plains. Models of coronae formation range from the delamination and deformation of the lithosphere via magma

upwelling (*Smrekar and Stofan*, 1997), the deformational response of the lithosphere when loaded via magmatic intrusion (*Dombard et al.*, 2007), upwelling-induced crustal convection (*Gerya*, 2014), to ring-like dripping via Rayleigh-Taylor instabilities of a dense layer at the base of the lithosphere at plume margins (*Piskorz et al.*, 2014). Arachnoids are thought to be formed by uplift and relaxation by magmatic diapirs formed over mantle plumes (*Aittola and Kostama*, 2000; *Krassilnikov*, 2002).

The distribution of coronae on Venus has been found to be non-random globally (*Stofan et al.*, 1992; *Squyres et al.*, 1993) with high concentrations noted in the Beta-Atla-Themis (BAT) region (Figures 4.2b & 4.2d) (*Squyres et al.*, 1993), and at mid-latitudes (*Stofan et al.*, 1992). *Martin et al.* (2007), however, found their distribution to be indistinguishable from random within 1,500 km of Parga Chasma (Figures 4.2b & 4.2d). An apparent link between coronae and rift systems is well documented (*Solomon et al.*, 1992; *Baer et al.*, 1994; *Smrekar and Stofan*, 1997; *Martin et al.*, 2007; *Piskorz et al.*, 2014), but has yet to be adequately explained. Arachnoids on the other hand, have previously been noted to tend to cluster on the plains in contrast to novae, which tend to follow sparse chains (*Aittola and Kostama*, 2000). Analysis of a subset of ∼100 coronae carried out by *Krassilnikov et al.* (2012) showed that 97% of the sample pre-dated the regional plains stratigraphic marker, but almost half displayed post regional plain emplacement volcanism, suggesting that coronae may be long-lived features. They also found type 2 coronae to be generally stratigraphically older than type 1 coronae. The late-stage volcanism identified by *Krassilnikov et al.* (2012) is cited as a component of the corona formation model described by *Gerya* (2014).

The geological history of Venus, the backdrop and context to volcanism on Venus, has been widely investigated. The model of planetary geological evolution described in *Basilevsky and Head* (1998), and subsequently extended (*Basilevsky and Head*, 2000a, 2002; *Ivanov and Head*, 2011, 2013, 2015), proposes a series of global epochs characterised by distinct geological regimes, with each period representing a globally synchronous stratigraphic marker characterised by the dominant volcanic/tectonic activity. This 'directional' model has however been challenged; *Guest and Stofan* (1999) cite nu-

merous examples evident in the Magellan data that suggests that these markers are not necessarily globally synchronous and may have been formed over longer periods, and more dispersed through time in a 'non-directional' model.

Although both models may have their merits, this study does not assume one or the other to be the case outright, and the results are examined for insights into this ongoing discussion. In the following work, spatial analysis is used to explore the relationships between volcanic and tectonic features, as a test of these models.

Former studies of the distribution of volcanism on Venus have generally been global (e.g. *Head et al.*, 1992; *Crumpler and Aubele*, 2000; *Canon-Tapia and Mendoza-Borunda*, 2014). However this work focuses on the region of most intense rifting, i.e., the BAT region. This region of Venus is a large, roughly triangular, area following three large rift zones connecting Beta, Atla, and Themis Regiones at the corners (Figure 4.2b). Focusing on this region allows us to highlight in more detail the spatial relationships within this key region of Venus. The area is well mapped and the volcanic features have been catalogued (*Head et al.*, 1992; *Crumpler and Aubele*, 2000; *Stofan et al.*, 2001b), and it includes a region of proposed currently active volcanism (*Shalygin et al.*, 2015). Although the exact mechanisms of rift formation are poorly understood, there does appear to be a broad correlation of rift features with enhanced volcanism (*Campbell et al.*, 1984).

The BAT rifts are zones characterised by extension, suggesting that they formed in association with mantle upwelling beneath the lithosphere, which drove volcanism at the surface. Actively diverging plate motion will not be as important on Venus, as the lack of subduction zones results in a corresponding lack of slab-pull force. A consequence of this is the requirement for another mechanism to bring magma to the surface, such as active plume-driven spreading. How the various types of volcanic features described in *Head et al.* (1992) are distributed with respect to the rifts, and to each other, may help to elucidate how and when the processes at depth resulting in these features occur.

In this study the spatial and temporal relationships between volcanic features on

Venus' surface are investigated, how they are organised with respect to each other and with respect to regions of rifting. The following is focused upon: can the distribution of volcanic features on the surface of Venus inform us of (1) internal driving volcano-tectonic processes, and (2) the directional/non-directional nature of Venus geology?

4.2 Methods

4.2.1 Data sources and mapping

The base geospatial environment onto which the volcanic features and rift zones are mapped is the Cycle 1 SAR radar maps retrieved by the NASA Magellan mission and resampled to 75 m resolution. The study area is defined as 40°N to 50°S and 90°E to 310°E, to capture the full BAT region. ArcGIS 10.0 was used to process the mapping and analysis.

In order to define the locations of the volcanic features prior to geospatial analysis, the coordinates from existing volcano databases were used. On Venus, certain mapping conventions needed to be decided upon to resolve conflicting definitions and incomplete data in the existing maps and databases outlined below. The volcano-tectonic feature catalogue of *Crumpler and Aubele* (2000), including all the features mapped in *Head et al.* (1992), was reduced down to the areal extent of the study region and added to the base map. Subsequently, the more comprehensive database of coronae outlined in *Stofan et al.* (2001b) was added to these data resulting in numerous conflicting classifications. Resolving this followed the convention of allowing the latter definitions to supersede the former, while retaining the former's definitions when they were absent from the latter database. In addition to these data, other observed features absent from both databases were included in order to expand the hybrid database. These additional features include previously unidentified, or for some other reason omitted, structures of all types shown in Figure 4.2d with the exception of fluted domes and calderas.

Shield volcano size classifications are defined based on their diameter as Large ($\geq$100 km), Intermediate ($\geq$20 km to <100 km), and Small (<20 km). Small volcanoes are so

numerous that they are not tabulated in the database unless they occur within shield fields, which are included as single entries. As the original database is only accurate to the nearest 0.5°, each point was subsequently centred on the feature in question. The rift sections were mapped onto the base map using the classification in *Krassilnikov et al.* (2012) incorporating old (pre-dating regional plains unit), and young (post-dating regional plains unit) rifts according to previously defined stratigraphic relationships (*Basilevsky and Head*, 2000a) and stored as polyline vector datasets. The rifts were mapped in this manner in order to gain a complete representation of rifts in the region in a way that could be used to test the concepts inherent to the directional model.

4.2.2 Analytical techniques

Once the volcanic features have been mapped, spatial analysis allows quantification of geospatial relationships to answer the following questions: 1) how do certain volcanic features occur relative to others of their own kind, 2) how do they occur relative to features of other kinds, and 3) how do they occur relative to rift axes?

The nearest neighbour index (NNI) was calculated for each type of volcanic feature. This quantity determines the ratio of the observed mean distance between points (D_O) to the expected mean distance between points in a random distribution (D_E). An NNI of 1 indicates a random distribution, while NNI>1 or <1 are indicative of, respectively, either more dispersed or more clustered distributions (*Mitchell*, 2005a). Previous applications of this method to analyse the clustering of geospatially-referenced data include the analysis of earthquakes in the Red Sea (*Al-Ahmadi et al.*, 2014). Equations 4.1 to 4.3 describe how ArcGIS 10.0 calculates the NNI,

$$NNI = \frac{D_O}{D_E} \tag{4.1}$$

$$D_O = \frac{\sum_{i=1}^{n} d_i}{n} \tag{4.2}$$

$$D_E = \frac{0.5}{\sqrt{\frac{n}{A}}} \tag{4.3}$$

where d_i is the distance between point i and its nearest neighbour, n is the number of points, and A is the total area of the study region. As a point of reference for each NNI calculated, 20 random distributions of points for each sample size, over the same area, was generated using the ArcGIS built-in algorithm, along with their own calculated NNI values. The mean random NNI for each sample size was calculated for comparison with the real populations with the corresponding sample size. In addition to calculating the NNI for each feature type, the distance to nearest neighbour value for each point, in both the observed and random datasets, was also stored so that the population distribution histograms could also be produced. Of the 20 simulated distributions, the one with the NNI closest to NNI=1 (true random) was selected for this purpose.

To determine the features' relationship with the rift axes, the distance of each feature point on the map from the nearest rift was measured in order to identify any preferred distance from, or affinity for, occurring near rifts. These distances were measured once more with just the distance to the young rifts considered. Population distribution histograms were also produced for these data as well as the corresponding results recorded using the previously selected random datasets for comparison.

In order to display on the map where any clustering may be concentrated, feature kernel density maps were produced. This was achieved using the number of similar features within a given search radius (10^3 km) from each point, giving a unique value to each cell (gridded to 5 km) as a measure of feature density. When displayed using a colour ramp, the density magnitude per cell (in features per km^2) for each feature type is then projected onto the base map in order to produce the feature density layer.

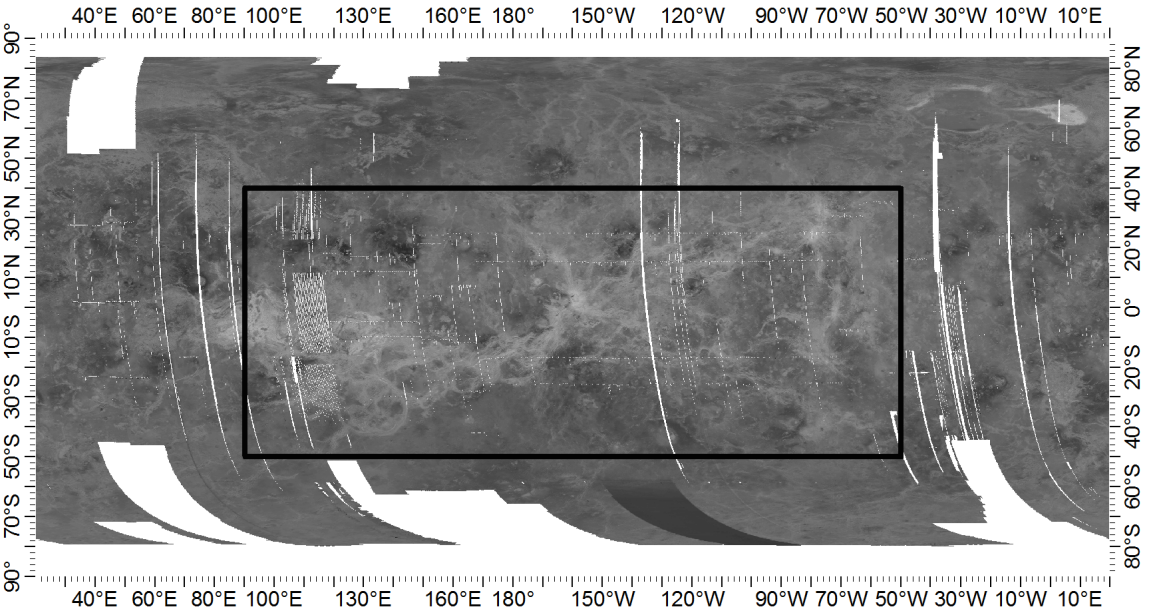
40°E 60°E 80°E 100°E 130°E 160°E 180° 150°W 120°W 90°W 70°W 50°W 30°W 10°W 10°E
90° 70°N 50°N 30°N 10°N 10°S 30°S 50°S 70°S 90°
80°N 60°N 40°N 20°N 0° 20°S 40°S 60°S 80°S

(a)

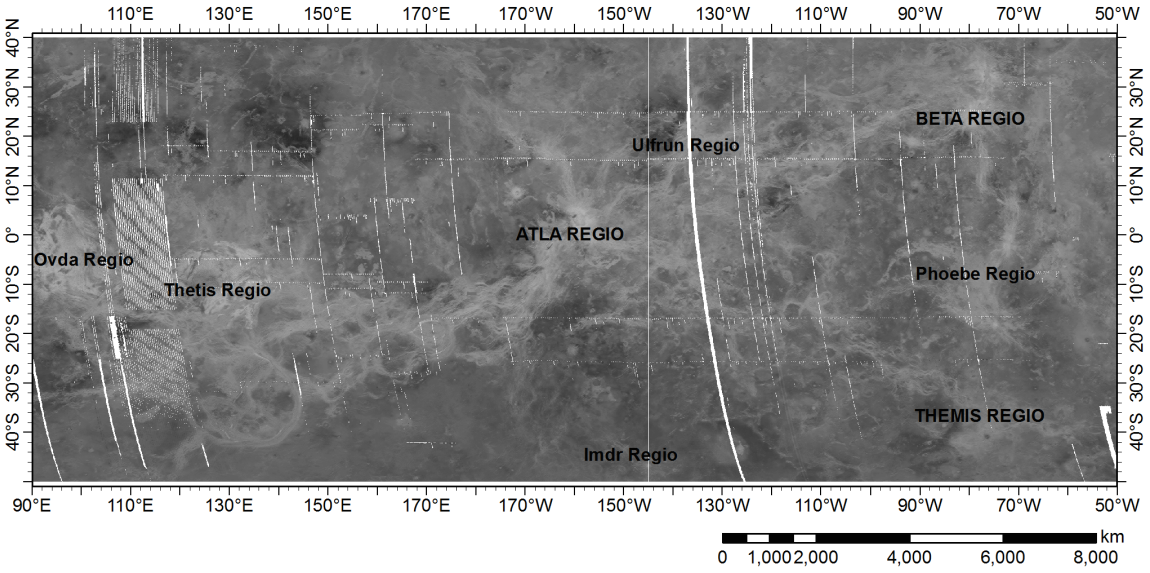
110°E 130°E 150°E 170°E 170°W 150°W 130°W 110°W 90°W 70°W 50°W
40°N 30°N 20°N 10°N 0° 10°S 20°S 30°S 40°S
BETA REGIO
Ulfrún Regio
ATLA REGIO
Ovda Regio
Thetis Regio
Phoebe Regio
THEMIS REGIO
Imdr Regio
km
0 1,000 2,000 4,000 6,000 8,000

(b)

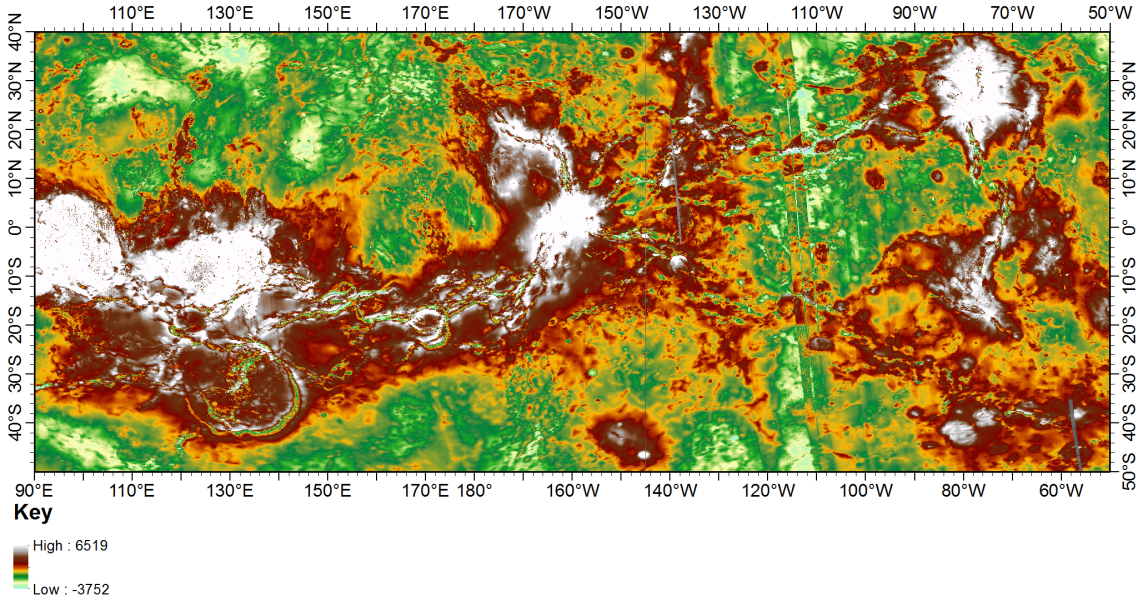

(c)

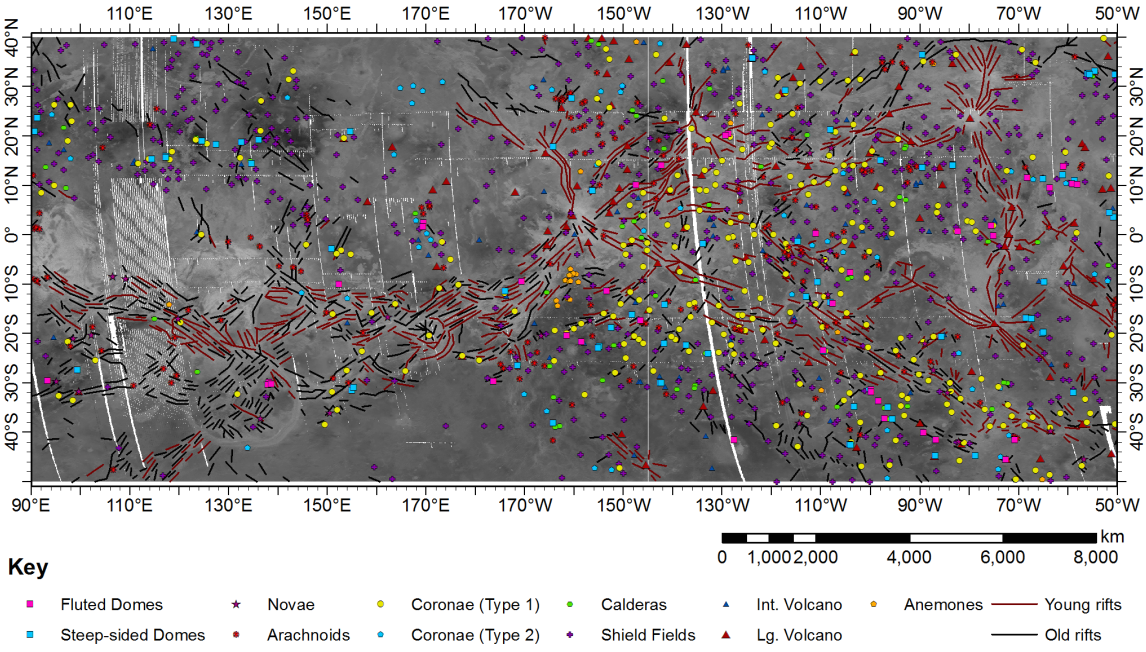

(d)

Figure 4.2: (a) Global Magellan SAR map of Venus, box marks the BAT (Beta-Atla-Themis) region which is the focus of this study, (b) detail of the BAT study region on Venus with named regions as referenced in the text, (c) topography of the BAT study region in metres with shading relative to the MPR, and (d) mapped rifts and volcano-tectonic features within the BAT region described in Section 4.1. The shading in (a), (b), and (d) describes variation in SAR backscatter. SAR and topography data, NASA/JPL.

4.3 Results

The NNI values for the volcanic feature datasets described in Section 4.2.2 are shown as the red crosses in Figure 4.3, sorted into their respective family groups as described in the key. Note that they fall predominantly in the lower half of the plot. With the exception of Group III, all the observed datasets fall, to a greater or lesser degree, comfortably outside the range of random distributions and within the 'clustered' field, statistically significant at $p = 0.05$. The blue dots represent the NNI values from the 20 simulated random distributions; their associated mean values are shown as the black circles. All the mean simulated random NNI values fall between 1 and 1.22, indicating a tendency of truly random distributions to appear slightly dispersed, given the small sample sizes. Table 4.1 shows the sample sizes and NNI for all the feature classes.

The magnitude to which random populations with smaller values of n fall in the 'dispersed' field can be shown to be dependent on the value of n as shown in Figure 4.4. The tendency for the volcanic feature data to fall clearly within the 'clustered' field, even given this skew towards NNI$>$ 1, accentuates the non-random nature of these population distributions.

Figure 4.5 shows the histograms of nearest neighbour distances for all feature types (grey) overplotted with the histograms of the random populations selected from the 20 examples to have an NNI nearest to NNI = 1 (blue). In most cases these best fit a gamma or exponential distribution, although some of the random populations are indistinguishable from a normal distribution. With the exception of shield fields and large volcanoes, the peaks of the observed frequency distributions always occur

Table 4.1: Sample size, mean random NNI (for a sample set of the same size), and observed NNI values for all feature classes as shown in Figure 4.3.

	Fluted domes	SS domes	All domes	Novae	Arachnoids	Coronae (1)	Coronae (2)	Coronae (1 & 2)	Coronoids	Calderas	Int. volcanoes	Shield fields	Large volcanoes	Anemones
n	38	74	112	29	171	250	53	303	503	57	70	531	109	22
NNI obs.	0.715	0.725	0.608	0.738	0.680	0.866	0.745	0.849	0.841	0.717	0.915	0.963	1.017	1.064
NNI ran.	1.175	1.105	1.072	1.149	1.061	1.049	1.110	1.042	1.028	1.131	1.135	1.031	1.058	1.217

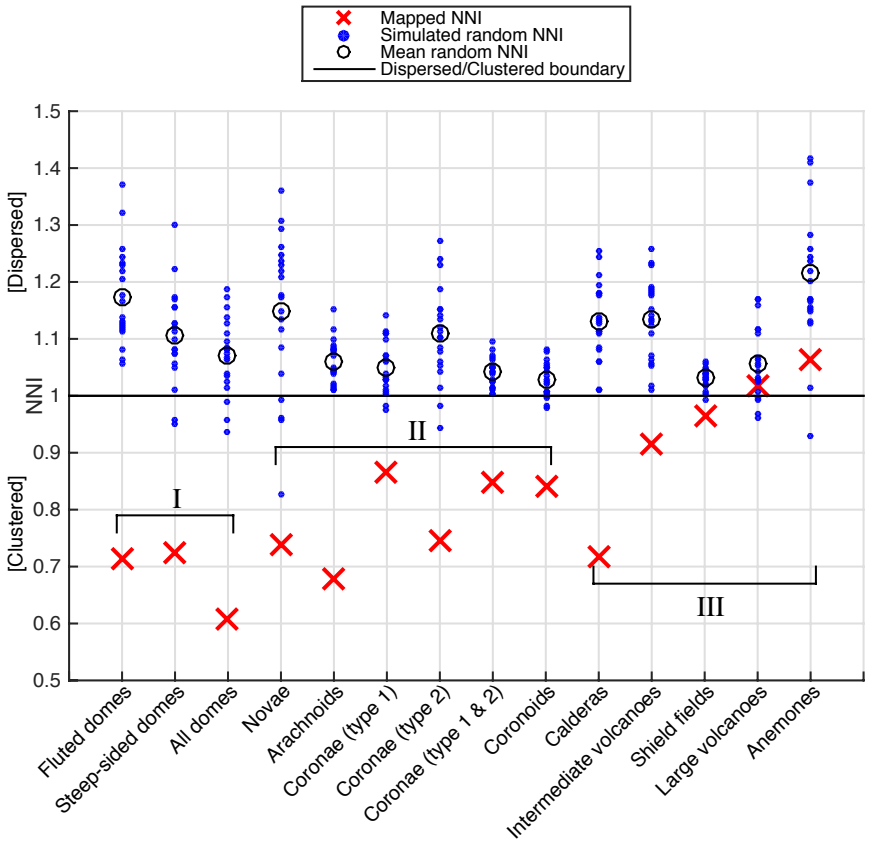

Figure 4.3: NNI values for mapped Venusian volcanic feature datasets (red crosses) and the results of 20 random distribution simulations of sample sizes corresponding to the feature dataset with which it is plotted (blue dots). Black circles represent mean values from the random datasets. The classifications I-III refer to the 'Dome', 'Coronoid', and 'Volcano' families.

at smaller nearest neighbour distances than those of the random distributions, again indicative of a tendency for clustering.

Figures 4.6 and 4.7 show the histograms of distance to nearest rift (both red and black lines in Figure 4.2d), and separately for distance to nearest post-plains rift (red lines only in Figure 4.2d) as interpreted by *Krassilnikov et al.* (2012) according to previously defined stratigraphic relationships (*Basilevsky and Head*, 2000a), for each volcano-tectonic feature class along with fitted frequency distribution curves. All distributions fit an exponential distribution and show the affinity for and/or preferred distance from the rift axes identified in Figure 4.2d.

Figure 4.3 groups the volcanic features of Venus into broader families, namely:

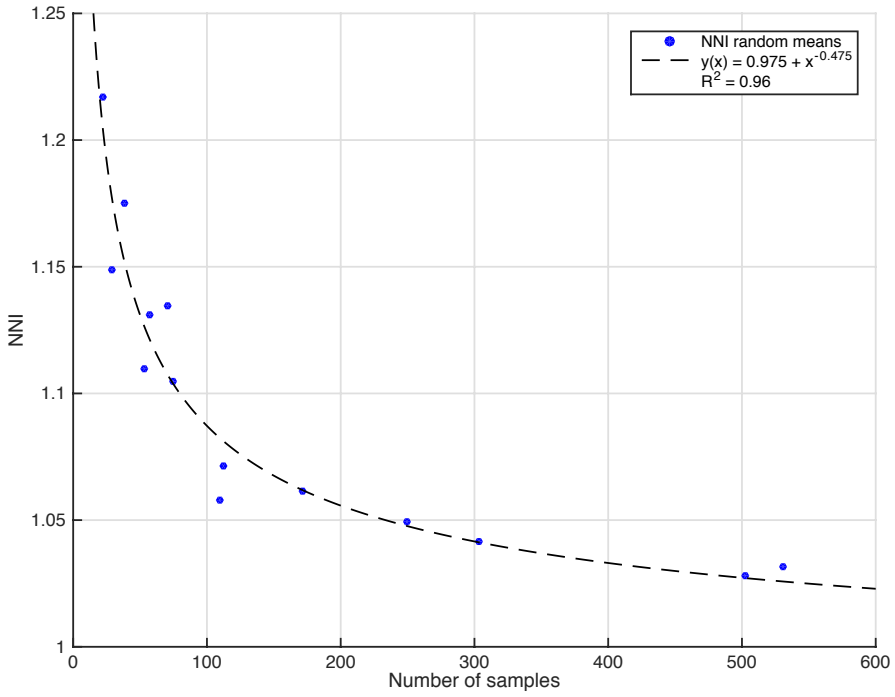

Figure 4.4: Plot of NNI against sample size for randomly generated point distributions. These data best fit a curve with the exponential equation $y(x) = 0.975 + x^{-0.475}$, giving a maximum $R^2 = 0.96$. Best-fit curve selected based this R^2 value. The intercept is not quite 1 as would be expected due to the lack of high-n data sets.

'Domes' (I), 'Coronoids' (II), and 'Volcanoes' (III), which share certain distribution characteristics:

Group I. This first group comprises the steep-sided and fluted domes. They show clear similarities in terms of their strong clustering, each displaying low NNIs of ∼0.72; when considered together as a single grouping they have an NNI of ∼0.6 (Figure 4.3). The exponential nearest neighbour frequency distribution and its large deviation from the normal and gamma distributions of the random populations (Figure 4.5a) highlight this strong tendency to occur in clusters, which is also evident on inspection of the feature density maps in Figure 4.8. It is likely that the features in this group share similar formation mechanisms; together, they represent a distinct sub-group in the database and warrant classification and analysis as a group feature set.

Both dome types show rift distance frequency distribution curves almost identical to the random distribution curves (Figures 4.6a and 4.7a), however Figure 4.8 indicates

that there could be some tendency to occur near-rift. Closer inspection of Figure 4.6a reveals a possible deviation from the random distribution ($\lesssim$100 km) when distance to any rift is considered, however it is slight and disappears completely where distance to post-plains rifts is considered (Figure 4.7a).

Group II. This group comprises the features making up the coronoids: the coronae, novae, and arachnoids. Figure 4.3 shows that this group is marginally more dispersed as a family compared to Group I, whilst still being strongly clustered, most notably the arachnoids (also see Figures 4.5b(ii) and 4.9b). Histograms in Figure 4.5b are more similar to the random distribution than the domes, however peaks in the data show that individual features are consistently closer to their nearest neighbours in general than the randomly generated data. The Novae (Figures 4.5b(i) and 4.9a) tend to cluster into loosely linear groupings, as opposed to discrete clusters. The type 1 coronae appear to be randomly distributed on a small scale, but are clustered across the BAT region at a large scale (Figure 4.9c).

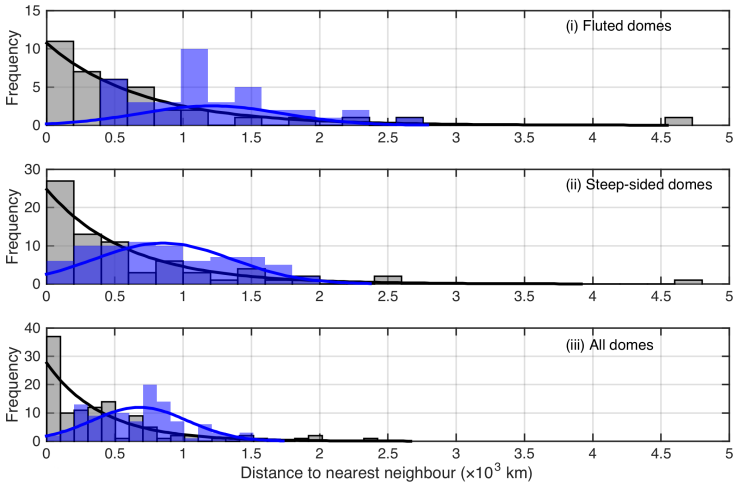
(i) Fluted domes
(ii) Steep-sided domes
(iii) All domes
Frequency
Distance to nearest neighbour (×10^3 km)

(a)

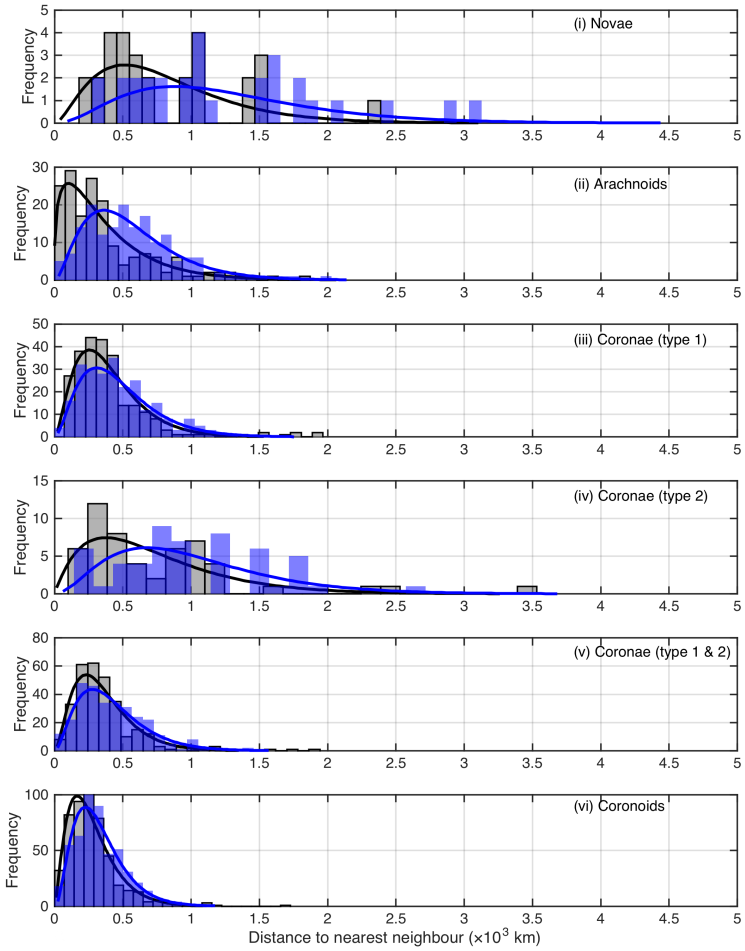
(i) Novae
(ii) Arachnoids
(iii) Coronae (type 1)
(iv) Coronae (type 2)
(v) Coronae (type 1 & 2)
(vi) Coronoids
Frequency
Distance to nearest neighbour (×10^3 km)

(b)

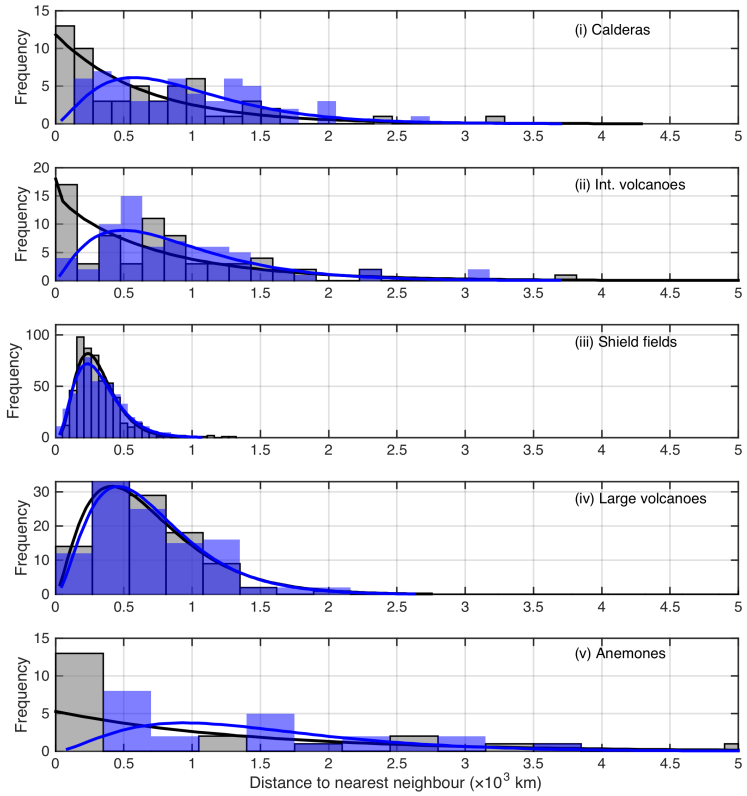

(c)

Figure 4.5: Frequency distribution histograms of distance to nearest neighbour for (a) Group I, (b) Group II, and (c) Group III, feature types as defined in Figure 4.3 and mapped in Figure 4.2d. Grey bars show the observed values with the blue bars representing the randomly distributed population closest to NNI = 1 of the same sample size distributed over the same area as each figure. Distributions are shown with gamma, exponential, or normal distribution curves as determined by best-fit to the data; black and blue curves correspond to the observed and random data respectively. All data are plotted on figures of a fixed x-axis interval width up to 5000 km to enable comparison between different datasets. Where the ranges of the datasets differ between the random and observed values, the random values are binned to intervals to match those of the observed data, rather than maintaining the same number of bins overall. This, as well, is intended to enable comparison between datasets. The y-axis data were fitted to plots of equal height to highlight the trends observed in the population distributions, rather than the absolute number of features.

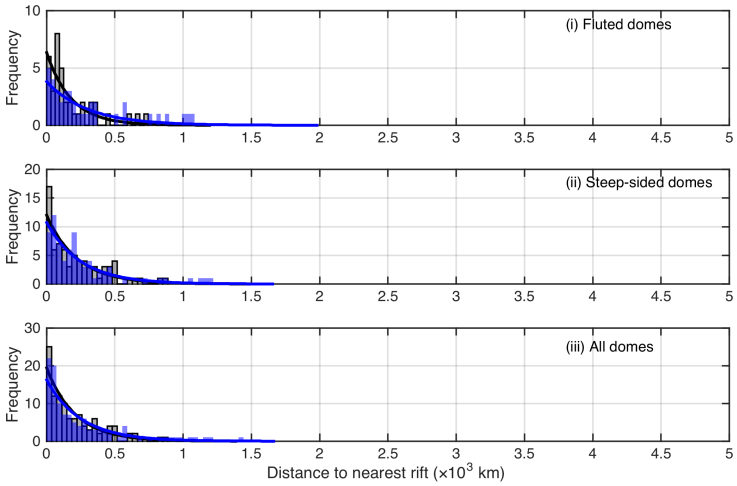
(i) Fluted domes
(ii) Steep-sided domes
(iii) All domes
Frequency
Distance to nearest rift (×10^3 km)

(a)

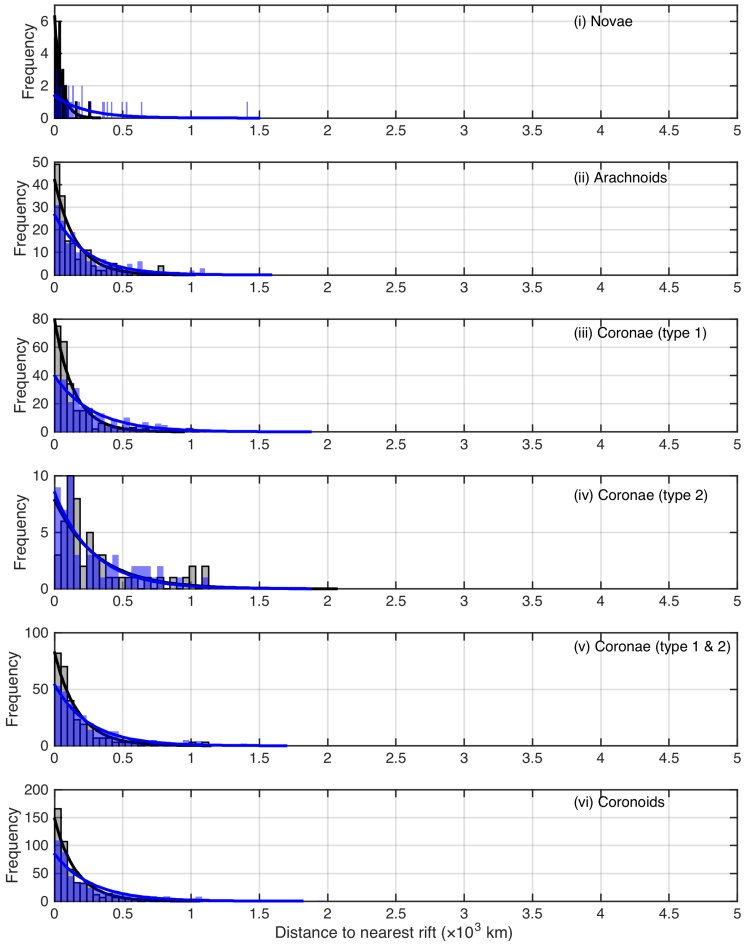
(i) Novae
(ii) Arachnoids
(iii) Coronae (type 1)
(iv) Coronae (type 2)
(v) Coronae (type 1 & 2)
(vi) Coronoids
Frequency
Distance to nearest rift (×10^3 km)

(b)

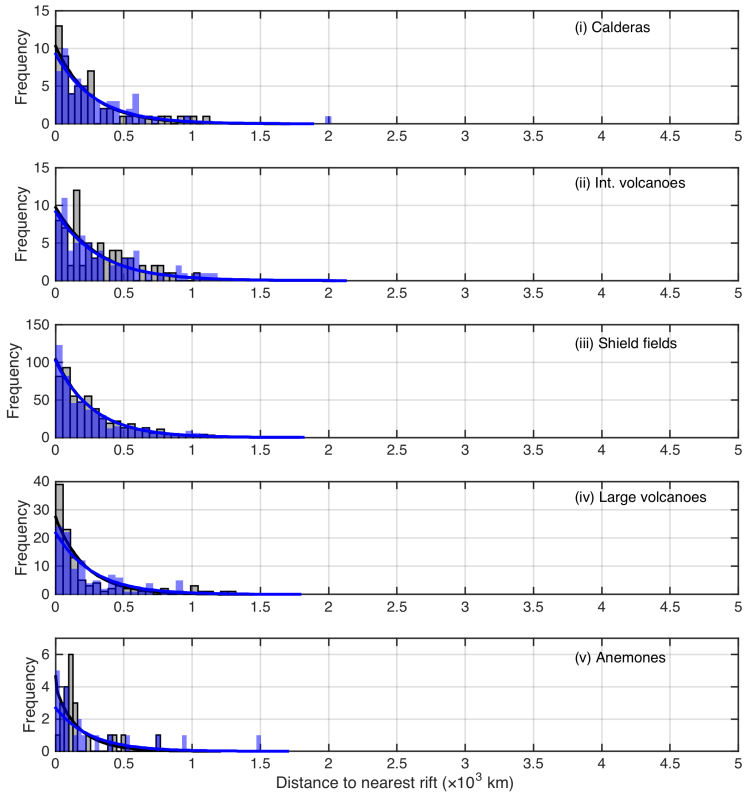

(c)

Figure 4.6: Frequency distribution histograms of distance to nearest rift for (a) Group I, (b) Group II, and (c) Group III, feature types as defined in Figure 4.3 and mapped in Figure 4.2d. Grey bars show the observed values with the blue bars representing the randomly distributed population closest to NNI = 1 of the same sample size distributed over the same area as each figure. Distributions are shown with gamma, exponential, or normal distribution curves as determined by best-fit to the data; black and blue curves correspond to the observed and random data respectively. All data are plotted on figures of a fixed x-axis interval width up to 5000 km to enable comparison between different datasets. Where the ranges of the datasets differ between the random and observed values, the random values are binned to intervals to match those of the observed data, rather than maintaining the same number of bins overall. This, as well, is intended to enable comparison between datasets. The y-axis data were fitted to plots of equal height to highlight the trends observed in the population distributions, rather than the absolute number of features.

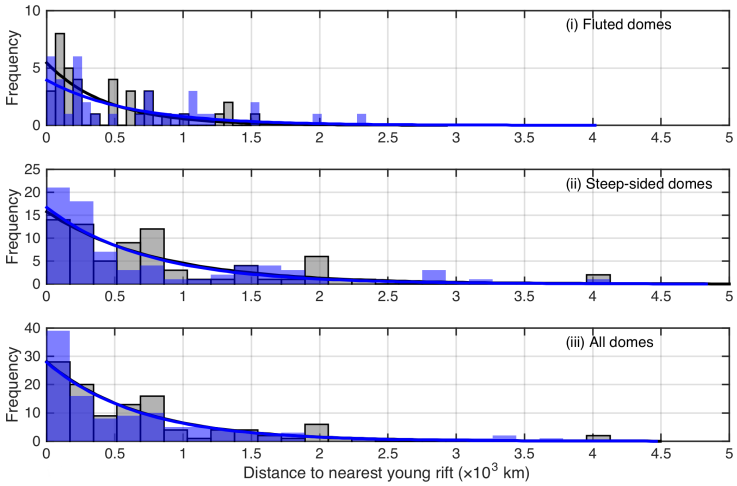
(i) Fluted domes
(ii) Steep-sided domes
(iii) All domes
Frequency
Distance to nearest young rift (×10^3 km)

(a)

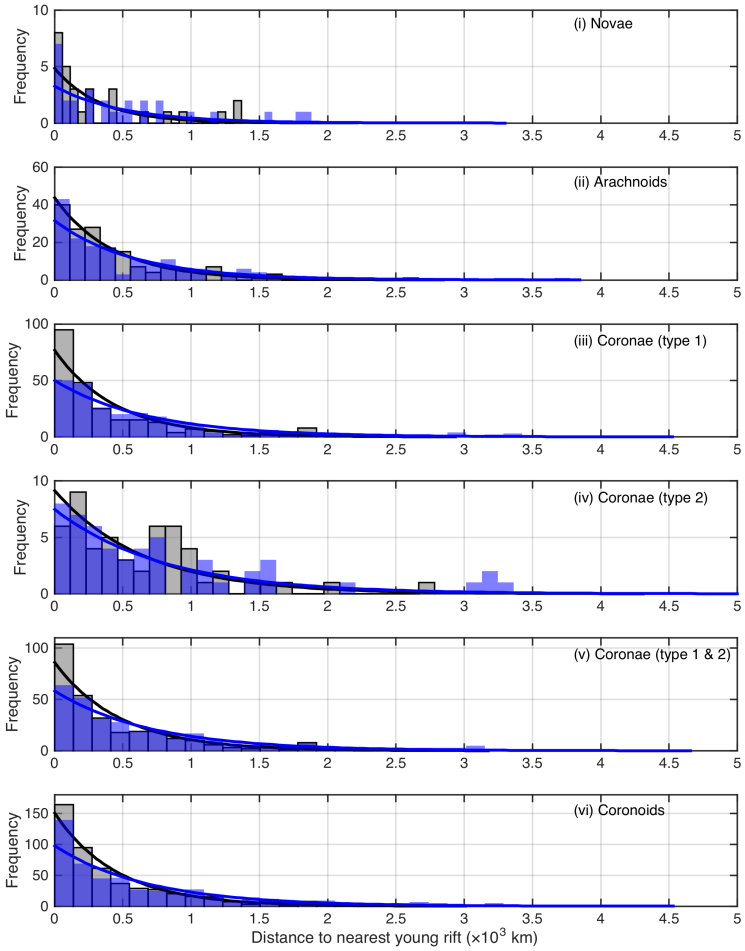
(i) Novae
(ii) Arachnoids
(iii) Coronae (type 1)
(iv) Coronae (type 2)
(v) Coronae (type 1 & 2)
(vi) Coronoids
Frequency
Distance to nearest young rift (×10^3 km)

(b)

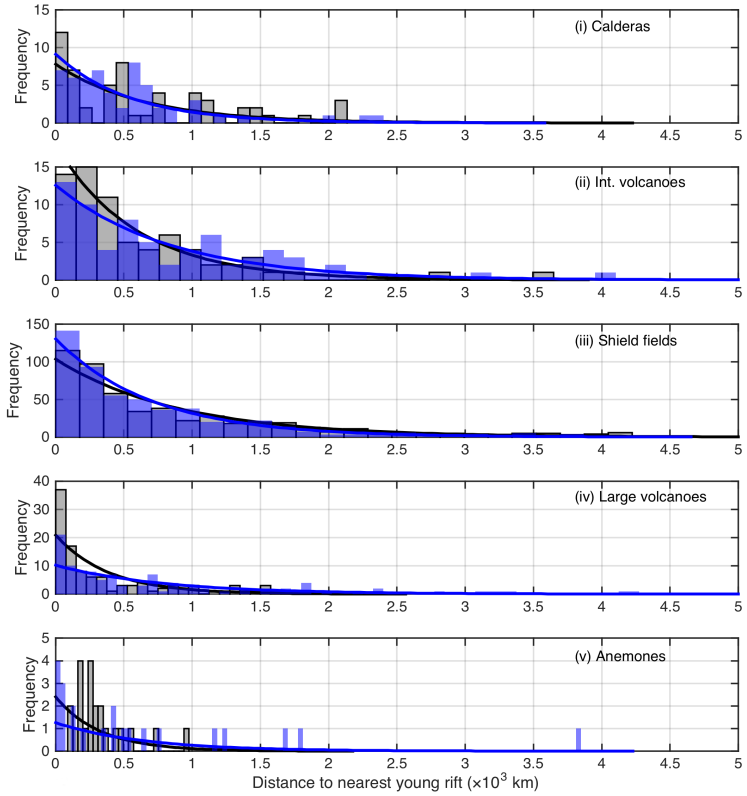

(c)

Figure 4.7: Frequency distribution histograms of distance to nearest post-plains rift as interpreted by *Krassilnikov et al.* (2012) according to previously defined stratigraphic relationships (*Basilevsky and Head*, 2000a) for (a) Group I, (b) Group II, and (c) Group III, feature types as defined in Figure 4.3 and mapped in Figure 4.2d. Grey bars show the observed values with the blue bars representing the randomly distributed population closest to NNI = 1 of the same sample size distributed over the same area as each figure. Distributions are shown with gamma, exponential, or normal distribution curves as determined by best-fit to the data; black and blue curves correspond to the observed and random data respectively. All data are plotted on figures of a fixed x-axis interval width up to 5000 km to enable comparison between different datasets. Where the ranges of the datasets differ between the random and observed values, the random values are binned to intervals to match those of the observed data, rather than maintaining the same number of bins overall. This, as well, is intended to enable comparison between datasets. The y-axis data were fitted to plots of equal height to highlight the trends observed in the population distributions, rather than the absolute number of features.

The histograms in Figure 4.6b show another important distinction of Group II compared with Group I, where Group I features may be showing some tendency to occur near-rift with a slight tendency to deviate from the random distribution, Group II features display a much stronger deviation in the form of steepening of the distribution curve away from the random distribution. This is seen most strongly for the novae (Figure 4.6b(i)) but is also observed for the arachnoids and type 1 coronae (Figures 4.6b(ii-iii)). Type 2 coronae are an exception and seem to occur off-rift and somewhat clustered (Figure 4.9d), as previously noted by *Stofan et al.* (2001b). The coronoids' general occurrence very close to or on rifts indicates a close link between this type of volcanic feature manifesting at the surface and the spatial association with the rifts. Figure 4.9 shows the feature density maps for Group II, highlighting the grouping characteristics and tendency to occur on-rift.

Group III structures are a more morphologically diverse group, with isolated calderas and volcanoes ranging in size from small volcanoes below the imaging resolution of the radar to features of up to >1000 km in diameter.

Calderas are distributed as shown in Figure 4.10a. There is some clustering, with an NNI of ∼0.72 and a significant jump in the histogram at a nearest neighbour distance of <250 km showing ∼40% of all calderas occurring at least this close to another caldera (Figure 4.5c(i)). Figure 4.10a also shows that, like the domes, most calderas lie in a near-rift setting. The tendency to occur in groups could be indicative of their occurrence over off-rift plumes, with one or two rare on-rift exceptions. The distance from rift data, in terms of both all rifts and young rifts, is indistinguishable from random, indicating a formation completely independent of rift location. Their location on both the older shield plains as well as more stratigraphically recent regional and lobate plains units (*Ivanov and Head*, 2015) suggests that these were not temporally restricted to any particular period of relative timing, and continued to form throughout the proposed transition in volcano-tectonic regime. The structure of these calderas, featuring faulting and subsidence, implies a tectonic component caused by the removal of a magma source suggests that shallow bodies of magma may have continued to affect

surface features throughout the regional plains emplacement.

The intermediate (≥20 km to <100 km diameter) volcanoes seem to display properties of both dispersed and clustered behaviour (Figures 4.5c(ii) and 4.10b) with the histogram resembling a normal distribution with the addition of a moderately high peak of 17 features (∼24%) occurring within ∼165 km of another intermediate volcano. Comparison of Figures 4.8c and 4.10b shows some similarity in the general distribution of all intermediately sized volcanic features (combining domes and intermediate volcanoes). The majority appear to occur close to, rather than on, rifts. Figure 4.6c(ii) illustrates this with the striking peak in the data at ∼160 km, a trend echoed in the fluted dome data (Figure 4.6a(i)) suggesting that these intermediately sized features may form via some rift related, albeit off-rift, mechanism.

The shield field histograms (Figures 4.5c(iii), 4.6c(iii), and 4.7c(iii)) show nearest neighbour and distance from rift distributions indistinguishable from random. However, in terms of clustering, Figure 4.5c(iii) may mask some distribution characteristics observed in Figure 4.10c where, for example, the signals from the more dispersed eastern portion of the study area and the more clustered western portion of the study area are lost when considered together. The vast majority of shield fields occur on the pre-regional plains 'shield plains' stratigraphic unit as proposed in the directional model of Venus geology (*Ivanov and Head*, 2011, 2013, 2015), in areas remaining unaffected by the regional plains emplacement along with the old rift features with which they commonly coincide.

The large (≥100 km diameter) volcanoes show a distribution almost identical to the randomly generated sample (Figure 4.5c(iv)), however inspection of Figure 4.10d suggests this may be due to the same 'actual' distribution dichotomy that affects the shield fields, that is, both dispersed and clustered sub-populations. The distance from all rifts data in Figure 4.6c(iv) displays a subtle divergence from the random sample due to a large spike in the leftmost bin with 39 large volcanoes (∼35%) occurring within ∼50 km of a rift segment. This deviation from random is even more prominent when young rifts are concerned (Figure 4.7c(iv)) suggesting a closer association with

the most recently active rift geometry. The large volcano classification encompasses a rather broad size range (100-1000 km diameter), so a new subclassification, very large volcanoes, is shown in Figure 4.10e. This subclass shows a strong a tendency to occur closer to the most recent rift features with, of the 17 very large volcanoes, 11 (around $^2/_3$) occurring within 200 km, and 13 (around $^3/_4$) occurring within 350 km, of a young rift segment. It is a small dataset however.

Due to the small sample size, it is hard to derive any spatial relationships in the anemone dataset (Figures 4.5c(v), 4.6c(v), 4.7c(v), and 4.10f), although strong clustering is evident in one particular location (south Beta Regio). The dispersed nature of the other anemones makes the NNI and distribution analysis somewhat meaningless in this case and have simply been included out of a sense of completeness.

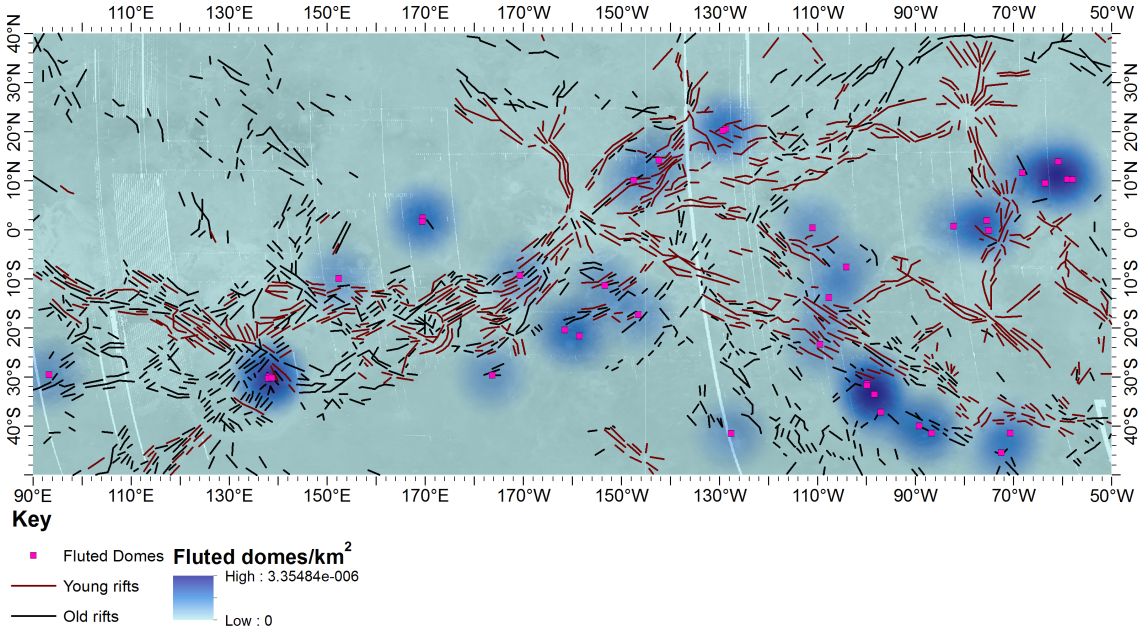
110°E
130°E
150°E
170°E
170°W
150°W
130°W
110°W
90°W
70°W
50°W
40°N
30°N
20°N
10°N
0°
10°S
20°S
30°S
40°S
Key
Fluted Domes
Young rifts
Old rifts
Fluted domes/km2
High : 3.35484e-006
Low : 0

(a)

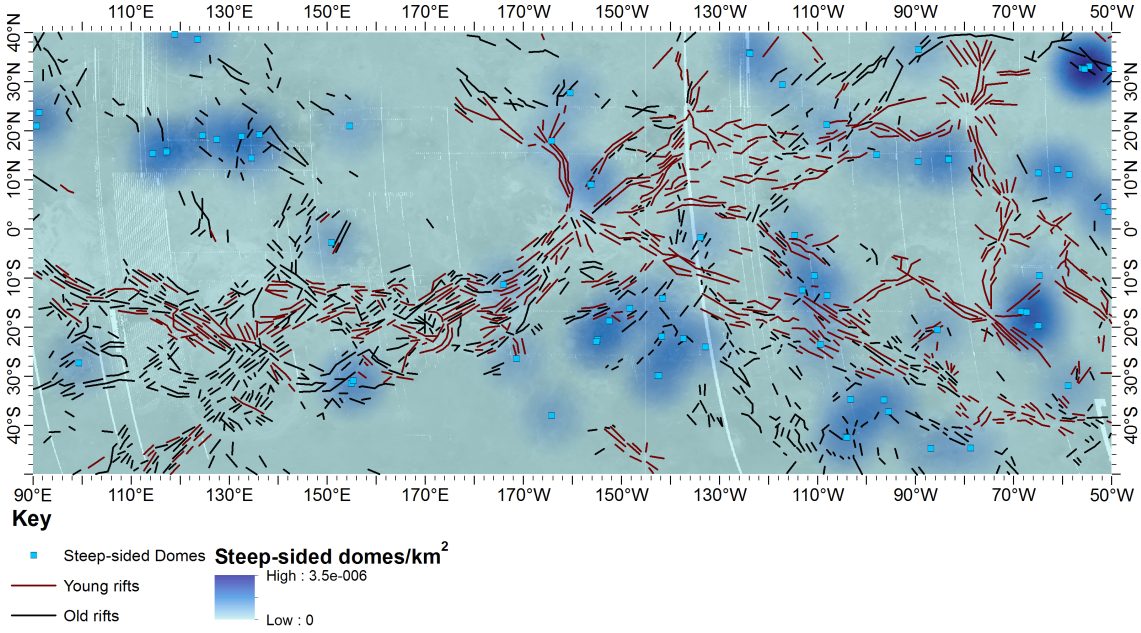
110°E
130°E
150°E
170°E
170°W
150°W
130°W
110°W
90°W
70°W
50°W
40°N
30°N
20°N
10°N
0°
10°S
20°S
30°S
40°S
Key
Steep-sided Domes
Young rifts
Old rifts
Steep-sided domes/km2
High : 3.5e-006
Low : 0

(b)

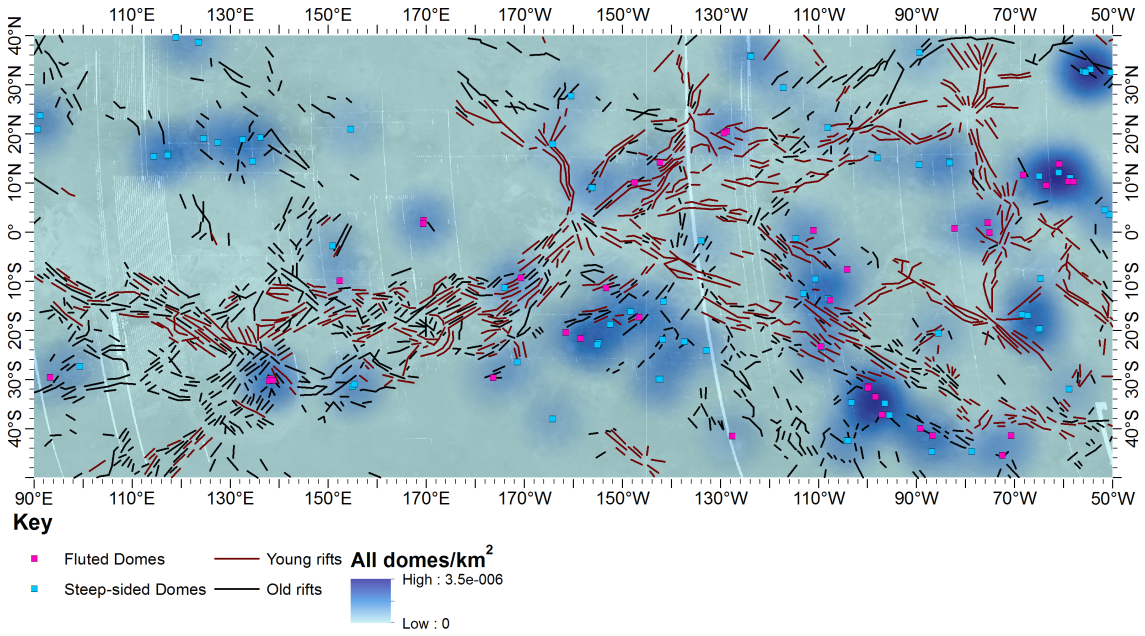

(c)

Figure 4.8: Feature density map for (a) fluted domes, (b) steep-sided domes, and (c) the dome family (Group I as defined in Figure 4.3). Points represent individual domes. The intensity of the shading of the cell surrounding each point indicates the density in points per km^2 within that cell.

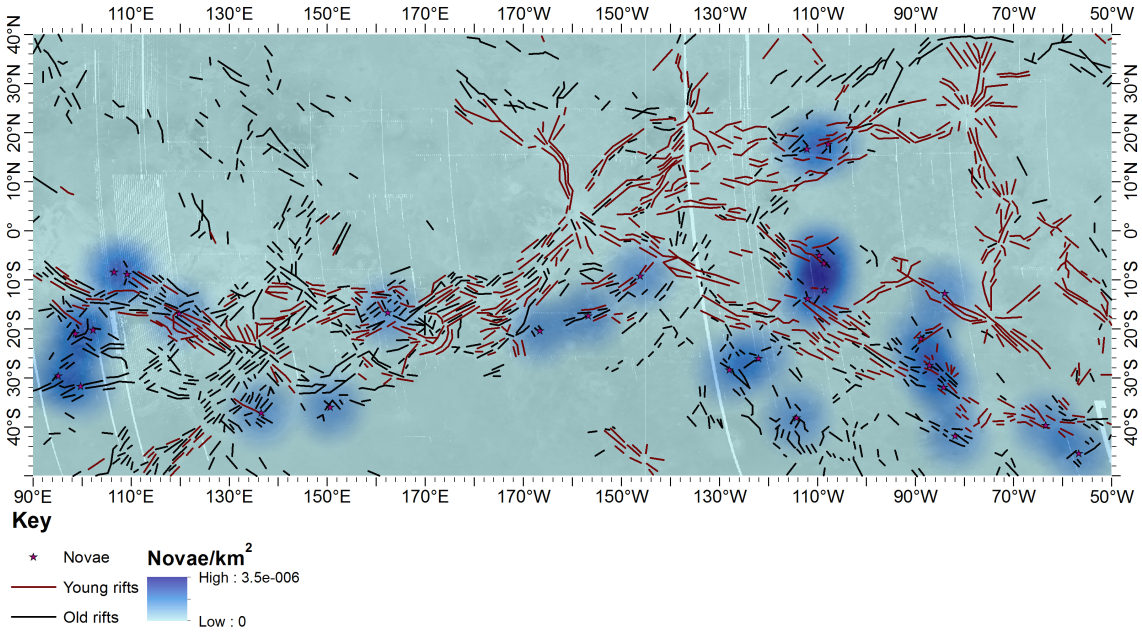
110°E
130°E
150°E
170°E
170°W
150°W
130°W
110°W
90°W
70°W
50°W
40°N
30°N
20°N
10°N
0°
10°S
20°S
30°S
40°S
Key
Novae
Young rifts
Old rifts
Novae/km2
High : 3.5e-006
Low : 0

(a)

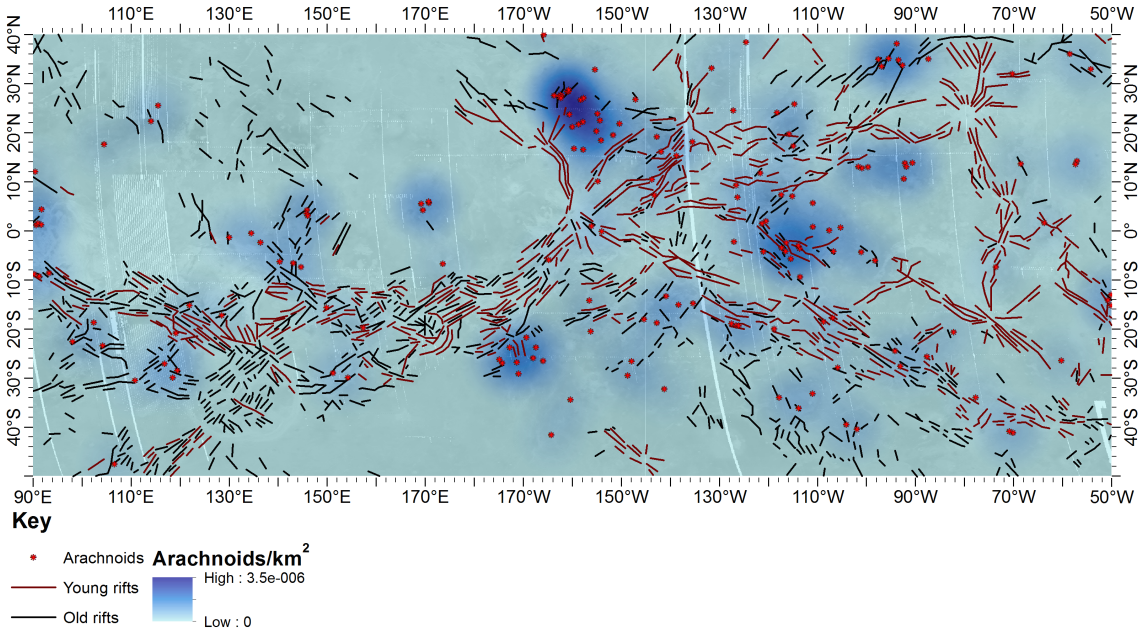
110°E
130°E
150°E
170°E
170°W
150°W
130°W
110°W
90°W
70°W
50°W
40°N
30°N
20°N
10°N
0°
10°S
20°S
30°S
40°S
Key
Arachnoids
Young rifts
Old rifts
Arachnoids/km2
High : 3.5e-006
Low : 0

(b)

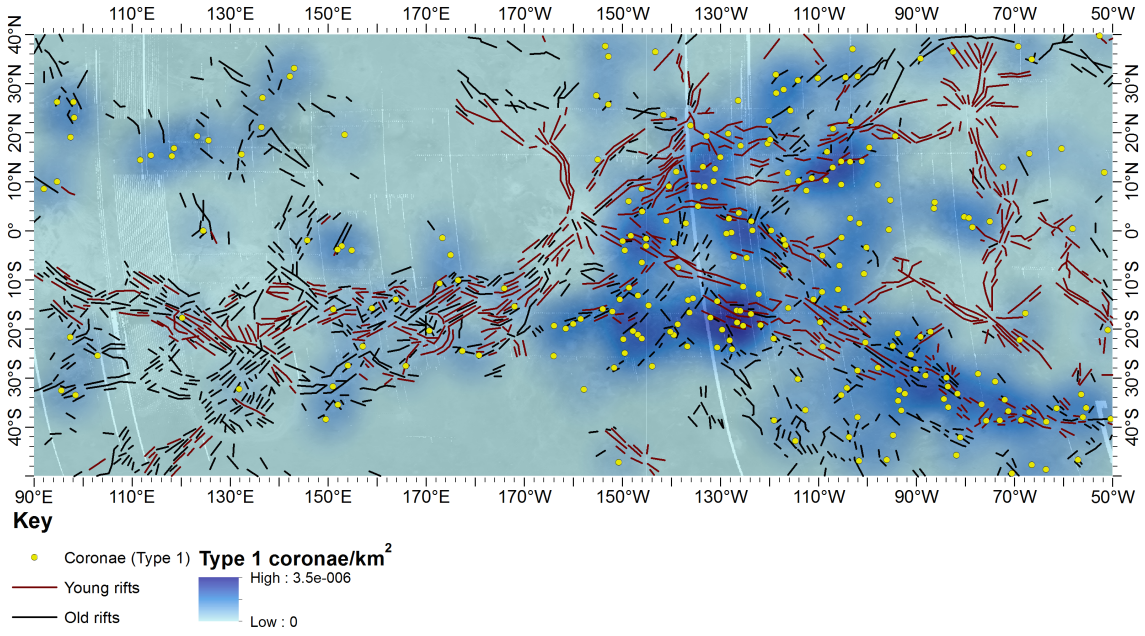
110°E
130°E
150°E
170°E
170°W
150°W
130°W
110°W
90°W
70°W
50°W
40°N
30°N
20°N
10°N
0°
10°S
20°S
30°S
40°S
Key
Coronae (Type 1)
Type 1 coronae/km2
Young rifts
Old rifts
High : 3.5e-006
Low : 0

(c)

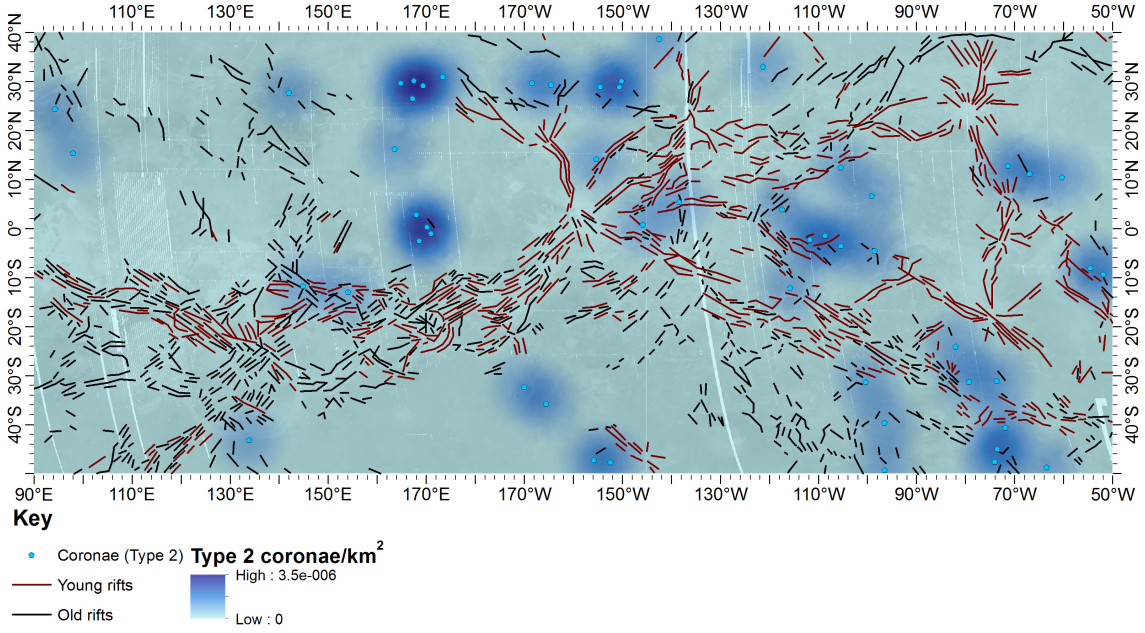
110°E
130°E
150°E
170°E
170°W
150°W
130°W
110°W
90°W
70°W
50°W
40°N
30°N
20°N
10°N
0°
10°S
20°S
30°S
40°S
Key
Coronae (Type 2)
Type 2 coronae/km2
Young rifts
Old rifts
High : 3.5e-006
Low : 0

(d)

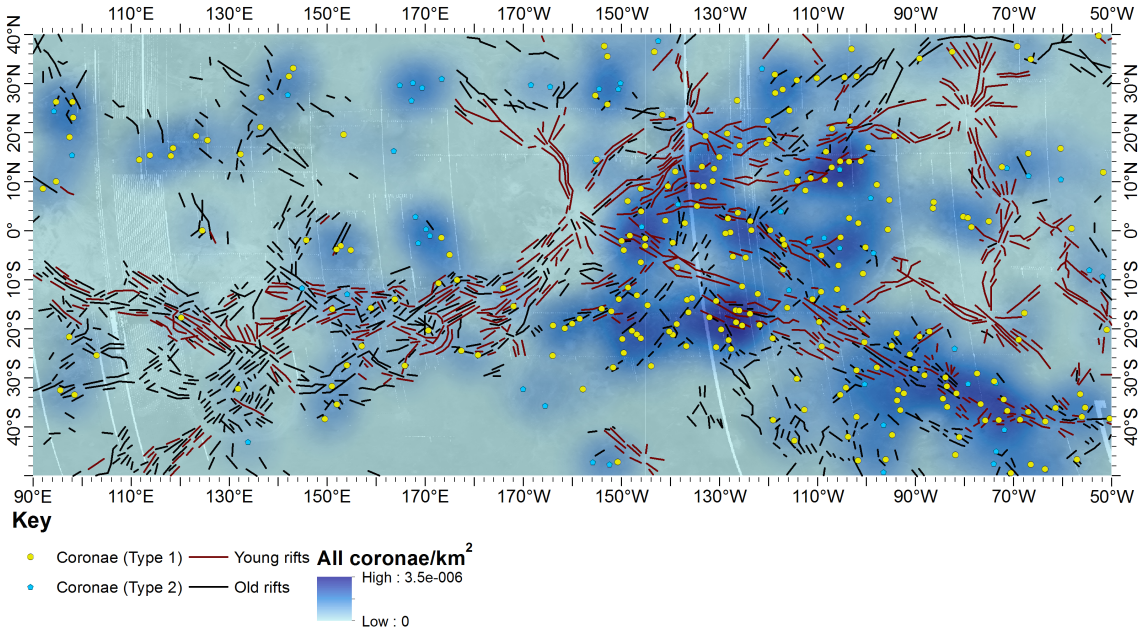

(e)

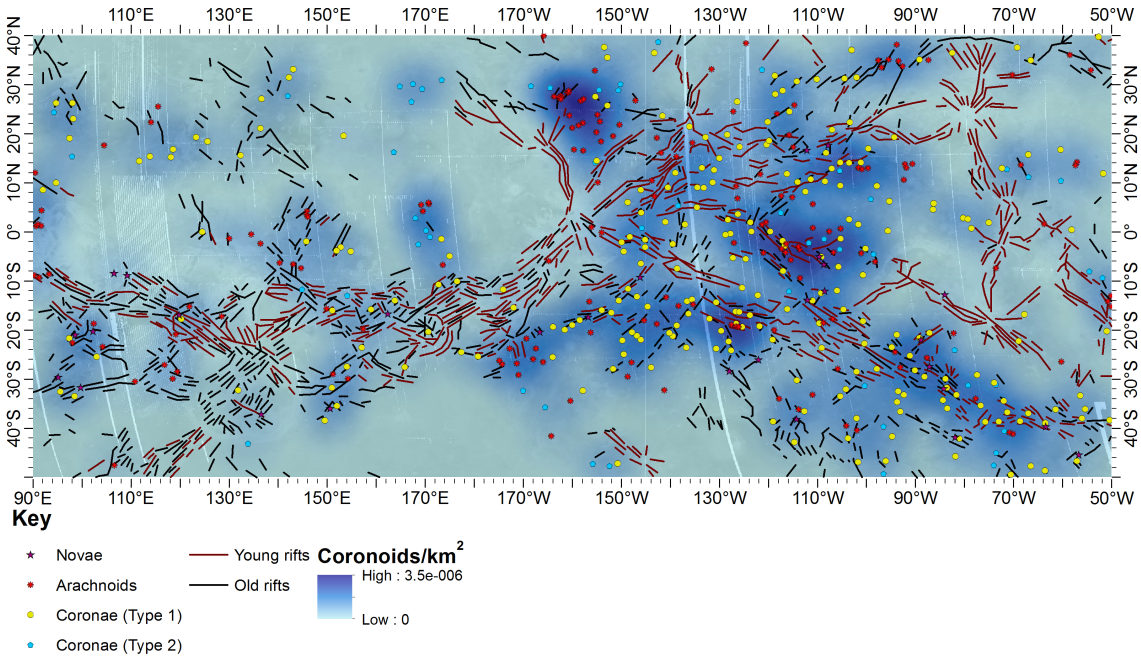

(f)

Figure 4.9: Feature density map for (a) novae, (b) arachnoids, (c) type 1 coronae, (d) type 2 coronae, (e) all coronae, and (f) all coronoids. Points represent individual features. The intensity of the shading of the cell surrounding each point indicates the density in points per km^2 within that cell.

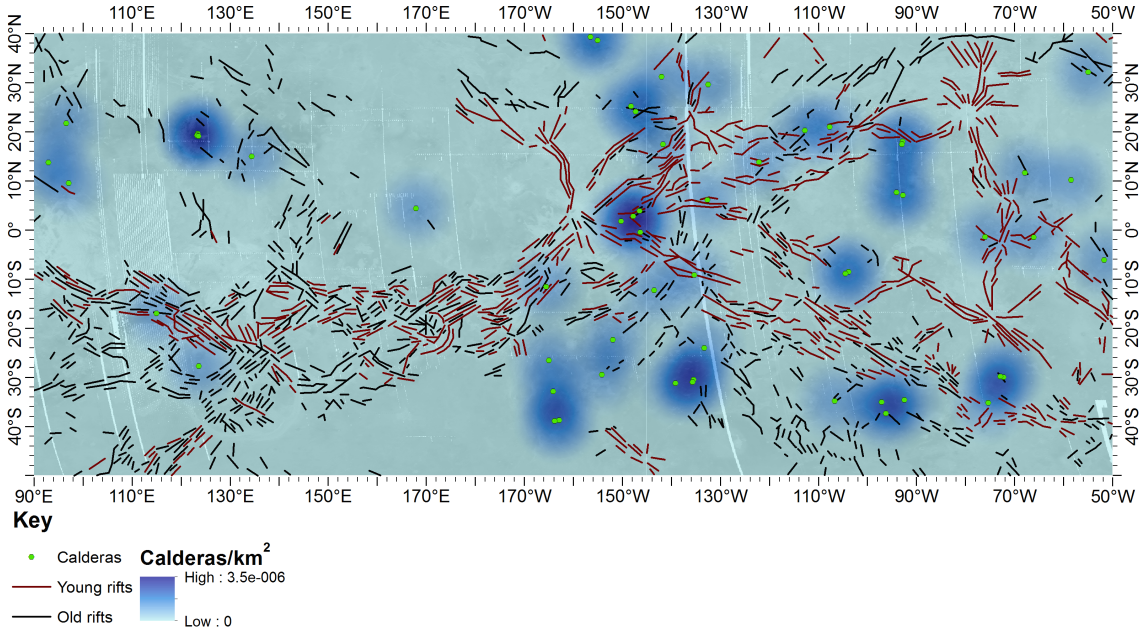
110°E
130°E
150°E
170°E
170°W
150°W
130°W
110°W
90°W
70°W
50°W
40°N
30°N
20°N
10°N
0°
10°S
20°S
30°S
40°S
Key
Calderas
Young rifts
Old rifts
Calderas/km2
High : 3.5e-006
Low : 0

(a)

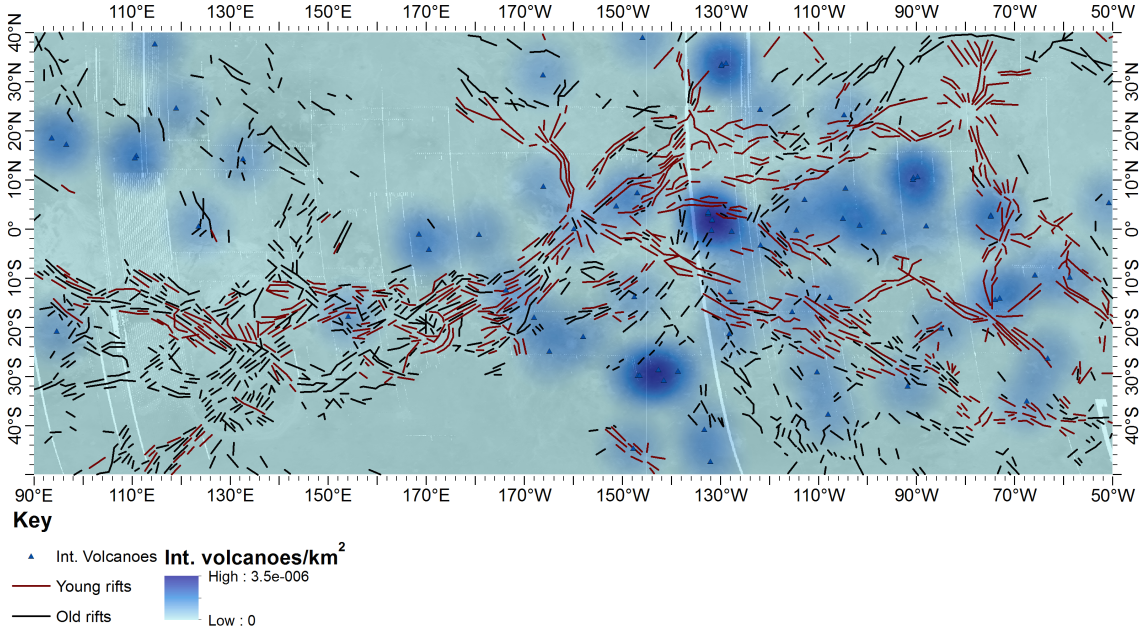
110°E
130°E
150°E
170°E
170°W
150°W
130°W
110°W
90°W
70°W
50°W
40°N
30°N
20°N
10°N
0°
10°S
20°S
30°S
40°S
Key
Int. Volcanoes
Young rifts
Old rifts
Int. volcanoes/km2
High : 3.5e-006
Low : 0

(b)

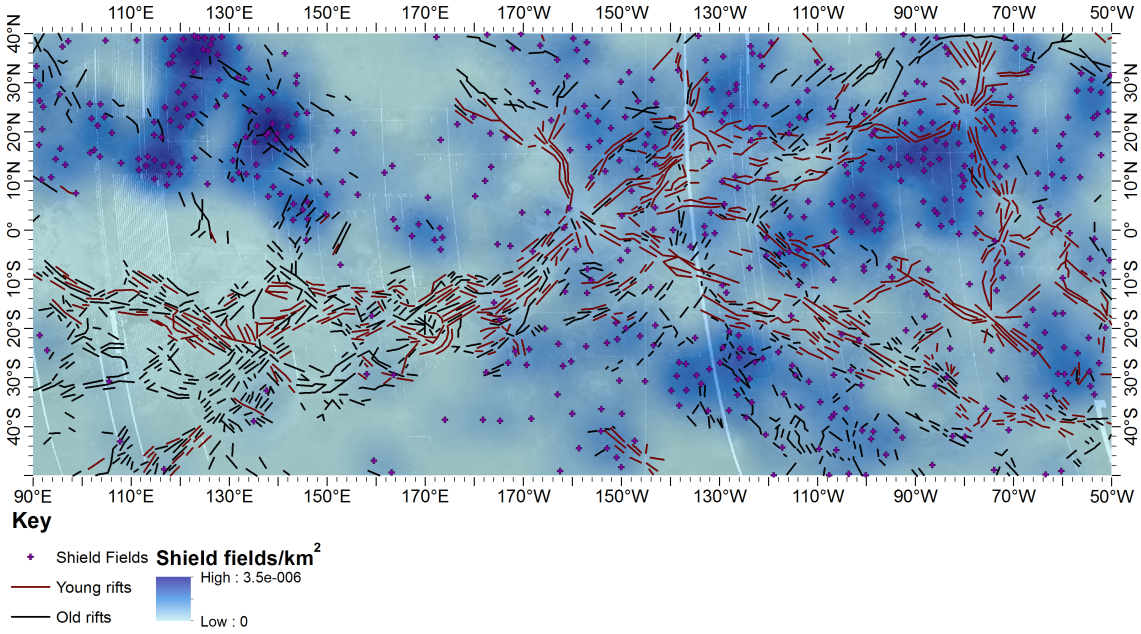
110°E
130°E
150°E
170°E
170°W
150°W
130°W
110°W
90°W
70°W
50°W
40°N
30°N
20°N
10°N
0°
10°S
20°S
30°S
40°S
Key
Shield Fields
Shield fields/km2
High : 3.5e-006
Young rifts
Old rifts
Low : 0

(c)

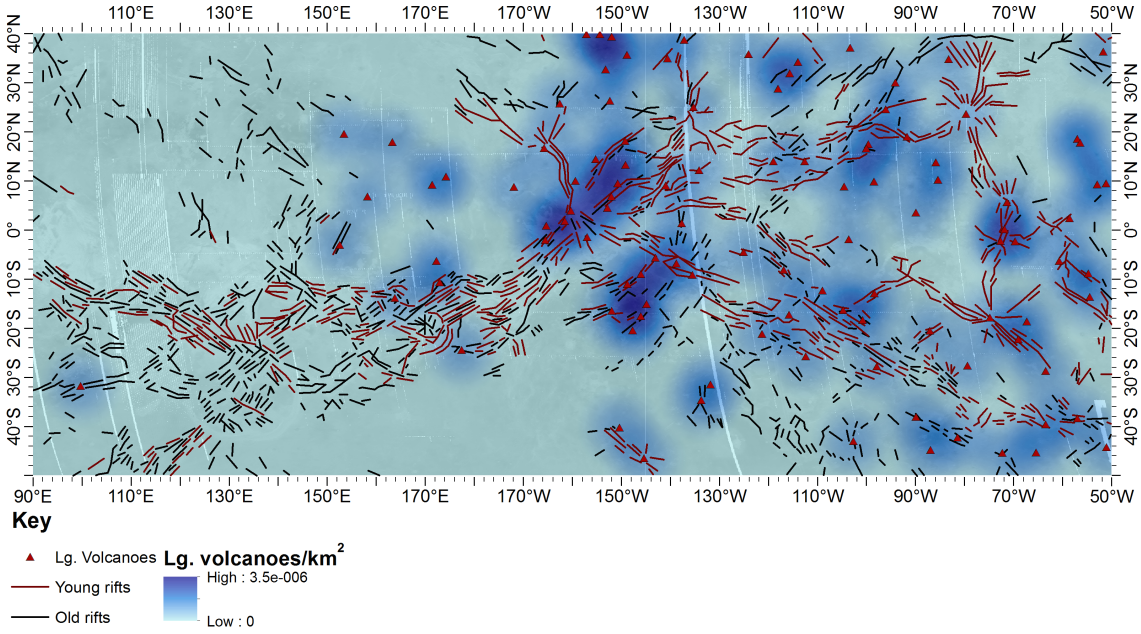
110°E
130°E
150°E
170°E
170°W
150°W
130°W
110°W
90°W
70°W
50°W
40°N
30°N
20°N
10°N
0°
10°S
20°S
30°S
40°S
Key
Lg. Volcanoes
Lg. volcanoes/km2
High : 3.5e-006
Young rifts
Old rifts
Low : 0

(d)

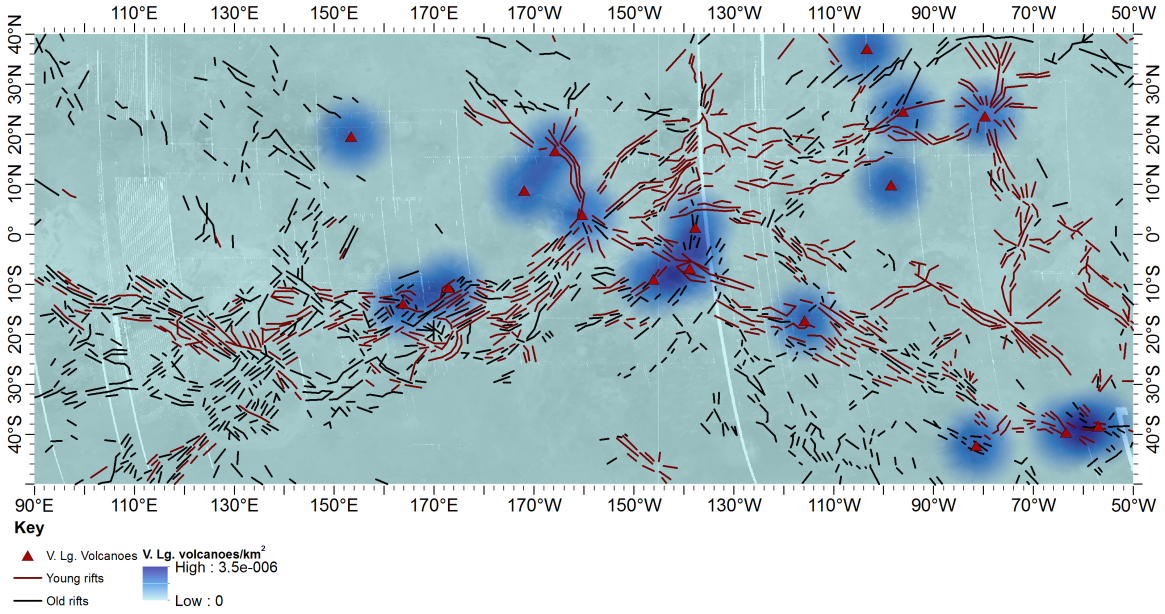

(e)

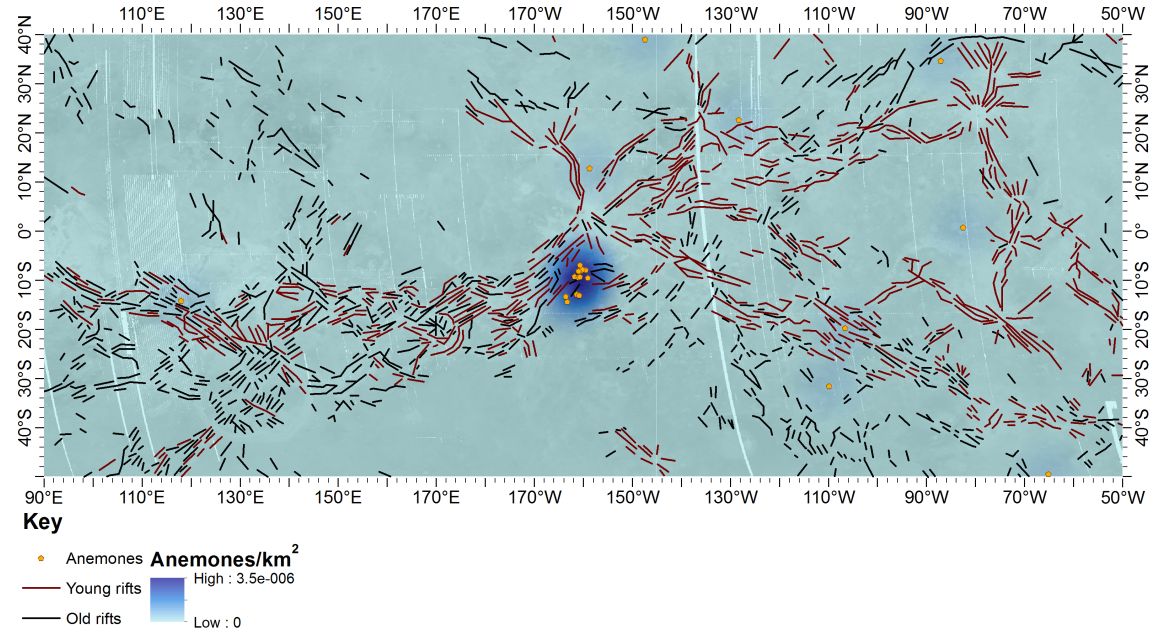

(f)

Figure 4.10: Feature density map for (a) calderas, (b) intermediate volcanoes (≥20 km to <100 km diameter), (c) shield fields, (d) large volcanoes (≥100 km diameter), (e) very large volcanoes (>500 km diameter), and (f) anemones. Points represent individual features. The intensity of the shading of the cell surrounding each point indicates the density in points per km^2 within that cell.

4.4 Discussion

4.4.1 Timing of volcano-tectonic events

Volcano-tectonic associations have been previously used to test models of Venus' geological evolution over time (e.g. *Solomon et al.*, 1992; *Stofan et al.*, 1992, 1995; *Basilevsky and Head*, 1998; *Guest and Stofan*, 1999). In section 4.3 the associations of the new database of volcanic features were plotted with both the old rifts and young rifts mapped by *Krassilnikov et al.* (2012). These old and young rifts have been proposed as representative of two distinct geological time periods on Venus with the division marked by the proposed globally synchronous stratigraphic marker of the regional plains unit (combining upper and lower regional plains units, Figure 4.11). These ideas are fundamental to the directional model of Venus geology (*Basilevsky and Head*, 1998, 2000a, 2002; *Ivanov and Head*, 2013, 2015). *Guest and Stofan* (1999), however, argue for a non-directional model, with processes such as plains emplacement and rifting occurring out of a fixed sequence, and instead largely randomly and interleaved over shorter periods. In this section the implications of these new findings in terms of the timing and evolution of Venus' volcanism, tectonism, and geology are explored.

First of all, the coronoids, with the exception of type 2 coronae, all show a strong association with rifts (Figure 4.6b(i-iii)). This association seems to become less significant when only young rifts are considered (Figure 4.7b(i-iii)). A plausible explanation for this is that corona formation events are broadly coincident with older rifting, predating the regional plains emplacement. Although the corona formation events may not necessarily be directly genetically linked with the initial rifting stage, if they are correlated in both time and space it is likely that there is a common underlying cause of their formation. It is possible, based on the observations in this study that coronae are associated with both young and old rifts, that they continued to form throughout both rifting episodes. The suggestion that they are more strongly associated with the older rifts is however strongly supported by the study of *Krassilnikov et al.* (2012). They examined a subset of coronae (20% of the global database) and concluded that

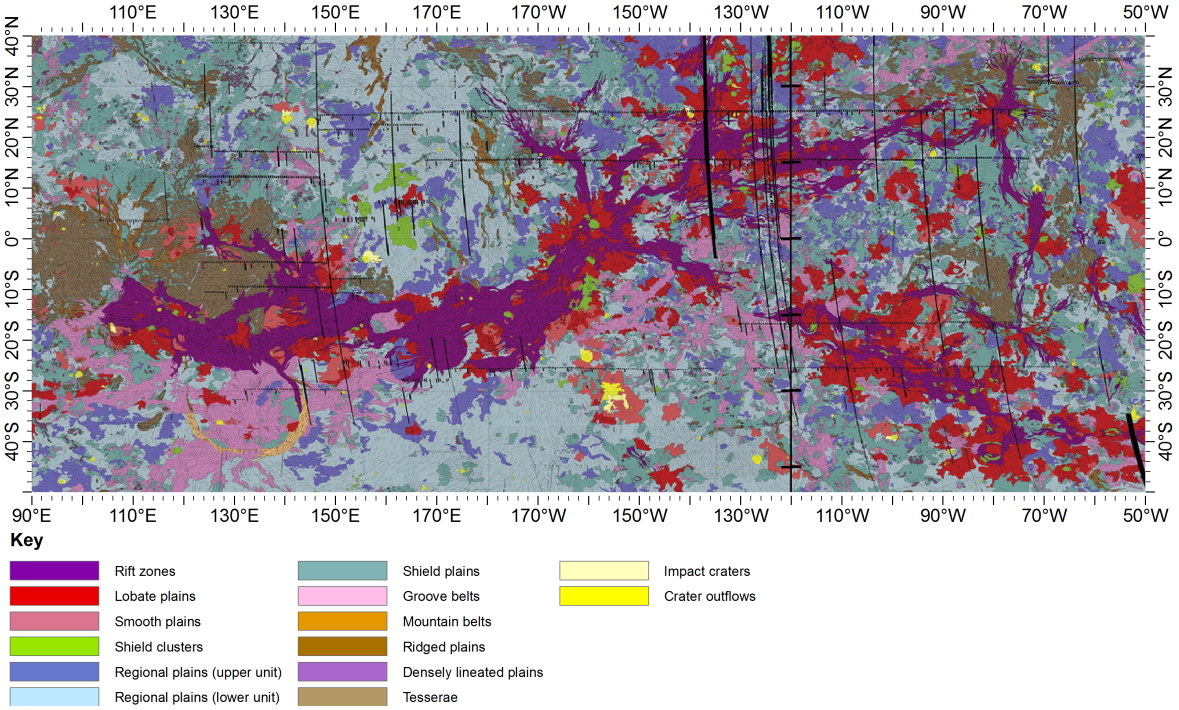

Figure 4.11: Detail of the study area taken from the global geological map of Venus (*Ivanov and Head*, 2011), redrawn to emphasise the BAT study region. Units most relevant to the interpretations in this study are, in the left hand column, the interpreted 'post-plains' rift zones (dark purple) and the regional plains themselves (pale blue and mid-blue); and in the centre column, the 'pre-plains' shield fields (teal) and groove belts (analogous with 'old rifts' pale pink).

as few as 3% of coronae formed after the regional plains (*Krassilnikov et al.*, 2012).

The distribution of shield fields is also informative, even though the population distributions for distance to either rift stage (older or younger) is indistinguishable from random (Figures 4.6c(iii) and 4.7c(iii)). It is evident on inspection of Figure 4.10c that the more prominent shield field clusters are most strongly associated with the terrain of the old rifting stage (regions of pre-regional plains rifting, black lines), largely coincident with the shield plains unit (Figure 4.11). Shield fields in areas coincident with either the regional plains or rift zones units are less common, but not entirely absent (Figures 4.10c and 4.11), suggesting that the bulk of shield field forming volcanism occurred prior to the regional plains emplacement.

The domes and calderas show strong clustering (Figures 4.5a(iii) and 4.5c(i)), with NNIs of 0.608 and 0.717 respectively (Figure 4.3). Intermediate volcanoes show only

moderate clustering (Figure 4.5c(ii)), with an NNI of 0.915 (Figure 4.3), which could be due to the weighting on the lower value bins of the histogram from the strongly clustered part of the population being diminished by the secondary peak at ∼700 km resulting in a bimodal distribution (grey bars, Figure 4.5c(ii)). The distributions with respect to the rifts of these three classes of dispersed, small to intermediately sized volcano-tectonic features do not differ greatly from random, providing no evidence for a genetic association. However, they all correlate broadly with the shield plains and groove belts regions (Figure 4.11).

Finally, the large volcanoes (>100 km diam.) show a population distribution with respect to all rifts that is indistinguishable from random. There is, however, is a strong spike in the leftmost bin corresponding to ∼35% of large volcanoes occurring within ∼50 km of a rift (Figure 4.6c(iv)). When only young rifts are considered (Figure 4.7c(iv)) this distribution remains strong, suggesting that it is largely this sub-population that is responsible for causing the population distribution to diverge from random, otherwise the difference from random would decrease commensurate with the reduction in the size of the population. This is further evidence of a link between young rift zones and persistent, large volcano-forming, centres of volcanism as suggested previously (e.g. *Basilevsky and Head*, 2000b). Further evidence for enhanced volcanism in this second stage of rifting is evident in post-emplacement volcanism at old coronae, which most commonly occurs coincident with the shield plains units, and less commonly into the post-regional plains period (*Krassilnikov et al.*, 2012), as well as in the recent Venus Express data suggesting direct evidence for active volcanism at Ganis Chasma (*Shalygin et al.*, 2015).

4.4.2 Implications for the underlying tectonics

The results of this study may also offer some insights into the evolution of processes at depth that result in this changing style of volcanism at the surface (assuming the sequence of events based on the two-stage rifting).

As discussed in section 4.4.1, the new evidence in this study supports the previ-

ously proposed occurrence of a period of globally dispersed pre-plains tectonic (corona formation) and volcanic (widespread small-scale volcanism) activity (*Ivanov and Head*, 2013). The underlying causes of these volcanic features are thought to be the interaction of subsurface mantle plumes or diapirs for the former (*Head et al.*, 1992; *Janes et al.*, 1992; *Squyres et al.*, 1992; *Stofan et al.*, 1992) and magma migration to the surface for the latter (*Head and Wilson*, 1986; *Head et al.*, 1992; *Crumpler and Aubele*, 2000). The dispersed nature of this initial phase of Venus volcanism could result from many widely dispersed small plumes impinging on the base of a globally relatively thin lithosphere in an earlier 'mobile lid' regime (*Moresi and Solomatov*, 1998). These plumes may cause buoyant uplift of the lithosphere; the crust then responds by gravitational collapse/flow. As a result, magmas can then propagate up into the rifts. As the lithosphere thickens (*Phillips and Hansen*, 1994; *Turcotte*, 1995; *Brown and Grimm*, 1999), the buoyant uplift will be increasingly associated only with larger plumes, which may have now started to coalesce as suggested by *Krassilnikov et al.* (2012). As long as there is a flux of magma into the crust (from partial melting in the plume), then there is a mechanism for continued magma-assisted rifting, by analogy with that which is proposed to occur at the Main Ethiopian Rift on Earth (*Kendall et al.*, 2005; *Corti*, 2009) and volcanism associated with rifts at the surface.

It is interesting to consider this volcanic surface evolution in terms of an underlying tectonic model. What processes would result in the two stages of surface activity implied by this study and the synthesis of previous work (i.e. *Ivanov and Head*, 2015) described in section 4.4.1? In a recent paper, *Ghail* (2015) proposed a mechanism by which the mantle part of the stagnant lid might be able to detach from the overlying crust, and be spread and recycled into the deeper mantle. This model would result in the transition from that illustrated in Figure 4.12a to that in Figure 4.12b. Figure 4.12a represents Venus' crust and upper mantle at a time before the episode of young rifting, where globally dispersed centres of magma upwelling generate a correspondingly globally dispersed incidence of volcanism and minor rifts. Conductive cooling and gradual thickening of the lithosphere over time (*Phillips and Hansen*, 1994; *Turcotte*,

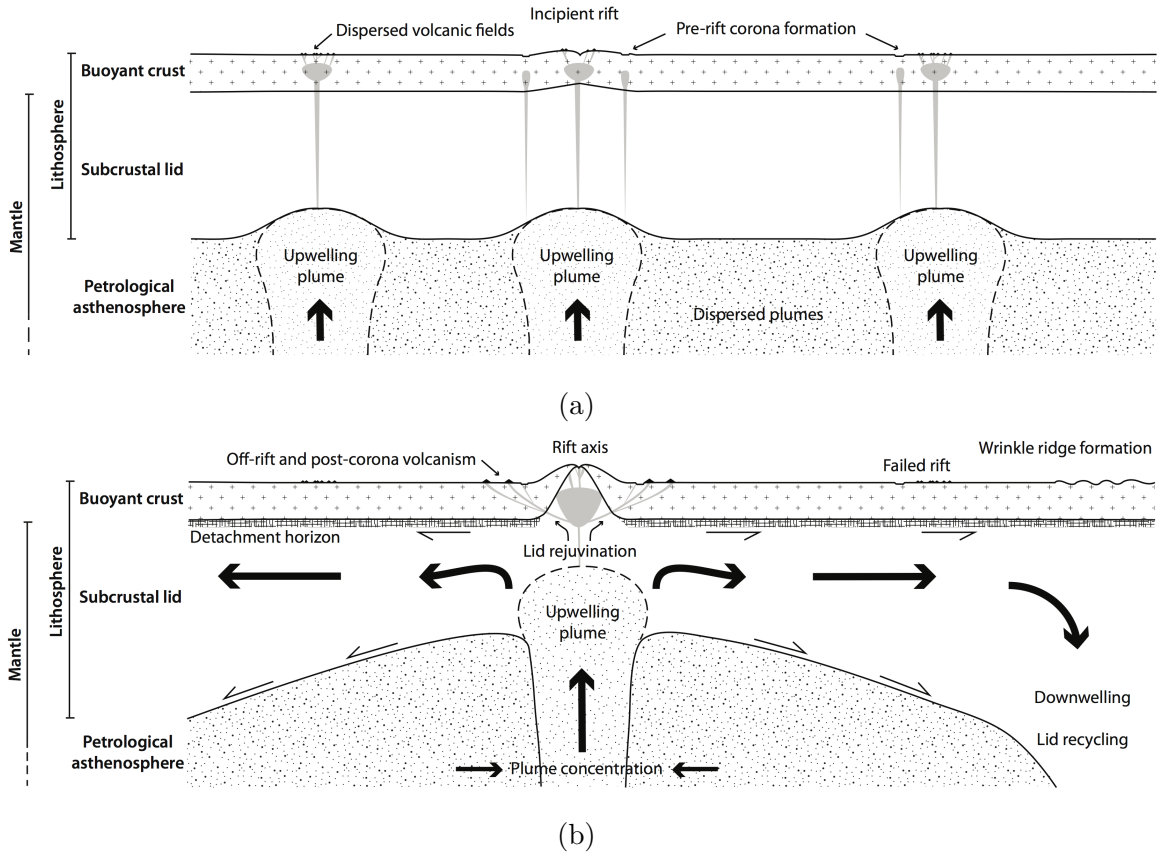

Figure 4.12: Cartoons to illustrate a proposed Venusian global tectonic regime (a) before and (b) after the onset of subcrustal spreading. In the model of *Ghail* (2015), a detachment layer at the base of the crust, as a result of the high surface temperature, along with a CO_2-induced 'petrological' asthenosphere facilitate spreading and recycling of the mantle 'lid'. Regions of upwelling result in lid rejuvenation and rift formation, whereas regions of downwelling may be responsible for stress-related features such as the wrinkle ridges found to affect the regional plains occurring at localised areas of compression.

1995; *Brown and Grimm*, 1999) results in the transition to Figure 4.12b, where mantle upwelling is concentrated and localised at rift axes and large-scale volcanism is then associated with larger rift zones. In the absence of any major subduction-related plate driving forces, it is proposed that the predominant mechanism by which major rift formation progresses is analogous to magma-assisted rifting (*Kendall et al.*, 2005; *Corti*, 2009). It is also possible that this proposed gradual change in tectonic regime may be part of a longer-term tectonic cycle punctuated with global resurfacing events that may periodically reset the system. These processes may provide a satisfactory tectonic evolution model for Venus, pending further study.

4.4.3 Synthesis of evidence for volcano-tectonic processes and timing

The evidence presented in sections 4.4.1 and 4.4.2 is broadly consistent with the sequence of events proposed to characterise the directional model of rift evolution (*Basilevsky and Head*, 2000a). These findings are summarised in Figure 4.13, which outlines the tectonic and volcanic evolution of Venus. The 'supporting evidence' row has been added to highlight the new evidence in this study. Although there is a broad consistency, there remains a degree of non-directional activity (*Guest and Stofan*, 1999), such as the rare post-plains coronae identified by *Krassilnikov et al.* (2012), and large volcanoes persisting away from young rifts (e.g. Ituana "Corona", a large volcano located at 19.5°N, 154°E, Figure 4.10e), suggesting that the ongoing sequence of events is more complex than either end member model.

4.4.4 A failed rift?

The chain of concentrated volcanic features including domes, coronae, and shield fields in southern Llorona Planitia located in the upper left of the study area at around 10-30°N and 90-150°E (Figures 4.8c, 4.9c, 4.10c, and 4.11) is a striking feature of the study region. As previously noted in sections 4.4.1-4.4.3, coronae are strongly associated with rifting, indicating that this region may have been in the early stages of transition into a 'young rift'. However, following the regional plains emplacement, there is no evidence of further rifting or development of large-scale volcanism in this region. This suggests that this rift section failed (illustrated on the right-hand side of Figure 4.12b), with the associated large-scale magmatism probably being diverted towards the more concentrated active young rifts as described in section 4.4.1 and Figure 4.12. This further example of evidence in support of a transition from widespread volcanism to concentrated rifting is consistent with the response to thickening lithosphere (and mobile to stagnant lid) described in *Phillips and Hansen* (1998).

On Earth, continental rifting is a well-studied component of plate tectonics (Fig-

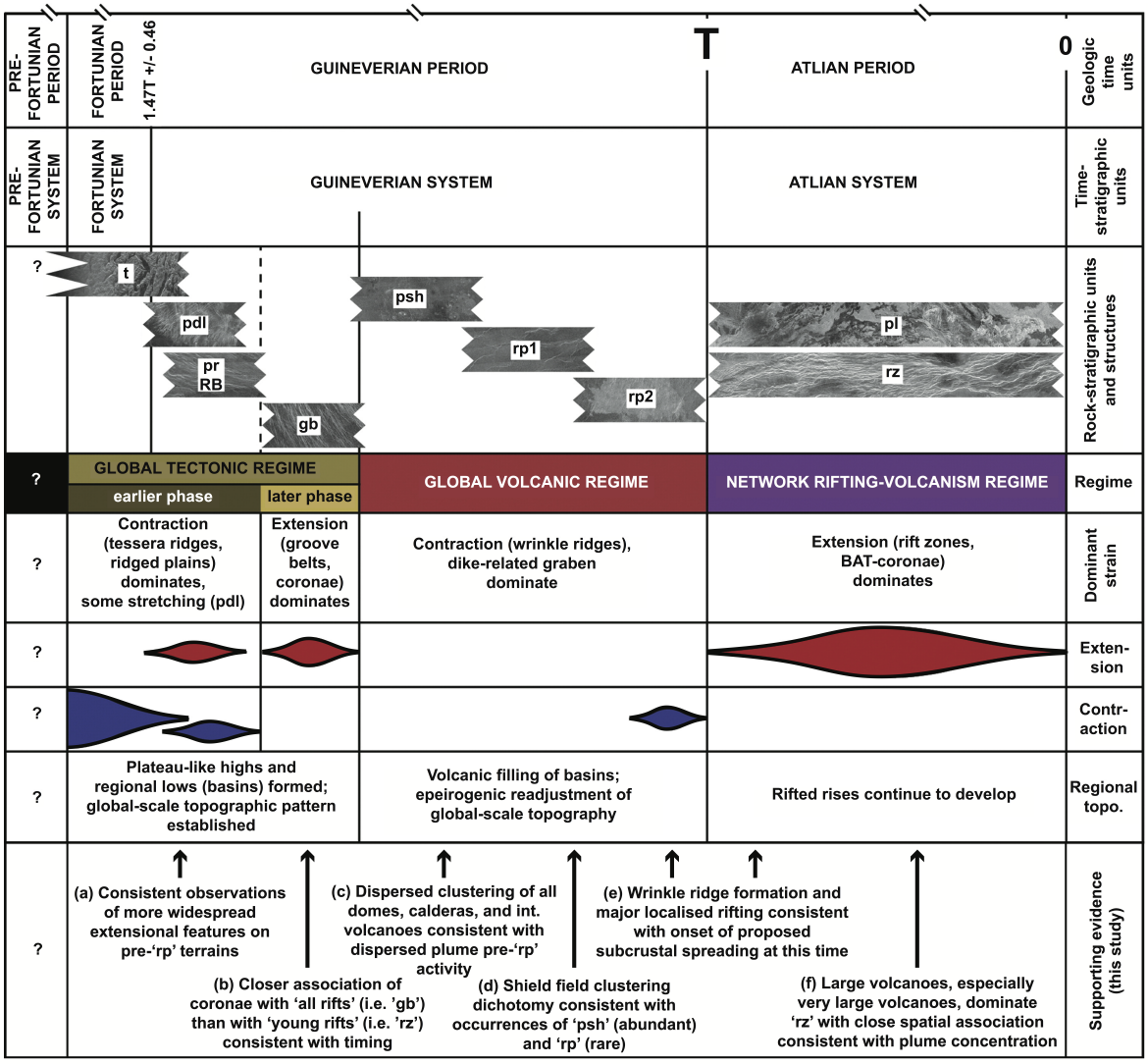

Figure 4.13: Summary of the tectonic history of Venus since tessera formation (oldest observed stratigraphic unit) as outlined in accordance with the directional model of Venus evolution. Modified from *Ivanov and Head* (2015). The model describes three main global volcano-tectonic regimes beginning with a tectonic regime characterised by intense tectonic deformation and the formation of minor rift features (groove belts corresponding to 'old rift features' in this study). This is followed by a volcanic regime characterised by sequential phases of plains emplacement. Finally, the network rifting-volcanism regime dominates along with the formation of the youngest and most intense rifting episodes. Unit names in the 'rock stratigraphic units and structures' row refer to regions mapped on Figure 4.11: tesserae (t), densely lineated plains (pdl), ridged plains/ridge belts (pr/RB), groove belts (gb), shield plains (psh), lower and upper regional plains (rp1 and rp2), lobate plains (pl), and rift zones (rz). Lettering in the 'supporting evidence' row refers to evidence cited in Figures: (a) 4.2; (b) 4.6b, 4.7b, and 4.9c; (c) 4.3, 4.5a, 4.5c, 4.8c, 4.10a, and 4.10b; (d) 4.3, 4.5c, 4.10c, and 4.11; (e) 4.12; (f) 4.7c, 4.10d, and 4.10e.

ure 4.1a). It is possible that this process may have characteristics analogous with the processes responsible for the rifts observed on Venus. The EARS has often been cited as potentially analogous to Venusian rifting, particularly the region between Beta and Phoebe Regiones (*McGill et al.*, 1981; *Campbell et al.*, 1984; *Stofan et al.*, 1989; *Foster and Nimmo*, 1996). This analogy is based primarily on the similarity of geomorphological characteristics in these two settings, with fault-bounded rift segments connecting domed regions of enhanced volcanism. The proposed failed rift on Venus may have been the result of a plume-lithosphere interaction similar to that responsible for the observed difference between the eastern (magma-rich, active) and western (magma-poor, failing?) branches of the central EARS on either side of the Tanzanian craton (centred at 3°S, 32°E, Figure 4.14) (*Roberts et al.*, 2012).

Koptev et al. (2015) modelled the possible geodynamic processes responsible for this EAR segment failure as a mantle plume head impacting on the base of a significantly thickened area of lithosphere (i.e. the Tanzanian craton). The plume is deflected by the craton in their model to form magma-rich (eastern high density of recent volcanism) and magma-poor (western low density of recent volcanism) branches of the rift on either side (Figure 4.14). If indeed plume-rift formation processes and interactions are in any way analogous on Earth and Venus, it seems likely that a similar event may have been responsible for the feature described above. Thetis Regio (Figure 4.2b), the easternmost area of the highland region Aphrodite Terra, is a region of thickened lithosphere (evidenced by its high topography) that occurs in between the proposed failed section and the system of young chasmata running along the southern fringe of Thetis Regio. It is plausible to suggest that the mechanism proposed by *Koptev et al.* (2015) might apply here too. The scale here differs significantly however; the distance between the rifts on either side of the thickened lithosphere on Venus is around 5 times that on Earth (∼3500 km and ∼700 km respectively). If this is the case, deflection or bifurcation of a plume beneath a much wider region of thickened lithosphere and the resulting surface expression implies a larger plume on Venus in order to result in the differing surface expressions on either side. Further geodynamic modelling to test the

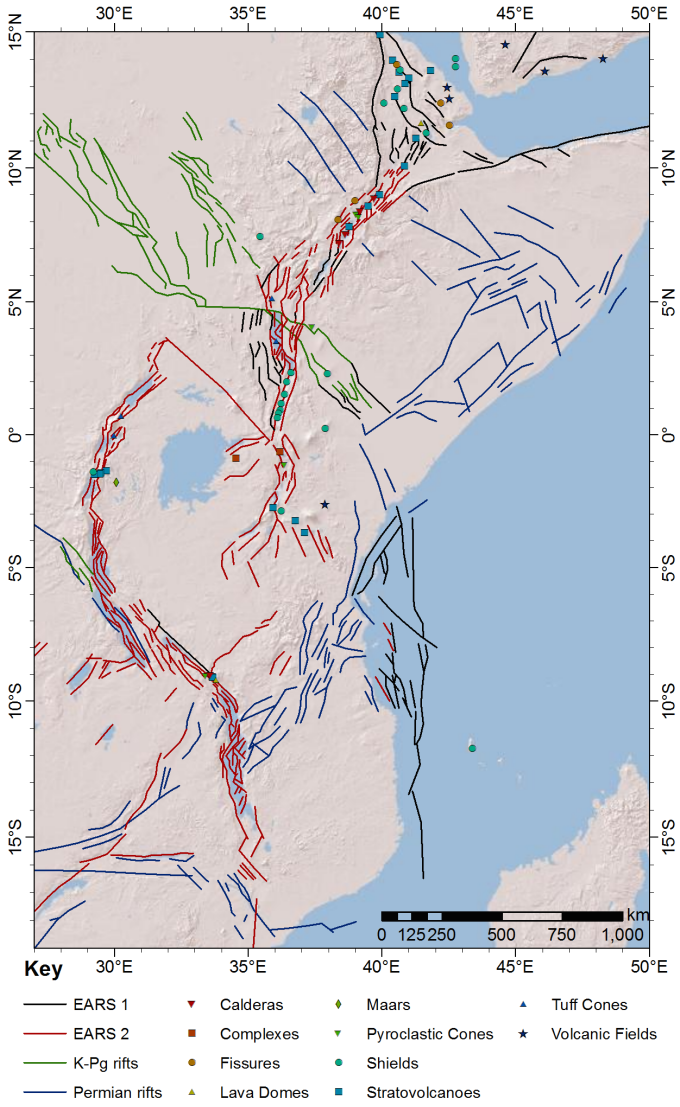

Figure 4.14: The East African Rift System. Data mapped using the locations and definitions of the Smithsonian Institution's Global Volcanism Program (GVP) database of Holocene volcanoes (www.volcano.si.edu). The rift sections of the Oligocene to Recent (EARS 1 and 2), as well as the separate older Cretaceous-Palaeogene and Permian rift sections were mapped using *Macgregor* (2015). Base map from the U.S. Geological Survey's SRTM (Shuttle Radar Topography Mission) 90 m resolution data topography.

plausibility of applying this model to this region of Venus is to be encouraged.

4.5 Conclusions

With the use of new geospatial analysis performed in ArcGIS, the quantification of spatial relationships between volcanic features and rifts on Venus was achieved and applied to planetary evolutionary concepts. The systematic study of nearest neighbour distances, distances from rifts, and distances from young rifts facilitated the comparison of spatial and temporal trends of volcanic behaviour. When these data analyses were compared with the directional evolutionary model for Venus (*Basilevsky and Head*, 1998, 2000a, 2002; *Ivanov and Head*, 2013, 2015), a number of observations were found to be independently consistent with the concept. When applying the methods independently to the two inferred relative rift ages, the differing associations discovered were indicative of a broad agreement with the sequence of events suggested in the directional model. Initial widely dispersed rifting structures with associated coronae indicative of pre-rift processes and broadly dispersed incidences of small-scale volcanism at shield fields dominated before the emplacement of the, thought to be, globally synchronous 'regional plains' unit. The new evidence in this study shows a closer association of coronae with 'all rifts' than with 'young rifts', which is consistent with this model. This early regime is attributed to a relatively thin lithosphere allowing the dispersed, relatively small, plumes impinging on the lithosphere to generate the widespread small-scale volcanism. As the lithosphere cools conductively and thickens, the plume activity is proposed to become concentrated to fewer, larger, plumes and is focused along the young, post-regional plains and rift zones. The evidence in this study supports this model, showing a stronger correlation of large volcanoes with young rifts than with both young and old rifts.

Relationships confirmed by this work are also consistent with the evolution from a stagnant lid regime to the hypothesised subcrustal spreading regime of *Ghail* (2015). The transition from widespread to more localised activity could result from the concentration of plumes in response to magma-assisted rifting, a thickening lithosphere, and crustal detachment of the subcrustal lid. These processes would promote subcrustal spreading and the enhanced recent volcanism concentrated along young rifts.

Although other processes could be cited to explain these observations, the stagnant lid to subcrustal spreading transition is an interesting proposition that warrants further investigation.

Evidence for rift failure cited includes a band of coronae, associated with old rifts, which did not develop into a young rift zone. It is proposed that the plume supplying this segment was diverted to the chasmata situated further south in response to a region of thickened lithosphere. It is noted that this process may be analogous, albeit on a larger scale, to a proposed model for the evolution of the East African Rift system (*Koptev et al.*, 2015).

Chapter 5

Summary and further work

This chapter synthesises the findings drawn from the preceding chapters' conclusions into three broad themes. First of all, the relevance of each chapter to the question of whether or not volcanic processes are currently active on Venus is drawn together. This is followed by similar treatments on the subjects of the likelihood of explosive activity and how volcanism affects global planetary processes. Finally, this then leads into some suggestions for further work based on the outstanding questions arising from this work.

5.1 Active volcanism on Venus

It is a very exciting time to be investigating volcanism on Venus as there is a growing body of evidence in support of active and geologically recent activity being published. Most notably, this includes the measurement of cyclical SO_2 concentrations above the clouds that may be volcanic in origin (*Marcq et al.*, 2013), infrared 'hot spots' indicative of young volcanic material (*Smrekar et al.*, 2010), and compelling evidence for dynamic volcanic events during the lifetime of Venus Express at Ganis Chasma (*Shalygin et al.*, 2015). The contrasting methods used in the preceding chapters, and the insights attained through the various studies, contribute to this ongoing discussion in several ways.

The modelling exercise in chapter 2 demonstrated that, under current Venusian conditions and likely geological scenarios, explosive volcanism in some form is not only feasible, but quite likely. Venus is similar to Earth in terms of its size and age, suggesting that by analogy with Earth, it must still possess sufficient internal heat to drive geological processes. Regardless of the style of volcanism, the manifestation of some form of volcanic processes at the surface of Venus is required in order to remove heat from the interior. Earlier suggestions for solving the heat budget led to the model of periodic global resurfacing events punctuating longer periods of quiescence (*Turcotte*, 1993). However, the accumulation of evidence for ongoing activity has led to this simplistic model being re-evaluated. The contribution to the discussion from this modelling effort is to support the notion that volcanism may be ongoing by demonstrating that the conditions observed/inferred would permit activity covering a range of potential eruptive styles. This work has also shown that the magmatic volatile concentration scenarios that would result in some of the observed deposits on Venus may be detectable with current data availability (*Airey et al.*, 2015), specifically the Venus Express VIRTIS H_2O measurements.

The analysis of radar datasets in chapter 3 has yielded possible indications of geologically recent activity in the form of microwave emissivity measurements. There is what appears to be material that is out of equilibrium with local P/T conditions resulting in emissivity anomalies. The cited examples of these high-emissivity deposits occur at the summits of Ma'at Mons and Tepev Mons where, according to the global high-altitude/low-emissivity anomaly, they should not be present, if assumed to be in equilibrium. This leads to the conclusion that, as they are yet to equilibriate with local conditions, they have been recently emplaced and may be the result of recent active volcanism. These anomalies are also seen in the emissivity profiles at some major rifts, providing further circumstantial evidence of active volcanism, as well as supporting the recent findings at Ganis Chasma by *Shalygin et al.* (2015).

The spatial analysis of rifts and volcanoes performed in chapter 4 provides new insights into the timing of volcanic processes and global tectonic behaviour. Although

there is no new evidence for active volcanism as such, the synthesis of the geospatial associations of volcanic features with rifts is consistent with both the directional model of Venus' evolution (*Basilevsky and Head*, 2000a), and the subcrustal spreading model of *Ghail* (2015). If indeed the *Ghail* (2015) model operates on Venus as proposed, this provides a tectonic framework where ongoing volcanism is not only facilitated, but expected.

5.2 Explosive volcanism on Venus

The eruptive style and explosivity of volcanic activity on Venus has been a key theme in this work. Chapter 2 addresses this most thoroughly in the systematic study of the physical, chemical, and environmental factors affecting these processes in the Venusian context. Given that Venusian mantle H_2O concentrations may not necessarily be as high as on Earth, consideration of the contribution of CO_2 forms a crucial part of this new approach. The main finding was that, given either H_2O or a combination of both H_2O and CO_2, plausible conditions arise whereby explosive activity may occur, albeit with rather high volatile concentrations ($\sim$3-5% H_2O under standard model conditions at MPR i.e. 5 km deep, 25 m radius conduit, 1200 K magma). It was also found however, that certain other parameters have an effect on explosivity, and can allow explosive responses from lower volatile concentrations. Examples include higher elevations and narrower conduits or networks of conduits. It is therefore physically possible to achieve magma fragmentation within a conduit given reasonable model test conditions (e.g. see Table 2.4). Should explosive conditions be achieved, the use of case studies was able to provide information on the range of explosive styles that may be observed. The key finding is that the conditions required for magma to fragment at the MPR are sufficient to permit buoyant subaerial plume rise at much higher altitudes, such as the peak of Ma'at Mons.

The observations in chapter 3 have provided a basis by which the emplacement mechanisms for Venusian volcanic deposits may be explored, via the measurement and

comparison of their radar attributes. Inferences can then be made about the explosivity of the eruption from which they are derived. It became apparent that a deposit identification scheme based on radar properties using terrestrial analogues is highly problematic at the current time, but not without potential. In contrast, on a regional basis, Venusian radar measurements can yield a wealth of useful information about the surface material properties. For example, the properties of the radar-bright halos that were suggested as possible pyroclastic deposits around Irnini and Anala Montes (*McGill*, 2000) were studied and found to corroborate with a past study of a pyroclastic deposit, Scathach Fluctus, (*Ghail and Wilson*, 2013) and expected reasonable ignimbrite-like values. When combined with the model findings in chapter 2, these observations provide strong evidence for explosive activity on Venus, once thought to be very unlikely.

5.3 Global processes

The global-scale implications of the studies carried out here are touched on throughout. Firstly, the GIS-based work in chapter 4 describes new evidence supporting aspects of the the directional model of Venus' evolution (*Basilevsky and Head*, 2000a). This shift from the globally dispersed, relatively small-scale, volcanism spread randomly across the planetary surface towards the gradually more rift-focused distribution is indicative of a corresponding shift in global tectonic regime. The model stages suggested here are that of a stagnant lid scenario, with widely dispersed, discrete zones of small plume-fed activity, followed by a transition via gradual conductive cooling to that of the subcrustal spreading regime mentioned in section 5.1 whereby continued and ongoing volcanism may persist in tandem with the directional model background.

The transition to a global tectonic regime favouring ongoing volcanic activity, as opposed to catastrophic resurfacing, is consistent with the previously published work cited and the findings from chapters 2 and 3, summarised in section 5.1. This provides a self-consistent view of the underlying planetary evolutionary trends throughout this

work.

The self-consistent view of volcanotectonic and surface evolution established here has implications for the consequent atmospheric impacts. As volcanism is suggested to have been ongoing throughout Venus' recent history, a volcanic input to the atmosphere must therefore also have been persistent for as long. This tallies with the modelling of *Bullock and Grinspoon* (2001), which suggests that a persistent input of SO_2 to the atmosphere is required in order to maintain the sulphuric acid clouds observed, at least in the last 20-50 Ma. These clouds would otherwise become diminished via atmosphere-surface interaction, such as the pyrite or calcite buffers described in chapter 1, as the sulphur is locked into the surface mineralogy. The additional input of H_2O and CO_2 resulting from active volcanism will also have long-term global atmospheric impacts. The CO_2 will assist in maintaining the atmospheric density, whereas the H_2O may cause localised anomalies which may potentially be detected in the Venus Express data, assisting in the identification of very recent volcanism. Outgassed H_2O, upon dispersal, then becomes part of the planetary atmospheric water vapour inventory, also becoming available for cloud formation processes.

5.4 Further work

All of the preceding investigations have resulted in the identification of numerous paths by which further work may be undertaken. There is potential for improvements to the methods, alternative applications for techniques devised, and extensions to the existing approaches. As there are many opportunities for further work, this section focuses on a selection of what may be some of the more scientifically valuable routes.

5.4.1 Modelling

The modelling exercise in chapter 2 has abundant scope for further study. In this exercise, a number of simplifications were made to the model in order to allow progress within the resources of a D.Phil. project. The most obvious course of further study

would be to address these and provide a more representative, complex model.

Firstly, the inclusion of SO_2 as a chief volatile should be incorporated into future iterations of the model. This is an important atmospheric component of Venus in terms of atmospheric chemistry and cloud formation, and could potentially provide further insight into the styles of volcanic activity occurring. This inclusion would also provide another method for investigating the implications for potential detection in conjunction with the H_2O. It would be possible to explore more complex magma chemistry and minor constituents, but given the degree of uncertainty, this is difficult to justify.

Another simplification that could possibly have interesting repercussions if included is the magma fragmentation threshold. The value of 0.75 volume fraction gas as the fragmentation criterion has been widely used in the past, but other work has made improvements to our understanding of this process (e.g. *Sparks*, 1978; *Gonnermann and Manga*, 2003; *Tuffen and Dingwell*, 2005) and it is found to vary over a range of ∼0.7-0.8. The model results in chapter 2 indicate that the sensitivity of fragmentation to the other variables can be quite high. For example, under standard model test conditions, varying the conduit radius from 10-100 m resulted in a change in volume fraction gas of ∼0.1, meaning that small changes to the fragmentation criterion applied can have potentially quite high magnitude responses.

Finally, the remaining further work I would suggest regarding the modelling would be to explore more realistic conduit geometries. Actual conduits are unlikely to be perfect cylinders and probably transition from dike to conduit at successive stages of ascent. It would be challenging, but informative, to model these processes in addition to the cylindrical ascent style in order to assess the effects of this simplification. In addition, fissure systems are cited as a possible way of producing high volume eruptions explosively with relatively low volatile concentrations as the individual vents are narrower than a single vent of the same cross-sectional area. Therefore fissure geometry would be an important improvement.

5.4.2 Radar analyses

The main reason for the comparative analyses attempted between terrestrial and Venusian volcanic deposits to fail to provide a serviceable deposit identification scheme was the disparity in data wavelengths. Further work on this should only be undertaken using data of the same or very similar wavelengths. In terms of the emissivity, the Venus Express VIRTIS data should be used in comparison with the MODIS data as these may provide a much more robust data pairing for comparative purposes. They could then potentially be used to investigate whether or not the high/low emissivity deposit type preference seen in the terrestrial data is reflected in the Venusian data. In terms of the SAR data, there is again disparity in the wavelengths, being C and S-band. This appears to have less of an effect than the emissivity data mismatch. However, the wavelength has a strong control on the roughness calculations, which is not fully resolved by using asperity. Further work should aim to better quantify the effect of wavelength on the backscatter values and use that information to create a more accurate synthetic S-band dataset for Earth.

Further to this, it would be informative to build on the success of the regional case study analyses by searching for other examples containing potential pyroclastics. These case studies, if reasonably confident identifications could be made, could be included in the comparative study with which to make more relevant comparisons.

5.4.3 Spatial analysis

The spatial analyses focused on the most important rifting region, the BAT region, in order to gain insight into the spatial relationships at that scale, as it was considered to be the most informative. However, it would be useful, in future work, to both expand the study to a global scale and to focus on smaller regions and individual rift segments. This would allow the effect of scaling to be assessed. The global approach may highlight nuances in the distribution response in the tail of the data, and localised studies may highlight smaller-scale trends.

Also of potential benefit to the findings in this chapter would be the geophysical modelling of the subcrustal spreading concept using a quantitative approach such as a 2D finite element model. This is a large project in itself, but would be very useful in providing context. The proposed processes in *Ghail* (2015) could be tested quantitatively to assess whether or not the transition from stagnant lid to subcrustal spreading is possible, and the predicted response of plume focussing on rifts could be explored more fully.

Bibliography

Abdrakhimov, A. M., and A. T. Basilevsky (2002), Geology of the Venera and Vega landing-site regions, *Solar System Research*, *36*(2), 136–159, doi:10.1023/A:1015222316518.

Airey, M. W., T. A. Mather, D. M. Pyle, L. S. Glaze, R. C. Ghail, and C. F. Wilson (2015), Explosive volcanic activity on Venus: The roles of volatile contribution, degassing, and external environment, *Planetary and Space Science*, *113 - 114*, 33 – 48, doi:http://dx.doi.org/10.1016/j.pss.2015.01.009.

Aittola, M., and V. Kostama (2000), Venusian novae and arachnoids: characteristics, differences and the effect of the geological environment, *Planetary and Space Science*, *48*(15), 1479–1489, doi:10.1016/S0032-0633(00)00093-3.

Aittola, M., and V. P. Kostama (2002), Chronology of the formation process of Venusian novae and the associated coronae, *Journal of Geophysical Research-Planets*, *107*(E11), doi:10.1029/2001je001528.

Al-Ahmadi, K., A. Al-Amri, and L. See (2014), A spatial statistical analysis of the occurrence of earthquakes along the Red Sea floor spreading: clusters of seismicity, *Arabian Journal of Geosciences*, *7*(7), 2893–2904, doi:10.1007/s12517-013-0974-6.

Anderson, D. L. (1981), Plate tectonics on Venus, *Geophysical Research Letters*, *8*(4), 309–311, doi:10.1029/GL008i004p00309.

Aplin, K. L. (2006), Atmospheric electrification in the solar system, *Surveys in Geophysics*, *27*(1), 63–108, doi:10.1007/s10712-005-0642-9.

Avduevsk, V. S., M. Y. Marov, and M. K. Rozhdest (1968), Model of atmosphere of planet Venus based on results of measurements made by soviet automatic interplanetary station Venera 4, *Journal of the Atmospheric Sciences*, *25*(4), 537–545, doi:10.1175/1520-0469(1968)025⟨0537:motaot⟩2.0.co;2.

Baer, G., G. Schubert, D. Bindschadler, and E. Stofan (1994), Spatial and temporal relations between coronae and extensional belts, northern Lada Terra, Venus, *Journal of Geophysical Research-Planets*, *99*(E4), 8355–8369, doi:10.1029/93JE03092.

Baines, K. H., S. Atreya, R. W. Carlson, D. Crisp, P. Drossart, V. Formisano, S. S. Limaye, W. J. Markiewicz, and G. Piccioni (2006), To the depths of Venus: Exploring

the deep atmosphere and surface of our sister world with Venus Express, *Planetary and Space Science*, *54*(13&14), 1263–1278, doi:10.1016/j.pss.2006.04.034.

Barabash, S., A. Fedorov, J. J. Sauvaud, R. Lundin, C. T. Russell, Y. Futaana, T. L. Zhang, H. Andersson, K. Brinkfeldt, A. Grigoriev, M. Holmstrom, M. Yamauchi, K. Asamura, W. Baumjohann, H. Lammer, A. J. Coates, D. O. Kataria, D. R. Linder, C. C. Curtis, K. C. Hsieh, B. R. Sandel, M. Grande, H. Gunell, H. E. J. Koskinen, E. Kallio, P. Riihela, T. Sales, W. Schmidt, J. Kozyra, N. Krupp, M. Franz, J. Woch, J. Luhmann, S. McKenna-Lawlor, C. Mazelle, J. J. Thocaven, S. Orsini, R. Cerulli-Irelli, M. Mura, M. Milillo, M. Maggi, E. Roelof, P. Brandt, K. Szego, J. D. Winningham, R. A. Frahm, J. Scherrer, J. R. Sharber, P. Wurz, and P. Bochsler (2007a), The loss of ions from Venus through the plasma wake, *Nature*, *450*(7170), 650–653, doi:10.1038/nature06434.

Barabash, S., J. A. Sauvaud, H. Gunell, H. Andersson, A. Grigoriev, K. Brinkfeldt, M. Holmström, R. Lundin, M. Yamauchi, K. Asamura, W. Baumjohann, T. L. Zhang, A. J. Coates, D. R. Linder, D. O. Kataria, C. C. Curtis, K. C. Hsieh, B. R. Sandel, A. Fedorov, C. Mazelle, J. J. Thocaven, M. Grande, H. E. J. Koskinen, E. Kallio, T. Säles, P. Riihela, J. Kozyra, N. Krupp, J. Woch, J. Luhmann, S. McKenna-Lawlor, S. Orsini, R. Cerulli-Irelli, M. Mura, M. Milillo, M. Maggi, E. Roelof, P. Brandt, C. T. Russell, K. Szego, J. D. Winningham, R. A. Frahm, J. Scherrer, J. R. Sharber, P. Wurz, and P. Bochsler (2007b), The Analyser of Space Plasmas and Energetic Atoms (ASPERA-4) for the Venus Express mission, *Planetary and Space Science*, *55*(12), 1772–1792, doi:10.1016/j.pss.2007.01.014.

Barath, F. T., J. Copeland, D. E. Jones, A. H. Barrett, and A. E. Lilley (1964), Mariner 2 microwave radiometer experiment and results, *Astronomical Journal*, *69*(1), 49–58, doi:10.1086/109227.

Barrett, A. H. (1960), Microwave absorption and emission in the atmosphere of Venus, *Journal of Geophysical Research*, *65*(6), 1835–1838, doi:10.1029/JZ065i006p01835.

Barrett, A. H. (1961), Microwave absorption and emission in the atmosphere of Venus, *Astrophysical Journal*, *133*(1), 281–293, doi:10.1086/147024.

Barstow, J. K., C. C. C. Tsang, C. F. Wilson, P. G. J. Irwin, F. W. Taylor, K. McGouldrick, P. Drossart, G. Piccioni, and S. Tellmann (2012), Models of the global cloud structure on Venus derived from Venus Express observations, *Icarus*, *217*(2), 542–560, doi:10.1016/j.icarus.2011.05.018.

Barsukov, V. L. (1992), Venusian igneous rocks, in *Venus Geology*, edited by V. L. Barsukov, A. T. Basilevsky, V. P. Volkov, and V. N. Zharkov, pp. 165–176, Univ. Arizona Press, Tucson.

Barsukov, V. L., A. T. Basilevsky, R. O. Kuzmin, A. A. Pronin, V. P. Kryuchkov, O. V. Nikolayeva, I. M. Chernaya, G. A. Burba, N. N. Bobina, V. P. Shashkina, M. S. Markov, and A. L. Sukhanov (1984), Geology of Venus from the results of

analysis of radar images taken by Venera-15 and Venera-16 probes - Preliminary data, *Geokhimiya*, (12), 1811–1820.

Barsukov, V. L., A. T. Basilevsky, G. A. Burba, N. N. Bobinna, V. P. Kryuchkov, R. O. Kuzmin, O. V. Nikolaeva, A. A. Pronin, L. B. Ronco, I. M. Chernaya, V. P. Shashkina, A. V. Garanin, E. R. Kushky, M. S. Markov, A. L. Sukhanov, V. A. Kotelnikov, O. N. Rzhiga, G. M. Petrov, Y. N. Alexandrov, A. I. Sidorenko, A. F. Bogomolov, G. I. Skrypnik, M. Y. Bergman, L. V. Kudrin, I. M. Bokshtein, M. A. Kronrod, P. A. Chochia, Y. S. Tyuflin, S. A. Kadnichansky, and E. L. Akim (1986), The geology and geomorphology of the Venus surface as revealed by the radar images obtained by Veneras 15 and 16, *Journal of Geophysical Research*, *91*(B4), 378–398.

Basilevsky, A. T. (1997), Venera 8 landing site geology revisited, *Journal of Geophysical Research-Planets*, *102*(E4), 9257–9262, doi:10.1029/97je00413.

Basilevsky, A. T., and J. W. Head (1998), The geologic history of Venus: A stratigraphic view, *Journal of Geophysical Research-Planets*, *103*(E4), 8531–8544, doi:10.1029/98JE00487.

Basilevsky, A. T., and J. W. Head (2000a), Geologic units on Venus: Evidence for their global correlation, *Planetary and Space Science*, *48*(1), 75–111, doi:10.1016/S0032-0633(99)00083-5.

Basilevsky, A. T., and J. W. Head (2000b), Rifts and large volcanoes on Venus: Global assessment of their age relations with regional plains, *Journal of Geophysical Research-Planets*, *105*(E10), 24,583–24,611, doi:10.1029/2000JE001260.

Basilevsky, A. T., and J. W. Head (2002), Venus: Timing and rates of geologic activity, *Geology*, *30*(11), 1015–1018, doi:10.1130/0091-7613(2002)030⟨1015:VTAROG⟩2.0.CO;2.

Basilevsky, A. T., E. V. Shalygin, D. V. Titov, W. J. Markiewicz, F. Scholten, T. Roatsch, M. A. Kreslavsky, L. V. Moroz, N. I. Ignatiev, B. Fiethe, B. Osterloh, and H. Michalik (2012), Geologic interpretation of the near-infrared images of the surface taken by the Venus Monitoring Camera, Venus Express, *Icarus*, *217*(2), 434–450, doi:10.1016/j.icarus.2011.11.003.

Belyaev, D., O. Korablev, A. Fedorova, J.-L. Bertaux, A. C. Vandaele, F. Montmessin, A. Mahieux, V. Wilquet, and R. Drummond (2008), First observations of SO_2 above Venus' clouds by means of Solar Occultation in the Infrared, *Journal of Geophysical Research-Planets*, *113*, doi:10.1029/2008je003143.

Belyaev, D., F. Montmessin, J.-L. Bertaux, A. C. Vandaele, A. Mahieux, and A. Fedorova (2009), Vertical profiling of SO_2 above Venus' clouds by means of SPICAV/SOIR occultations, *Bulletin of the American Astronomical Society*, *41*, 1120–1120.

Belyaev, D. A., F. Montmessin, J.-L. Bertaux, A. Mahieux, A. A. Fedorova, O. I. Korablev, E. Marcq, Y. L. Yung, and X. Zhang (2012), Vertical profiling of SO_2 and SO above Venus' clouds by SPICAV/SOIR solar occultations, *Icarus*, *217*(2), 740–751, doi:10.1016/j.icarus.2011.09.025.

Bertaux, J.-L., D. Nevejans, O. Korablev, E. Villard, E. Quémerais, E. Neefs, F. Montmessin, F. Leblanc, J. P. Dubois, E. Dimarellis, A. Hauchecorne, F. Lefèvre, P. Rannou, J. Y. Chaufray, M. Cabane, G. Cernogora, G. Souchon, F. Semelin, A. Reberac, E. Van Ransbeek, S. Berkenbosch, R. Clairquin, C. Muller, F. Forget, F. Hourdin, O. Talagrand, A. Rodin, A. Fedorova, A. Stepanov, I. Vinogradov, A. Kiselev, Y. Kalinnikov, G. Durry, B. Sandel, A. Stern, and J. C. Gérard (2007), SPICAV on Venus Express: Three spectrometers to study the global structure and composition of the Venus atmosphere, *Planetary and Space Science*, *55*(12), 1673–1700, doi:10.1016/j.pss.2007.01.016.

Bertucci, C., F. Duru, N. Edberg, M. Fraenz, C. Martinecz, K. Szego, and O. Vaisberg (2011), The induced magnetospheres of Mars, Venus, and Titan, *Space Science Reviews*, *162*(1-4), 113–171, doi:10.1007/s11214-011-9845-1.

Bézard, B., C. C. C. Tsang, R. W. Carlson, G. Piccioni, E. Marcq, and P. Drossart (2009), Water vapor abundance near the surface of Venus from Venus Express/VIRTIS observations, *Journal of Geophysical Research-Planets*, *114*, doi:10.1029/2008je003251.

Bézard, B., A. Fedorova, J.-L. Bertaux, A. Rodin, and O. Korablev (2011), The 1.10- and 1.18-μm nightside windows of Venus observed by SPICAV-IR aboard Venus Express, *Icarus*, *216*(1), 173–183, doi:10.1016/j.icarus.2011.08.025.

Bjonnes, E. E., V. L. Hansen, B. James, and J. B. Swenson (2012), Equilibrium resurfacing of Venus: Results from new Monte Carlo modeling and implications for Venus surface histories, *Icarus*, *217*(2), 451–461, doi:10.1016/j.icarus.2011.03.033.

Bouvier, A., and M. Wadhwa (2010), The age of the Solar System redefined by the oldest Pb-Pb age of a meteoritic inclusion, *NATURE GEOSCIENCE*, *3*(9), 637–641, doi:10.1038/NGEO941.

Brace, L. H., and A. J. Kliore (1991), The structure of the Venus ionosphere, *Space Science Reviews*, *55*(1-4), 81–163.

Branca, S., M. Coltelli, G. Groppelli, and F. Lentini (2011), Geological map of Etna volcano, 1:50,000 scale, *Italian Journal of Geosciences*, *130*(3), 265–291, doi:10.3301/IJG.2011.15.

Bray, V. J., D. B. J. Bussey, R. C. Ghail, A. P. Jones, and K. T. Pickering (2007), Meander geometry of Venusian canali: Constraints on flow regime and formation time, *Journal of Geophysical Research-Planets*, *112*(E4), doi:10.1029/2006je002785.

Brown, C. D., and R. E. Grimm (1999), Recent tectonic and lithospheric thermal evolution of Venus, *Icarus*, *139*(1), 40–48, doi:10.1006/icar.1999.6083.

Bullock, M. A., and D. H. Grinspoon (1996), The stability of climate on Venus, *Journal of Geophysical Research-Planets*, *101*(E3), 7521–7529, doi:10.1029/95je03862.

Bullock, M. A., and D. H. Grinspoon (2001), The recent evolution of climate on Venus, *Icarus*, *150*(1), 19–37, doi:10.1006/icar.2000.6570.

Campbell, B. A. (1994), Merging Magellan emissivity and SAR data for analysis of Venus surface dielectric properties, *Icarus*, *112*(1), 187–203, doi:http://dx.doi.org/10.1006/icar.1994.1177.

Campbell, B. A. (1995), Use and presentation of Magellan quantitative data in Venus mapping, Open-file report 95-519, *Report*, U.S. Dept. of the Interior, U.S. Geological Survey.

Campbell, B. A., and D. B. Campbell (1992), Analysis of volcanic surface-morphology on Venus from comparison of Arecibo, Magellan, and terrestrial airborne radar data, *Journal of Geophysical Research-Planets*, *97*(E10), 16,293–16,314.

Campbell, B. A., and P. G. Campbell (2002), Geologic map of the Bell Regio Quadrangle (V-9), Venus [map].

Campbell, B. A., and P. G. Rogers (1994), Bell Regio, Venus - integration of remote-sensing data and terrestrial analogs for geologic analysis, *Journal of Geophysical Research-Planets*, *99*(E10), 21,153–21,171, doi:10.1029/94je01862.

Campbell, B. A., L. S. Glaze, and P. G. Rogers (1998), Pyroclastic deposits on Venus: Remote-sensing evidence and modes of formation [abstract], *Lunar and Planetary Science Conference XXIX*.

Campbell, B. A., D. B. Campbell, and C. H. DeVries (1999), Surface processes in the Venus highlands: Results from analysis of Magellan and Arecibo data, *Journal of Geophysical Research-Planets*, *104*(E1), 1897–1916, doi:10.1029/1998je900022.

Campbell, D., J. Head, J. Harmon, and A. Hine (1984), Venus - Volcanism and rift formation in Beta Regio, *Science*, *226*(4671), 167–170, doi:10.1126/science.226.4671.167.

Campbell, D. B., N. J. S. Stacy, W. I. Newman, R. E. Arvidson, E. M. Jones, G. S. Musser, A. Y. Roper, and C. Schaller (1992), Magellan observations of extended impact crater related features on the surface of Venus, *Journal of Geophysical Research-Planets*, *97*(E10), 16,249–16,277.

Canon-Tapia, E., and R. Mendoza-Borunda (2014), Insights into the dynamics of planetary interiors obtained through the study of global distribution of volcanoes I: Empirical calibration on Earth, *Journal of Volcanology and Geothermal Research*, *281*, 53–69, doi:10.1016/j.jvolgeores.2014.05.015.

Carlson, R. W., L. W. Kamp, K. H. Baines, J. B. Pollack, D. H. Grinspoon, T. Encrenaz, P. Drossart, and F. W. Taylor (1993), Variations in Venus cloud particle properties - a new view of Venus cloud morphology as observed by the Galileo near-infrared mapping spectrometer, *Planetary and Space Science*, *41*(7), 477–485, doi:10.1016/0032-0633(93)90030-6.

Clauser, C. (2011), Radiogenic heat production in rocks, in *Encyclopedia of soild Earth geophysics*, edited by H. Gupta, 2nd ed., pp. 1–10, Springer, Dordrecht.

Clifford, S. M., J. Lasue, E. Heggy, J. Boisson, P. McGovern, and M. D. Max (2010), Depth of the Martian cryosphere: Revised estimates and implications for the existence and detection of subpermafrost groundwater, *Journal of Geophysical Research-Planets*, *115*, 17, doi:10.1029/2009je003462.

Coates, A. J., R. A. Frahm, D. R. Linder, D. O. Kataria, Y. Soobiah, G. Collinson, J. R. Sharber, J. D. Winningham, S. J. Jeffers, S. Barabash, J. A. Sauvaud, R. Lundin, M. Holmstrom, Y. Futaana, M. Yamauchi, A. Grigoriev, H. Andersson, H. Gunell, A. Fedorov, J. J. Thocaven, T. L. Zhang, W. Baumjohann, E. Kallio, H. Koskinen, J. U. Kozyra, M. W. Liemohn, Y. Ma, A. Galli, P. Wurz, P. Bochsler, D. Brain, E. C. Roelof, P. Brandt, N. Krupp, J. Woch, M. Fraenz, E. Dubinin, S. McKenna-Lawlor, S. Orsini, R. Cerulli-Irelli, A. Mura, A. Milillo, M. Maggi, C. C. Curtis, B. R. Sandel, K. C. Hsieh, K. Szego, A. Asamura, and M. Grande (2008), Ionospheric photoelectrons at Venus: Initial observations by ASPERA-4 ELS, *Planetary and Space Science*, *56*(6), 802–806, doi:10.1016/j.pss.2007.12.008.

Cole, P., E. Calder, T. Druitt, R. Hoblitt, R. Robertson, R. Sparks, and S. Young (1998), Pyroclastic flows generated by gravitational instability of the 1996-97 lava dome of Soufriere Hills Volcano, Montserrat, *Geophysical Research Letters*, *25*(18), 3425–3428, doi:10.1029/98GL01510.

Collins, G. C., J. W. Head, A. T. Basilevsky, and M. A. Ivanov (1999), Evidence for rapid regional plains emplacement on Venus from the population of volcanically embayed impact craters, *Journal of Geophysical Research-Planets*, *104*(E10), 24,121–24,139, doi:10.1029/1999je001041.

Copernicus, N. (1543), *De revolutionibus orbium coelestium (On the revolutions of the heavenly spheres)*, 196 pp., Johannes Petreius, Nuremberg.

Corti, G. (2009), Continental rift evolution: From rift initiation to incipient break-up in the Main Ethiopian Rift, East Africa, *Earth-Science Reviews*, *96*(1-2), 1–53, doi:10.1016/j.earscirev.2009.06.005.

Cottini, V., N. I. Ignatiev, G. Piccioni, P. Drossart, D. Grassi, and W. J. Markiewicz (2012), Water vapor near the cloud tops of Venus from Venus Express/VIRTIS dayside data, *Icarus*, *217*(2), doi:10.1016/j.icarus.2011.06.018.

Crisp, D. (1986), Radiative forcing of the Venus mesosphere 1. Solar fluxes and heating rates, *Icarus*, *67*(3), 484–514, doi:10.1016/0019-1035(86)90126-0.

Crumpler, L. S., and J. C. Aubele (2000), Volcanism on Venus, in *Encyclopedia of volcanoes*, edited by H. Sigurdsson, pp. 727–769, Academic Press, San Diego.

Crumpler, L. S., J. C. Aubele, D. A. Senske, S. T. Keddie, K. P. Magee, and J. W. Head (1997), Volcanoes and Centers of Volcanism on Venus, in *Venus II: Geology, Geophysics, Atmosphere, and Solar Wind Environment*, edited by S. W. Bougher, D. M. Hunten, and R. J. Phillips, pp. 697–756, University of Arizona Press, Tucson.

De Bergh, C., B. Bezard, T. Owen, D. Crisp, J. P. Maillard, and B. L. Lutz (1991), Deuterium on Venus - observations from Earth, *Science*, *251*(4993), 547–549, doi: 10.1126/science.251.4993.547.

Diez, M. (2006), Solution and parametric sensitivity study of a coupled conduit and eruption column model, in *Statistics in volcanology*, edited by H. M. Mader, S. G. Coles, C. B. Connor, and L. J. Connor, Special Publications of IAVCEI, No. 1, book section 15, The Geological Society, London.

Dixon, J. E. (1997), Degassing of alkalic basalts, *American Mineralogist*, *82*(3-4), 368–378.

Dombard, A. J., C. L. Johnson, M. A. Richards, and S. C. Solomon (2007), A magmatic loading model for coronae on Venus, *Journal of Geophysical Research-Planets*, *112*(E4), doi:10.1029/2006je002731.

Donahue, T., J. Hoffman, R. Hodges, and A. Watson (1982), Venus was wet: A measurement of the ratio of deuterium to hydrogen, *Science*, *216*(4546), doi: 10.1126/science.216.4546.630.

Donahue, T. M. (1999), New analysis of hydrogen and deuterium escape from Venus, *Icarus*, *141*(2), 226–235, doi:10.1006/icar.1999.6186.

Drossart, P., G. Piccioni, A. Adriani, F. Angrilli, G. Arnold, K. H. Baines, G. Bellucci, J. Benkhoff, B. Bézard, J. P. Bibring, A. Blanco, M. I. Blecka, R. W. Carlson, A. Coradini, A. Di Lellis, T. Encrenaz, S. Erard, S. Fonti, V. Formisano, T. Fouchet, R. Garcia, R. Haus, J. Helbert, N. I. Ignatiev, P. G. J. Irwin, Y. Langevin, S. Lebonnois, M. A. Lopez-Valverde, D. Luz, L. Marinangeli, V. Orofino, A. V. Rodin, M. C. Roos-Serote, B. Saggin, A. Sanchez-Lavega, D. M. Stam, F. W. Taylor, D. Titov, G. Visconti, M. Zambelli, R. Hueso, C. C. C. Tsang, C. F. Wilson, and T. Z. Afanasenko (2007), Scientific goals for the observation of Venus by VIRTIS on ESA/Venus Express mission, *Planetary and Space Science*, *55*(12), 1653–1672, doi:10.1016/j.pss.2007.01.003.

Elkins-Tanton, L. T., S. E. Smrekar, P. C. Hess, and E. M. Parmentier (2007), Volcanism and volatile recycling on a one-plate planet: Applications to Venus, *Journal of Geophysical Research-Planets*, *112*(E4), doi:E04s0610.1029/2006je002793.

Engel, A. E. J., and C. G. Engel (1964), Composition of basalts from mid-atlantic ridge, *Science*, *144*(362), 1330–1333, doi:10.1126/science.144.3624.1330.

Ernst, R. E., and D. W. Desnoyers (2004), Lessons from Venus for understanding mantle plumes on Earth, *Physics of the Earth and Planetary Interiors*, *146*(1-2), 195–229, doi:10.1016/j.pepi.203.10.012.

Esposito, L. W. (1984), Sulfur-dioxide - episodic injection shows evidence for active Venus volcanism, *Science*, *223*(4640), 1072–1074, doi:10.1126/science.223.4640.1072.

Esposito, L. W. (1985), Long term changes in Venus sulfur dioxide, *Advances in Space Research*, *5*(9), 85–90, doi:10.1016/0273-1177(85)90274-1.

Esposito, L. W., R. G. Knollenberg, M. Y. Marov, O. B. Toon, and R. P. Turco (1983), *The clouds and hazes of Venus*, Venus, 484-564 pp., University of Arizona Press.

Esposito, L. W., J. L. Bertaux, V. A. Krasnopolsky, V. I. Moroz, and L. V. Zasova (1997), Chemistry of lower atmosphere and clouds, in *Venus II: Geology, Geophysics, Atmosphere, and Solar Wind Environment*, edited by S. W. Bougher, D. M. Hunten, and R. J. Phillips, pp. 415–458, University of Arizona Press, Tuscon AZ.

Esposito, L. W., E. R. Stofan, and T. E. Cravens (2007), Exploring Venus: Major scientific issues and directions, in *Exploring Venus as a terrestrial planet: Geophysical monograph 176*, edited by L. W. Esposito, E. R. Stofan, and E. Cravens, American Geophysical Union, Washington, DC.

Fagents, S. A., and L. Wilson (1995), Explosive volcanism on Venus: Transient volcanic explosions as a mechanism for localized pyroclast dispersal, *Journal of Geophysical Research-Planets*, *100*(E12), 26,327–26,338, doi:10.1029/95je03202.

Fegley, B. (2004), Venus, in *Meteorites, Comets, and Planets*, vol. 1 Treatise on Geochemistry, edited by A. M. Davis, book section 21, pp. 487–507, Elsevier-Pergamon, Oxford.

Fegley, B., and R. G. Prinn (1989), Estimation of the rate of volcanism on Venus from reaction-rate measurements, *Nature*, *337*(6202), 55–58, doi:10.1038/337055a0.

Field, L., J. Blundy, R. A. Brooker, T. Wright, and G. Yirgu (2012), Magma storage conditions beneath Dabbahu volcano (Ethiopia) constrained by petrology, seismicity and satellite geodesy, *Bulletin of Volcanology*, *74*(5), 981–1004, doi: 10.1007/s00445-012-0580-6.

Fierstein, J., and C. Wilson (2005), Assembling an ignimbrite: Compositionally defined eruptive packages in the 1912 Valley of Ten Thousand Smokes ignimbrite, Alaska, *Geological Society of America Bulletin*, *117*(7-8), 1094–1107, doi:10.1130/B25621.1.

Fink, J. H., N. T. Bridges, and R. E. Grimm (1993), Shapes of Venusian pancake domes imply episodic emplacement and silicic composition, *Geophysical Research Letters*, *20*(4), 261–264, doi:10.1029/92gl03010.

Folkes, C. B., H. M. Wright, R. A. F. Cas, S. L. de Silva, C. Lesti, and J. G. Viramonte (2011), A re-appraisal of the stratigraphy and volcanology of the Cerro Galán volcanic system, NW Argentina, *Bulletin of Volcanology*, *73*(10), 1427–1454, doi:10.1007/s00445-011-0459-y.

Ford, J. P., J. J. Plaut, C. M. Weitz, T. G. Farr, D. A. Senske, E. R. Stofan, G. Michaels, and T. J. Parker (1993), *Guide to Magellan image interpretation*, JPL, Pasadena.

Ford, P. G. (1991), Global altimetry and radiometry data records, MIT-MGN-GxDR SIS version 2.3, 40 pp.

Ford, P. G., and G. H. Pettengill (1992), Venus topography and kilometer scale slopes, *Journal of Geophysical Research-Planets*, *97*(E8), 13,103–13,114.

Foster, A., and F. Nimmo (1996), Comparisons between the rift systems of East Africa, Earth and Beta Regio, Venus, *Earth and Planetary Science Letters*, *143*(1-4), 183–195, doi:10.1016/0012-821x(96)00146-x.

Fung, A. K., and K. S. Chen (2010), *Microwave scattering and emission models for users*, Artech House, Norwood, MA.

Garvin, J. B., J. W. Head, and L. Wilson (1982), Magma vesiculation and pyroclastic volcanism on venus, *Icarus*, *52*(2), 365–372, doi:http://dx.doi.org/10.1016/0019-1035(82)90119-1.

Gerya, T. V. (2014), Plume-induced crustal convection: 3D thermomechanical model and implications for the origin of novae and coronae on Venus, *Earth and Planetary Science Letters*, *391*, 183–192, doi:10.1016/j.epsl.2014.02.005.

Ghail, R. C. (2015), Rheological and petrological implications for a stagnant lid regime on Venus, *Planetary and Space Science*, *113*, 2–9, doi:10.1016/j.pss.2015.02.005.

Ghail, R. C., and L. Wilson (2013), A pyroclastic flow deposit on Venus, *Geological Society, London, Special Publications*, *401*, doi:10.1144/sp401.1.

Ghiorso, M. S., and R. O. Sack (1995), Chemical mass-transfer in magmatic processes IV: A revised and internally consistent thermodynamic model for the interpolation and extrapolation of liquid-solid equilibria in magmatic systems at elevated temperatures and pressures, *Contributions to Mineralogy and Petrology*, *119*(2-3), 197–212, doi:10.1007/bf00307281.

Gilbert, J. S., S. J. Lane, R. S. J. Sparks, and T. Koyaguchi (1991), Charge measurements on particle fallout from a volcanic plume, *Nature*, *349*(6310), 598–600, doi:10.1038/349598a0.

Giordano, D., J. K. Russell, and D. B. Dingwell (2008), Viscosity of magmatic liquids: A model, *Earth and Planetary Science Letters*, *271*(1-4), 123–134, doi:10.1016/j.epsl.2008.03.038.

Glaze, L. S. (1999), Transport of SO_2 by explosive volcanism on Venus, *Journal of Geophysical Research-Planets*, *104*(E8), 18,899–18,906, doi:10.1029/1998je000619.

Glaze, L. S., S. M. Baloga, and L. Wilson (1997), Transport of atmospheric water vapor by volcanic eruption columns, *Journal of Geophysical Research-Atmospheres*, *102*(D5), 6099–6108, doi:10.1029/96jd03125.

Glaze, L. S., S. M. Baloga, and J. Wimert (2011), Explosive volcanic eruptions from linear vents on Earth, Venus, and Mars: Comparisons with circular vent eruptions, *Journal of Geophysical Research-Planets*, *116*, doi:10.1029/2010je003577.

Gonnermann, H. M., and M. Manga (2003), Explosive volcanism may not be an inevitable consequence of magma fragmentation, *Nature*, *426*(6965), 432–435, doi:10.1038/nature02138.

Gonnermann, H. M., and M. Manga (2012), Dynamics of magma ascent in the volcanic conduit, in *Modeling volcanic processes: The physics and mathematics of volcanism*, edited by S. A. Fagents, T. K. P. Gregg, and R. M. C. Lopes, Cambridge University Press, Cambridge.

Greeley, R., R. E. Arvidson, C. Elachi, M. A. Geringer, J. J. Plaut, R. S. Saunders, G. Schubert, E. R. Stofan, E. J. P. Thouvenot, S. D. Wall, and C. M. Weitz (1992), Aeolian features on Venus - preliminary Magellan results, *Journal of Geophysical Research-Planets*, *97*(E8), 13,319–13,345.

Gregg, T. K. P., and R. Greeley (1993), Formation of Venusian canali - considerations of lava types and their thermal behaviors, *Journal of Geophysical Research-Planets*, *98*(E6), 10,873–10,882, doi:10.1029/93je00692.

Grinspoon, D. H. (1993), Implications of the high D/H ratio for the sources of water in Venus atmosphere, *Nature*, *363*(6428), 428–431, doi:10.1038/363428a0.

Grinspoon, D. H., J. B. Pollack, B. R. Sitton, R. W. Carlson, L. W. Kamp, K. H. Baines, T. Encrenaz, and F. W. Taylor (1993), Probing Venus cloud structure with Galileo NIMS, *Planetary and Space Science*, *41*(7), 515–542, doi:10.1016/0032-0633(93)90034-y.

Grosfils, E. B., S. M. Long, E. M. Venechuk, D. M. Hurwitz, J. W. Richards, B. Kastl, D. E. Drury, and J. Hardin (2011), Geologic map of the Ganiki Planitia Quadrangle (V-14), Venus [map].

Guest, J., M. Bulmer, J. Aubele, K. Beratan, R. Greeley, J. Head, G. Michaels, C. Weitz, and C. Wiles (1992), Small volcanic edifices and volcanism in the plains of Venus, *Journal of Geophysical Research-Planets*, *97*(E10), 15,949–15,966.

Guest, J. E., and E. R. Stofan (1999), A new view of the stratigraphic history of Venus, *Icarus*, *139*(1), 55–66, doi:http://dx.doi.org/10.1006/icar.1999.6091.

Gurnett, D. A., W. S. Kurth, A. Roux, R. Gendrin, C. F. Kennel, and S. J. Bolton (1991), Lightning and plasma-wave observations from the Galileo flyby of Venus, *Science*, *253*(5027), 1522–1525, doi:10.1126/science.253.5027.1522.

Haar, L., J. S. Gallagher, and G. S. Kell (1984), *NBS/NRC Steam Tables*, 320 pp., Hemisphere Publishing Corporation, New York.

Hansell, S. A., W. K. Wells, and D. M. Hunten (1995), Optical detection of lightning on Venus, *Icarus*, *117*(2), 345–351, doi:10.1006/icar.1995.1160.

Harrison, R. G., K. L. Aplin, F. Leblanc, and Y. Yair (2008), Planetary atmospheric electricity, *Space Science Reviews*, *137*(1-4), 5–10, doi:10.1007/s11214-008-9419-z.

Hashimoto, G. L., and T. Imamura (2001), Elucidating the rate of volcanism on Venus: Detection of lava eruptions using near-infrared observations, *Icarus*, *154*(2), 239–243, doi:10.1006/icar.2001.6713.

Häusler, B., M. Pätzold, G. L. Tyler, R. A. Simpson, M. K. Bird, V. Dehant, J. P. Barriot, W. Eidel, R. Mattei, S. Remus, J. Selle, S. Tellmann, and T. Imamura (2006), Radio science investigations by VeRa onboard the Venus Express spacecraft, *Planetary and Space Science*, *54*(13&14), 1315–1335, doi:10.1016/j.pss.2006.04.032.

Head, J. W., and L. Wilson (1986), Volcanic processes and landforms of Venus - theory, predictions, and observations, *Journal of Geophysical Research-Solid Earth and Planets*, *91*(B9), 9407–9446, doi:10.1029/JB091iB09p09407.

Head, J. W., and L. Wilson (1992), Magma reservoirs and neutral buoyancy zones on Venus: Implications for the formation and evolution of volcanic landforms, *Journal of Geophysical Research*, *97*(E3), 3877–3903, doi:10.1029/92je00053.

Head, J. W., D. B. Campbell, C. Elachi, J. E. Guest, D. P. McKenzie, R. S. Saunders, G. G. Schaber, and G. Schubert (1991), Venus volcanism - initial analysis from Magellan data, *Science*, *252*(5003), 276–288, doi:10.1126/science.252.5003.276.

Head, J. W., L. S. Crumpler, J. C. Aubele, J. E. Guest, and R. S. Saunders (1992), Venus volcanism - classification of volcanic features and structures, associations, and global distribution from Magellan data, *Journal of Geophysical Research-Planets*, *97*(E8), 13,153–13,197.

Herrick, R. R., and R. J. Phillips (1994), Implications of a global survey of Venusian impact craters, *Icarus*, *111*(2), 387–416, doi:10.1006/icar.1994.1152.

Herrick, R. R., and M. E. Rumpf (2011), Postimpact modification by volcanic or tectonic processes as the rule, not the exception, for Venusian craters, *Journal of Geophysical Research-Planets*, *116*, doi:10.1029/2010je003722.

Herrick, R. R., J. Dufek, and P. J. McGovern (2005), Evolution of large shield volcanoes on Venus, *Journal of Geophysical Research-Planets*, *110*(E1), doi:10.1029/2004je002283.

Holland, H. D. (2006), The oxygenation of the atmosphere and oceans, *Philosophical Transactions of the Royal Society B-Biological Sciences*, *361*(1470), 903–915, doi: 10.1098/rstb.2006.1838.

Ivanov, M., and J. Head (2004), Stratigraphy of small shield volcanoes on Venus: Criteria for determining stratigraphic relationships and assessment of relative age and temporal abundance, *Journal of Geophysical Research-Planets*, *109*(E10), doi: 10.1029/2004JE002252.

Ivanov, M. A., and J. W. Head (1999), Stratigraphic and geographic distribution of steep-sided domes on Venus: Preliminary results from regional geological mapping and implications for their origin, *Journal of Geophysical Research-Planets*, *104*(E8), 18,907–18,924, doi:10.1029/1999je001039.

Ivanov, M. A., and J. W. Head (2011), Global geological map of Venus, *Planetary and Space Science*, *59*(13), 1559–1600, doi:10.1016/j.pss.2011.07.008.

Ivanov, M. A., and J. W. Head (2013), The history of volcanism on Venus, *Planetary and Space Science*, *84*, 66–92, doi:10.1016/j.pss.2013.04.018.

Ivanov, M. A., and J. W. Head (2015), The history of tectonism on Venus: A stratigraphic analysis, *Planetary and Space Science*, *113114*, 10 – 32, doi:10.1016/j.pss.2015.03.016.

Jakosky, B. M., R. O. Pepin, R. E. Johnson, and J. L. Fox (1994), Mars atmospheric loss and isotopic fractionation by solar-wind-induced sputtering and photochemical escape, *Icarus*, *111*(2), 271–288, doi:10.1006/icar.1994.1145.

James, E. P., O. B. Toon, and G. Schubert (1997), A numerical microphysical model of the condensational Venus cloud, *Icarus*, *129*(1), 147–171, doi:10.1006/icar.1997.5763.

James, M. R., S. J. Lane, and J. S. Gilbert (2000), Volcanic plume electrification: Experimental investigation of a fracture-charging mechanism, *Journal of Geophysical Research-Solid Earth*, *105*(B7), 16,641–16,649, doi:10.1029/2000jb900068.

James, M. R., L. Wilson, S. J. Lane, J. S. Gilbert, T. A. Mather, R. G. Harrison, and R. S. Martin (2008), Electrical charging of volcanic plumes, *Space Science Reviews*, *137*(1-4), 399–418, doi:10.1007/s11214-008-9362-z.

Janes, D., S. Squyres, D. Bindschadler, G. Baer, G. Schubert, V. Sharpton, and E. Stofan (1992), Geophysical models for the formation and evolution of coronae on Venus, *Journal of Geophysical Research-Planets*, *97*(E10), 16,055–16,067.

Jones, A. P., and K. T. Pickering (2003), Evidence for aqueous fluid-sediment transport and erosional processes on Venus, *Journal of the Geological Society*, *160*, 319–327, doi:10.1144/0016-764902-111.

Kargel, J. S., G. Komatsu, V. R. Baker, and R. G. Strom (1993), The volcanology of Venera and Vega landing sites and the geochemistry of Venus, *Icarus*, *103*(2), 253–275, doi:10.1006/icar.1993.1069.

Kargel, J. S., R. L. Kirk, B. Fegley, and A. H. Treiman (1994), Carbonate sulfate volcanism on Venus, *Icarus*, *112*(1), 219–252, doi:10.1006/icar.1994.1179.

Kasting, J. F. (1993), Earth's early atmosphere, *Science*, *259*(5097), 920–926, doi:10.1126/science.11536547.

Kaula, W. M. (1999), Constraints on Venus evolution from radiogenic argon, *Icarus*, *139*(1), 32–39, doi:10.1006/icar.1999.6082.

Keddie, S. T., and J. W. Head (1994), The height and altitude distribution of large volcanoes on Venus, *Planetary and Space Science*, *42*(6), 455–462, doi:10.1016/0032-0633(94)90088-4.

Keddie, S. T., and J. W. Head (1995), Formation and evolution of volcanic edifices on the Dione-Regio rise, Venus, *Journal of Geophysical Research-Planets*, *100*(E6), 11,729–11,754, doi:10.1029/95je00822.

Kendall, J., G. Stuart, C. Ebinger, I. Bastow, and D. Keir (2005), Magma-assisted rifting in Ethiopia, *Nature*, *433*(7022), 146–148, doi:10.1038/nature03161.

Kerzhanovich, V. V., and S. S. Limaye (1985), Circulation of the atmosphere from the surface to 100 km, *Advances in Space Research*, *5*(11), 59–83, doi:http://dx.doi.org/10.1016/0273-1177(85)90198-X.

Kim, Y. J., E. Rodríguez, and S. L. Durden (1992), A numerical assessment of rough-surface scattering theories: Vertical polarization, *Radio Science*, *27*(4), 515–527, doi:10.1029/91RS02637.

Klose, K. B., J. A. Wood, and A. Hashimoto (1992), Mineral equilibria and the high radar reflectivity of Venus mountaintops, *Journal of Geophysical Research-Planets*, *97*(E10), 16,353–16,369.

Knollenberg, R. G., and D. M. Hunten (1980), The microphysics of the clouds of Venus: Results of the Pioneer Venus particle size spectrometer experiment, *Journal of Geophysical Research*, *85*(A13), 8039–8058, doi:10.1029/JA085iA13p08039.

Koptev, A., E. Calais, E. Burov, S. Leroy, and T. Gerya (2015), Dual continental rift systems generated by plume-lithosphere interaction, *Nature Geoscience*, *8*(5), 388–392, doi:10.1038/NGEO2401.

Krasnopolsky, V. A. (1980), Lightning on Venus according to information obtained by the satellites Venera 9 and 10, *Cosmic Research*, *18*(3), 325–330.

Krasnopolsky, V. A. (1983), Lightnings and nitric oxide on Venus, *Planetary and Space Science*, *31*(11), 1363–1369, doi:10.1016/0032-0633(83)90072-7.

Krasnopolsky, V. A. (2006), A sensitive search for nitric oxide in the lower atmospheres of Venus and Mars: Detection on Venus and upper limit for Mars, *Icarus*, *182*(1), 80–91, doi:10.1016/j.icarus.2005.12.003.

Krasnopolsky, V. A., and J. B. Pollack (1994), H_2O-H_2SO_4 system in Venus clouds and OCS, CO, and H_2SO_4 profiles in Venus troposphere, *Icarus*, *109*(1), 58–78, doi:10.1006/icar.1994.1077.

Krassilnikov, A., V.-P. Kostama, M. Aittola, E. Guseva, and O. Cherkashina (2012), Relationship of coronae, regional plains and rift zones on Venus, *Planetary and Space Science*, *68*(1), 56–75, doi:http://dx.doi.org/10.1016/j.pss.2011.11.017.

Krassilnikov, A. S. (2002), Tectonic structure, classification, and evolution of arachnoids on Venus: Preliminary results, *Solar System Research*, *36*(5), 374–402, doi:10.1023/a:1020411404593.

Krassilnikov, A. S., and J. W. Head (2003), Novae on Venus: Geology, classification, and evolution, *Journal of Geophysical Research-Planets*, *108*(E9), doi:10.1029/2002je001983.

Krotikov, V. D. (1962), Some electrical properties of earth rocks and their comparison with those of the lunar surface layer, *Uchebn. Zaved. Radiofiz.*, *5*, 1057–1061.

Ksanfomaliti, L. V., V. M. Zubkova, N. A. Morozov, and N. A. Petrova (1982), Microseisms at the landing sites of Venera 13 and Venera 14, *Soviet Astronomy Letters*, *8*(4), 241–242.

Ksanfomaliti, L. V., F. L. Scarf, and W. W. L. Taylor (1983), The electrical activity of the atmosphere of Venus, in *Venus*, edited by D. M. Hunten, L. Colin, T. M. Donahue, and V. I. Moroz, pp. 565–603, University of Arizona Press.

Langmuir, C. H., E. M. Klein, and T. Plank (1992), Petrological systematics of mid-ocean ridge basalts - constraints on melt generation beneath ocean ridges, in *Mantle flow and melt generation at mid-ocean ridges*, *Geophysical Monograph Series*, vol. 71, edited by J. Morgan, D. Blackman, and J. Sinton, pp. 183–280.

Le Gall, A., M. A. Janssen, L. C. Wye, A. G. Hayes, J. Radebaugh, C. Savage, H. Zebker, R. D. Lorenz, J. I. Lunine, R. L. Kirk, R. M. C. Lopes, S. Wall, P. Callahan, E. R. Stofan, T. Farr, and C. R. Team (2011), Cassini SAR, radiometry, scatterometry and altimetry observations of Titans dune fields, *Icarus*, *213*(2), 608–624, doi:10.1016/j.icarus.2011.03.026.

Lebonnois, S., F. Hourdin, V. Eymet, A. Crespin, R. Fournier, and F. Forget (2010), Superrotation of Venus' atmosphere analyzed with a full general circulation model, *Journal of Geophysical Research-Planets*, *115*, doi:10.1029/2009je003458.

Lee, C. (2006), Modelling the atmosphere of venus, PhD Thesis.

Lee, C., S. R. Lewis, and P. L. Read (2005), A numerical model of the atmosphere of Venus, in *Planetary Atmospheres, Ionospheres, and Magnetospheres*, *Advances in Space Research*, vol. 36, edited by O. S. M. A. Witasse, pp. 2142–2145, doi:10.1016/j.asr.2005.03.120.

Lee, C., S. R. Lewis, and P. L. Read (2007), Superrotation in a Venus general circulation model, *Journal of Geophysical Research-Planets*, *112*(E4), doi:10.1029/2006je002874.

Lepetit, P., L. Viereck-Goette, R. Schumacher, U. Mues-Schumacher, and M. Abratis (2009), Parameters controlling the density of welded ignimbrites - A case study on the Incesu Ignimbrite, Cappadocia, Central Anatolia, *Chemie der Erde - Geochemistry*, *69*(4), 341–357, doi:http://dx.doi.org/10.1016/j.chemer.2009.05.004.

Lesne, P., S. C. Kohn, J. Blundy, F. Witham, R. E. Botcharnikov, and H. Behrens (2011), Experimental simulation of closed-system degassing in the system basalt-H_2O-CO_2-S-Cl, *Journal of Petrology*, *52*(9), 1737–1762, doi:10.1093/petrology/egr027.

López, I. (2011), Embayed intermediate volcanoes on Venus: Implications for the evolution of the volcanic plains, *Icarus*, *213*(1), 73–85, doi:10.1016/j.icarus.2011.02.022.

López, I., R. Oyarzun, A. Marquez, F. Doblas-Reyes, and A. Laurrieta (1998), Progressive build up of CO_2 in the atmosphere of Venus through multiple volcanic resurfacing events, *Earth Moon and Planets*, *81*(3), 187–192, doi:10.1023/a:1006369831384.

Macgregor, D. (2015), History of the development of the East African Rift System: A series of interpreted maps through time, *Journal of African Earth Sciences*, *101*, 232–252, doi:10.1016/j.jafrearsci.2014.09.016.

Mallama, A., D. Wang, and R. A. Howard (2006), Venus phase function and forward scattering from H_2SO_4, *Icarus*, *182*(1), 10–22, doi:10.1016/j.icarus.2005.12.014.

Marcq, E., D. Belyaev, F. Montmessin, A. Fedorova, J.-L. Bertaux, A. C. Vandaele, and E. Neefs (2011), An investigation of the SO_2 content of the Venusian mesosphere using SPICAV-UV in nadir mode, *Icarus*, *211*(1), 58–69, doi:10.1016/j.icarus.2010.08.021.

Marcq, E., J.-L. Bertaux, F. Montmessin, and D. Belyaev (2013), Variations of sulphur dioxide at the cloud top of Venus's dynamic atmosphere, *Nature Geosci*, *6*(1), 25–28, doi:http://www.nature.com/ngeo/journal/v6/n1/abs/ngeo1650.html#supplementary-information.

Markiewicz, W. J., D. V. Titov, N. Ignatiev, H. U. Keller, D. Crisp, S. S. Limaye, R. Jaumann, R. Moissl, N. Thomas, L. Esposito, S. Watanabe, B. Fiethe, T. Behnke, I. Szemerey, H. Michalik, H. Perplies, M. Wedemeier, I. Sebastian, W. Boogaerts, S. F. Hviid, C. Dierker, B. Osterloh, W. Böker, M. Koch, H. Michaelis, D. Belyaev, A. Dannenberg, M. Tschimmel, P. Russo, T. Roatsch, and K. D. Matz (2007), Venus

Monitoring Camera for Venus Express, *Planetary and Space Science*, *55*(12), 1701–1711, doi:10.1016/j.pss.2007.01.004.

Marsh, S. P., D. H. Richter, S. Ludington, E. Soria-Escalante, and A. Escobar-Diaz (1995), Digital geologic map of the Altiplano and Cordillera Occidental, Bolivia [Open-file report 95-0494], *Report 95-494*, USGS.

Martin, R. S., T. A. Mather, and D. M. Pyle (2007), Volcanic emissions and the early Earth atmosphere, *Geochimica Et Cosmochimica Acta*, *71*(15), 3673–3685, doi:10.1016/j.gca.2007.04.035.

Mastin, L. G., and M. S. Ghiorso (2000), A numerical program for steady-state flow of magma-gas mixtures through vertical eruptive conduits [Open-file report 00-209], *Report 00-209*, USGS.

Mather, T. A., and R. G. Harrison (2006), Electrification of volcanic plumes, *Surveys in Geophysics*, *27*(4), 387–432, doi:10.1007/s10712-006-9007-2.

Mayer, C. H., T. P. McCullough, and R. M. Sloanaker (1958), Observations of Venus at 3.15 cm wave length, *Astrophysical Journal*, *127*(1), 1–10, doi:10.1086/146433.

McGill, G., S. Steenstrup, C. Barton, and P. Ford (1981), Continental rifting and the origin of Beta Regio, Venus, *Geophysical Research Letters*, *8*(7), 737–740, doi:10.1029/GL008i007p00737.

McGill, G. E. (2000), Geolgic map of the Sappho Patera Quadrangle (V-20), Venus [map].

McGovern, P. J., and S. C. Solomon (1998), Growth of large volcanoes on Venus: Mechanical models and implications for structural evolution, *Journal of Geophysical Research-Planets*, *103*(E5), 11,071–11,101, doi:10.1029/98je01046.

McKenzie, D., and M. J. Bickle (1988), The volume and composition of melt generated by extension of the lithosphere, *Journal of Petrology*, *29*(3), 625–679.

McKenzie, D., P. G. Ford, C. Johnson, B. Parsons, D. Sandwell, S. Saunders, and S. C. Solomon (1992), Features on Venus generated by plate boundary processes, *Journal of Geophysical Research-Planets*, *97*(E8), 13,533–13,544.

Melosh, H. J., and A. M. Vickery (1989), Impact erosion of the primordial atmosphere of Mars, *Nature*, *338*(6215), 487–489, doi:10.1038/338487a0.

Michael, M., S. N. Tripathi, W. J. Borucki, and R. C. Whitten (2009), Highly charged cloud particles in the atmosphere of Venus, *Journal of Geophysical Research-Planets*, *114*, doi:10.1029/2008je003258.

Mitchell, A. (2005a), *The ESRI guide to GIS analysis, Volume 2: Spatial measurements and statistics*, ESRI, Redlands, CA.

Mitchell, K. L. (2005b), Coupled conduit flow and shape in explosive volcanic eruptions, *Journal of Volcanology and Geothermal Research*, *143*(1-3), 187–203, doi:10.1016/j.jvolgeores.2004.09.017.

Miura, T., T. Koyaguchi, and Y. Tanaka (2002), Measurements of electric charge distribution in volcanic plumes at Sakurajima Volcano, Japan, *Bulletin of Volcanology*, *64*(2), 75–93, doi:10.1007/s00445-001-0182-1.

Moresi, L., and V. Solomatov (1998), Mantle convection with a brittle lithosphere: thoughts on the global tectonic styles of the Earth and Venus, *Geophysical Journal International*, *133*(3), 669–682, doi:10.1046/j.1365-246X.1998.00521.x.

Morton, B. R., G. Taylor, and J. S. Turner (1956), Turbulent gravitational convection from maintained and instantaneous sources, *Proceedings of the Royal Society of London Series a-Mathematical and Physical Sciences*, *234*(1196), 1–23, doi:10.1098/rspa.1956.0011.

Mueller, N., J. Helbert, G. L. Hashimoto, C. C. C. Tsang, S. Erard, G. Piccioni, and P. Drossart (2008), Venus surface thermal emission at 1 μm in VIRTIS imaging observations: Evidence for variation of crust and mantle differentiation conditions, *Journal of Geophysical Research-Planets*, *113*, doi:10.1029/2008je003118.

Nagy, A. F., T. E. Cravens, S. G. Smith, J. Taylor, H. A., and H. C. Brinton (1980), Model calculations of the dayside ionosphere of Venus: Ionic composition, *Journal of Geophysical Research*, *85*(A13), 7795–7801, doi:10.1029/JA085iA13p07795.

Newman, S., and J. B. Lowenstern (2002), VOLATILECALC: a silicate melt-H_2O-CO_2 solution model written in Visual Basic for excel, *Computers & Geosciences*, *28*(5), 597–604, doi:Piis0098-3004(01)00081-410.1016/s0098-3004(01)00081-4.

Nikolaeva, O. V., and A. A. Ariskin (1999), Geochemical constraints on petrogenic processes on Venus, *Journal of Geophysical Research-Planets*, *104*(E8), 18,889–18,897, doi:10.1029/1996je000337.

Nimmo, F., and D. McKenzie (1996), Modelling plume-related uplift, gravity and melting on Venus, *Earth and Planetary Science Letters*, *145*(1-4), 109–123, doi:10.1016/s0012-821x(96)00200-2.

Nimmo, F., and D. McKenzie (1998), Volcanism and tectonics on Venus, *Annual Review of Earth and Planetary Sciences*, *26*, 23–51, doi:10.1146/annurev.earth.26.1.23.

Papale, P. (1999), Strain-induced magma fragmentation in explosive eruptions, *Nature*, *397*(6718), 425–428, doi:10.1038/17109.

Papale, P., and F. Dobran (1994), Magma flow along the volcanic conduit during the plinian and pyroclastic flow phases of the May 18, 1980, Mount-St-Helens eruption, *Journal of Geophysical Research-Solid Earth*, *99*(B3), 4355–4373, doi:10.1029/93jb02972.

Papale, P., and M. Polacci (1999), Role of carbon dioxide in the dynamics of magma ascent in explosive eruptions, *Bulletin of Volcanology*, *60*(8), 583–594, doi:10.1007/s004450050253.

Papale, P., A. Neri, and G. Macedonio (1998), The role of magma composition and water content in explosive eruptions: 1. Conduit ascent dynamics, *Journal of Volcanology and Geothermal Research*, *87*(1-4), 75–93, doi:10.1016/s0377-0273(98)00101-2.

Papale, P., R. Moretti, and D. Barbato (2006), The compositional dependence of the saturation surface of H_2O+CO_2 fluids in silicate melts, *Chemical Geology*, *229*(1-3), 78–95, doi:10.1016/j.chemgeo.2006.01.013.

Pavri, B., J. W. Head, K. B. Klose, and L. Wilson (1992), Steep-sided domes on Venus - characteristics, geologic setting, and eruption conditions from Magellan data, *Journal of Geophysical Research-Planets*, *97*(E8), 13,445–13,478.

Perfit, M. R., and J. P. Davidson (2000), Plate tectonics and volcanism, in *Encyclopedia of volcanoes*, edited by H. Sigurdsson, pp. 89–113, Academic Press, San Diego.

Pettengill, G. H., H. W. Briscoe, J. V. Evans, L. G. Kraft, R. Price, E. Gehrels, G. M. Hyde, and W. B. Smith (1962), Radar investigation of Venus, *Astronomical Journal*, *67*(4), 181, doi:10.1086/108692.

Pettengill, G. H., E. Eliason, P. G. Ford, G. B. Loriot, H. Masursky, and G. E. McGill (1980), Pioneer Venus radar results altimetry and surface properties, *J. Geophys. Res.*, *85*(A13), 8261–8270, doi:10.1029/JA085iA13p08261.

Phillips, R., and V. Hansen (1994), Tectonic and magmatic evolution of Venus, *Annual Review of Earth and Planetary Sciences*, *22*, 597, doi:10.1146/annurev.ea.22.050194.003121.

Phillips, R., and V. Hansen (1998), Geological evolution of Venus: Rises, plains, plumes, and plateaus, *Science*, *279*(5356), 1492–1497, doi:10.1126/science.279.5356.1492.

Phillips, R. J., R. F. Raubertas, R. E. Arvidson, I. C. Sarkar, R. R. Herrick, N. Izenberg, and R. E. Grimm (1992), Impact craters and Venus resurfacing history, *Journal of Geophysical Research-Planets*, *97*(E10), 15,923–15,948.

Piskorz, D., L. T. Elkins-Tanton, and S. E. Smrekar (2014), Coronae formation on Venus via extension and lithospheric instability, *Journal of Geophysical Research-Planets*, *119*(12), 2568–2582, doi:10.1002/2014JE004636.

Pollack, H. N., S. J. Hurter, and J. R. Johnson (1993a), Heat-flow from the earths interior - analysis of the global data set, *Reviews of Geophysics*, *31*(3), 267–280, doi:10.1029/93rg01249.

Pollack, J. B., and C. Sagan (1967), An analysis of Mariner 2 microwave observations of Venus, *Astrophysical Journal*, *150*(1P1), 327–333, doi:10.1086/149334.

Pollack, J. B., J. B. Dalton, D. Grinspoon, R. B. Wattson, R. Freedman, D. Crisp, D. A. Allen, B. Bezard, C. Debergh, L. P. Giver, Q. Ma, and R. Tipping (1993b), Near-infrared light from Venus nightside - a spectroscopic analysis, *Icarus*, *103*(1), 1–42, doi:10.1006/icar.1993.1055.

Richards, M. A., W. S. Yang, J. R. Baumgardner, and H. P. Bunge (2001), Role of a low-viscosity zone in stabilizing plate tectonics: Implications for comparative terrestrial planetology, *Geochemistry Geophysics Geosystems*, *2*.

Richardson, R. S. (1955), Observations of Venus made at Mount wilson in the winter of 1954-55, *Publications of the Astronomical Society of the Pacific*, *67*(398), 304, doi:10.1086/126824.

Richardson, R. S. (1958), Spectroscopic observations of Venus for rotation made at Mount Wilson in 1956, *Publications of the Astronomical Society of the Pacific*, *70*(414), 251–260, doi:10.1086/127220.

Roberts, E. M., N. J. Stevens, P. M. O'Connor, P. H. G. M. Dirks, M. D. Gottfried, W. C. Clyde, R. A. Armstrong, A. I. S. Kemp, and S. Hemming (2012), Initiation of the western branch of the East African Rift coeval with the eastern branch, *Nature Geoscience*, *5*(4), 289–294, doi:10.1038/NGEO1432.

Robinson, C. A., and J. A. Wood (1993), Recent volcanic activity on Venus - evidence from radiothermal emissivity measurements, *Icarus*, *102*(1), 26–39, doi:10.1006/icar.1993.1030.

Robinson, C. A., G. D. Thornhill, and E. A. Parfitt (1995), Large-scale volcanic activity at Maat-Mons - can this explain fluctuations in atmospheric chemistry observed by Pioneer Venus?, *Journal of Geophysical Research-Planets*, *100*(E6), 11,755–11,763, doi:10.1029/95je00147.

Robledo-Martinez, A., H. Sobral, and A. Ruiz-Meza (2011), Space charge effects and arc properties of simulated lightning on Venus, *Journal of Geophysical Research-Space Physics*, *116*, doi:10.1029/2010ja015856.

Rodríguez, E., Y. J. Kim, and S. L. Durden (1992), A numerical assessment of rough-surface scattering theories: Horizontal polarization, *Radio Science*, *27*(4), 497–513, doi:10.1029/92RS00502.

Rosich, B., and P. Meadows (2004), Absolute calibration of ASAR level 1 products generated with PF-ASAR [ESA technical note], (1), 1–26.

Rossi, M. (1997), Morphology of the 1984 open-channel lava flow at Krafla volcano, northern Iceland, *Geomorphology*, *20*(1-2), 95–112, doi:10.1016/S0169-555X(97)00007-X.

Russell, C. T., R. J. Strangeway, and T. L. Zhang (2006), Lightning detection on the Venus Express mission, *Planetary and Space Science*, *54*(13-14), 1344–1351, doi:10.1016/j.pss.2006.04.026.

Russell, C. T., J. G. Luhmann, T. E. Cravens, A. F. Nagy, and R. J. Strangeway (2007a), Venus upper atmosphere and plasma environment: Critical issues for future exploration, in *Exploring Venus as a terrestrial planet: Geophysical monograph 176*, edited by L. W. Esposito, E. R. Stofan, and E. Cravens, American Geophysical Union, Washington, DC.

Russell, C. T., T. L. Zhang, M. Delva, W. Magnes, R. J. Strangeway, and H. Y. Wei (2007b), Lightning on Venus inferred from whistler-mode waves in the ionosphere, *Nature*, *450*(7170), 661–662, doi:10.1038/nature05930.

Russell, C. T., T. L. Zhang, and H. Y. Wei (2008), Whistler mode waves from lightning on Venus: Magnetic control of ionospheric access, *Journal of Geophysical Research-Planets*, *113*, doi:10.1029/2008je003137.

Russell, C. T., R. J. Strangeway, J. T. M. Daniels, T. L. Zhang, and H. Y. Wei (2011), Venus lightning: Comparison with terrestrial lightning, *Planetary and Space Science*, *59*(10), 965–973, doi:10.1016/j.pss.2010.02.010.

Rybin, A., M. Chibisova, P. Webley, T. Steensen, P. Izbekov, C. Neal, and V. Realmuto (2011), Satellite and ground observations of the June 2009 eruption of Sarychev Peak volcano, Matua Island, Central Kuriles, *Bulletin of Volcanology*, *73*(9), 1377–1392, doi:10.1007/s00445-011-0481-0.

Sagan, C. (1960), The surface temperature of Venus, *Astronomical Journal*, *65*(6), 352–353, doi:10.1086/108265.

Sagan, C. (1962), Structure of the lower atmosphere of Venus, *Icarus*, *1*(2), 151–169.

Salisbury, M. J., B. R. Jicha, S. L. de Silva, B. S. Singer, N. C. Jimenez, and M. H. Ort (2011), Ar-40/Ar-39 chronostratigraphy of Altiplano-Puna volcanic complex ignimbrites reveals the development of a major magmatic province, *Geological Society of America Bulletin*, *123*(5-6), 821–840, doi:10.1130/B30280.1.

Sandor, B. J., R. T. Clancy, G. Moriarty-Schieven, and F. P. Mills (2010), Sulfur chemistry in the Venus mesosphere from SO_2 and SO microwave spectra, *Icarus*, *208*(1), 49–60, doi:10.1016/j.icarus.2010.02.013.

Scandone, R., and S. D. Malone (1985), Magma supply, magma discharge and readjustment of the feeding system of Mount St Helens during 1980, *Journal of Volcanology and Geothermal Research*, *23*(3-4), 239–262, doi:10.1016/0377-0273(85)90036-8.

Schaber, G. G., R. G. Strom, H. J. Moore, L. A. Soderblom, R. L. Kirk, D. J. Chadwick, D. D. Dawson, L. R. Gaddis, J. M. Boyce, and J. Russell (1992), Geology and distribution of impact craters on Venus - what are they telling us, *Journal of Geophysical Research-Planets*, *97*(E8), 13,257–13,301.

Seiff, A., J. T. Schofield, A. J. Kliore, F. W. Taylor, S. S. Limaye, H. E. Revercomb, L. A. Sromovsky, V. V. Kerzhanovich, V. I. Moroz, and M. Y. Marov (1985), Models of the structure of the atmosphere of Venus from the surface to 100 kilometers

altitude, *Advances in Space Research*, *5*(11), 3–58, doi:http://dx.doi.org/10.1016/0273-1177(85)90197-8.

Senske, D. A., G. G. Schaber, and E. R. Stofan (1992), Regional topographic rises on Venus - geology of western Eistla Regio and comparison to Beta Regio and Atla Regio, *Journal of Geophysical Research-Planets*, *97*(E8), 13,395–13,420.

Shalygin, E. V., W. J. Markiewicz, A. T. Basilevsky, D. V. Titov, N. I. Ignatiev, and J. W. Head (2015), Active volcanism on Venus in the Ganiki Chasma rift zone, *Geophysical Research Letters*, *42*(12), 4762–4769, doi:10.1002/2015GL064088.

Shellnutt, J. G. (2013), Petrological modeling of basaltic rocks from Venus: A case for the presence of silicic rocks, *Journal of Geophysical Research-Planets*, *118*(6), 1350–1364, doi:10.1002/jgre.20094.

Shirley, J. H. (1998), *Seismicity*, Chapman and Hall, London.

Smrekar, S., and E. Stofan (1997), Corona formation and heat loss on Venus by coupled upwelling and delamination, *Science*, *277*(5330), 1289–1294.

Smrekar, S. E., and E. M. Parmentier (1996), The interaction of mantle plumes with surface thermal and chemical boundary layers: Applications to hotspots on Venus, *Journal of Geophysical Research-Solid Earth*, *101*(B3), 5397–5410, doi:10.1029/95jb02877.

Smrekar, S. E., and E. R. Stofan (1999), Origin of corona-dominated topographic rises on Venus, *Icarus*, *139*(1), 100–115, doi:10.1006/icar.1999.6090.

Smrekar, S. E., E. R. Stofan, N. Mueller, A. Treiman, L. Elkins-Tanton, J. Helbert, G. Piccioni, and P. Drossart (2010), Recent hotspot volcanism on Venus from VIRTIS emissivity data, *Science*, *328*(5978), 605–608, doi:10.1126/science.1186785.

Solomatov, V. S., and L. N. Moresi (1996), Stagnant lid convection on Venus, *Journal of Geophysical Research-Planets*, *101*(E2), 4737–4753, doi:10.1029/95je03361.

Solomon, S., S. Smrekar, D. Bindschadler, R. Grimm, W. Kaula, G. Mcgill, R. Phillips, R. Saunders, G. Schubert, S. Squyres, and E. Stofan (1992), Venus tectonics - an overview of magellan observations, *Journal of Geophysical Research-Planets*, *97*(E8), 13,199–13,255.

Sparks, R. S. J. (1978), The dynamics of bubble formation and growth in magmas - a review and analysis, *Journal of Volcanology and Geothermal Research*, *3*(1-2), 1–37, doi:10.1016/0377-0273(78)90002-1.

Sparks, R. S. J. (1986), The dimensions and dynamics of volcanic eruption columns, *Bulletin of Volcanology*, *48*(1), 3–15, doi:10.1007/bf01073509.

Squyres, S., D. Janes, G. Baer, D. Bindschadler, G. Schubert, V. Sharpton, and E. Stofan (1992), The morphology and evolution of coronae on Venus, *Journal of Geophysical Research-Planets*, *97*(E8), 13,611–13,634.

Squyres, S. W., D. M. Janes, G. Schubert, D. L. Bindschadler, J. E. Moersch, D. L. Turcotte, and E. R. Stofan (1993), The spatial distribution of coronae and related features on Venus, *Geophysical Research Letters*, *20*(24), 2965–2968, doi:10.1029/93GL00866.

Stofan, E., J. Head, D. Campbell, S. Zisk, A. Bogomolov, O. Rzhiga, A. Basilevsky, and N. Armand (1989), Geology of a rift-zone on Venus - Beta-Regio and Devana Chasma, *Geological Society of America Bulletin*, *101*(1), 143–156, doi:10.1130/0016-7606(1989)101⟨0143:GOARZO⟩2.3.CO;2.

Stofan, E., V. Sharpton, G. Schubert, G. Baer, D. Bindschadler, D. Janes, and S. Squyres (1992), Global distribution and characteristics of coronae and related features on Venus - implications for origin and relation to mantle processes, *Journal of Geophysical Research-Planets*, *97*(E8), 13,347–13,378.

Stofan, E., J. Guest, and D. Copp (2001a), Development of large volcanoes on Venus: Constraints from Sif, Gula, and Kunapipi Montes, *Icarus*, *152*(1), 75–95, doi:10.1006/icar.2001.6633.

Stofan, E., S. Smrekar, S. Tapper, J. Guest, and P. Grindrod (2001b), Preliminary analysis of an expanded corona database for Venus, *Geophysical Research Letters*, *28*(22), 4267–4270, doi:10.1029/2001GL013307.

Stofan, E. R., and S. E. Smrekar (2005), Large topographic rises, coronae, large flow fields, and large volcanoes on Venus: Evidence for mantle plumes?, in *Plates, Plumes And Paradigms*, *Geological Society of America Special Papers*, vol. 388, edited by G. Foulger, J. Natland, and D. Presnall, Geological Soc Amer Inc, 3300 Penrose Pl, PO Box 9140, Boulder, CO 80301 USA, doi:10.1130/2005.2388(47).

Stofan, E. R., S. E. Smrekar, D. L. Bindschadler, and D. A. Senske (1995), Large topographic rises on Venus - implications for mantle upwelling, *Journal of Geophysical Research-Planets*, *100*(E11), 23,317–23,327, doi:10.1029/95je01834.

Stofan, E. R., S. W. Anderson, D. A. Crown, and J. J. Plaut (2000), Emplacement and composition of steep-sided domes on Venus, *Journal of Geophysical Research-Planets*, *105*(E11), 26,757–26,771, doi:10.1029/1999je001206.

Strangeway, R. J., C. T. Russell, and C. M. Ho (1993), Observation of intense wave bursts at very-low altitudes within the Venus nightside ionosphere, *Geophysical Research Letters*, *20*(23), 2771–2774, doi:10.1029/93gl02702.

Strom, R. G., G. G. Schaber, and D. D. Dawson (1994), The global resurfacing of Venus, *Journal of Geophysical Research-Planets*, *99*(E5), 10,899–10,926, doi:10.1029/94je00388.

Svedhem, H., D. V. Titov, D. McCoy, J. P. Lebreton, S. Barabash, J.-L. Bertaux, P. Drossart, V. Formisano, B. Hausler, O. Korablev, W. J. Markiewicz, D. Nevejans, M. Patzold, G. Piccioni, T. L. Zhang, F. W. Taylor, E. Lellouch, D. Koschny,

O. Witasse, H. Eggel, M. Warhaut, A. Accomazzo, J. Rodriguez-Canabal, J. Fabrega, T. Schirmann, A. Clochet, and M. Coradini (2007a), Venus Express - the first European mission to Venus, *Planetary and Space Science*, *55*(12), 1636–1652, doi:10.1016/j.pss.2007.01.013.

Svedhem, H., D. V. Titov, F. W. Taylor, and O. Witasse (2007b), Venus as a more Earth-like planet, *Nature*, *450*(7170), 629–632, doi:10.1038/nature06432.

Taylor, F., and D. Grinspoon (2009), Climate evolution of Venus, *Journal of Geophysical Research-Planets*, *114*, doi:10.1029/2008je003316.

Taylor, F. W. (2010), *Planetary atmospheres*, Oxford University Press, Oxford.

Taylor, F. W. (2011), Comparative planetology, climatology and biology of Venus, Earth and Mars, *Planetary and Space Science*, *59*(10), 889–899, doi:10.1016/j.pss.2010.11.009.

Taylor, F. W., D. J. Diner, L. S. Elson, D. J. McCleese, J. V. Martonchik, J. Delderfield, S. P. Bradley, J. T. Schofield, J. C. Gille, and M. T. Coffey (1979a), Temperature, cloud structure, and dynamics of Venus middle atmosphere by infrared remote-sensing from Pioneer Orbiter, *Science*, *205*(4401), 65–67, doi:10.1126/science.205.4401.65.

Taylor, F. W., R. Beer, M. T. Chahine, D. J. Diner, L. S. Elson, R. D. Haskins, D. J. McCleese, J. V. Martonchik, P. E. Reichley, S. P. Bradley, J. Delderfield, J. T. Schofield, C. B. Farmer, L. Froidevaux, J. Leung, M. T. Coffey, and J. C. Gille (1980), Structure and meteorology of the middle atmosphere of Venus: Infrared remote sensing from the Pioneer Orbiter, *J. Geophys. Res.*, *85*(A13), 7963–8006, doi:10.1029/JA085iA13p07963.

Taylor, W. W. L., F. L. Scarf, C. T. Russell, and L. H. Brace (1979b), Evidence for lightning on Venus, *Nature*, *279*(5714), 614–616, doi:10.1038/279614a0.

Thornhill, G. D. (1993), Theoretical modeling of eruption plumes on Venus, *Journal of Geophysical Research-Planets*, *98*(E5), 9107–9111, doi:10.1029/93je00255.

Titov, D. V., F. W. Taylor, H. Svedhem, N. I. Ignatiev, W. J. Markiewicz, G. Piccioni, and P. Drossart (2008), Atmospheric structure and dynamics as the cause of ultraviolet markings in the clouds of Venus, *Nature*, *456*(7222), 620–623, doi:10.1038/nature07466.

Titov, D. V., W. J. Markiewicz, N. I. Ignatiev, L. Song, S. S. Limaye, A. Sanchez-Lavega, J. Hesemann, M. Almeida, T. Roatsch, K.-D. Matz, F. Scholten, D. Crisp, L. W. Esposito, S. F. Hviid, R. Jaumann, H. U. Keller, and R. Moissl (2012), Morphology of the cloud tops as observed by the Venus Express Monitoring Camera, *Icarus*, *217*(2), 682–701, doi:10.1016/j.icarus.2011.06.020.

Treiman, A. H. (2007), Geochemistry of Venus' surface: Current limitations as future opportunities, in *Exploring Venus as a Terrestrial Planet: Geophysical monograph 176*, edited by L. W. Esposito, E. R. Stofan, and E. Cravens, American Geophysical Union, Washington, DC.

Tuffen, H., and D. Dingwell (2005), Fault textures in volcanic conduits: Evidence for seismic trigger mechanisms during silicic eruptions, *Bulletin of Volcanology*, *67*(4), 370–387, doi:10.1007/s00445-004-0383-5.

Turcotte, D. L. (1993), An episodic hypothesis for Venusian tectonics, *Journal of Geophysical Research: Planets*, *98*(E9), 17,061–17,068, doi:10.1029/93JE01775.

Turcotte, D. L. (1995), How does Venus lose heat, *Journal of Geophysical Research-Planets*, *100*(E8), 16,931–16,940, doi:10.1029/95JE01621.

Tyler, G. L., R. A. Simpson, M. J. Maurer, and E. Holmann (1992), Scattering properties of the Venusian surface: Preliminary results from Magellan, *Journal Of Geophysical Research-Planets*, *97*(E8), 13,115–13,139.

Ulaby, F. T., T. H. Bengal, M. C. Dobson, J. R. East, J. B. Garvin, and D. L. Evans (1990), Microwave dielectric properties of dry rocks, *IEEE Transactions on Geoscience and Remote Sensing*, *28*(3), 325–336, doi:10.1109/36.54359.

Urey, H. C. (1952), *The planets, their origin and development*, Yale University Press, New Haven, Conn.

Valentine, G. A., and K. H. Wohletz (1989), Numerical-models of plinian eruption columns and pyroclastic flows, *Journal of Geophysical Research-Solid Earth and Planets*, *94*(B2), 1867–1887, doi:10.1029/JB094iB02p01867.

Vinograd, A. P., U. A. Surkov, and C. P. Florensk (1968), Chemical composition of Venus atmosphere based on data of interplanetary station Venera 4, *Journal of the Atmospheric Sciences*, *25*(4), 535–536, doi:10.1175/1520-0469(1968)025⟨0535:tccotv⟩2.0.co;2.

Wallace, P. J. (2005), Volatiles in subduction zone magmas: concentrations and fluxes based on melt inclusion and volcanic gas data, *Journal of Volcanology and Geothermal Research*, *140*(1-3), 217–240, doi:10.1016/j.jvolgeores.2004.07.023.

Watson, S., and D. McKenzie (1991), Melt generation by plumes - a study of Hawaiian volcanism, *Journal of Petrology*, *32*(3), 501–537.

Waythomas, C. F., W. E. Scott, S. G. Prejean, D. J. Schneider, P. Izbekov, and C. J. Nye (2010), The 7-8 August 2008 eruption of Kasatochi Volcano, central Aleutian Islands, Alaska, *Journal of Geophysical Research-Solid Earth*, *115*, doi:10.1029/2010JB007437.

Wiart, P., and C. Oppenheimer (2005), Large magnitude silicic volcanism in north Afar: The Nabro Volcanic Range and Ma'alalta volcano, *Bulletin of Volcanology*, *67*(2), 99–115, doi:10.1007/s00445-004-0362-x.

Williams, D. (2013), Venus fact sheet, `http://nssdc.gsfc.nasa.gov/planetary/factsheet/venusfact.html`.

Williams-Jones, G., A. E. Williams-Jones, and J. Stix (1998), The nature and origin of Venusian canali, *Journal of Geophysical Research-Planets*, *103*(E4), 8545–8555, doi:10.1029/98je00243.

Wilson, C. F., S. Guerlet, P. G. J. Irwin, C. C. C. Tsang, F. W. Taylor, R. W. Carlson, P. Drossart, and G. Piccioni (2008), Evidence for anomalous cloud particles at the poles of Venus, *Journal of Geophysical Research-Planets*, *113*, doi:10.1029/2008je003108.

Wilson, L., R. S. J. Sparks, T. C. Huang, and N. D. Watkins (1978), The control of volcanic column heights by eruption energetics and dynamics, *Journal of Geophysical Research*, *83*(NB4), 1829–1836, doi:10.1029/JB083iB04p01829.

Wilson, L., R. S. J. Sparks, and G. P. L. Walker (1980), Explosive volcanic eruptions 4. The control of magma properties and conduit geometry on eruption column behavior, *Geophysical Journal of the Royal Astronomical Society*, *63*(1), 117–148, doi:10.1111/j.1365-246X.1980.tb02613.x.

Witham, F., J. Blundy, S. C. Kohn, P. Lesne, J. Dixon, S. V. Churakov, and R. Botcharnikov (2012), SolEx: A model for mixed COHSCl-volatile solubilities and exsolved gas compositions in basalt, *Computers & Geosciences*, *45*, 87–97, doi:10.1016/j.cageo.2011.09.021.

Woods, A. W. (1988), The fluid dynamics and thermodynamics of eruption columns, *Bulletin of Volcanology*, *50*(3), 169–193, doi:10.1007/bf01079681.

Woods, A. W. (1995), The dynamics of explosive volcanic eruptions, *Reviews of Geophysics*, *33*(4), 495–530, doi:10.1029/95rg02096.

Woods, A. W., and S. M. Bower (1995), The decompression of volcanic jets in a crater during explosive volcanic-eruptions, *Earth and Planetary Science Letters*, *131*(3-4), 189–205, doi:10.1016/0012-821x(95)00012-2.

Woolfson, M. (2000), The origin and evolution of the Solar System, *Astronomy & Geophysics*, *41*(1), 12–19, doi:10.1046/j.1468-4004.2000.00012.x.

Yamamoto, M. (2011), Microscale simulations of Venus' convective adjustment and mixing near the surface: Thermal and material transport processes, *Icarus*, *211*(2), 993–1006, doi:10.1016/j.icarus.2010.11.019.

Yamamoto, M., and M. Takahashi (2003), The fully developed superrotation simulated by a general circulation model of a Venus-like atmosphere, *Journal of the Atmospheric Sciences*, *60*(3), 561–574, doi:10.1175/1520-0469(2003)060⟨0561:tfdssb⟩2.0.co;2.

Young, A. T. (1973), Are clouds of Venus sulfuric-acid?, *Icarus*, *18*(4), 564–582, doi:10.1016/0019-1035(73)90059-6.

Yung, Y. L., and W. B. DeMore (1982), Photochemistry of the stratosphere of Venus - implications for atmospheric evolution, *Icarus*, *51*(2), 199–247, doi:10.1016/0019-1035(82)90080-x.

Zasova, L. V., N. Ignatiev, I. Khatuntsev, and V. Linkin (2007), Structure of the Venus atmosphere, *Planetary and Space Science*, *55*(12), 1712–1728, doi:10.1016/j.pss.2007.01.011.

Zhang, T. L., W. Baumjohann, M. Delva, H. U. Auster, A. Balogh, C. T. Russell, S. Barabash, M. Balikhin, G. Berghofer, H. K. Biernat, H. Lammer, H. Lichtenegger, W. Magnes, R. Nakamura, T. Penz, K. Schwingenschuh, Z. Vörös, W. Zambelli, K. H. Fornacon, K. H. Glassmeier, I. Richter, C. Carr, K. Kudela, J. K. Shi, H. Zhao, U. Motschmann, and J. P. Lebreton (2006), Magnetic field investigation of the Venus plasma environment: Expected new results from Venus Express, *Planetary and Space Science*, *54*(13&14), 1336–1343, doi:10.1016/j.pss.2006.04.018.

Zhang, X., M.-C. Liang, F. Montmessin, J.-L. Bertaux, C. Parkinson, and Y. L. Yung (2010), Photolysis of sulphuric acid as the source of sulphur oxides in the mesosphere of Venus, *Nature Geoscience*, *3*(12), doi:10.1038/ngeo989.

Zhang, Y. X. (1999), A criterion for the fragmentation of bubbly magma based on brittle failure theory, *Nature*, *402*(6762), 648–650, doi:10.1038/45210.

Appendix A

```
%%%%%%%%%%%%%%%%                  %%%%%                  %%%%%%%%%%%%%%%%
%%%%%%%%%%%%%%%%%%%%%%%%%%%%%%%%%%%%%%%%%%%%%%%%%%%%%%%%%%%%%%%%%%%%%%%%%%%
%%%%%%%%%%%%%%%%%%%%%%%%%%%%%% IMPORTANT %%%%%%%%%%%%%%%%%%%%%%%%%%%%%%%%%%%%
%%%%%%%%%%%%%%%%%%%%%% RUN SOLEX - OUTPUT TO DESKTOP %%%%%%%%%%%%%%%%%%%%%%%%
%%%%%%%%%%%%%%%%%%%%%%%%%%%%%%% FIRST %%%%%%%%%%%%%%%%%%%%%%%%%%%%%%%%%%%%%
%%%%%%%%%%%%%%%%%%%%%%%%%%%%%%%%%%%%%%%%%%%%%%%%%%%%%%%%%%%%%%%%%%%%%%%%%%%
%%%%%%%%%%%%%%%%                  %%%%%                  %%%%%%%%%%%%%%%%

%% Model for conduit ascent

% Equations from M. Diez (2006) 'Statistics in Volcanology', Ch. 15
% and Connor_Uni_SFla.pdf

% Using SolEx (Witham et al. 2012) to calculate degassing

% Assuming:
% Homogeneous flow (no melt/gas ascent differential)
% Conduit of constant x-sectional area

% clearvars -global; clear;
close all;
set(0,'DefaultFigureWindowStyle','docked');
set(0,'DefaultAxesColorOrder',cool(6));

global w rhoc0 pc0 A g Lc Patm Q SolEx Tm rhom0 nc0 nm0 Cmelt Hmelt C H ...
    Rc0 RCO2 RH2O RSO2 f00 rc0 D etam etag

%% Load and plot SolEx data

%%%%%%%%%%%%%%%%%%%%%%%%%%%%%% SolEx %%%%%%%%%%%%%%%%%%%%%%%%%%%%%%%%%%%%%%

SolEx = dlmread('SolEx_output.txt','\t',11,0); % read in degassing data
SolEx = flipud(SolEx); % invert data
range = 0:1:4000; % generate interpolation range
SolEx = interp1(SolEx(:,1),SolEx(:,:),range,'linear','extrap'); % interp/extrap
for per = 1:5 % remove extrapolation errors over 100%
    if SolEx(per,6) > 100
        SolEx(per,6) = 100;
    end
end
SolEx(:,1) = SolEx(:,1)./10; % convert pressure to MPa
% SolEx(:,1) = SolEx(:,1).*1e5; % convert pressure to Pa
SolEx(:,6) = SolEx(:,6)./100; % convert per cent to fraction
    % -k --b -.r
% figure(1);plot(SolEx(:,6),SolEx(:,1),'-.r','LineWidth',2);set(gca,'YDir','reverse'); % plot vf gas
% xlabel('volume fraction exsolved gas','FontSize',14);
% ylabel('Pressure (MPa)','FontSize',14);
% set(gca,'FontSize',14,'XLim',[0 1],'YLim',[0 300]);
% grid on;
% hold on;
clear per range; % remove redundant var
% load('PPs1Venus');
% load('PPs2Venus');
% legend('5% H_2O, 0% CO_2','2.5% H_2O, 2.5% CO_2','0% H_2O, 5% CO_2','Location','SouthEast');
```

```
% substitution
% legend('3% H_2O, 0% CO_2','3% H_2O, 1% CO_2','3% H_2O, 3% CO_2','Location','SouthEast');
% addition
% scatter(PPs1Venus(5,1),PPs1Venus(5,5)/1e6,'xk'); % substitution
% scatter(PPs1Venus(3,1),PPs1Venus(5,5)/1e6,'xr'); % substitution
% scatter(PPs1Venus(1,1),PPs1Venus(5,5)/1e6,'xb'); % substitution
% scatter(PPs2Venus(5,1),PPs2Venus(5,5)/1e6,'xr'); % addition
% scatter(PPs2Venus(3,1),PPs2Venus(3,5)/1e6,'xb'); % addition
% scatter(PPs2Venus(1,1),PPs2Venus(1,5)/1e6,'xk'); % addition

%% Load and plot VIRA atmos pressure data with depth pressure

planet = 'venus'; % 'earth' or 'venus'

%      0     1     2     3     4     5     6     7     8     9     10  km
if planet == 'earth'
P = [0.100,0.090,0.080,0.070,0.062,0.054,0.048,0.041,0.036,0.030,0.027]; % Earth
else
P = [9.210,8.645,8.109,7.601,7.120,6.665,6.235,5.828,5.444,5.081,4.739]; % Venus
end
P = P'; % transpose data
P = flipud(P); % invert data
Pd = 0:1:10; % generate atmospheric altitude range
Pd = Pd'; % transpose data
Pd = flipud(Pd); % invert data
P(:,2) = Pd; % concatenate atmopsheric pressure to altitude
P = fliplr(P); % flip dataset
Pu = -10:1:-1; % generate depth array
Pu = Pu'; % transpose data
Pu = flipud(Pu); % invert data
Pu(1:10,2) = ((abs(Pu(1:10,1))*1e3*2800*8.41)./1e6)+9.21; % calculate pressure at depth at MPR
P(12:21,1:2) = Pu; % concatenate atmospheric with depth pressures
clear Pd Pu; % remove redundant var

tt = 2:11;tt = fliplr(tt); % generate array to select surface pressure elements
for t = 1:10 % loop to calculate pressure at depth for different surface elevations
    P(:,t+2) = P(:,t+1); % copy previous profile to new elevation (new column)
    P(tt(t):tt(t)+9,t+2) = ((abs(P(12:21,1))*1e3*2800*8.41)./1e6)+P(tt(t)-1,t+2); % calculte new depth
     % arrary for elevation
    P(tt(t)+10:end,t+2) = NaN; % remove values below 10 km depth
end
P(1:10,13) = ((abs(P(12:21,1))*1e3*2800*8.41)./1e6)+4.416; % individual calculation for depth at 10 km
P(11:end,13) = NaN; % remove values below 10 km depth
clear t tt; % remove redundant var

P5 = P;
P5(17:end,:) = [];
P5(16,3) = NaN;
P5(15:end,4) = NaN;
P5(14:end,5) = NaN;
P5(13:end,6) = NaN;
P5(12:end,7) = NaN;
P5(11:end,8) = NaN;
P5(10:end,9) = NaN;
P5(9:end,10) = NaN;
P5(8:end,11) = NaN;
P5(7:end,12) = NaN;
P5(6:end,13) = NaN;

% figure(2);clf;plot(P(:,2:2:13),P(:,1)); % plot atmospheric/subsurface
% pressure profiles 10 km
% xlabel('Pressure (MPa)','FontSize',14);
% ylabel('Depth or Altitude (km  MPR)','FontSize',14);
% set(gca,'FontSize',14,'XLim',[0 280],'YLim',[-10 10]);
% legend('0 km','2 km','4 km','6 km','8 km','10 km');
% legendtitle('Surface Elevation','FontSize',10);
% grid on;
```

```
% figure(2);clf;plot(P5(:,2:2:13),P5(:,1),'LineWidth',2);
% plot atmospheric/subsurface pressure profiles 5 km
% xlabel('Pressure (MPa)','FontSize',20);
% ylabel('Depth or Altitude (km  MPR)','FontSize',20);
% set(gca,'FontSize',16,'XLim',[0 130],'YLim',[-5 10],'YTick',[-5:1:10]);
% legend('0 km','2 km','4 km','6 km','8 km','10 km','Location','NorthEast');
% % legendtitle('Surface Elevation','FontSize',16);
% text(114,10.3,'Surface Elevation','FontSize',16);
% grid on;

%% Conduit flow code

%%%%%%%%%%%%%%%%%%%%%%%%%%%%%% Presets %%%%%%%%%%%%%%%%%%%%%%%%%%%%%%

% SolEx composition should be set to (Treiman, 2007)
% SiO2=48.7 Al2O3=17.9 FeO=8.8 CaO=10.3
% MgO=8.1 Na2O=?? K2O=0.2
% Set volatile fractions and temperature

%%%%%%%%%%%%%%%%%%%%%%%%%%%%%% Instructions %%%%%%%%%%%%%%%%%%%%%%%%%%%%%%

%%%%%%%%%%%%%%%%%%%%%% clear vars before first run %%%%%%%%%%%%%%%%%%%%%%

% 1. Run SolEx
% 2. Load SolEx (above)
% 2. Rename file in save cmd here, in load cmd in "Plot" section, and at end
% of "Display" section
% 3. Comment out load cmd in "Plot" section unles data previously generated
% 4. Specify volatile contents below
% 5. Specify temperature below
% 6. Comment out plot sections
% 7. Run separately for each temperature (full elev range calculated in each run)
% 8. Specify conduit length/radius below (optional)
% 9. After all temps run command below e.g. save('H1C0.mat','H1C0');
% save('m3H3C3.mat','m3H3C3');
% 10. Change filename in plot section, uncomment and run plots

% starting velocity outside elev loop so that each successive iteration
% commences at the 'final' initial velocity, reducing code run time
ustart = 82;
elev = 9; % specific surface elevation (km MPR)
% for elev = 10:-1:0 % all surface elevations ((un)comment 'end' statement too)

% for uc0 = 1:-0.05:0 % initial flow velocity (m s^-1)

% row = 1;
H2O = 5; % (wt%)
% H2O = input('H_2O wt% (e.g. 1, 2, 3, etc.): '); % (wt%)
CO2 = 50000; % (ppm)
% CO2 = input('CO_2 ppm (e.g. 20000 = 2%): '); % (ppm)
SO2 = 0; % (ppm)
Lc = 5000; % conduit length (m)
width = 70;
length = 100;
rc0 = 25; % conduit radius (m)
geometry = 'cir'; % lin or cir
flare = 'n'; % conduit flare y or n
flarebase = 50; % depth of onset of flaring
Tm = 1200; % magma temperature (K)
rhom0 = 2600; % magma density (kg m^-3) (Conflow calculates this as
      % ~2550-2600 for 1700-1200 K)
rhocrust = 2800; % mean crustal density (kg m^-3)
deep = 0-(Lc/1000);
% Vx = 0.2; % vf xtls
% Vmax = 0.6;

% Constants and calculated properties
```

```
RH2O = 462; % H2O gas constant (J kg^-1 K^-1)
RCO2 = 189; % CO2 gas constant (J kg^-1 K^-1)
RSO2 = 130; % SO2 gas constant (J kg^-1 K^-1)
volatile = H2O+(CO2/1e4)+(SO2/1e4); % wt% total volatile
nc00 = volatile/100; % initial volatile volume fraction in the mixture
if planet == 'earth'
    g = 9.81;
else
    g = 8.41; % gravitational acceleration (m s^-2)
end
Patm = interp1(P(1:11,1),P(1:11,2),elev); % calculate atmospheric pressure at
 % surface for given elevation
f00 = 0.0025; % friction coefficent
if geometry == 'cir'
    A0 = pi*rc0^2; % conduit x-sect area (m^2)
    D0 = rc0*2; % conduit diameter (m)
elseif geometry == 'lin'
    A0 = width*length;
    D0 = width/2;
    % D (for friction calcs) is equivalent to half width of conduit as open
    % ends assumed to have negligable friction
end
% logetam = -10.737+1.8183*(10000/Tm); % log viscosity of magma
% logetam = 2.5;
% etam = exp(logetam);%10^logetam; % viscosity of magma (Pa s)
% fracH2O = 3/(H2O+CO2/1e4);
% etaH2O = interp1(etagtemp,etagviscH2O,Tm);
% etaCO2 = interp1(etagtemp,etagviscCO2,Tm);
% etag = (fracH2O*etaH2O)+((1-fracH2O)*etaCO2); % gas viscosity (Pa s)
z = fliplr(0:1:Lc)';

%   1   2   3   4   5   6   7   8   9  10  11  12  13  14  15  16  17  18
19  20  21  22  23  24  25  26  27  28  29  30  31
% Temp,1/0,2/0,3/0,4/0,5/0,1/1,2/1,3/1,4/1,5/1,2/1,2/2,2/3,2/4,2/5,3/1,3/2,
3/3,3/4,3/5,4/1,4/2,4/3,4/4,4/5,5/1,5/2,5/3,5/4,5/5.
Tmlogetam = [ 973.15;1073.15;1173.15;1273.15;1373.15;1473.15];
% viscosities calculated using Giordano D, Russell JK, & Dingwell DB (2008)
% EPSL 271 for a melt of Venera 14 composition with average H2O = 2%

if H2O >= 0 && H2O < 2 && CO2 >= 0 && CO2 <10000
    Tmlogetam(:,2) = [6.39;4.44;3.08;2.08;1.31;0.70]; %
elseif H2O >= 2 && H2O < 3 && CO2 >= 0 && CO2 <10000
    Tmlogetam(:,2) = [5.64;3.93;2.72;1.80;1.10;0.53]; %
elseif H2O >= 3 && H2O < 4 && CO2 >= 0 && CO2 <10000
    Tmlogetam(:,2) = [5.28;3.68;2.52;1.66;0.98;0.43]; %
elseif H2O >= 4 && H2O < 5 && CO2 >= 0 && CO2 <10000
    Tmlogetam(:,2) = [5.04;3.51;2.40;1.55;0.89;0.36]; %
elseif H2O >= 5 && H2O <= 10 && CO2 >= 0 && CO2 <10000
    Tmlogetam(:,2) = [4.86;3.38;2.30;1.47;0.83;0.31]; %
elseif H2O >= 0 && H2O < 2 && CO2 >= 10000 && CO2 <20000
    Tmlogetam(:,2) = [6.09;4.25;2.96;2.00;1.25;0.66]; %
elseif H2O >= 2 && H2O < 3 && CO2 >= 10000 && CO2 <20000
    Tmlogetam(:,2) = [5.57;3.90;2.70;1.80;1.10;0.54]; %
elseif H2O >= 3 && H2O < 4 && CO2 >= 10000 && CO2 <20000
    Tmlogetam(:,2) = [5.28;3.69;2.54;1.68;1.00;0.46]; %
elseif H2O >= 4 && H2O < 5 && CO2 >= 10000 && CO2 <20000
    Tmlogetam(:,2) = [5.06;3.54;2.43;1.59;0.93;0.39]; %
elseif H2O >= 5 && H2O <= 10 && CO2 >= 10000 && CO2 <20000
    Tmlogetam(:,2) = [4.89;3.41;2.33;1.51;0.86;0.34]; %
elseif H2O >= 0 && H2O < 2 && CO2 >= 20000 && CO2 <30000
    Tmlogetam(:,2) = [5.92;4.15;2.89;1.95;1.23;0.64]; %
elseif H2O >= 2 && H2O < 3 && CO2 >= 20000 && CO2 <30000
    Tmlogetam(:,2) = [5.54;3.89;2.70;1.81;1.11;0.55]; %
elseif H2O >= 3 && H2O < 4 && CO2 >= 20000 && CO2 <30000
    Tmlogetam(:,2) = [5.28;3.71;2.57;1.70;1.03;0.48]; %
elseif H2O >= 4 && H2O < 5 && CO2 >= 20000 && CO2 <30000
    Tmlogetam(:,2) = [5.09;3.57;2.46;1.62;0.96;0.42]; %
elseif H2O >= 5 && H2O <= 10 && CO2 >= 20000 && CO2 <30000
```

```
    Tmlogetam(:,2) = [4.93;3.44;2.36;1.54;0.89;0.37]; %
elseif H2O >= 0 && H2O < 2 && CO2 >= 30000 && CO2 <40000
    Tmlogetam(:,2) = [5.82;4.09;2.86;1.94;1.22;0.64]; %
elseif H2O >= 2 && H2O < 3 && CO2 >= 30000 && CO2 <40000
    Tmlogetam(:,2) = [5.52;3.89;2.71;1.82;1.13;0.57]; %
elseif H2O >= 3 && H2O < 4 && CO2 >= 30000 && CO2 <40000
    Tmlogetam(:,2) = [5.30;3.73;2.59;1.73;1.05;0.51]; %
elseif H2O >= 4 && H2O < 5 && CO2 >= 30000 && CO2 <40000
    Tmlogetam(:,2) = [5.12;3.60;2.49;1.65;0.98;0.45]; %
elseif H2O >= 5 && H2O <= 10 && CO2 >= 30000 && CO2 <40000
    Tmlogetam(:,2) = [4.95;3.48;2.40;1.57;0.92;0.40]; %
elseif H2O >= 0 && H2O < 2 && CO2 >= 40000 && CO2 <50000
    Tmlogetam(:,2) = [5.76;4.06;2.85;1.93;1.22;0.65]; %
elseif H2O >= 2 && H2O < 3 && CO2 >= 40000 && CO2 <50000
    Tmlogetam(:,2) = [5.51;3.90;2.73;1.84;1.15;0.59]; %
elseif H2O >= 3 && H2O < 4 && CO2 >= 40000 && CO2 <50000
    Tmlogetam(:,2) = [5.31;3.75;2.62;1.75;1.08;0.53]; %
elseif H2O >= 4 && H2O < 5 && CO2 >= 40000 && CO2 <50000
    Tmlogetam(:,2) = [5.14;3.62;2.52;1.67;1.01;0.48]; %
elseif H2O >= 5 && H2O <= 10 && CO2 >= 40000 && CO2 <50000
    Tmlogetam(:,2) = [4.98;3.50;2.43;1.60;0.95;0.42]; %
elseif H2O >= 0 && H2O < 2 && CO2 >= 50000 && CO2 <100001
    Tmlogetam(:,2) = [5.72;4.05;2.85;1.94;1.23;0.66]; %
elseif H2O >= 2 && H2O < 3 && CO2 >= 50000 && CO2 <100001
    Tmlogetam(:,2) = [5.52;3.91;2.74;1.86;1.17;0.61]; %
elseif H2O >= 3 && H2O < 4 && CO2 >= 50000 && CO2 <100001
    Tmlogetam(:,2) = [5.33;3.77;2.64;1.78;1.10;0.55]; %
elseif H2O >= 4 && H2O < 5 && CO2 >= 50000 && CO2 <100001
    Tmlogetam(:,2) = [5.16;3.65;2.54;1.70;1.04;0.50]; %
elseif H2O >= 5 && H2O <= 10 && CO2 >= 50000 && CO2 <100001
    Tmlogetam(:,2) = [5.00;3.53;2.45;1.63;0.98;0.45]; %
end

Tmrng = 1000:100:1700;
etams = zeros(8,2);
etams(:,1) = Tmrng;
etams(:,2) = interp1(Tmlogetam(:,1),Tmlogetam(:,2),Tmrng,'pchip','extrap');
etams(16) = 0;
etams(:,3) = 10.^(etams(:,2));
% figure(16);clf;
% plot(etams(:,1),etams(:,2));hold on;

logetam = interp1(etams(:,1),etams(:,2),Tm); % log viscosity of magma
etam = interp1(etams(:,1),etams(:,3),Tm); % viscosity of magma (Pa s)
etag = 5.3e-5; % gas viscosity (Pa s) slight difference when introducing CO2
   % has infinitesimal effect

% Initial conditions for varying quantities

pc0 = (rhom0*g*Lc)+(Patm*1e6); % lithostatic pressure at chamber top/conduit base (Pa)
pc0M = pc0/1e6; % conduit pressure (MPa)
C = interp1(SolEx(:,1),SolEx(:,8),pc0M); % proportion of exsolved gas = CO2
H = interp1(SolEx(:,1),SolEx(:,7),pc0M); % proportion of exsolved gas = H2O
Rc0 = (C*RCO2)+(H*RH2O); % Mixed gas constant (J kg^-1 K^-1)
Hmelt = interp1(SolEx(:,1),SolEx(:,3),pc0M)/1e4; % H2O dissolved in the melt (wt%)
Cmelt = interp1(SolEx(:,1),SolEx(:,2),pc0M); % CO2 dissolved in the melt (wt%)
nm0 = (Hmelt+Cmelt)/100; % volatile mass fraction dissolved in the melt
nc0 = ((nc00-nm0)/(1-nm0)); % mass of volatiles exolved from the magma
rhoc0inv = ((nc0*Rc0*Tm)/pc0)+((1-nc0)/rhom0); % inverse mixture density (kg m^-3)
rhoc0 = 1/rhoc0inv; % mixture density (kg m^-3)
% Q = rhoc0*uc0*A; % mass flow rate (kg s^-1)
% us0 = (((Rc0*Tm)/nc0)^0.5)*(nc0+(1-nc0)*(pc0/(rhom0*Rc0*Tm)));
% speed of sound in the mixture (m s^-1)
% M0 = uc0/us0; % Mach number
% phi0 = interp1(SolEx(:,1),SolEx(:,6),pc0M);
% vesicle content (expressed as void fraction)
% if phi0 <= 0.75 % viscosity of mixture (Pa s)
%     eta0 = etam/(1-phi0);
```

```
% elseif phi0 > 0.75
%     eta0 = etag*(1-((1-phi0)/0.62))^-1.56;
% end
% f0 = ((16*eta0)/rhoc0*uc0*D)+f00;% friction factor
% Re0 = (D*rhoc0*uc0)/eta0; % Reynold's number

%% Flare section

rc = rc0*ones(1,Lc+1); % create array for varying radius
rcadd = flarebase*tan(30*(pi/180)); % calculate additional radius from 30 deg crater
rctop = rc0+rcadd; % crater top radius

if flare == 'y' % add flaring radii to array radius
    rc((Lc+1)-flarebase:end) = rc0:rcadd/flarebase:rctop;
end

% figure(99); % visualise conduit
% conduit(1,:) = rc;
% conduit(2,:) = 1:1:Lc+1;
% plot(conduit(1,:),conduit(2,:),'k');axis equal;
% set(gca,'XLim',[0 rctop],'YLim',[0 Lc]);
% hold on;

%% Conduit iterations

% Generate array per depth level
% [ 1  2   3    4    5    6     7      8    9     10   11   12  13  14]
% [ h  P  H2Om CO2m SO2m totm masgas vfgas Rmix invrho rho  uc  us  M ]
%                                          (or rhog)

w = zeros(Lc,17);
q = 8314; % universal gas constant
% s = 6.8e-10;
% b = 0.7;
% ustart = 1;

for k = 1:500

Q = rhoc0*ustart*A0; % mass flow rate (kg s^-1)
Pbase = (rhom0*g*Lc)+(Patm*1e6); % lithostatic pressure at chamber top/conduit base (Pa)
inc = 0;

for i = 1:1:Lc+1

    rcz = rc(i);

    if geometry == 'cir'
        A = pi*rcz^2; % conduit x-sect area (m^2)
        D = rcz*2; % conduit diameter (m)
    elseif geometry == 'lin'
        A = width*length;
        D = width/2;
        % D (for friction calcs) is equivalent to half width of conduit as open
        % ends assumed to have negligable friction
    end

    w(i,15) = (Pbase+inc); % mixture pressure (Pa) 15
    w(i,1)  = Lc-i+1; % depth (m)
    w(i,2)  = ((rhom0*g*w(i,1))+Patm*1e6); % depth pressure (Pa) 3
    w(i,3)  = interp1(SolEx(:,1),SolEx(:,2),w(i,15)/1e6); % wt% H2O 4
    w(i,4)  = (interp1(SolEx(:,1),SolEx(:,3),w(i,15)/1e6))/1e4; % wt% CO2 in melt 5
    w(i,5)  = (interp1(SolEx(:,1),SolEx(:,4),w(i,15)/1e6))/1e4; % wt% SO2 in melt 6
    w(i,6)  = w(i,3)+w(i,4)+w(i,5); % wt% total volatile in melt 7
%     w(i,6)  = s*w(i,15)^b; % wt% total volatile in melt 7
%     w(i,7)  = (nc00-w(i,6))/(1-w(i,6)); % mass gas 8
    w(i,7)  = (nc00-(w(i,6)/100))/(1-(w(i,6)/100)); % mass gas 8
    w(i,8)  = interp1(SolEx(:,1),SolEx(:,6),w(i,15)/1e6); % volume fraction gas 9
    w(i,9)  = (interp1(SolEx(:,1),SolEx(:,7),w(i,15)/1e6)*RH2O)+ ...
```

```
            (interp1(SolEx(:,1),SolEx(:,8),w(i,15)/1e6)*RCO2)+ ...
            (interp1(SolEx(:,1),SolEx(:,9),w(i,15)/1e6)*RSO2); % mixed gas constant 10
   w(i,10) = ((w(i,7)*w(i,9)*Tm)/(w(i,15)))+((1-w(i,7))/rhom0); % inverse mixture density
   w(i,11) = 1/w(i,10); % mixture density (kg m^3) 11
%     w(i,10) = (w(i,2)*1e6*(interp1(SolEx(:,1),SolEx(:,7),w(i,2))*18.02)+ ...
%               (interp1(SolEx(:,1),SolEx(:,8),w(i,2))*44.01)+ ...
%               (interp1(SolEx(:,1),SolEx(:,9),w(i,2))*32.10))/(q*Tm); % gas density
%     w(i,11) = 1/((w(i,7)/w(i,10))+((1-w(i,7))/rhom0)); % mixture density (kg m^3) 11
    w(i,12) = Q/(w(i,11)*A); % ascent velocity 12
    w(i,13) = (sqrt((w(i,9)*Tm)/w(i,7)))*(w(i,7)+(1-w(i,7))* ...
              (((w(i,15))/(rhom0*w(i,9)*Tm)))); % speed of sound in mixture 13
    w(i,14) = w(i,12)/w(i,13); % Mach number 14
    phi = w(i,8);
    if w(i,8) <= 0.75
        w(i,16) = (etam/(1-phi)); % melt viscosity - eta
%         w(i,16) = w(i,16)*(1-(Vx/Vmax))^-2.5; % melt+xtls viscosity - eta
    else
        w(i,16) = (etag*(1-((1-phi)/0.62))^-1.56); % Diez, 2006
%         w(i,16) = (etag*((1-phi)/0.62)^-1.56); % Mastin, 2000
    end
    w(i,17) = ((16*w(i,16))/(w(i,11)*w(i,12)*D))+f00; % friction factor - f

%     if w(i,15) <=Patm*1e6
%         break
%     end

Pbase = w(i,15);
inc = (((-(w(i,11)*g))-((w(i,11)*w(i,12)^2*(w(i,17))/rcz)))/(1-w(i,14)^2));

end

disp(['Initial velocity = ' num2str(ustart) ' m/s : M = ' num2str(w(end,14)) '...
 : Pressure = ' num2str(w(end,15)) ' Pa : vfgas = ' num2str(w(end,8))]);
% disp(['Pressure = ' num2str(w(end,15)) ' Pa : vfgas = ' num2str(w(end,8))]);
% disp(num2str(w(i,2)));
% disp(num2str(w(i,15)));

if planet == 'venus'

    if w(end,15) < Patm*1e6*0.9999
        break
        %ustart = ustart*0.1;
    elseif w(end,15) > Patm*1e6*0.9999 && w(end,15) < Patm*1e6*1.0001
        break
    elseif w(end,15) > Patm*1e6*1.0001

        if w(end,14) <0.5 && w(end,15) < Patm*1e6+(Patm*1e6*0.01)
            ustart = ustart+0.1;
        elseif w(end,14) <0.5 && w(end,15) >= Patm*1e6+(Patm*1e6*0.01)
            ustart = ustart+(10*(1-w(end,14)));
        elseif w(end,14) >=0.5 && w(end,14) < 0.8
            ustart = ustart+(5*(1-w(end,14)));
        elseif w(end,14) >= 0.8 && w(end,14) < 0.9999
            ustart = ustart+((1-w(end,14))/2);
        elseif w(end,14) > 1.0001
            ustart = ustart*0.99999;
        else
            break
        end

    else
        break
    end

elseif planet == 'earth'

    if w(end,15) < Patm*1e6*0.9
        break
```

```
        %ustart = ustart*0.1;
    elseif w(end,15) > Patm*1e6*0.9 && w(end,15) < Patm*1e6*1.1
        break
    elseif w(end,15) > Patm*1e6*1.1

        if w(end,14) <0.5 && w(end,15) < Patm*1e6+(Patm*1e6*0.01)
            ustart = ustart+0.1;
        elseif w(end,14) <0.5 && w(end,15) >= Patm*1e6+(Patm*1e6*0.01)
            ustart = ustart+(1*(1-w(end,14)));
        elseif w(end,14) >=0.5 && w(end,14) < 0.8
            ustart = ustart+(0.5*(1-w(end,14)));
        elseif w(end,14) >= 0.8 && w(end,14) < 0.9999
            ustart = ustart+((1-w(end,14))/2);
        elseif w(end,14) > 1.0001
            ustart = ustart*0.999;
        else
            break
        end

    else
        break
    end

end

end

%% remove values below surface <Patm (ascent stalled in conduit)

[X Y] = find(w(:,15)<Patm*1e6);
w(X,:) = [];
% Mastin_Airey_comparisons

%% Display results for plot and store in matrix

% Generates 3D matrix of surface volume fraction gas (m,n,1), exit vel.
% (m,n,2), mass flow rate (m,n,3), mixture density (m,n,4), pressure
% (m,n,5), and fragmentation depth (m,n,6) in this parameter space:
%   10
%    9
%    8
%  e 7
%  l 6
%  e 5
%  v 4
%    3
%    2
%    1
%    0
%     1200 1300 1400 1500 1600 1700
%               Temp
disp(['planet = ' planet]);
disp(['H2O = ' num2str(H2O) '%']);
disp(['CO2 = ' num2str(CO2) ' ppm']);
disp(['elev = ' num2str(elev) ' km']);
disp(['con radius = ' num2str(rc0) ' m']);
disp(['temp = ' num2str(Tm) ' K']);
disp(['vfgas = ' num2str(w(end,8))]);
disp(['vel = ' num2str(w(end,12)) ' m s^-^1']);
disp(['dense = ' num2str(w(end,11)) ' kg m^-^3']);
disp(['press = ' num2str(w(end,15)) ' Pa']);
disp(['visc = ' num2str(w(end,16)) ' Pa s']);
if w(end,14) > 1.0001
    aa = 'supersonic';
elseif  w(end,14) < 0.9999
    aa = 'subsonic  ';
else
    aa = '    choked';
```

```
end
disp([aa ' at M = ' num2str(w(end,14))]);
disp('-------');

if aa == '    choked'
    Decompressed_Jet
end

xxx = ((Tm-1000)/100)-1;
elevr = 10:-1:0;
r = 1:11;
i = interp1(elevr,r,elev);
% Specify name of matrix (x3 below) to store values to reflect volatile contributions
temp(i,xxx,1) = w(end,8);
temp(i,xxx,2) = w(end,12);
temp(i,xxx,3) = Q;

elev_presH3C0(i) = w(end,15);

%% Plot conduit data

figure(3);
subplot(1,4,1);
plot(w(:,15),w(:,1),'k');set(gca,'YDir','reverse');
title(['Mixture pressure = ' num2str(w(end,15)/1e6) ' MPa']);
subplot(1,4,2);
plot(w(:,8),w(:,1),'k');set(gca,'YDir','reverse');
title(['Volume fraction gas = ' num2str(w(end,8))]);
subplot(1,4,3);
plot(w(:,14),w(:,1),'k');set(gca,'YDir','reverse');
title(['Mach number = ' num2str(w(end,14))]);
subplot(1,4,4);
plot(w(:,12),w(:,1),'k');set(gca,'YDir','reverse');
title(['Velocity = ' num2str(w(end,12)) ' m s^-^1']);
```

Appendix B

```
%% Decompressed_Jet.m

% run Solex and conduit_v7_solex.m prior to execution

nc = w(end,7);
Rc = w(end,9);
pc = w(end,15);
rhom = rhom0;
spb = w(end,6)/100;
uc = w(end,12);
rhoc = w(end,11);

%% Calculate decompressed density

rhod = (Patm*1e6)/(nc00*Rc*Tm);

%% Calculate decompressed velocity

gamma = 1+(((1-nc)*pc)/(nc*Rc*Tm*rhom));

delta = ((nc00-spb)/(nc00^0.5*(nc00-(spb/2)*(1+(pc/(Rc*Tm*rhom))))^0.5));

ud = (((nc00*Rc*Tm)^0.5)*gamma*delta*(1+(nc/(nc00*gamma*delta^2)*(1-(Patm*1e6/pc)))));

%% Calculate decompressed area and radius

Q = rhoc*uc*A;

Ad = Q/(ud*rhod);

rd = (Ad/pi)^0.5;

% Q2 = rhod*ud*Ad; % sanity check
% Ad2 = pi*rd^2; % sanity check

%% Display output

disp(['Mass flux  = ' num2str(Q) ' kg s^-^1']);
disp(['Density  = ' num2str(rhod) ' kg m^-^3']);
disp(['Velocity = ' num2str(ud) ' m s^-^1']);
disp(['Area     = ' num2str(Ad) ' m^2']);
disp(['Radius   = ' num2str(rd) ' m']);
disp('-------');
```

Appendix C

```
%% h_l_calc.m
% set(0,'DefaultFigureWindowStyle','docked');

% clear;
% clf;

% Uncomment lines 42-49 to plot graph iterations
% Much slower; recommend increasing starting l value

% Define the SAR parameters
theta=40;
sigma0_SAR=0.1644;
epsilon=5.2;


% Define the altimeter parameters
rho=0.15;
phi=3.0;


% Don't change these parameters
k=0.12570/(2*pi);
alpha=((epsilon-1)/((cos((theta*pi)/180))+...
    (sqrt(epsilon-sin(((theta*pi)/180)^2))))^2);
r=1000*log(epsilon)/log(1.96);
sigma0_alt=(rho/((phi*(pi/180))^2)/2);


% Starting conditions
l=0.01;


for i=0:1:50000

    W=((l^2/2)*exp(-(k*l*sin((theta*pi)/180))))/...
        (2*k*sin((theta*pi)/180));

    h_SAR=sqrt(sigma0_SAR/(8*k*cos(((theta*pi)/180))^4*(abs(alpha))^2*...
    W*2*k*sin((theta*pi)/180)));

    h_alt=sqrt((rho^2*l^2)/(4*sigma0_alt));

%     plot(i,h_SAR,i,h_alt,i,l);
%     legend(gca,'h_S_A_R','h_a_l_t','l','Location','Best');
%     title(gca,['h_S_A_R = ',num2str(h_SAR),', h_a_l_t = ',num2str(h_alt),', l = ',num2str(l)],...
%  'FontSize',14,'FontName','arial');
%     xlabel('Iteration','FontSize',14,'FontName','arial');
%     ylabel('RMS height, correlation length/m','FontSize',14,'FontName','arial');
%     set(gca,'FontSize',14,'FontName','arial');
%     drawnow;
%     hold on;

    if h_alt>=h_SAR;
```

```
            break
        end

        l=l+0.001;

    end
```